

DESIGN, MODELLING AND ANALYSIS OF A NOVEL IMPLANTABLE BONE  
CONDUCTION HEARING AID WITH A PIEZOELECTRIC ACTUATOR

A THESIS SUBMITTED TO  
THE GRADUATE SCHOOL OF NATURAL AND APPLIED SCIENCES  
OF  
MIDDLE EAST TECHNICAL UNIVERSITY

BY

ANIL KOYUNCU

IN PARTIAL FULLFILLMENT OF THE REQUIREMENTS  
FOR  
THE DEGREE OF DOCTOR OF PHILOSOPHY  
IN  
MECHANICAL ENGINEERING

SEPTEMBER 2022



Approval of the thesis:

**DESIGN, MODELLING AND ANALYSIS OF A NOVEL IMPLANTABLE  
BONE CONDUCTION HEARING AID WITH A PIEZOELECTRIC  
ACTUATOR**

submitted by **ANIL KOYUNCU** in partial fulfillment of the requirements for the degree of **Doctor of Philosophy in Mechanical Engineering Department, Middle East Technical University** by,

Prof. Dr. Halil Kalıpçılar  
Dean, Graduate School of **Natural and Applied Sciences**

\_\_\_\_\_

Prof. Dr. M. A. Sahir Arıkan  
Head of Department, **Mechanical Engineering**

\_\_\_\_\_

Prof. Dr. H. Nevzat Özgüven  
Supervisor, **Mechanical Engineering Dept., METU**

\_\_\_\_\_

Assoc. Prof. Dr. Melin Şahin  
Co-supervisor, **Aerospace Engineering Dept., METU**

\_\_\_\_\_

**Examining Committee Members:**

Prof. Dr. Ender Cığeroğlu  
Mechanical Engineering Dept., METU

\_\_\_\_\_

Prof. Dr. H. Nevzat Özgüven  
Mechanical Engineering Dept., METU

\_\_\_\_\_

Assoc. Prof. Dr. M. Bülent Özer  
Mechanical Engineering Dept., METU

\_\_\_\_\_

Assoc. Prof. Dr. Can U. Doğruer  
Mechanical Engineering Dept., Hacettepe University

\_\_\_\_\_

Assoc. Prof. Dr. Tuncay Karaçay  
Mechanical Engineering Dept., Gazi University

\_\_\_\_\_

**Date:** 01/09/2022

**I hereby declare that all information in this document has been obtained and presented in accordance with academic rules and ethical conduct. I also declare that, as required by these rules and conduct, I have fully cited and referenced all material and results that are not original to this work.**

Name, Last Name : Anıl Koyuncu

Signature :

## **ABSTRACT**

### **DESIGN, MODELLING AND ANALYSIS OF A NOVEL IMPLANTABLE BONE CONDUCTION HEARING AID WITH A PIEZOELECTRIC ACTUATOR**

Koyuncu, Anıl

Ph.D., Department of Mechanical Engineering

Supervisor: Prof. Dr. H. Nevzat Özgüven

Co-supervisor: Assoc. Prof. Dr. Melin Şahin

September 2022, 184 Pages

This thesis study proposes a novel bone conduction (BC) transducer design, which intends to overcome the drawbacks of conventional bone conduction hearing aids (BCHAs). A piezoelectric actuator design with a rhombus-type mechanical amplifier is chosen as a BC transducer in the first step, and a commercial amplified piezoelectric actuator (APA) is selected for trials. The dynamics of the mechanical amplifier and embedded stacked piezoelectric actuator are formulated separately based on linear analytical approaches. The output displacement of the coupled system is then calculated using linear vibration analysis under low harmonic voltage inputs. Based on the linear analytical model, a new APA is designed as a BC transducer with an attached tip mass, and the new APA prototype is manufactured.

Constant-voltage amplitude stepped-sine tests indicate strong softening nonlinearity with the jump phenomenon observed in the frequency response at high voltage levels.

Therefore, an accurate dynamical model of an APA is obtained by using a recently developed nonlinear system identification method, namely Response-Controlled stepped-sine Testing (RCT). Then the describing function of the predicted nonlinearity is identified by using describing surface method (DSM), and a nonlinear multi-degree of freedom (MDOF) model is obtained by substructure coupling of the APA and the attached tip mass. Based on the simulation results of the nonlinear MDOF BCHA model, the tip mass of the BCHA prototype is adjusted. The transmitted force-frequency response tests are performed with the optimized BCHA prototype attached to Brüel and Kjær (B&K) type 4930 artificial mastoid in order to validate the nonlinear MDOF BCHA model and compare the performance of the proposed BC transducer design with a conventional electromagnetic bone vibrator (Radioear B71). Finally, hearing threshold tests are performed on normal hearing participants and hearing-impaired patients with the BCHA prototype and the B71 bone vibrator. It is observed that the difference in the threshold level spectrum between the BCHA prototype and the B71 bone vibrator is consistent with the difference in the transmitted force level spectrum obtained from the artificial mastoid tests

Consequently, in the thesis study, a novel BCHA transducer is proposed based on a miniature stacked piezoelectric actuator used as a BC transducer for the first time. The sophisticated dynamics of the proposed BCHA transducer are modeled by employing linear modeling and nonlinear identification. By virtue of recently proposed nonlinear dynamic modeling techniques, valuable contributions have been made to the limited body of knowledge on the nonlinear dynamics of APAs. It is demonstrated that the nonlinear dynamics of the BCHA can be captured accurately by the proposed methodology, which can be presented as an exceptional method in the pre-clinical performance evaluation of BC hearing implants.

**Keywords:** Bone Conduction Transducer, Amplified Piezoelectric Transducer, Nonlinear Identification, Response Controlled Stepped-sine Testing, Describing Surface Method, Describing Function Method, Nonlinear Structural Coupling

## ÖZ

# ÖZGÜN BİR PİEZOELEKTRİK EYLEYİCİLİ KEMİK İLETİMLİ İMLANT İŞİTME CİHAZININ TASARIM, MODELLEME VE ANALİZİ

Koyuncu, Anıl

Doktora, Makine Mühendisliği Bölümü

Tez Yöneticisi: Prof. Dr. H. Nevzat Özgüven

Eş Tez Yöneticisi: Doç. Dr. Melin Şahin

Eylül 2022, 184 Sayfa

Bu tez çalışması, geleneksel kemik iletimli işitme cihazlarının (KİİC) dezavantajlarını ortadan kaldırmayı amaçlayan yeni bir kemik iletimli (Kİ) dönüştürücü tasarımı önermektedir. İlk adımda Kİ dönüştürücüsü olarak eşkenar dörtgen tipi mekanik yükselticiye sahip piezoelektrik eyleyici tasarımı tercih edilmiştir ve denemeler için ticari bir mekanik güçlendirilmiş piezoelektrik eyleyici (MGPE) seçilmiştir. Mekanik yükselticinin ve gömülü katmanlı piezoelektrik eyleyicisinin dinamikleri, doğrusal analitik yaklaşımlara göre ayrı ayrı formüle edilmiştir. Daha sonra, birleştirilen sistemin çıkış deplasmanları düşük harmonik gerilim girdileri altında yapılan doğrusal titreşim analizleriyle hesaplanmıştır. Kİ dönüştürücü olarak ucuna kütle bağlanmış yeni bir MGPE doğrusal analitik modele dayanarak tasarlanmıştır ve tasarlanan yeni MGPE prototipi üretilmiştir.

Yapılan sabit gerilim genlikli kademeli sinüs testlerinde, frekans yanıtında yüksek gerilim seviyelerinde gözlemlenen atlama durumu yumuşayan karakterde güçlü bir doğrusal olmama durumunu göstermiştir. Bu nedenle, MGPE'nin dinamik modelini doğru elde edebilmek için yakın zamanda geliştirilmiş bir doğrusal olmayan sistem

tanımlama yöntemi olan cevap kontrollü kademeli sinüs testi (CKT) kullanılmıştır. Daha sonra, tanımlama yüzeyi yöntemi (TYY) kullanılarak tahmin edilen doğrusal olmama fonksiyonu teşhis edilmiştir ve MGPE ile ona bağlı uç kütlelerinin yapısal olarak birleştirilmesi sonucunda doğrusal olmayan çok serbestlik dereceli (ÇSD) model elde edilmiştir. Doğrusal olmayan ÇSD KİİC modeli kullanılarak yapılan Kİ simülasyonlarının sonuçlarına göre KİİC prototipinin uç kütlesi değiştirilmiştir. Doğrusal olmayan ÇSD KİİC modelinin geçerliliğini göstermek ve önerilen Kİ dönüştürücü tasarımını geleneksel bir elektromanyetik dönüştürücü (Radioear B71) ile karşılaştırmak için KİİC prototipini Brüel&Kjær (B&K) tip 4930 yapay mastoide bağlayarak aktarılan kuvvet frekans cevabı ölçülmüştür. Son olarak, KİİC prototipi ve B71 kemik titreştiricisi ile normal işitmeye sahip katılımcılar ve işitme engelli hastalarda işitme eşiği testleri gerçekleştirilmiştir. KİİC prototipi ile B71 kemik titreştiricisi arasındaki eşik seviyesi spektrumu farkının yapay mastoid testlerinden elde edilen iletilen aktarılan kuvvet seviyesi spektrumu farkıyla tutarlı olduğu gözlemlenmiştir.

Sonuç olarak, bu tez çalışmasında, ilk kez bir minyatür katmanlı tip piezoelektrik eyleyicinin Kİ dönüştürücü olarak kullanılmasına dayalı yeni bir KİİC dönüştürücüsü önerilmiştir. Önerilen KİİC dönüştürücüsünün karmaşık dinamikleri, doğrusal modelleme ve doğrusal olmayan tanımlama kullanılarak modellenmiştir. Yakın zamanda geliştirilmiş doğrusal olmayan dinamik modelleme teknikleri sayesinde, MGPE'lerin doğrusal olmayan dinamikleri hakkındaki sınırlı bilgi birikimine değerli katkılar yapılmıştır. KİİC'nin doğrusal olmayan dinamiklerinin önerilen yöntem tarafından doğru şekilde yakalanabilmesi Kİ işitme implantlarının klinik öncesi performanslarının değerlendirmesinde istisnai bir yöntem olarak sunulabileceğini göstermiştir.

**Anahtar kelimeler:** Kemik İletimli Dönüştürücü, Güçlendirilmiş Piezoelektrik Eyleyici, Doğrusal Olmayan Tanımlama, Cevap Kontrollü Kademeli Sinüs Testi, Tanımlama Yüzeyi Yöntemi, Tanımlama Fonksiyonu Yöntemi, Doğrusal Olmayan Yapısal Birleştirme.



To Müge and Eylül

## ACKNOWLEDGEMENTS

I would like to express my sincere appreciation to my supervisor, Prof. Dr. H. Nevzat Özgüven and my co-supervisor Assoc. Prof. Dr. Melin Şahin for their boundless help, excellent supervision and leading guidance from beginning to end of thesis work.

The author also would like to thank and Prof. Dr. Ender Ciğeroğlu, Assoc. Prof. Dr. M. Bülent Özer, Assoc. Prof. Dr. Can U. Doğruer and Assoc. Prof. Dr. Tuncay Karaçay for their guidance as members of the thesis progress committee.

I am especially thankful to my dear wife Müge for her love, support, patience, and encouragement to complete this study.

I dedicate this thesis to my lovely daughter Eylül, whose birth has brought wonderful fun, great motivation and bright inspiration into my life.

I would like to express my special thanks to my colleagues, Dr. Taylan Karağaçlı and Dr. Kenan Ahıska, for their continuous technical and moral support throughout this work.

I would like to thank my managers, Halim Çağlayan and Şaban Karakaya, for giving me the opportunity to use the computational and testing capabilities in ASELSAN Inc.

I would like to thank Assist. Prof. Asuman Alınçık and audiologist Berfin Eylül Aydemir from Başkent University Department of Audiology for helping me with hearing tests.

The financial support provided by ASELSAN Inc. is thankfully acknowledged

## TABLE OF CONTENTS

ABSTRACT .....	v
ÖZ .....	vii
ACKNOWLEDGEMENTS .....	x
TABLE OF CONTENTS .....	xi
LIST OF TABLES .....	xiv
LIST OF FIGURES .....	xv
LIST OF SYMBOLS .....	xxi
LIST OF ABBREVIATIONS .....	xxv
CHAPTERS	
1. INTRODUCTION.....	1
1.1. Hearing Physiology and Deafness .....	1
1.2. Hearing Aids .....	2
1.3. Bone Conduction Hearing Aids (BCHA) .....	4
1.3.1. Electromagnetic Bone Conduction Transducers .....	8
1.3.2. Literature Survey On Piezoelectric Bone Conduction Transducers ....	12
1.4. Motivation and Scope of the Thesis .....	17
1.5. Outline of the Thesis.....	18
2. DESIGN AND MODELING OF PIEZOELECTRIC TRANSDUCER FOR IMPLANTABLE BONE CONDUCTION HEARING AIDS .....	23
2.1. Theory of the Piezoelectric Actuator Modeling .....	27
2.1.1. Formulation of an RCM Using Analytical Dynamics .....	28
2.1.2. Eigensolution for the RCM.....	30
2.1.3. Comparison of Analytical Model of RCM via FEA.....	36

2.1.4. Analytical Formulation of the MSPA.....	37
2.1.5. Comparison of Analytical Model of MSPA via FEA.....	39
2.1.6. Coupling of the RCM and the MSPA using Dynamic Substructuring	41
2.2. Experimental Verification of Dynamic Model of the APA .....	44
3. OPTIMIZATION OF THE PIEZOELECTRIC-BASED BONE CONDUCTION TRANSDUCER.....	49
4. EXPERIMENTAL MODAL ANALYSIS OF NONLINEAR AMPLIFIED PIEZOELECTRIC ACTUATORS BY USING RESPONSE-CONTROLLED STEPPED-SINE TESTING.....	63
4.1. Methodology of the Experimental Modal Analysis with RCT.....	68
4.2. Experimental Work.....	71
4.2.1. Experimental Setup.....	71
4.2.2. Results of Constant-Voltage Stepped Sine Tests.....	73
4.2.3. Identification of Nonlinear Modal Parameters by Using the RCT Method .....	74
4.2.4. Validation of the Nonlinear Modal Model .....	78
5. NONLINEAR IDENTIFICATION AND EXPERIMENTAL MODAL ANALYSIS OF THE BONE CONDUCTION ACTUATOR BY USING DESCRIBING SURFACE METHOD .....	83
5.1. The Theory of the Describing Function and the Describing Surface Methods .....	84
5.2. Experimental Studies on the Proposed BCHA .....	88
5.2.1. Determination of Piezoelectric Actuation Force .....	91
5.2.2. Preliminary Constant-Voltage Stepped Sine Tests.....	95
5.2.3. Describing Surface Identification by using RCT Method .....	96

5.2.4. Validation of Identified Describing Function.....	99
6. ELECTRO-ACOUSTIC PERFORMANCE OF THE NOVEL BONE CONDUCTION HEARING AID.....	103
6.1. Performance Evaluation Tests on the Artificial Mastoid Test Setup.....	104
6.1.1. The Constant-Voltage Stepped Sine Tests .....	106
6.1.2. Identification of Nonlinear Modal Parameters by using the RCT Method .....	107
6.1.3. Validation of Nonlinear Modal Model and Describing Functions of the Identified Nonlinearity .....	111
6.2. Performance Simulation of the BCHA on the Skull Simulator .....	112
6.3. Evaluation of the Hearing Perception of the BCHA.....	113
7. SUMMARY AND CONCLUSIONS .....	117
7.1. General Conclusions .....	117
7.2. Novel Contributions.....	120
7.3. Recommendation for Future Work.....	121
REFERENCES.....	123
APPENDICES .....	139
A. Boundary Conditions of the RCM.....	139
B. Derivation of the Transfer Matrices of the RCM .....	143
C. Proof of the Normal Mode Orthogonality for the RCM.....	153
D. Derivation Of The Transfer Matrices of the MSPA .....	159
E. Published Papers During Phd .....	163
CURRICULUM VITAE .....	183

## LIST OF TABLES

### TABLES

<b>Table 2.1</b>	Geometric Dimensions of the Beam Segments of the RCM (APA35XS).....	36
<b>Table 2.2</b>	First four in plane modes of vibration of the fixed-free RCM .....	37
<b>Table 2.3</b>	Physical Properties of the MSPA .....	40
<b>Table 2.4</b>	The first five in-plane modes of the MSPA.....	40
<b>Table 2.5</b>	Fixed-free resonance frequency of the APA.....	47
<b>Table 3.1</b>	Optimized Parameters of the Amplified Piezoelectric Actuator	59
<b>Table 6.1</b>	Bone conduction hearing treshold difference between B71 and BCHA.....	115
<b>Table B.1</b>	The constants of the first beam segment for the fixed-free and free-free conditions .....	145

## LIST OF FIGURES

### FIGURES

<b>Figure 1.1</b>	Anatomy of the human ear [1].....	1
<b>Figure 1.2</b>	Working principle of (a) conventional [8], (b) bone conduction [9] and (c) implantable [10] hearing aids.....	3
<b>Figure 1.3</b>	Illustration of a cochlear implant [12] .....	4
<b>Figure 1.4</b>	The family of bone-conduction devices .....	4
<b>Figure 1.5</b>	Conventional BCHAs a) BC headband[14], b) BC eyeglasses [15] ..	5
<b>Figure 1.6</b>	a) Conventional BC device coupled with static pressure b) bone-anchored hearing aid (BAHA) attached with screwed abutment [21]	6
<b>Figure 1.7</b>	a) a Sophono system, b) bone conduction implant (BCI) [21].....	7
<b>Figure 1.8</b>	Design and cross-sectional view of B71 electromagnetic transducer [30].....	8
<b>Figure 1.9</b>	Cross-sectional view and magnetic circuitry of B81 electromagnetic transducer [31] .....	10
<b>Figure 1.10</b>	The measurement setup of the electrodynamic transducers [31] .....	11
<b>Figure 1.11</b>	Mean THDs of B71 and B81 under 1 V <sub>rms</sub> input voltage[31] .....	11
<b>Figure 1.12</b>	Mean frequency responses of B71 and B81 under 1 V <sub>rms</sub> input voltage [31].....	12
<b>Figure 1.13</b>	Force-deflection characteristic of piezoelectric and electromagnetic transducers [32] .....	13
<b>Figure 1.14</b>	A Piezoelectric BC transducer prototype [33].....	13
<b>Figure 1.15</b>	a) Rectangular piezoelectric bender at Point A and BAHA abutment at Point B, b) circular piezoelectric bender at Point B[34].....	14
<b>Figure 1.16</b>	a) Perspective view of the bone conductor transducer, b) exploded view of the bone conductor transducer [38] .....	15

<b>Figure 1.17</b>	Force response of different THUNDER transducers and B71 [38]..16
<b>Figure 1.18</b>	Section view of the bone conductor transducer with piezoelectric actuator: a) undeformed position, b) deformed position[39].....17
<b>Figure 1.19</b>	General flowchart of the thesis .....22
<b>Figure 2.1</b>	a) Lever-type, b) Flextensional-type, c) Moonie-type, d) Rainbow-type, e) Cymbal-type Flextensional Compliant Mechanisms[51] ....24
<b>Figure 2.2</b>	a) Bridge-type, b) rhombus-type flextensional compliant mechanisms[53] .....25
<b>Figure 2.3</b>	Working principle of an amplified piezo-actuator (APA) .....25
<b>Figure 2.4</b>	Photograph of the Amplified Piezo-actuator-APA35XS by Cedrat Technologies [58] .....27
<b>Figure 2.5</b>	The half APA models: a) fixed-free b) free-free end conditions .....28
<b>Figure 2.6</b>	a) Planar beams connected in series, b) misaligned planar beams ...29
<b>Figure 2.7</b>	The first four in-plane modes of vibration of the fixed-free RCM: the first mode (a), the second mode (b), the third mode (c), and the fourth mode (d).....37
<b>Figure 2.8</b>	8-layer FE model of the half MSPA .....40
<b>Figure 2.9</b>	Comparison of harmonic responses at the free end of the MSPA obtained from the analytical and FE model .....41
<b>Figure 2.10</b>	Free-body diagrams and dynamic coupling of the RCM and the MSPA models .....42
<b>Figure 2.11</b>	(a) APA35XS fixed from its base to the testing table, and (b) non-contact displacement measurement with a laser displacement sensor .....45
<b>Figure 2.12</b>	FEM of the APA (APA35XS) .....45
<b>Figure 2.13</b>	Calculated and measured tip displacement frequency responses .....46
<b>Figure 3.1</b>	The pathways contributing to BC hearing [70] .....50
<b>Figure 3.2</b>	The mechanical impedance (a) amplitude and (b) phase of live subjects, the mean values, and the artificial mastoid [75] .....51
<b>Figure 3.3</b>	Mechanical impedance measurement setup from Cortes's study [75]:



	a) top view, b) back view.....	52
<b>Figure 3.4</b>	Comparison of the measured stimulation force applied on the live subjects (mean values) and the artificial mastoid [75] .....	53
<b>Figure 3.5</b>	The calibration arrangement of a BC transducer with the artificial mastoid.....	54
<b>Figure 3.6</b>	Measured a) mechanical impedance and b) phase response of the artificial mastoid .....	54
<b>Figure 3.7</b>	The schematic view of the artificial mastoid test setup.....	55
<b>Figure 3.8</b>	The reference equivalent threshold force levels (RETFLs)[80].....	56
<b>Figure 3.9</b>	The free-body diagram of the APA with a tip mass attached to the artificial mastoid .....	57
<b>Figure 3.10</b>	The frequency response curves of B71(measured) and APA35XS (calculated) transducers with different tip masses.....	58
<b>Figure 3.11</b>	Comparison of the frequency response curves of the B71(measured), APA35XS (calculated) with different tip masses, and the optimized BC transducer (calculated) .....	60
<b>Figure 3.12</b>	a) The design of the optimized APA b) the prototype of the optimized APA .....	61
<b>Figure 3.13</b>	a) The design of the new BC implant b) cross-sectional view of the new BC implant .....	61
<b>Figure 3.14</b>	Outer dimensions of the new BC implant design a) top view b) front view ( <i>all the dimensions in mm</i> ).....	62
<b>Figure 4.1</b>	Operation modes of piezoelectric actuators: a) the stacked type in d33 mode, b) the patch type in d31 mode.....	64
<b>Figure 4.2</b>	Schematic view of the experimental setup .....	71
<b>Figure 4.3</b>	FRFs measured by constant-voltage stepped-sine testing .....	73
<b>Figure 4.4</b>	Quasi-linear constant-response FRFs measured by RCT .....	75
<b>Figure 4.5</b>	Comparison of the constant-response FRF synthesized by using the identified modal parameters with the one measured by RCT .....	76
<b>Figure 4.6</b>	Variation of the modal parameters corresponding to the nonlinear	

	normal mode of the APA35XS with respect to the response level: a) Natural frequency, b) modal damping ratio.....	77
<b>Figure 4.7</b>	Variation of the modal constant corresponding to the nonlinear normal mode of the APA35XS with respect to the response level.....	78
<b>Figure 4.8</b>	a) Harmonic excitation voltage spectra of the APA measured during RCT, b) HFS of the free end constructed by combining harmonic excitation voltage spectra with linear interpolation.....	79
<b>Figure 4.9</b>	Comparison of constant-voltage frequency response curves extracted from HFS with the ones synthesized by using nonlinear modal parameters.....	80
<b>Figure 4.10</b>	Comparison of the backbone curve extracted from HFS with the one obtained by using nonlinear modal parameters .....	80
<b>Figure 5.1</b>	a) Schematic view of the proposed BCHA design, b) photograph of the BCHA prototype under test .....	89
<b>Figure 5.2</b>	Schematic view of the experimental test setup.....	90
<b>Figure 5.3</b>	The linear FRFs of the tip mass on the APA .....	91
<b>Figure 5.4</b>	HFS of the free end of the stand-alone APA is constructed by combining harmonic excitation voltage spectra with linear interpolation.....	92
<b>Figure 5.5</b>	The point FRFs of the coordinate $p$ for the underlying linear APA without tip mass .....	94
<b>Figure 5.6</b>	Relation between analytical force-frequency response and experimentally obtained voltage frequency response under low level of oscillations a) with tip mass b) without tip mass.....	95
<b>Figure 5.7</b>	FRFs measured by constant-voltage stepped-sine testing .....	96
<b>Figure 5.8</b>	Quasi-linear FRFs of the tip mass measured by RCT at various constant displacement amplitudes .....	97
<b>Figure 5.9</b>	Real (a) and imaginary (b) parts of the partial derivative of the describing surface of the nonlinearity.....	98
<b>Figure 5.10</b>	Real (a) and imaginary (b) parts of the describing surface of	

	nonlinearity .....	98
<b>Figure 5.11</b>	Real (a) and imaginary (b) parts of the describing function of nonlinearity .....	99
<b>Figure 5.12</b>	Comparison of tip point frequency responses of the APA with 10 g tip mass frequency responses obtained by the HFS, DSM, and DFM at 1 V (a) and 3 V (b) constant voltage levels .....	100
<b>Figure 5.13</b>	Comparison of tip point frequency responses of the APA with 16 g tip mass frequency responses obtained by the HFS, DFM, and voltage-controlled stepped sine tests at 1 V (a) and 3 V (b) constant voltage levels .....	101
<b>Figure 6.1</b>	The force transmitted from the B71 and the BCHA prototype to the artificial mastoid under 1 V <sub>rms</sub> input voltage level .....	105
<b>Figure 6.2</b>	A comparison of THDs of B71 and the BHCA prototype was driven at 1 V <sub>rms</sub> input voltage level.....	106
<b>Figure 6.3</b>	Transmitted force-frequency response measured by constant-voltage stepped-sine testing.....	107
<b>Figure 6.4</b>	Transmitted force-frequency response measured by constant-voltage stepped-sine testing.....	108
<b>Figure 6.5</b>	Transmitted force frequency responses around fundamental resonance frequency: a) measured by constant-voltage stepped-sine testing, b) constant-response FRFs extracted from the HFS .....	109
<b>Figure 6.6</b>	Variation of the modal parameters of the quasi-linear FRFs with respect to the transmitted force level: a) natural frequency, b) modal damping ratio .....	110
<b>Figure 6.7</b>	Variation of the modal constants of the quasi-linear FRFs with respect to the transmitted force level .....	110
<b>Figure 6.8</b>	Comparison of the measured transmitted force frequency responses with ones synthesized by using nonlinear modal parameters and simulated with the identified DF .....	111
<b>Figure 6.9</b>	a) The photograph and b) mechanical impedance of the miniaturized	

	artificial mastoid TU-1000 [137] .....	112
<b>Figure 6.10</b>	The force transmitted from the BCHA and the BCI to the artificial mastoid under 1 V <sub>rms</sub> input voltage level .....	113
<b>Figure 6.11</b>	a) A photograph from a hearing threshold test, b) an audiogram of left ear air and bone threshold values[141] .....	114

## LIST OF SYMBOLS

$\bar{A}_{pjr}$	Modal constants of $r^{th}$ mode
$A_i$	Cross-section area of the $i^{th}$ beam
$A_{jk}$	Accelerance of the point $j$ when excited from point $k$
$\mathbf{B}_i$	Transfer matrix between the constant vector and eigenfunction state vector for $i^{th}$ beam segment.
$c$	Viscous damping coefficient
$c_r$	Modal damping coefficient of $r^{th}$ mode
$c_s$	Compliance of the suspension spring
$[C]$	Viscous damping matrix
$\bar{d}_0$	Electromechanical coefficient of the MSPA
$e_{33}$	Axial electromechanical coupling coefficient of the piezoelectric actuator
$E$	Modulus of elasticity
$f_r$	Resonance frequency of an electromagnetic transducer
$\{f\}$	Generalized harmonic forcing vector
$\{F\}$	Amplitude vector of generalized harmonic force
$\{f_{NL}\}$	Internal nonlinear restoring forcing vector
$F_{tr}$	Amplitude of the harmonic force transmitted to the artificial mastoid

$i$	Unit imaginary number
$I$	Second moment of the cross-section area
$\mathbf{H}$	Receptance matrix
$k_r$	Modal stiffness of the $r^{th}$ mode
$[K]$	Stiffness matrix
$m_t$	Equivalent moving mass of the transducer
$m_r$	Modal mass of the $r^{th}$ mode
$M_i$	Bending moment acting on the $i^{th}$ beam
$[M]$	Mass matrix
$N$	Amplitude of the internal nonlinear restoring force vector
$N_r$	Harmonic forcing vector of $r^{th}$ generalized coordinate
$N_p$	Number of layers in piezoelectric stack
$P_i$	Axial force acting on the $i^{th}$ beam
$q_r$	$r^{th}$ generalized coordinate
$Q_i$	Shear force acting on the $i^{th}$ beam
$\mathbf{R}$	Coefficient matrix of the characteristic equation
$t$	Time
$\mathbf{T}_i$	Transfer matrix between the constant vector of $i^{th}$ beam segment and eigenfunction state vector of the $(i - 1)^{th}$ beam segment
$u_i$	Longitudinal displacement of the $i^{th}$ beam

$u_p$	Longitudinal displacement of the stacked piezoelectric actuator
$w_i$	Transverse displacement of the $i^{th}$ beam
$w_p$	Transverse displacement of the stacked piezoelectric actuator
$x_i$	Generalized spatial variable of the $i^{th}$ beam
$x_p$	Generalized spatial variable of the stacked piezoelectric actuator
$\{x\}$	Generalized displacement vector
$\{\dot{x}\}$	Generalized velocity vector
$\{\ddot{x}\}$	Generalized acceleration vector
$\{X\}$	Amplitude vector of complex steady state harmonic displacements
$V_{in}$	Input voltage
$y_i$	Generalized spatial variable of the $i^{th}$ beam
$\mathbf{Z}$	Dynamic stiffness matrix
$[\Delta]$	Nonlinearity matrix
$\bar{\Lambda}_i$	Transfer matrix between the constant vector of $i^{th}$ beam segment and the constant vector of the $(i + 1)^{th}$ beam segment
$\eta_r$	Modal damping constant of the $r^{th}$ mode
$\lambda$	Eigenvalue constant
$\rho$	Density
$\nu$	Describing function representation of the nonlinearity
$\bar{\nu}$	Modified describing function representation of the nonlinearity

$\theta_i$	Generic inclination angle between the $i^{th}$ and $(i - 1)^{th}$ beam segments
$\phi_0$	Static magnetic flux
$\phi_{\sim}$	Dynamic magnetic flux
$\omega$	Frequency



## LIST OF ABBREVIATIONS

AC	Air conduction
AM	Artificial mastoid
AP	Audio processor
APA	Amplified piezoelectric actuator
B&K	Brüel&Kjaer
BAHA	Bone anchored hearing aids
BBC	Bridging bone conductor
BC	Bone conduction
BCHA	Bone conduction hearing aid
BCI	Bone conduction implant
BEST	Balanced electromagnetic separation transducers
C-BEST	Capsuled balanced electromagnetic separation transducers
DF	Describing Function
DFM	Describing function method
DHL	Disabling hearing loss
DSM	Describing surface method
DSP	Digital signal processor
DOF	Degree of freedom
EMI	Electromagnetic interference
FE	Finite element

FEA	Finite element analysis
FEM	Finite element method
FRF	Frequency response function
HFS	Harmonic force surface
HL	Hearing loss
MDOF	Multi degree of freedom
MSPA	Multi-layered stacked piezoelectric actuator
NNM	Nonlinear normal mode
PLL	Phase-locked-loop
PZT	Piezoceramic material lead-zirconate-titanate
PZTA	Piezoelectric transduction actuator
RCM	Rhombus-type flextensional compliant mechanisms
RCT	Response controlled stepped-sine testing
SPAHA	Subcutaneous piezoelectric attached hearing actuator
THD	Total harmonic distortion
RETFL	Reference equivalent threshold force level
WHO	World Health Organization





## CHAPTER 1

### INTRODUCTION

#### 1.1. Hearing Physiology and Deafness

Hearing is a process of perceiving sounds by transducing sound waves into electrical signals to be transmitted to the auditory section of the brain. Ears are the transducers that convert sound vibrations into nerve impulses. The anatomy of the human ear is illustrated in Figure 1.1.

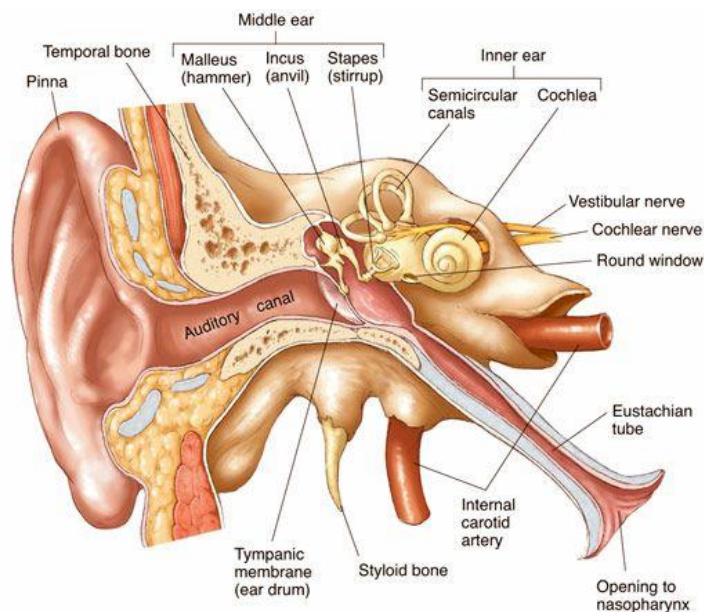


**Figure 1.1** Anatomy of the human ear [1]

Sound waves are collected by the pinna and transferred to the auditory canal. Collected sound waves propagate through the auditory canal, making the tympanic membrane (or ear drum) vibrate. Vibrations of the tympanic membrane are transferred from the middle ear to the cochlea by means of three little bones named the malleus, incus, and

stapes (ossicular chain). Malleus is also connected to a part of the temporal bone known as mastoid bone. The cochlea (inner ear) transduces sound vibrations into electrical signals and transmits signals to the brain [2].

Audible sound frequency ranges from 20 Hz to 20 kHz for humans [3]. Humans are most sensitive to sound forms having frequencies between 3 kHz and 4 kHz due to the resonating structure of the ear canal [2]. The sound intensity range is between 0 and 100 dB for comfortable hearing.

Mild, moderate, or profound hearing deficiencies are called hearing impairment, hearing loss, or deafness. 40 dB and 30 dB hearing losses with respect to the better hearing ear are defined as disabling hearing loss (DHL) for adults and children, respectively [4]. According to World Health Organization (WHO) report, in 2020, 430 million people (over 5% of the world's population) suffered from DHL [5]. Hearing loss can be categorized as conductive, sensorineural, and mixed hearing loss [6]. Conductive hearing loss describes hearing problems caused by improper conduction of sound waves from the outer ear to the inner ear. Sensorineural hearing loss refers to hearing problems in the inner ear and auditory nerve pathways.

Hearing tests (or audiometric tests) are performed to diagnose a patient's hearing loss. Levels of audible sounds are measured at particular frequencies for each ear during the test. Then, the measured levels are compared with threshold values representing a healthy ear's hearing level in decibels. The recommended procedure for pure-tone audiometry is explained in the report published by the British Society of Audiology [7].

## **1.2. Hearing Aids**

Conductive hearing loss problems can be fixed with medical or surgical treatments. Conventional hearing aids, BC devices, and implantable hearing aids can be used for conductive hearing loss, depending on the hearing loss diagnosis. Conventional hearing aids convey sounds to the middle ear via air conduction. A conventional hearing device captures sounds from environments and transmits the amplified sounds

into the ear canal (Figure 1.2a). BC devices are used when air conduction of the sound is not possible in the ear. The working principle of a BC device is to generate sound vibrations in the middle ear by vibrating the mastoid bones of the skull (Figure 1.2b). On the other hand, implantable hearing aids transmit sounds directly to the cochlea by vibrating the bones of the middle ear (Figure 1.2c).

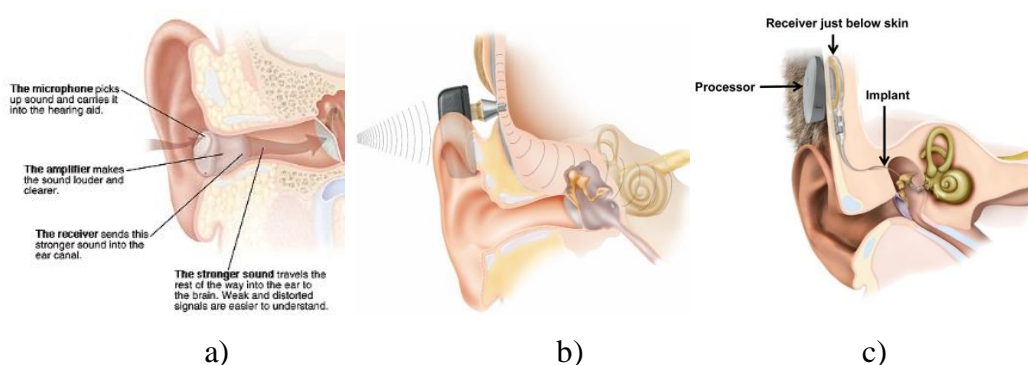


**Figure 1.2** Working principle of (a) conventional [8], (b) bone conduction [9] and (c) implantable [10] hearing aids

More sophisticated treatments need to be utilized for sensorineural hearing loss patients. Cochlear implants are the most popular surgical treatment for inner ear problems. Cochlear implants have external and internal parts. The external part of the implant collects sounds from the environment and processes them. The processed sounds are transmitted to the internal part of the cochlear implant and converted into electric impulses. An electrode array transfers electric impulses to various auditory nerve locations [11]. Although the brain cannot perceive normal hearing, a deaf patient can understand speech with a cochlear implant. The external and internal parts of a cochlear implant are illustrated in Figure 1.3.

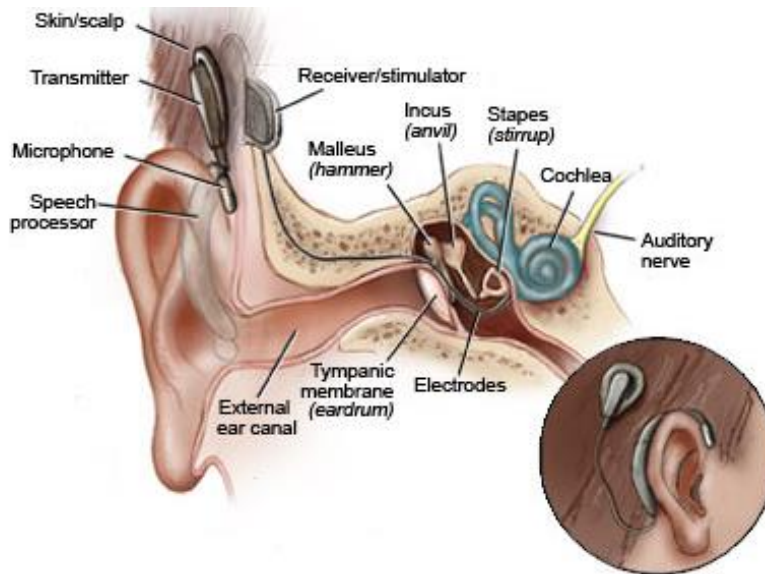


**Figure 1.3** Illustration of a cochlear implant [12]

### 1.3. Bone Conduction Hearing Aids (BCHA)

There are four types of bone conduction hearing aids (BCHA) commonly used by conductive hearing loss patients:

- Conventional bone conduction (BC) hearing devices,
- Bone anchored hearing aids (BAHA),
- Sophono systems,
- Bone conduction implants (BCI).

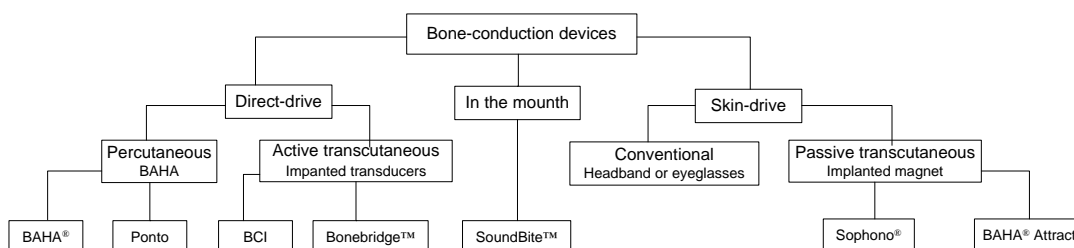


**Figure 1.4** The family of bone-conduction devices



Conventional BC hearing devices have a microphone and sound processor, like air conduction (AC) hearing aids. However, BC devices excite the skull with a micro shaker (transducer) instead of air. The patient wears conventional BC devices with flexible headbands (Figure 1.5a) or template tips of eyeglasses (Figure 1.5b). Reinfeldt et al. comment that to efficiently transfer vibration to the skull, the transducer should be placed on the skin with a significant static pressure, which can cause discomfort and some skin tissue problems, illustrated in Figure 1.6a [13]. It is expressed in [13] that the damping effect of the skin also reduces the transmissibility of device sensitivity at higher frequencies, which can be considered a significant drawback. Since the microphone and the transducer are packaged closely in conventional BC devices, transmitted sound from the transducer can also be collected by the microphone and yield disturbance in the received sound of the microphone.



**Figure 1.5** Conventional BCHAs a) BC headband[14], b) BC eyeglasses [15]

Bone-anchored hearing aid (BAHA) transmits sound waves directly to the mastoid by employing an attached titanium abutment [16]. The abutment is screwed to the mastoid surgically. BAHA presents a single device that contains a microphone, battery, digital signal processor (DSP), and an electromagnetic transducer (Figure 1.6b). BAHA system has better wearing comfort and sound transmissibility compared with conventional BC systems [17]. BAHAs are used for patients who have single-sided deafness, middle ear problems, and external ear malformations. BAHA surgeries are

not suggested for children younger than 4 or 5 years of age due to thin skull bones [18]. It is reported that BAHA systems need daily maintenance at the abutment zone since permanent skin penetration may cause some hard tissue and soft tissue problems [19, 20].

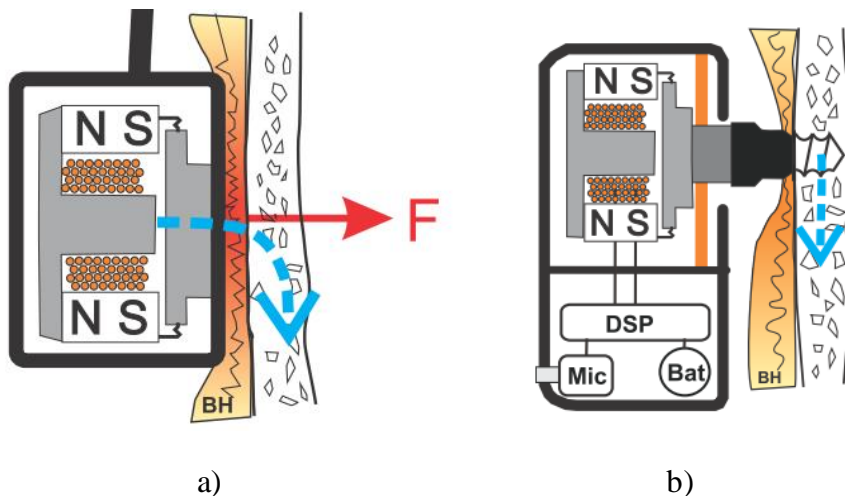


**Figure 1.6** a) Conventional BC device coupled with static pressure b) bone-anchored hearing aid (BAHA) attached with screwed abutment [21]

Sophonon Inc. develops a new transcutaneous type bone-anchored hearing device Sophono Alpha 2, to eliminate percutaneous abutment usage. The transducer is attached by magnetic coupling between the transducer and the implanted magnet under soft tissue, shown in Figure 1.7a [22]. The implanted magnet is bonded to the skull with small screws. The vibrations of the transducer are transmitted through the skin to the skull, which yields some energy loss, especially for higher frequency excitations [23, 24]. The magnetic coupling force between the transducer and the implanted magnet creates static pressure on the skin, which may cause soft tissue complications and wearing comfort problems [25].

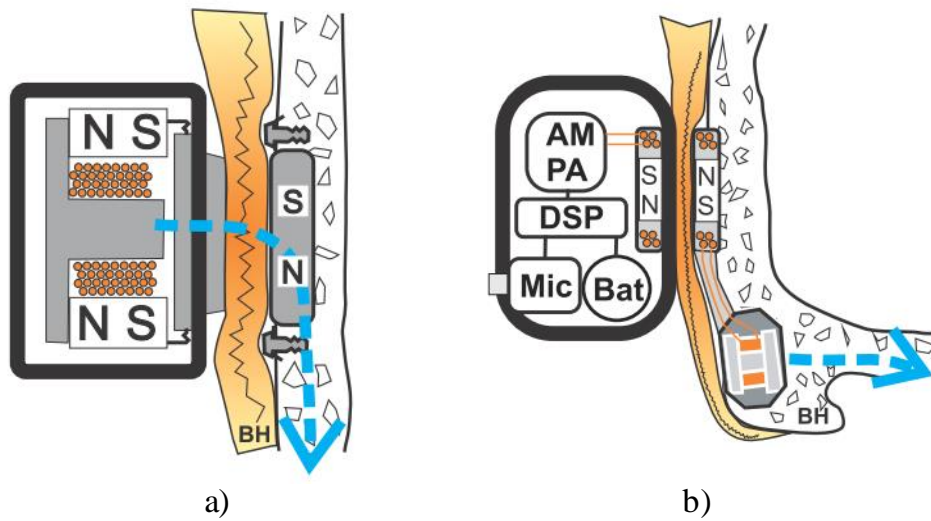


**Figure 1.7** a) a Sophono system, b) bone conduction implant (BCI) [21]

The bone conduction implant (BCI) is a unique active transcutaneous hearing aid. BCI consists of external and implanted parts developed by Hakansson et al. [26]. The external part of the device (audio processor, AP) has a power supply, microphone, sound processor, and inductive signal transmitter (Figure 1.7b). The AP is held on the skin with a magnetic retention force. The implanted part (bridging bone conductor, BBC) has a receiver coil and a transducer. The transducer is embedded into a pocket hole drilled on the skull bone and fastened with screws. The surgical procedure of the BCI placement is explained in detail in the study of Zernotti et al. [27]. Electromagnetic induction is used to transmit power over the skin in order to drive the transducer. The power loss is about 10 to 15 dB at the inductive link. Nevertheless, locating the transducer closer to the cochlea is claimed to compensate for the power loss [28]. The main drawbacks of the BCI systems are placement and size of the transducer and magnetic resonance compatibility of the implant. The BCI hearing aids use capsuled balanced electromagnetic separation transducers (C-BEST). A 16 mm diameter hole with 4 mm depth should be needed on the skull to fit the transducer. BCI surgeries are not recommended unless bone thickness and quality of the skull bone are sufficient. BCI treatment is suitable for children aged five years or older [29].

### 1.3.1. Electromagnetic Bone Conduction Transducers

The purpose of an efficient BC transducer is to transfer electrical energy into vibratory motion with acceptable distortion. Low distortion in the BC stimulations is essential to obtain higher quality sound conduction for a hearing aid. BC transducers may have different working principles, such as electromagnetic, magnetostrictive, and piezoelectric. The electromagnetic transducer B71, a Radioear Corporation product, has been one of the market's most popular BC transducers since the 1970s. The internal design of B71 is illustrated in Figure 1.8. The outer dimensions of B71 are 32x18.3x18.9 mm<sup>3</sup>. The electrical current passing through the coil creates varying magnetic flux, while the permanent magnet creates static magnetic flux on the armature. Generated transducer force is proportional to the square of the total flux. The nonlinear characteristic of the transducer force causes harmonic distortions during operations. One way to prevent the nonlinear effect is to increase static flux such that dynamic flux becomes negligible. However, the increasing static flux increases the static force on the suspension spring, and a stiffer spring is required to maintain the air gap.

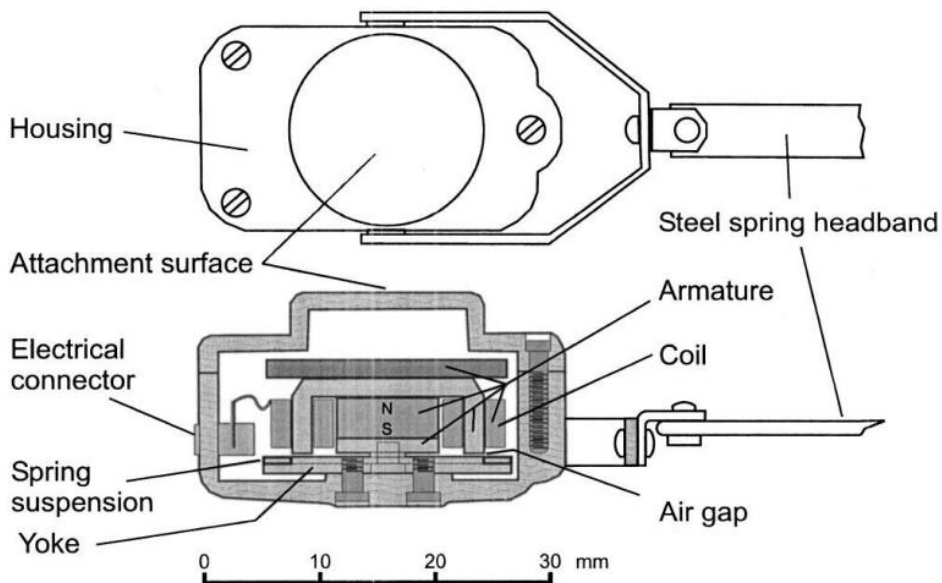


**Figure 1.8** Design and cross-sectional view of B71 electromagnetic transducer

[30]

Based on an SDOF lumped parameter assumption, the resonance frequency of an electromagnetic transducer can be expressed as follows:

$$f_r \approx \frac{1}{2\pi\sqrt{m_t c_s}} \quad (1.1)$$

where  $m_t$  is the equivalent moving mass of the transducer, and  $c_s$  is the compliance of the suspension spring. The first natural frequency of a BC transducer is tuned to the lowest frequency of threshold testing, which is between 250-500 Hz, to improve its performance at low frequencies. [30]. Additional mass is to be inserted into the armature to tune the resonance frequency. On the other hand, increasing the moving mass of the transducer results in heavier and oversized transducers. Limitations in the design make B71 unpromising as a BCHA transducer for the future.

A recently developed balanced electromagnetic separation transducer (BEST) was designed by Håkansson [30]. The BESTs are adapted in the new version of B71 named Radioear B81. In the new design shown in Figure 1.9, four magnets are placed upper and lower parts of the transducer to have desired balanced electromagnetic force. The outer dimensions of the B81 are 31.7x18.9x16 mm<sup>3</sup>. Electromagnetic forces on lower and upper suspension springs are given Eq.(1.2) and Eq.(1.3) , respectively

$$F_{lower} \propto \left(\frac{\phi_0}{2} + \phi_{\sim}\right)^2 = \left(\frac{\phi_0^2}{4} + \phi_{\sim} \cdot \phi_0 + \phi_{\sim}^2\right), \quad (1.2)$$

$$F_{upper} \propto \left(\frac{\phi_0}{2} - \phi_{\sim}\right)^2 = \left(\frac{\phi_0^2}{4} - \phi_{\sim} \cdot \phi_0 + \phi_{\sim}^2\right). \quad (1.3)$$

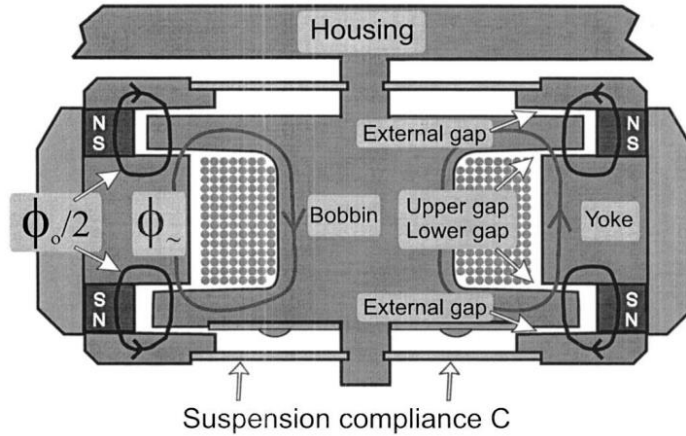


**Figure 1.9** Cross-sectional view and magnetic circuitry of B81 electromagnetic transducer [31]

where  $\phi_0$  and  $\phi_{\sim}$  are static and dynamic magnetic fluxes. The total force acting on the moving mass is equal to the difference between  $F_{lower}$  and  $F_{upper}$ , as expressed in Eq(1.4)

$$F_{tot} = F_{lower} - F_{upper} \propto 2\phi_0\phi_{\sim}. \quad (1.4)$$

Since static and varying forces are canceled out, the total electromagnetic force becomes almost linear. Nonlinear distortion effects in the BEST bone conductor are less than a standard variable reluctance type transducer.

A measurement setup is used to evaluate the performance of B71 and B81 transducers in Jansson and Håkansson's study [31]. The transducer is attached to the artificial mastoid B&K 4930 in the test setup illustrated in Figure 1.10. Measured total harmonic distortions (THDs) of B71 and B81 transducers are shown in Figure 1.11. Measured values represent the mean values of six different B71 and B81 transducers. B71 transducers have high harmonic distortions between 100 Hz to 1000 Hz; in contrast, B81 transducers have low THD throughout the entire bandwidth. Frequency response measurements are performed for six different B71 and B81 bone conductors. Averaged frequency responses are illustrated in Figure 1.12. The frequency responses of the B71 and the B81 transducers look alike except between 400 Hz and 1500 Hz, where the

frequency responses of B81 are approximately 5 dB higher than those of B71. In this section, the state-of-art electromagnetic BC transducers are reviewed. The main objective of the review is to explain the superiorities and the limitations of electrodynamic BC transducers in detail.

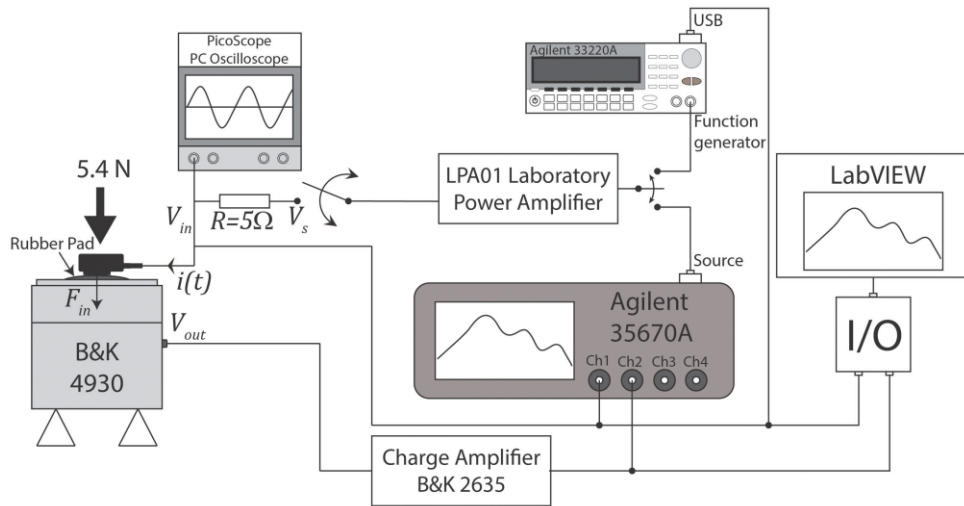


**Figure 1.10** The measurement setup of the electrodynamic transducers [31]

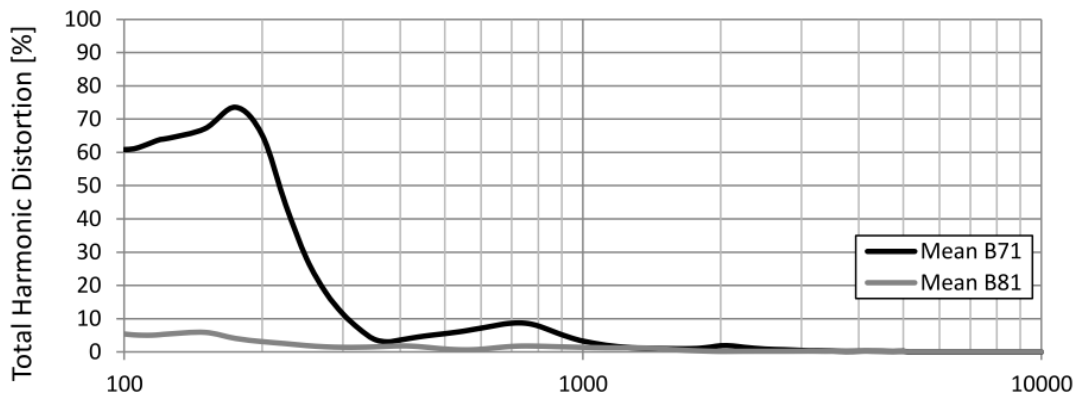


**Figure 1.11** Mean THDs of B71 and B81 under 1  $V_{rms}$  input voltage[31]

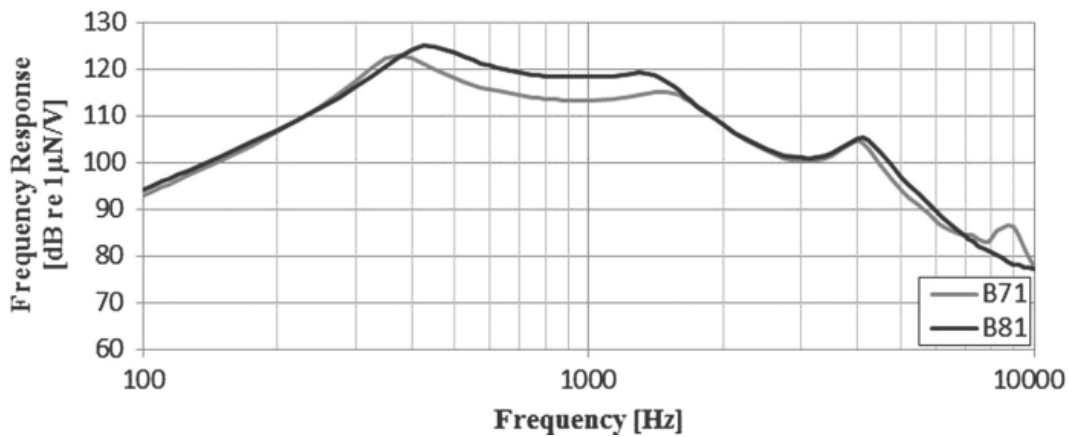


**Figure 1.12** Mean frequency responses of B71 and B81 under 1 V<sub>rms</sub> input voltage [31]

### 1.3.2. Literature Survey On Piezoelectric Bone Conduction Transducers

Although electromagnetic BC transducers are unique commercial products in the market, the limitations of current transducers lead researchers to study alternative transducers. Piezoelectric materials have been used as actuators for decades as direct or indirect mode electroactive actuators. Direct mode piezoelectric actuators are single or multi-layered piezoelectric ceramics corresponding to off-the-shelf piezoelectric actuators in the market. Direct mode piezoelectric actuators can generate a limited amplitude of displacements and strains (Figure 1.13). On the other hand, an indirect mode piezoelectric transducer exhibits more significant displacements and strains via a hybrid structure consisting of piezoelectric, metallic, and elastomeric elements.



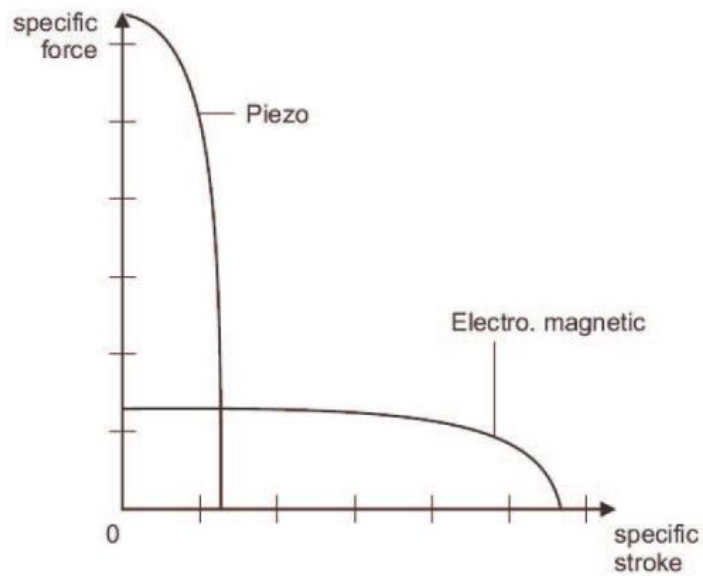


**Figure 1.13** Force-deflection characteristic of piezoelectric and electromagnetic transducers [32]

Sun et al. propose a bimorph piezoelectric transducer alternative to conventional BC devices [33]. The prototype is illustrated in Figure 1.14. In the study, the proposed design is verified experimentally. However, the effect of mastoid bone is not considered in the finite element analysis (FEA) and the experiments. Obtained results do not give convincing information about the performance of the proposed transducer attached to the skull.

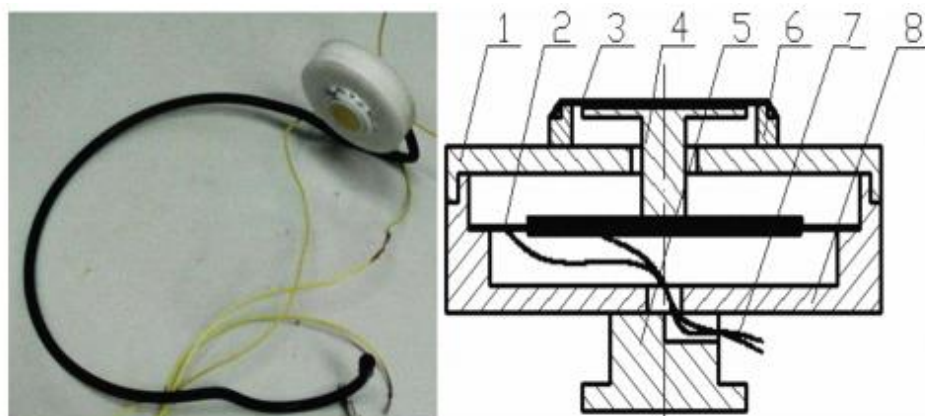


**Figure 1.14** A Piezoelectric BC transducer prototype [33]

Attaching bimorph piezoelectric benders directly to the skull is studied by Adamson et al. [34]. The subcutaneous piezoelectric attached hearing actuators (SPAHAAs) are used to deform the skull bone rather than vibrating the inertial mass of the transducer. The performance of the SPAHAAs is shown experimentally in a cadaver experiment. Piezoelectric transducers used in the experiments are a  $10 \times 30 \times 0.25 \text{ mm}^3$  rectangular and a circular piezoelectric transducer with a 10 mm diameter and 0.15 mm thickness (Figure 1.15). Vibration velocities of the cochlear promontory of the cadaver heads are measured during the experiment. The performance of each transducer is evaluated by calculating *efficacies* based on the ratio of the squared velocity of the cochlear promontory to the input power. The authors claim that if piezoelectric transducers are used with appropriate electronics SPAHAAs can outperform BAHA transducers in practical applications, which is not supported by any evidence in the study. On the other hand, the current state-of-the-art studies about piezoelectric benders point out the difficulties of using these types of piezoelectric actuators in applications where high force output is desired [35–37].

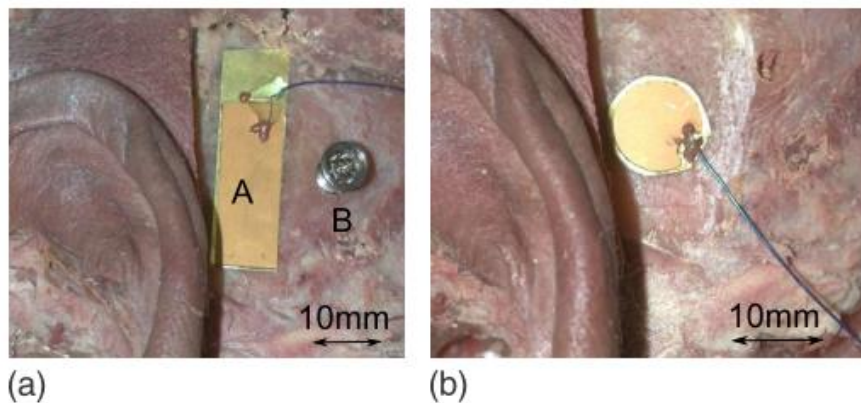


**Figure 1.15** a) Rectangular piezoelectric bender at Point A and BAHA abutment at Point B, b) circular piezoelectric bender at Point B[34]

A piezoelectric bone conductor design invented by Face International Corporation was published in 2007 [38]. The sketches representing the external and internal design of the transducer are shown in Figure 1.16. The bone conductor has an indirect mode flextensional piezoelectric transducer named as THUNDER actuator manufactured by

Face International Corporation (Figure 1.16b-12). THUNDER actuators are unimorph layered composite structures with a lead-zirconate-titanate (PZT) piezoceramic wafer sandwiched between two metal plates with a special adhesive. The THUNDER actuator is a 15 mm diameter circular membrane with 0.5-0.8 mm total thickness, and there are different types of THUNDER actuators in the market depending on PZT and metal plate thicknesses. The bone conductor is tested with different THUNDER actuators and compared with the B71 BC transducer. The tests are conducted by attaching the THUNDER actuators to the artificial mastoid B&K 4930, and the frequency responses of the actuators are measured. The bone conductors are driven at 2 V<sub>rms</sub> input voltage, and the frequency responses of the transducer are compared with the frequency response of B71 driven at 0.1 V<sub>rms</sub> input voltage (Figure 1.17). Although the THUNDER transducers seem to outperform B71, the study should also consider the power efficacies.

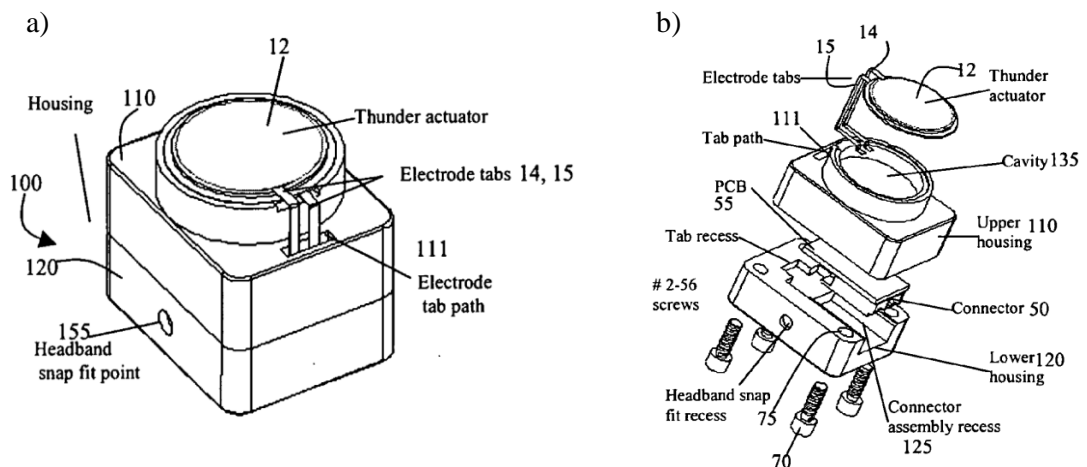


**Figure 1.16** a) Perspective view of the bone conductor transducer, b) exploded view of the bone conductor transducer [38]

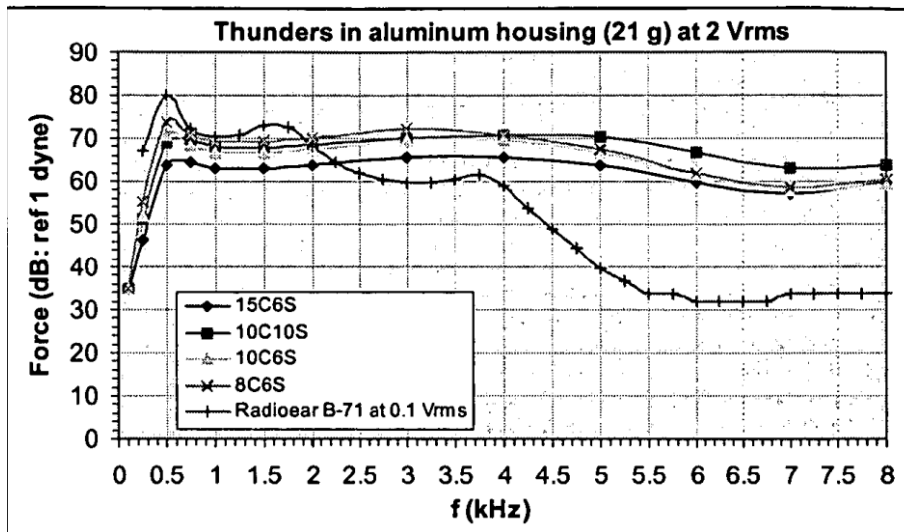


**Figure 1.17** Force response of different THUNDER transducers and B71 [38]

A new piezoelectric actuator-based subcutaneous BCHA has been developed and patented by Cochlear Limited [39]. The proposed design consists of piezoelectric bimorph actuators (Figure 1.18a) that deform in response to an applied input voltage, and the attached mass (Figure 1.18b) moves with the geometric center of the upper piezoelectric bimorph actuator. The relative motion of the mass generates output force (Figure 1.18b). The performance of the piezoelectric transduction actuator (PZTA) is evaluated by Dobrev et al. [40]. In the study, the PZTA has implanted in three different locations of the whole cadaver head, and a laser Doppler vibrometer measured promontory motions of the cadaver head while the PZTA was driven by 1 V<sub>rms</sub> harmonic voltage input in the frequency range from 100 Hz-10 kHz. Although the motivation of the study is to find an ideal location for PZTA placement, the measured frequency responses of the promontory motions show that the performance of the PZTA is reduced at frequencies below 400 Hz and above 7000 Hz.

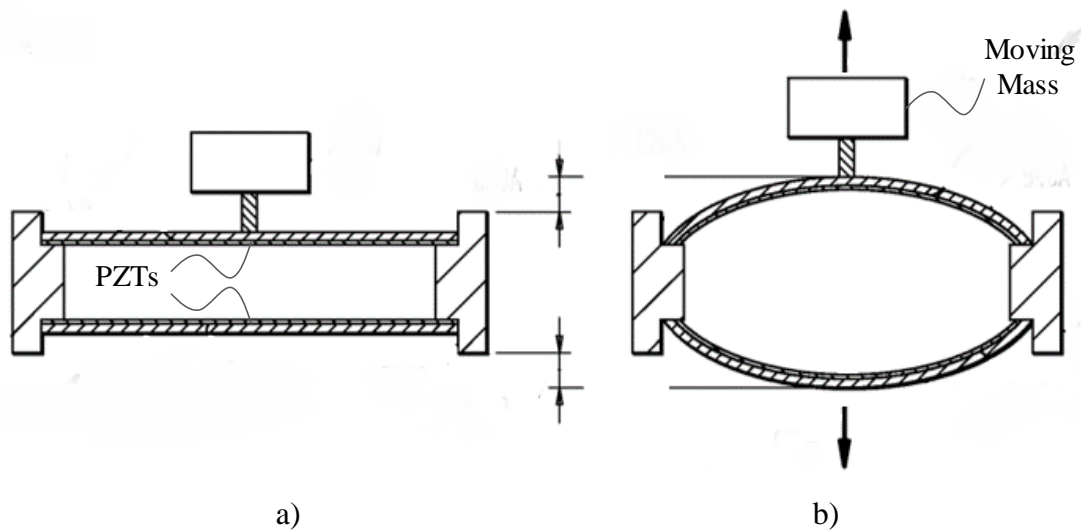


**Figure 1.18** Section view of the bone conductor transducer with piezoelectric actuator: a) undeformed position, b) deformed position[39]

It is shown in this section that the research field about piezoelectric BC transducers requires significant contributions as the available studies on piezoelectric-based BC transducers are currently not providing convincing enough results for BCHA implant applications.

#### 1.4. Motivation and Scope of the Thesis

Electromagnetic BC transducers are the unique devices used in BCHA in the market. There exist some drawbacks and limitations on available variable reluctance type electromagnetic transducers. A large number of components in an electromagnetic transducer design causes inherent problems regarding the reliability of the product. Thus, the transducers need periodic recalibration. Another drawback is poor THDs, as shown in Figure 1.11. The frequency response of the Radioear B71 and B81 transducers drops drastically above 4000 Hz (Figure 1.12). Magnetic transducers contain the risk of electromagnetic interference (EMI) during operation. Any external source which can cause electromagnetic induction may disrupt the transducer. Moreover, the size of the conventional implantable transducers limits osseointegration surgeries for infants before the age of 5 years.

The technological limitation on the BC transducers leads researchers to investigate alternative transducers such as piezoelectric ones. However, few studies and patents about piezoelectric bone transducers exist in the literature. The state-of-the-art studies on piezoelectric BC transducers are mainly about the performance outputs of conceptual designs. Nevertheless, experimental studies about piezoelectric bone conductors do not present extensive results. The patent studies propose an efficient BC transducer for wearable hearing aids. Based on the best knowledge of the author, the proposed piezoelectric actuators are not able to provide the same performance outputs as the standard electromagnetic BC transducers.

This thesis study proposes a novel design of an implantable BC transducer. The purpose of the study is to develop a piezoelectric transducer that is

- Lighter and smaller than conventional BC transducers,
- Operating efficiently in the frequency range from 100 Hz to 8000 Hz,
- Having low THD in the desired frequency range,
- Tuneable for different patient anatomy.

## **1.5. Outline of the Thesis**

Chapter 1 is dedicated to a comprehensive literature review of BC hearing loss and state-of-art BCHAs. Detailed descriptions of the standard BC transducer applications are also covered in this section. The motivation and objectives of the thesis study are presented at the end of this chapter.

In Chapter 2, multi-layer stacked piezoelectric actuators (MSPA) with rhombus type compliant mechanism (RCM) are proposed as a BCHA transducer. Transducer design is explained in detail by considering application limitations. Basic concepts of the piezoelectric theory are also given in this section. Generalized constitutive equations of the proposed piezoelectric transducer are determined based on structural dynamic

analyses. Analytical formulations of the MSPA and the RCM are developed separately, and a dynamic model of the entire piezoelectric actuator is obtained by coupling the MSPA and the RCM in the modal domain. The validity of the mathematical model is checked by comparing the frequency responses of the actuator analytically and numerically (FEA). The mathematical model of the piezoelectric transducer is verified through experimental studies. Frequency responses of the tip displacement of the actuator are measured by means of a laser displacement sensor, while the actuator is driven by a sinusoidal input voltage. It is shown that the linear dynamic model of the piezoelectric transducer represents the dynamic behavior of the transducer at low voltage levels.

Based on the linear mathematical model of APA verified in Chapter 2, the proposed BCHA design is optimized in Chapter 3 by using the genetic algorithm optimization method. The material of the mechanical amplifier and type of embedded MSPA are predefined considering the performance requirements of the application. Basic dimensions of the mechanical amplifier and weight of the attached tip mass are selected as optimization parameters. The optimization scheme aims to maximize the force output of the proposed BC transducer coupled with a skull simulator (B&K 4930 Artificial Mastoid). The transmitted actuator forces on the artificial mastoid are calculated using dynamic structural coupling methods. At the end of the optimization stage, the performance of the optimized BC transducer is ranked by comparing it with available commercial products. Cedrat Technologies have manufactured the optimized piezoelectric transducer for this Ph.D. study.

In Chapter 4, a series of constant voltage stepped-sine tests are performed on the manufactured APA prototypes. The test results show that the fundamental resonance frequency drops as the voltage level increases, indicating softening nonlinearity. Therefore, in this chapter, experimental modal analysis methods are studied in the first step, and then the nonlinear frequency responses of the piezoelectric transducer are determined by the response and force-controlled stepped sine tests. Modal parameters are experimentally identified from the quasi-linear FRFs obtained from the response

control stepped-sine test (RCT), and nonlinear modal parameters of the APA are defined as functions of response amplitude of the free end of the APA. This section aims to obtain a transfer function that establishes an accurate relationship between the level of input voltage and the amplitude of the output tip displacement in the frequency domain without needing any constitutive relation about the APA.

Although the experimental modal model obtained in Chapter 4 has high accuracy for the particular test case, a nonlinear MDOF model is needed to estimate the dynamics of BCHA in situations when it is coupled to different structures. Therefore, Chapter 5 is dedicated to the nonlinearity identification of the new BCHA prototype, a piezoelectric transducer with an attached tip mass, utilizing the response control test method described in Chapter 4. The describing surface and describing function of the underlying nonlinear behavior of the BCHA prototype are identified by using the constant displacement Frequency Response Functions (FRFs) and the linear APA model. The nonlinear MDOF BCHA model is validated experimentally by testing the APA prototype with different tip masses.

In Chapter 6, the actual electro-acoustic performance of the new piezoelectric BCHA is evaluated on the actual artificial mastoid by comparing it with conventional electromagnetic transducers. In the first step, the attached tip mass of the BCHA is tuned by re-applying the genetic algorithm optimization scheme with the nonlinear MDOF BCHA model obtained in Chapter 5 to enhance the transmitted force of the BCHA to the artificial mastoid. Then, a series of stepped-sine tests are performed on the modified BCHA attached to the artificial mastoid, and the transmitted BC forces to the artificial mastoid are recorded. An accurate nonlinear modal model is constructed using the method explained in Chapter 4, and the modal model is used to calculate the transmitted force frequency responses, which are compared with those obtained from the MDOF nonlinear BCHA model given in Chapter 5. The frequency response of the transmitted force, hearing level, and total harmonic distortion (THD) are measured during comparison tests. Hearing threshold tests are performed for discrete frequencies on a group of normal-hearing and hearing-impaired participants



with the conventional electromagnetic transducers and the new piezoelectric transducer in an anechoic chamber.

Chapter 7 gives the conclusions of this thesis study and also provides recommendations for future work.

The general flowchart of the thesis is given in Figure 1.19 to demonstrate the logical sequence of the thesis to the reader better.

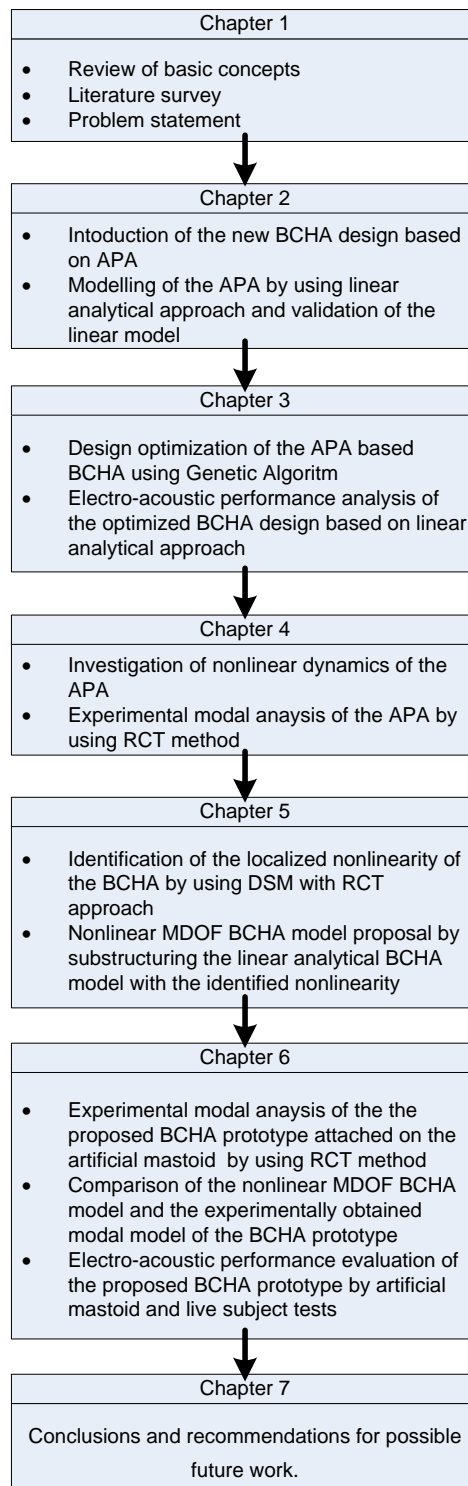


**Figure 1.19** General flowchart of the thesis

## CHAPTER 2

### DESIGN AND MODELING OF PIEZOELECTRIC TRANSDUCER FOR IMPLANTABLE BONE CONDUCTION HEARING AIDS

Although variable reluctance type electrodynamic bone conduction transducers are the most commonly used products in the market, the drawbacks of conventional transducers lead to the development of alternative transducers. Piezoelectric actuators have become widespread in robotics and mechatronics, and modified forms of piezoelectric actuators also appear in bio-robotic applications. Additionally, the non-magnetic and non-ferrous characteristics of the piezoelectric actuators provide safe robot-assisted surgical operations in MRI machines [41].

High resolution, large output force, high output displacement, compact size, wide frequency bandwidth, and solid-state design are the features of the ideal piezoelectric actuator [42]. Piezoelectric bimorph actuators can generate high tip displacements; however, their slight blocking force characteristic limits their usage as an actuator [36]. Multi-layer stacked piezoelectric actuators (MSPA) have a considerable blocking force compared with bimorph actuators [43]. On the other hand, the significant limitations of the MSPAs are their small output displacement range and reduced positioning accuracy due to hysteresis [44, 45]. Displacement sensors are used with MSPAs in a closed-loop control scheme to increase positioning accuracy [46]. The output displacement of the MSPAs is enhanced by utilizing compliant mechanisms while reducing the output force [47]. Compliant mechanisms are flexure-hinged based monolithic structures. Strain amplification is achieved by relative rotation of adjacent rigid parts of the compliant mechanism around the flexure hinges. The precisely manufactured monolithic compliant mechanisms promise high accuracy without backlash, wear, and friction [48–50]. Early compliant mechanisms are classified into

lever-type and flextensional type compliant mechanisms having advantages over lever-type ones, such as high stiffness, compact design, and symmetric behavior [51]. Moonie, cymbal, and rainbow are the first generations of piezo-driven flextensional compliant mechanisms where the topologies of different flexure-hinge compliant mechanisms are represented in Figure 2.1.

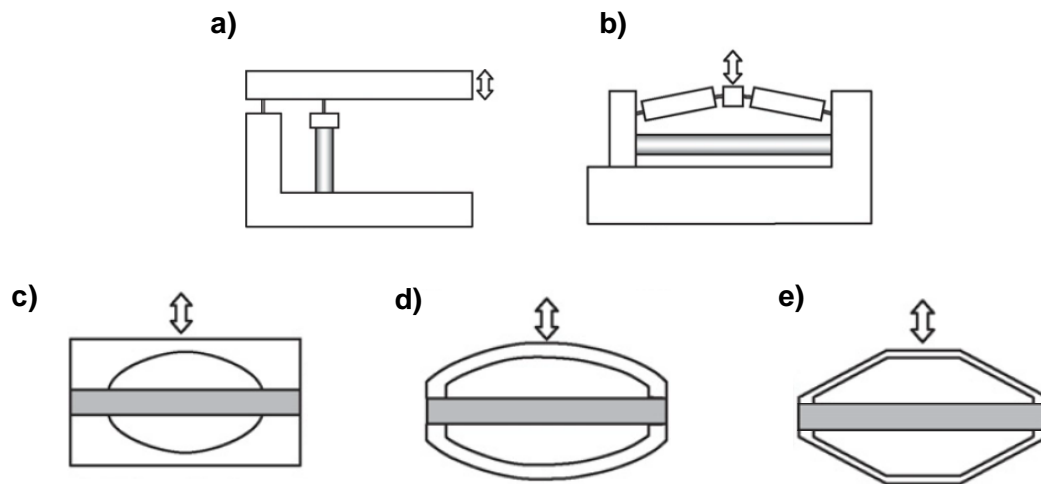


**Figure 2.1** a) Lever-type, b) Flextensional-type, c) Moonie-type, d) Rainbow-type, e) Cymbal-type Flextensional Compliant Mechanisms[51]

Rhombus-type and bridge-type mechanisms are the topologically optimized new generation flextensional compliant mechanisms (Figure 2.2) that take the place of the formers [52]. Despite enhanced strain amplification ratio, bridge-type compliant mechanisms are vulnerable to fatigue failure due to stress concentrations at the flexural hinge regions. Bridge-type structures are susceptible to manufacturing tolerances, which makes the behavior of bridge-type compliant mechanisms unpredictable. Rhombus-type or ellipse-type compliant mechanisms promise robust and reliable designs with large blocking force and relatively high output displacement [37].

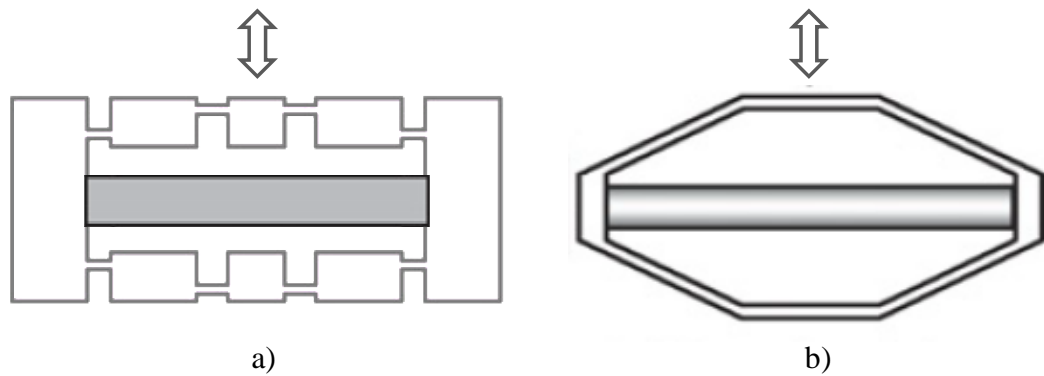


**Figure 2.2** a) Bridge-type, b) rhombus-type flextensional compliant mechanisms[53]

Commercialized forms of MSPAs with rhombus-type flextensional compliant mechanisms (RCM) are widely used in various engineering fields under amplified piezoelectric actuators (APAs) shown in Figure 2.3 [54]. APAs are available in the market as a family of products. Each product exhibits different performance limitations such as maximum stroke, working voltage range, working frequency range, operating temperatures, maximum blocking force, mechanical stiffness, resolution of displacement, and hysteresis. The performance outputs of the piezoelectric actuator should be precisely specified if it operates in a dynamic application. An accurate dynamic model of a piezoelectric actuator is required to determine an appropriate design for bone conduction applications.

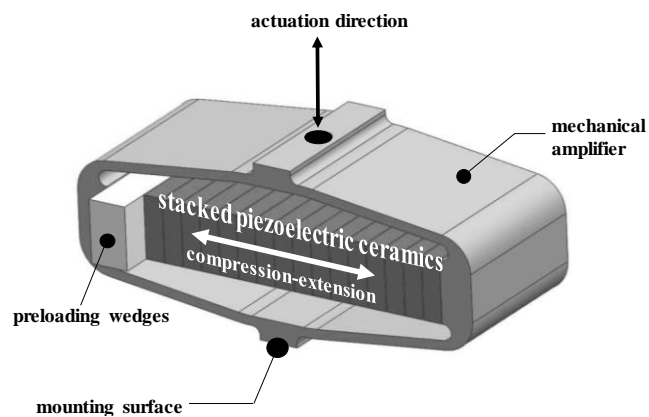


**Figure 2.3** Working principle of an amplified piezo-actuator (APA)

Most of the studies in the literature are based on kinematic analysis of the actuators under static loading conditions [50, 53, 55]. Statically determined constitutive relations of an actuator may not be valid under high-frequency dynamic actuation cases. Some studies perform dynamic analysis considering only the inertial properties of the lumped elements, such as the MSPA [37]. The inertial effects of the compliant mechanism become important while the high-frequency input voltage drives the piezoelectric actuator. Tolliver et al. [56] use finite element modeling software to compare the displacement frequency responses of different APAs with experimental results measured under  $1 V_{\text{rms}}$  harmonic voltage input. The numerically obtained frequency response of the actuators does not match up with the experimentally obtained ones in that study.

Kumar and Dasgupta propose a dynamic model for piezoelectric actuators with rhombic-compliant mechanisms (APA120ML, Cedrat Technologies) [57]. In their study, the lever arms of the compliant mechanism are modeled as four connected Euler-Bernoulli beams, and the piezoelectric stacked is modeled as a stiffness element. The fundamental frequency obtained from the modal solution is in the range of the catalog values of the APA120ML supplied by the manufacturer. However, the proposed dynamic model should also be verified with FEAs, considering the percentage difference between the evaluated fundamental frequency and the nominal one in the product catalog.

This section determines generalized constitutive equations of an APA working in fixed-free conditions based on structural dynamic analysis. The dynamic modeling of APA35XS by Cedrat is studied at this stage since APA35XS is one of the most popular and available miniature amplified piezoelectric actuators in the market [58] (Figure 2.4). The left half of the APA is modeled thanks to its symmetric design. The compliant mechanism is modeled as connected Euler-Bernoulli beams shown in Figure 2.5a and Figure 2.5b. Analytical formulations of an MSPA and RCM are developed separately by utilizing the distributed-parameter system approach and Hamilton's principle. The

eigenvalue problems of the equation of motion are solved numerically. The dynamic deflection functions of the MSPA and RCM are obtained by modal superposition.

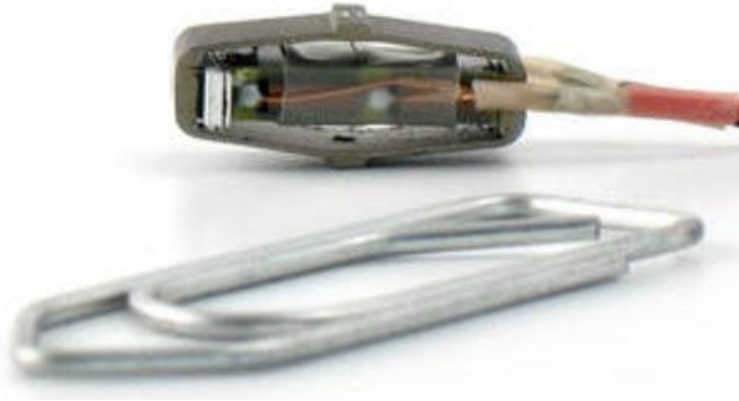


**Figure 2.4** Photograph of the Amplified Piezo-actuator-APA35XS by Cedrat Technologies [58]

Then, dynamic stiffness matrices of MSPA and the RCM are obtained for selected coordinates. Finally, the dynamic model of the entire APA is obtained by coupling the dynamic stiffness matrices of MSPA and the RCM in the frequency domain. The validity of the mathematical model is checked by comparing the frequency response of the actuator output displacements obtained analytically, numerically (i.e., FEA), and experimentally.

### **2.1. Theory of the Piezoelectric Actuator Modeling**

According to the proposed method, the RCM and the MSPA will be analyzed separately. The RPA model can be reduced to a half model by defining appropriate symmetry boundary conditions, as shown in Figure 2.5. The mathematical formulations of the half RCM and the half MSPA under dynamic loading are determined by using the Euler-Bernoulli beam theory and linear distributed parameter model of piezoelectric actuators in axial configuration.

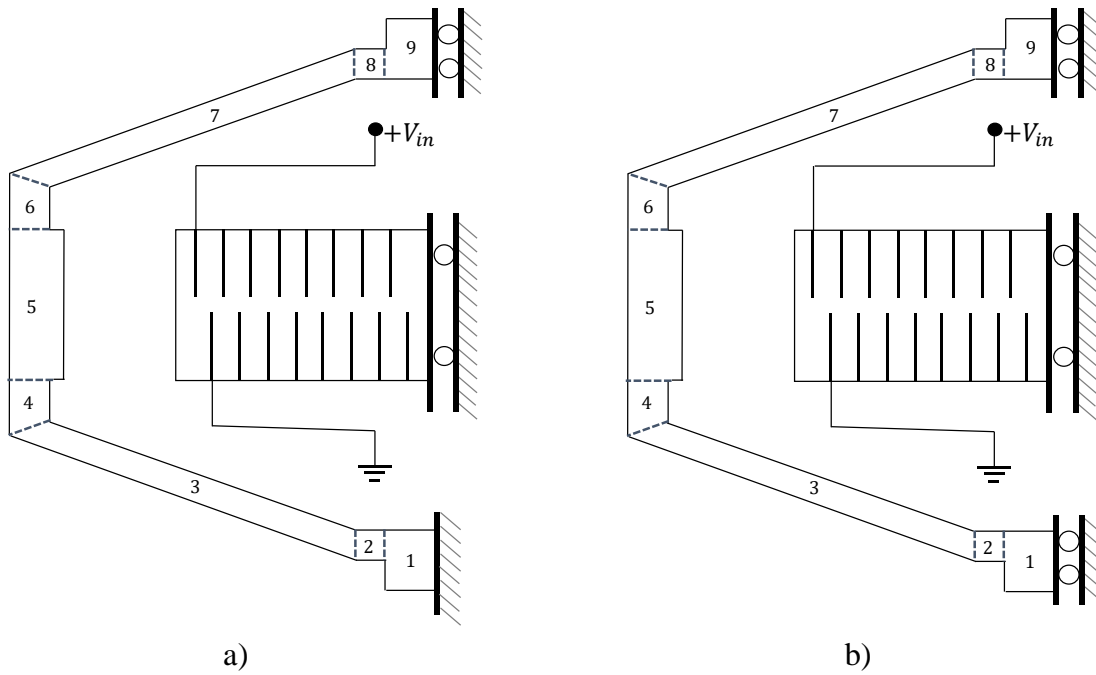


**Figure 2.5** The half APA models: a) fixed-free b) free-free end conditions

### 2.1.1. Formulation of an RCM Using Analytical Dynamics

A standard RCM can be decomposed into planar beams connected in series with different angles,  $\theta_i$ , illustrated in Figure 2.6a and Figure 2.6b. The half RCM model consists of nine series connected planar beams. Equations of motions for each beam can be written considering longitudinal and transverse deflections in the beam coordinate systems, as shown in Figure 2.6a. The discontinuity at the end conditions due to the misaligned neutral axis of the consecutive planar beams is considered in Figure 2.6b.



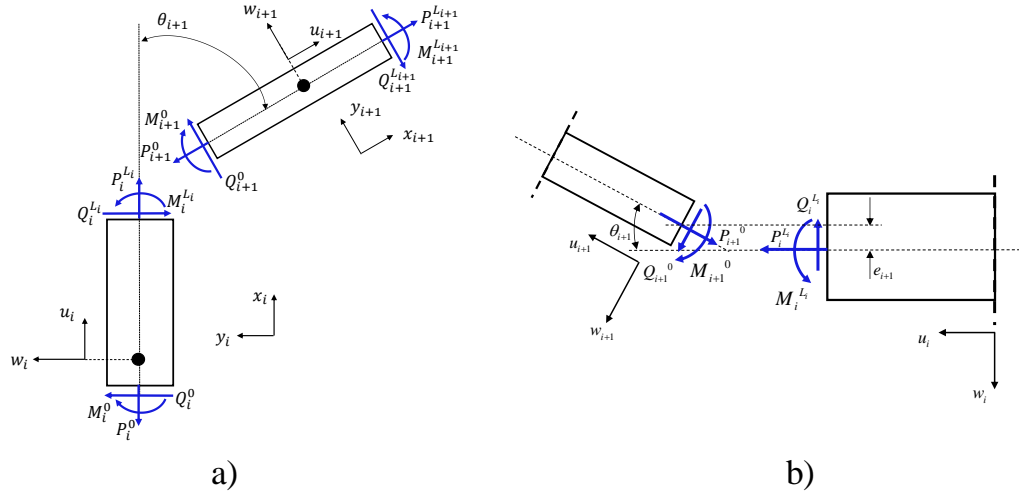


**Figure 2.6** a) Planar beams connected in series, b) misaligned planar beams

The undamped equation of motions for longitudinal and transverse vibrations of beams are given in Eq.(2.1) and Eq.(2.2), respectively. The beams are assumed to have uniform cross-sectional area and density.

$$\rho A_i \frac{\partial^2 u_i(x_i, t)}{\partial t^2} - EA_i \frac{\partial^2 u_i(x_i, t)}{\partial x_i^2} = f_i^a(x_i, t), \quad (2.1)$$

$$EI_i \frac{\partial^4 w_i(x_i, t)}{\partial x_i^4} + \rho A_i \frac{\partial^2 w_i(x_i, t)}{\partial t^2} = f_i^t(x_i, t), \quad (2.2)$$

$$i = 1, 2, \dots, 9, \quad (2.3)$$

where  $\rho$  is the density,  $A$  is the cross-section area,  $E$  is the modulus of elasticity,  $I$  is the second moment of the cross-section area,  $u$  and  $w$  are longitudinal and transverse displacements of the beams,  $f^a$  and  $f^t$  are axial and transverse external forces on the beams,  $x$  and  $t$  are spatial and temporal variables, respectively. The subscript  $i$  refers to the beam indices (Eq.(2.3)).

The generalized boundary condition equations are written for intermediate beam connection points. There are two boundary condition equations for each longitudinal

vibration equation and four for each transverse vibration equation. The total number of boundary condition equations is 54 for the half RCM model. Boundary conditions of connected beams are given in Appendix-A.

### 2.1.2. Eigensolution for the RCM

$$\rho A_i \frac{\partial^2 u_i(x_i, t)}{\partial t^2} = EA_i \frac{\partial^2 u_i(x_i, t)}{\partial x_i^2} \quad i = 1, 2, \dots, 9, \quad (2.4)$$

$$EI_i \frac{\partial^4 w_i(x_i, t)}{\partial x_i^4} + \rho A_i \frac{\partial^2 w_i(x_i, t)}{\partial t^2} = 0 \quad i = 1, 2, \dots, 9. \quad (2.5)$$

The partial differential equations Eqs.(2.4) and (2.5) are solved by employing the method of separation of variables. The longitudinal and transverse displacements are assumed to be in the forms given in Eqs.(2.6) and (2.7)

$$u_i(x_i, t) = U_i(x_i)T(t), \quad (2.6)$$

$$w_i(x_i, t) = W_i(x_i)T(t). \quad (2.7)$$

The general solutions for  $T(t)$ ,  $U_i(x_i)$  and  $W(x_i)$  are obtained by assuming solutions in the form of

$$T(t) = a \cos(\omega t) + b \sin(\omega t), \quad (2.8)$$

$$U_i(x_i) = c_1^i \cos(\lambda^2 x_i) + c_2^i \sin(\lambda^2 x_i), \quad (2.9)$$

$$W_i(x_i) = d_1^i \cosh(C_i \lambda x_i) + d_2^i \sinh(C_i \lambda x_i) + d_3^i \cos(C_i \lambda x_i) + d_4^i \sin(C_i \lambda x_i), \quad (2.10)$$

where  $\omega$  is the eigenfrequency of the RCM.  $a$ ,  $b$ ,  $c_j^i$  and  $d_j^i$  are the unknown constants of the eigenvalue problem. The parameters  $\lambda$  and  $C_i$  are introduced in Eqs.(2.9) and (2.10) for the sake of simplification.

$$\lambda^2 = \sqrt{\frac{\rho}{E}}\omega, C_i = \sqrt[4]{\frac{A_i}{I_i}}. \quad (2.11)$$

In Appendix B, the relation between the motion constants of  $i^{th}$  and  $(i + 1)^{th}$  beams can be obtained by making algebraic manipulations on Eq.(B.22) and Eq.(B.23).

$$\begin{Bmatrix} c_1 \\ c_2 \\ d_1 \\ d_2 \\ d_3 \\ d_4 \end{Bmatrix}^{i+1} = \mathbf{T}_{i+1}(\lambda)^{-1} \mathbf{B}_i(\lambda) \begin{Bmatrix} c_1 \\ c_2 \\ d_1 \\ d_2 \\ d_3 \\ d_4 \end{Bmatrix}^i = \mathbf{\Lambda}_i(\lambda) \begin{Bmatrix} c_1 \\ c_2 \\ d_1 \\ d_2 \\ d_3 \\ d_4 \end{Bmatrix}^i. \quad (2.12)$$

Vectorized form of motion constants of the last beam can be expressed as

$$\begin{Bmatrix} c_1 \\ c_2 \\ d_1 \\ d_2 \\ d_3 \\ d_4 \end{Bmatrix}^9 = \prod_{i=1}^8 \mathbf{\Lambda}_{8-i}(\lambda) \begin{Bmatrix} c_1 \\ c_2 \\ d_1 \\ d_2 \\ d_3 \\ d_4 \end{Bmatrix}^1. \quad (2.13)$$

The relation between motion constants of the first and the last beams can be determined by substituting Eq.(B.14) into Eq.(2.13)

$$\begin{Bmatrix} c_1 \\ c_2 \\ d_1 \\ d_2 \\ d_3 \\ d_4 \end{Bmatrix}^9 = \left( \prod_{i=1}^8 \mathbf{\Lambda}_{8-i}(\lambda) \right)_{(6 \times 6)} \begin{bmatrix} 0 & 0 & 0 \\ 1 & 0 & 0 \\ 0 & 1 & 0 \\ 0 & 0 & 1 \\ 0 & -1 & 0 \\ 0 & 0 & -1 \end{bmatrix}_{(6 \times 3)} \begin{Bmatrix} c_2 \\ d_1 \\ d_2 \end{Bmatrix}^1. \quad (2.14)$$

The system of equations in Eq.(2.14) can be turned into the linearly independent set of equations given in Eq.(2.15) by multiplying the left-hand side with  $\bar{\Lambda}_9(\lambda)$

$$\mathbf{R}(\lambda) \begin{Bmatrix} c_2 \\ d_1 \\ d_2 \end{Bmatrix} = \begin{Bmatrix} 0 \\ 0 \\ 0 \end{Bmatrix}, \quad (2.15)$$

where

$$\mathbf{R}(\lambda)_{(3 \times 3)} = \bar{\Lambda}_9(\lambda)_{(3 \times 6)} \left( \prod_{i=1}^8 \Lambda_{8-i}(\lambda) \right)_{(6 \times 6)} \bar{\Lambda}_1(\lambda)_{(6 \times 3)}. \quad (2.16)$$

Numerical solution of  $\det(\mathbf{R}(\lambda)) = 0$  will give the eigenvalues of the half RCM model. Numerical methods are used to determine the roots of the determinant. The solution can be expressed as follows by using the expansion theorem

$$u_i(x_i, t) = \sum_{r=1}^N U_{ir}(x_i) q_r(t), \quad (2.17)$$

$$w_i(x_i, t) = \sum_{r=1}^N W_{ir}(x_i) q_r(t), \quad (2.18)$$

where  $N$  is the number of eigenvalues determined from the numerical solution and  $q_r$  is the  $r^{th}$  generalized coordinate. Eq.(2.17) and Eq.(2.18) are inserted into Eq.(2.1) and Eq.(2.2), respectively.

$$\rho A_i \sum_{r=1}^N U_{ir}(x_i) \ddot{q}_r(t) - EA_i \sum_{r=1}^N \frac{d^2 U_{ir}(x_i)}{dx_i^2} q_r(t) = f_i^a(x_i, t), \quad (2.19)$$

$$\rho A_i \sum_{r=1}^N W_{ir}(x) \ddot{q}_r(t) + EI_i \sum_{r=1}^N \frac{d^4 W_{ir}(x)}{dx^4} q_r(t) = f_i^t(x, t). \quad (2.20)$$

Eqs.(2.19) and (2.20) are multiplied with  $U_{is}$  and  $W_{is}$ , respectively as follows;

$$\begin{aligned} & \sum_{r=1}^N \left[ \int_0^{L_i} \rho A_i U_{ir}(x_i) U_{is}(x_i) dx_i \right] \ddot{q}_r(t) - \sum_{r=1}^N \left[ \int_0^{L_i} E A_i \frac{d^2 U_{ir}(x_i)}{dx_i^2} U_{is}(x_i) dx_i \right] q_r(t), \\ & = \int_0^{L_i} U_{is}(x_i) f_i^a(x_i, t) dx_i, \end{aligned} \quad (2.21)$$

$$\begin{aligned} & \sum_{r=1}^N \left[ \int_0^{L_i} \rho A_i W_{ir}(x_i) W_{is}(x_i) dx_i \right] \ddot{q}_r(t) + \sum_{r=1}^N \left[ \int_0^{L_i} E I_i \frac{d^4 W_{ir}(x_i)}{dx_i^4} W_{is}(x_i) dx_i \right] q_r(t), \\ & = \int_0^{L_i} W_{is}(x_i) f_i^t(x_i, t) dx_i. \end{aligned} \quad (2.22)$$

Eq.(2.23) is obtained by adding up Eqs.(2.21) and (2.22)

$$\begin{aligned} & \sum_{r=1}^N \left[ \int_0^{L_i} \rho A_i (W_{ir}(x_i) W_{is}(x_i) + U_{ir}(x_i) U_{is}(x_i)) dx_i \right] \ddot{q}_r(t) + \\ & \sum_{r=1}^N \left[ \int_0^{L_i} E \left( I_i \frac{d^4 W_{ir}(x_i)}{dx_i^4} W_{is}(x_i) - A_i \frac{d^2 U_{ir}(x_i)}{dx_i^2} U_{is}(x_i) \right) dx_i \right] q_r(t), \\ & = \int_0^{L_i} W_{is}(x_i) f_i^t(x_i, t) dx_i + \int_0^{L_i} U_{is}(x_i) f_i^a(x_i, t) dx_i. \end{aligned} \quad (2.23)$$

Summation of Eq.(2.23) for all connected beams can be expressed as

$$\begin{aligned} & \sum_{i=1}^9 \sum_{r=1}^N \left[ \int_0^{L_i} \rho A_i (W_{ir}(x_i) W_{is}(x_i) + U_{ir}(x_i) U_{is}(x_i)) dx_i \right] \ddot{q}_r(t) + \\ & \sum_{i=1}^9 \sum_{r=1}^N \left[ \int_0^{L_i} E \left( I_i \frac{d^4 W_{ir}(x_i)}{dx_i^4} W_{is}(x_i) - A_i \frac{d^2 U_{ir}(x_i)}{dx_i^2} U_{is}(x_i) \right) dx_i \right] q_r(t), \\ & = \sum_{i=1}^9 \left[ \int_0^{L_i} W_{is}(x_i) f_i^t(x_i, t) dx_i + \int_0^{L_i} U_{is}(x_i) f_i^a(x_i, t) dx_i \right]. \end{aligned} \quad (2.24)$$

Eq.(2.24) can be simplified to Eq.(2.25) by using the orthogonality property of the normal modes (*see Appendix-C for the proof*)

$$\begin{aligned}
& \sum_{i=1}^9 \left[ \int_0^{L_i} \rho A_i (W_{ir}^2(x_i) + U_{ir}^2(x_i)) dx \right] \ddot{q}_r(t) + \\
& \sum_{i=1}^9 \left[ \int_0^{L_i} E \left( I_i W_{ir}^2(x_i)'' + A_i U_{ir}^2(x_i)' \right) dx_i \right] \dot{q}_r(t), \quad (2.25) \\
& = \sum_{i=1}^9 \left[ \int_0^{L_i} W_{is}(x_i) f_i^t(x_i, t) dx + \int_0^{L_i} U_{is}(x_i) f_i^a(x_i, t) dx_i \right].
\end{aligned}$$

Eq.(2.25) can be rewritten in a more simple form as given in Eq.(2.26)

$$m_r \ddot{q}_r(t) + k_r q_r(t) = N_r(t), \quad (2.26)$$

where

$$m_r = \sum_{i=1}^9 \left[ \int_0^{L_i} \rho A_i (W_{ir}^2(x_i) + U_{ir}^2(x_i)) dx_i \right], \quad (2.27)$$

$$k_r = \sum_{i=1}^9 \left[ \int_0^{L_i} E \left( I_i W_{ir}''(x_i)^2 + A_i U_{ir}'(x_i)^2 \right) dx_i \right], \quad (2.28)$$

$$N_r(t) = \sum_{i=1}^9 \left[ \int_0^{L_i} W_{is}(x) f_i^t(x, t) dx + \int_0^{L_i} U_{is}(x) f_i^a(x, t) dx \right]. \quad (2.29)$$

It is assumed that the RCM has proportional viscous damping introduced in Eq.(2.30)

$$m_r \ddot{q}_r(t) + c_r \dot{q}_r(t) + k_r q_r(t) = N_r(t), \quad (2.30)$$

where the modal damping coefficient is defined as  $c_r = \alpha m_r + \beta k_r$   $\alpha$  and  $\beta$  are real positive constants. The solution of the generalized coordinate of the  $r^{th}$  mode is obtained for harmonic forcing  $N_r(t)$  in Eq.(2.31).

$$q_r(t) = \frac{N_r(t)}{k_r - \omega^2 m_r + i c_r \omega}. \quad (2.31)$$

After obtaining the generalized coordinate  $q_r$ , the solution of any point on the RCM can be determined by using the expansion theorem. The response of the coordinates under interest can be determined by assuming the RCM is subjected to external forcing at coupling coordinates only. Tip displacement of the RCM and longitudinal, transverse, and angular deformation of the connection point of MSPA are given in Eqs.(2.32)-(2.35), respectively:

$$w_9(L_9, t) = \sum_{r=1}^K W_{9r}(L_9) q_r(t), \quad (2.32)$$

$$u_5\left(\frac{L_5}{2}, t\right) = \sum_{r=1}^K U_{5r}\left(\frac{L_5}{2}\right) q_r(t), \quad (2.33)$$

$$w_5\left(\frac{L_5}{2}, t\right) = \sum_{r=1}^K W_{5r}\left(\frac{L_5}{2}\right) q_r(t), \quad (2.34)$$

$$\psi_5\left(\frac{L_5}{2}, t\right) = \sum_{r=1}^K W'_{5r}\left(\frac{L_5}{2}\right) q_r(t). \quad (2.35)$$

The equations Eq.(2.32)-(2.35) are represented in matrix form in the frequency domain as follows

$$\begin{Bmatrix} W_{9,L_9}(\omega) \\ U_{5,L_{5/2}}(\omega) \\ W_{5,L_{5/2}}(\omega) \\ \Psi_{5,L_{5/2}}(\omega) \end{Bmatrix} = \mathbf{H}_{RCM}(\omega) \begin{Bmatrix} F_9^t \\ F_5^a \\ F_5^t \\ M_5 \end{Bmatrix}, \quad (2.36)$$

where  $\mathbf{H}_{RCM}$  is receptance matrix of the 4-DOF RCM given in Eq.(B.25) in Appendix-B.  $F_5^a$ ,  $F_5^t$  and  $M_5$  are the coupling forces and the moment between the RCM and the MSPA.  $F_9^t$  is the coupling force between the RCM and attached tip mass.

### 2.1.3. Comparison of Analytical Model of RCM via FEA

Preliminary stand-alone modal analyses of the RCM are performed using the analytical formulation developed in the previous section and a commercial FEA software ANSYS Workbench R19.2<sup>®</sup> to demonstrate the validity of the analytical model. The RCM is the stainless-steel mechanical amplifier of the APA35XS, which is represented by serially connected beams whose geometric properties are given in Table 2.1.

**Table 2.1** Geometric dimensions of the beam segments of the RCM (APA35XS)

Beam Number	Length, $L$ [mm]	Thickness, $t$ [mm]	Width, $w$ [mm]	Angle, $\theta$ [°]	Offset, $e$ [mm]
1	0.62	0.69	5.00	0.00	0.00
2	0.48	0.30	5.00	0.00	0.19
3	4.86	0.30	5.00	7.00	0.00
4	0.61	0.60	5.00	83.00	-0.20
5	2.00	1.14	5.00	0.00	0.05
6	0.61	0.60	5.00	83.00	-0.05
7	4.86	0.30	5.00	7.00	0.20
8	0.48	0.30	5.00	0.00	0.00
9	0.62	0.69	5.00	0.00	-0.19

The frequencies of the first four in-plane elastic modes are evaluated by solving  $\det(\mathbf{R}(\lambda)) = 0$  numerically and compared with the ones obtained from the FEA solution shown in Figure 2.7. The results in Table 2.2 validate the accuracy of the analytical model by FE simulations. The percentage difference between the analytical and FE model is less than 3%. It should be noted that in-plane modes are considered during FEA, and the other modes are disregarded.



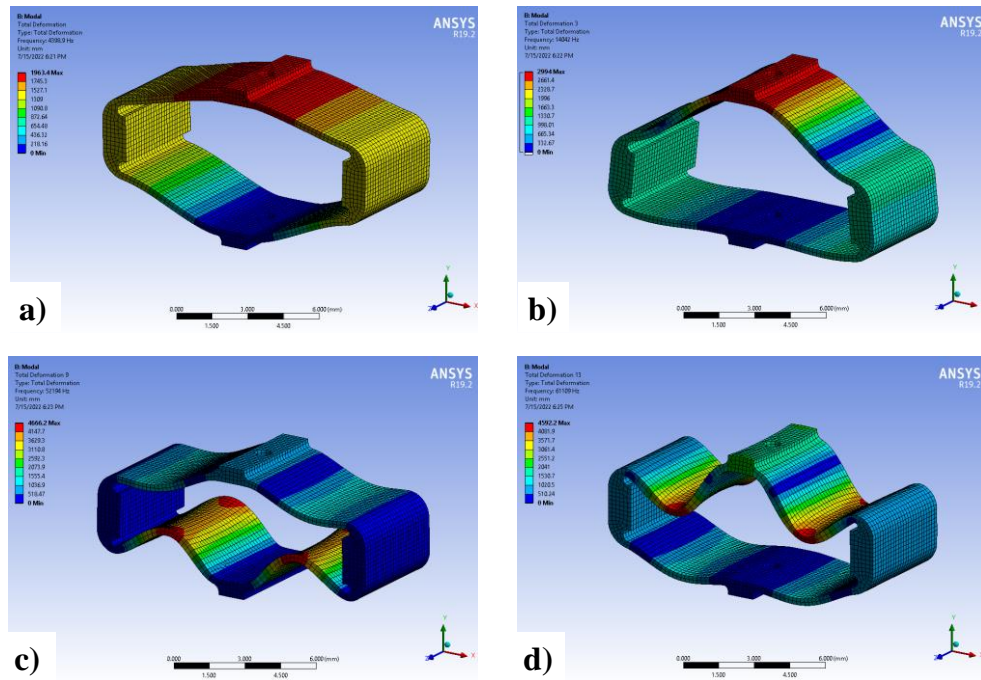


**Figure 2.7** The first four in-plane modes of vibration of the fixed-free RCM: the first mode (a), the second mode (b), the third mode (c), and the fourth mode (d)

**Table 2.2** The first four in-plane modes of vibration of the fixed-free RCM

Mode	Analytical Model [Hz]	FE Model [Hz]	Percentage Difference [%]
First	4400	4399	0.02
Second	13815	14042	1.63
Third	53758	52194	2.95
Forth	61362	61109	0.41

#### 2.1.4. Analytical Formulation of the MSPA

Many methods dedicated to modeling the dynamic behavior of MSPAs exist in the literature [56, 59–62]. A distributed parameter model is employed to determine the analytical solution of MSPA under harmonic excitations. MSPA is composed of  $N_p$  number of physically coupled piezoelectric layers with electrodes electrically connected in parallel (Figure 3.1a). The half MSPA is modeled as a uniform Euler-

Bernoulli beam that vibrates in axial and transverse directions with appropriate symmetry boundary conditions illustrated in Figure 3.1b.

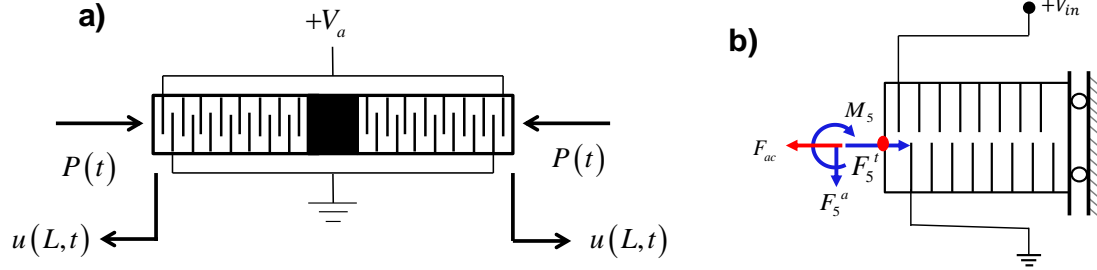


**Figure 3.1** a) The MSPA Model, b) the Half MSPA Model

Governing equation of motion of MSPAs can be written as

$$\begin{aligned} \rho_p A_p \frac{\partial^2 u_p(x_p, t)}{\partial t^2} - E_p A_p \frac{\partial^2 u_p(x_p, t)}{\partial x_p^2} - c_p \frac{\partial u_p(x_p, t)}{\partial t} \\ = \frac{V_{in}(t) e_{33} A_p N_p}{L_p} \delta(x_p - L_p) + F_p^a(t) \delta(x_p - L_p), \end{aligned} \quad (2.37)$$

$$\begin{aligned} E_p I_p \frac{\partial^4 w_p(x_p, t)}{\partial x_p^4} + c_p \frac{\partial w_p(x_p, t)}{\partial t} + \rho_p A_p \frac{\partial^2 w_p(x_p, t)}{\partial t^2} \\ = F_p^t(t) \delta(x_p - L_p) + M_p^a(t) \frac{d\delta(x_p - x_p')}{dx_p'} \Big|_{x'=L_p}, \end{aligned} \quad (2.38)$$

where  $\rho_p$  is the density,  $A_p$  is the cross-section area,  $E_p$  is the modulus of elasticity,  $I_p$  is the second moment of cross-section area,  $c_p$  damping ratio,  $N_p$  is the number of layers in the piezoelectric stack actuator, and  $e_{33}$  is the axial electromechanical coupling coefficient of the piezoelectric actuator.  $u_p$  and  $w_p$  are longitudinal and transverse displacements of the stacked piezoelectric actuator, respectively.  $F_p^a$ ,  $F_p^t$  and  $M_p$  are the coupling forces and the moment between the MSPA and the RCM,

respectively.  $V_{in}$  is the input voltage applied between the electrical ports of the electrodes connected in parallel.

The standard modal analysis described for the RCM is performed for the homogeneous and undamped versions of Eqs.(2.37) and (2.38). Derivation of the modal eigenfunctions and eigenfrequencies of MSPA is explained in Appendix-D. Longitudinal, transverse, and angular displacements of coupled coordinates of MSPA are expressed in matrix form in Eq.(2.39)

$$\begin{Bmatrix} W_{p,L_p}(\omega) \\ U_{p,L_p}(\omega) \\ \Psi_{p,L_p}(\omega) \end{Bmatrix} = \mathbf{H}_{MSPA}(\omega) \left( \begin{Bmatrix} F_p^t \\ F_p^a \\ M_p \end{Bmatrix} + \begin{Bmatrix} 0 \\ F_{ac} \\ 0 \end{Bmatrix} \right), \quad (2.39)$$

where  $\mathbf{H}_{MSPA}$  is the receptance matrix of the 3-DOF MSPA given in Eq.(D.18) in Appendix-D.  $F_{ac}$  is the equivalent piezoelectric actuation force corresponding to the input voltage  $V_{in}$ .

$$F_{ac} = \frac{V_{in} e_{33} A_p N_p}{L_p}. \quad (2.40)$$

### 2.1.5. Comparison of Analytical Model of MSPA via FEA

In this section, modal analyses are performed for the MSPA by using the mathematical model developed in the previous section and also with ANSYS Workbench R19.2<sup>®</sup> with the multiphysics solver (Figure 2.8). The physical properties of the embedded MSPA of the APA35XS are given in Table 2.3. The MSPA has 90 piezoelectric layers, which are not practical to be modeled in an FE environment. For the sake of simplicity, the optimal number of layers is determined by repeating FEA with the MSPA models having different numbers of layers.

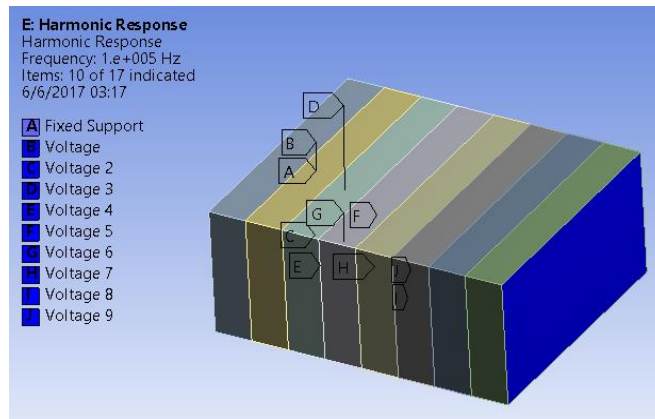


**Figure 2.8** 8-layer FE model of the half MSPA

**Table 2.3** Physical Properties of the MSPA

$\rho_p$	$7930 \text{ kg/m}^3$
$E_p$	$5.2 \times 10^{10} \text{ N/m}^2$
$L_p$	$10 \text{ mm}$
$t_p$	$2 \text{ mm}$
$h_p$	$5 \text{ mm}$
$e_{33}$	$30.1 \text{ N/(m.V)}$
$N_p$	90

The FE modal analysis solutions are compared with the analytical ones in Table 2.4. The natural frequencies of longitudinal modes appeared to be the same for the analytical and FEA solutions. On the other hand, there is a significant difference between the analytical and FEA model in terms of the transverse mode-based natural frequencies. The difference is caused by the fact that ANSYS Workbench R19.2<sup>®</sup> uses Timoshenko beam elements by default, whereas the analytical formulation is based on the Euler-Bernoulli beam theory. Since the length of the MSPA is relatively short compared to its width and height, the effect of the beam theory on the MSPA modeling becomes apparent in stand-alone simulations. However, the effect of elastic transverse modes of the MSPA on the APA structure is not significant.

**Table 2.4** The first five in-plane modes of the MSPA

Mode	Analytical Model [Hz]	FE Model [Hz]	Percentage Difference [%]
Rigid Body Mode (Transverse)	0	0	0.0
First (Transverse)	52644	42946	20.3
Second (Longitudinal)	128045	128045	0.0
Third (Transverse)	284480	189650	40.0
Fourth (Longitudinal)	384113	384113	0.0

The tip displacement frequency responses of the MSPA obtained from the analytical model, and the FEM simulations are shown in Figure 2.9. It is observed that the outputs of FEM simulations converge to the ones determined from the analytical model as the number of piezoelectric layers increases. Eight piezoelectric layers are used in FEM simulations for the rest of the study.

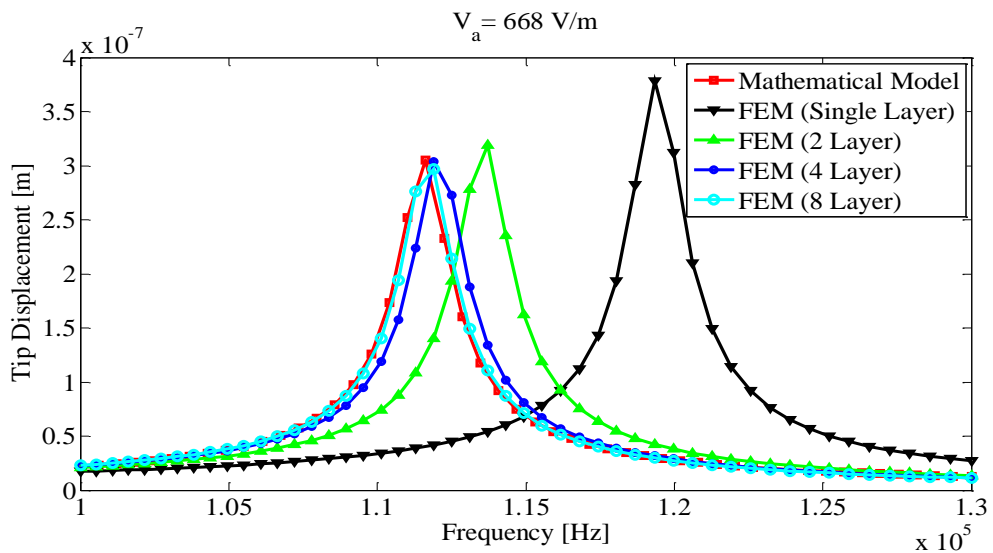


**Figure 2.9** Comparison of harmonic responses at the free end of the MSPA obtained from the analytical and FE model

### 2.1.6. Coupling of the RCM and the MSPA using Dynamic Substructuring

In general, dynamic substructuring techniques are utilized to obtain the dynamic response of complex structures composed of multiple subcomponents in an assembly, as illustrated in Figure 2.10.

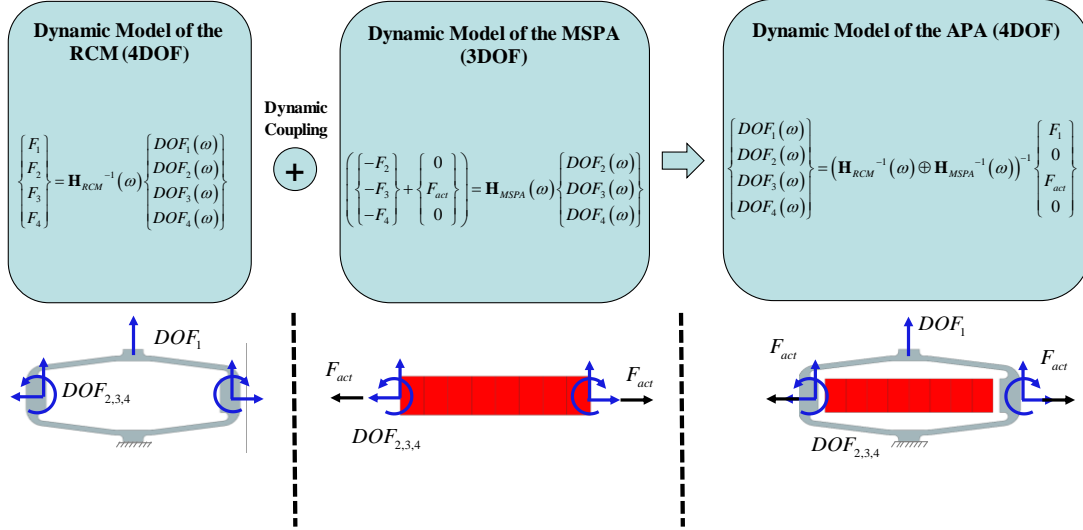


**Figure 2.10** Free-body diagrams and dynamic coupling of the RCM and the MSPA models

In this study, dynamic substructuring operations are performed in the frequency domain since the primary interest is to predict the harmonic responses of the main structure. The behavior of the substructures is assumed to be linear (or linearized), time-invariant, and steady-state for dynamic substructuring in the frequency domain. The equation of motion of the substructures is written in the frequency domain in Eq.(2.41) and (2.42)

$$\mathbf{Z}_{RCM}(\omega) \begin{Bmatrix} W_{9,L_9} \\ U_{5,L_{5/2}} \\ W_{5,L_{5/2}} \\ \Psi_{5,L_{5/2}} \end{Bmatrix} = \begin{Bmatrix} F_9^t \\ F_5^a \\ F_5^t \\ M_5 \end{Bmatrix}, \quad (2.41)$$

$$\mathbf{Z}_{RCM}(\omega) \begin{Bmatrix} W_{9,L_9} \\ U_{5,L_{5/2}} \\ W_{5,L_{5/2}} \\ \Psi_{5,L_{5/2}} \end{Bmatrix} = \begin{Bmatrix} F_9^t \\ F_5^a \\ F_5^t \\ M_5 \end{Bmatrix}, \quad (2.42)$$

where  $\mathbf{Z}_{RCM}$  and  $\mathbf{Z}_{MSPA}$  are dynamic stiffness matrices of the RCM and the MSPA, respectively. Dynamic stiffness matrices are obtained by taking the inverses of the receptance matrices of the RCM and the MSPA.

The degree of freedom of the connection point of the MSPA and the RCM is called interface DOF. The compatibility of the displacements and the forces at the interface is given in Eqs.(2.43)-(2.48).

$$u_5\left(\frac{L_5}{2}, t\right) = w_p(L_p, t), \quad (2.43)$$

$$w_5\left(\frac{L_5}{2}, t\right) = u_p(L_p, t), \quad (2.44)$$

$$\left. \frac{\partial w_5}{\partial x_5} \right|_{x_5=\frac{L_5}{2}} = - \left. \frac{\partial w_p}{\partial x_p} \right|_{x_p=L_p}, \quad (2.45)$$

$$F_5^t(t) + F_p^a(t) = 0, \quad (2.46)$$

$$F_5^a(t) + F_p^t(t) = 0, \quad (2.47)$$

$$M_5(t) - M_p(t) = 0. \quad (2.48)$$

The equation of motion of the APA is obtained by inserting the compatibility equations into the equation of motions of the RCM and the MSPA. The resultant harmonic responses of the APA are given in Eq.(2.49). It is noted that the dynamic stiffness

matrix of the APA is obtained directly by making simple algebraic operations. On the other hand, the procedure used in this case may be insufficient for more complex substructuring problems, which can be handled by employing the techniques presented in [63].

$$\begin{Bmatrix} F_9^t \\ 0 \\ F_{act} \\ 0 \end{Bmatrix} = \begin{bmatrix} Z_{RCM}^{11} & Z_{RCM}^{12} & Z_{RCM}^{13} & Z_{RCM}^{14} \\ Z_{RCM}^{21} & Z_{RCM}^{22} + Z_{MSPA}^{11} & Z_{RCM}^{23} + Z_{MSPA}^{12} & Z_{RCM}^{24} - Z_{MSPA}^{13} \\ Z_{RCM}^{31} & Z_{RCM}^{32} + Z_{MSPA}^{21} & Z_{RCM}^{33} + Z_{MSPA}^{22} & Z_{RCM}^{34} - Z_{MSPA}^{23} \\ Z_{RCM}^{41} & Z_{RCM}^{42} - Z_{MSPA}^{31} & Z_{RCM}^{43} - Z_{MSPA}^{32} & Z_{RCM}^{44} + Z_{MSPA}^{33} \end{bmatrix} \begin{Bmatrix} W_{9,L_9}(\omega) \\ U_{5,L_{5/2}}(\omega) \\ W_{5,L_{5/2}}(\omega) \\ \Psi_{5,L_{5/2}}(\omega) \end{Bmatrix} \quad (2.49)$$

## 2.2. Experimental Verification of Dynamic Model of the APA

The mathematical model of the APA is validated through experimental studies and FEA. In the experimental test setup, the miniature piezoelectric actuator APA35XS is fixed from its base to the testing table with a high-strength adhesive (Figure 2.11a). A laser displacement sensor (Micro-Epsilon OptoNCDT-2300) [64] is used to measure tip displacements of the piezoelectric transducer (Figure 2.11b). The laser displacement sensor is placed on top of the actuators employing a tripod, and its output analog signal is connected to the LMS SCADAS system, which is used as both a data acquisition system and a signal generator [65]. LMS Test Lab is used as the software interface of the LMS SCADAS system during tests. MIMO Stepped Sine Testing module in LMS Test Lab software is used to frontend control the input voltage for periodic chirp excitation. In the experiment, a 0.5 V periodic chirp signal with 10 kHz bandwidth is applied to the piezoelectric actuator as the source of excitation.



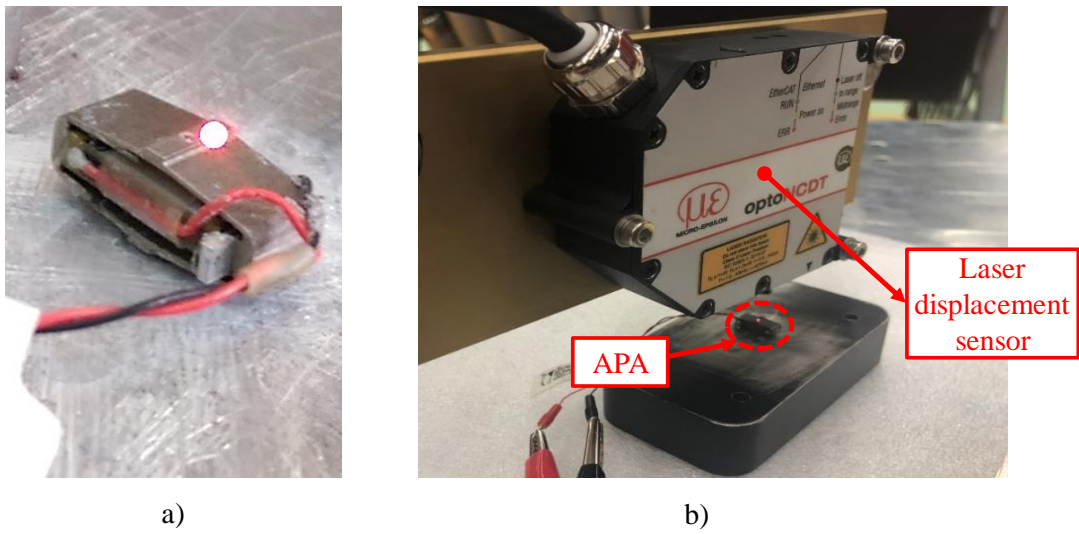


**Figure 2.11** (a) APA35XS fixed from its base to the testing table, and (b) non-contact displacement measurement with a laser displacement sensor

The experimental case study is simulated on the standard FEM tool as well. FRFs are calculated under harmonic voltage inputs using ANSYS Multiphysics solver with piezoelectric extension (Figure 2.12).

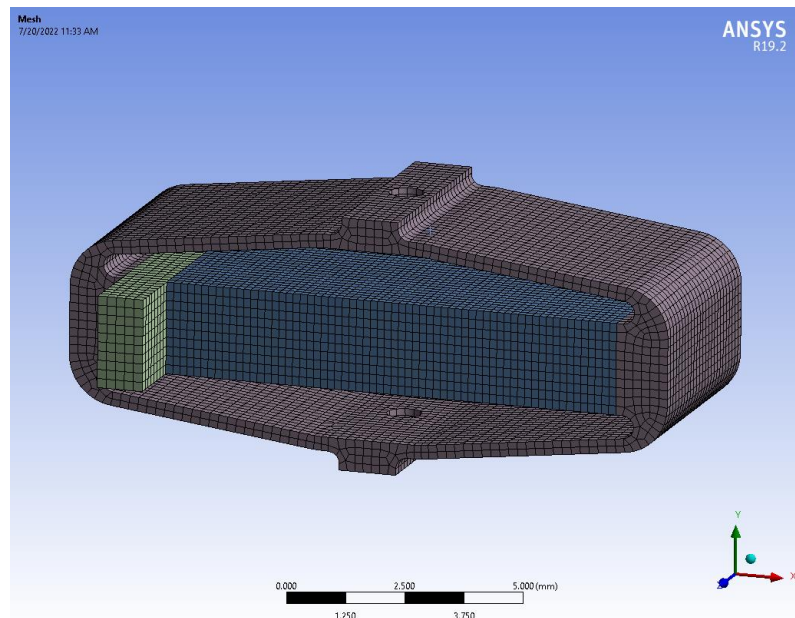


**Figure 2.12** FEM of the APA (APA35XS)

The comparison of the calculated FRFs with the experimental one is illustrated in Figure 2.13. It can be observed from the figure that the calculated and measured FRFs are very closed to each other, considering the uncertainties of the tested item. The resonance frequencies of FRFs in Figure 2.13 are given in Table 2.5. It can be concluded that the resonance frequency of the actual APA is estimated within 3% relative error, which demonstrates the accuracy of the analytical and FE model. A slight difference has been observed between the displacement amplitudes at resonances due to misestimating the damping coefficient of the APA. It is concluded that the level of accuracy of the APA model is sufficient for dynamic substructure coupling studies. Under linear assumptions, the analytical model will provide a dynamic relation between the measured and the unmeasured DOFs.

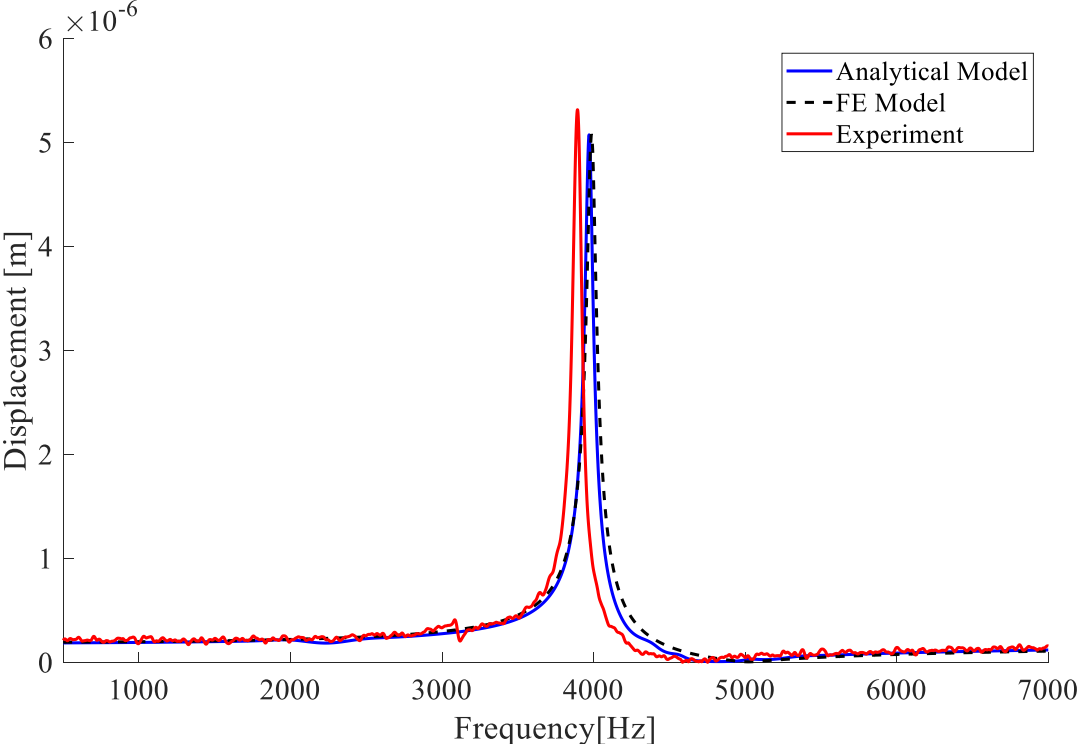


**Figure 2.13** Calculated and measured tip displacement frequency responses

**Table 2.5** The fixed-free resonance frequency of the APA

<b>Experiment [Hz]</b>	<b>FE model [Hz]</b>	<b>Relative error in FE result [%]</b>	<b>Analytical model [Hz]</b>	<b>Relative error in analytical result [%]</b>
3895	3985	2.31	3971	2.28



## CHAPTER 3

### OPTIMIZATION OF THE PIEZOELECTRIC-BASED BONE CONDUCTION TRANSDUCER

In the present chapter, the proposed BCHA design is optimized using a standard optimization tool based on the linear APA model verified in Chapter 2. The objective of the optimization problem is to obtain the best BC hearing under constant amplitude harmonic voltage input in the defined optimization domain. Therefore, a quantitative representation of BC hearing should be defined as a function of BC transducer output. Note that the performance evaluation of the proposed BC transducer is implemented under linear assumptions.

Many researchers have studied the physiology behind the BC hearing for decades [66–70]. These investigations mainly aim to explain the BC sound perception and factors contributing to BC hearing. The major factors contributing to BC hearing identified in the study of Stenfelt and Goode [70] are given as

- Transmitted sound from the skull interior,
- The relative motion of the middle ear ossicular chain,
- Inertial effects on the cochlea fluids,
- Elastic deformations on the cochlear walls,
- Sound pressure in the ear canal.

A schematic view of the different BC pathways is illustrated in Figure 3.1.

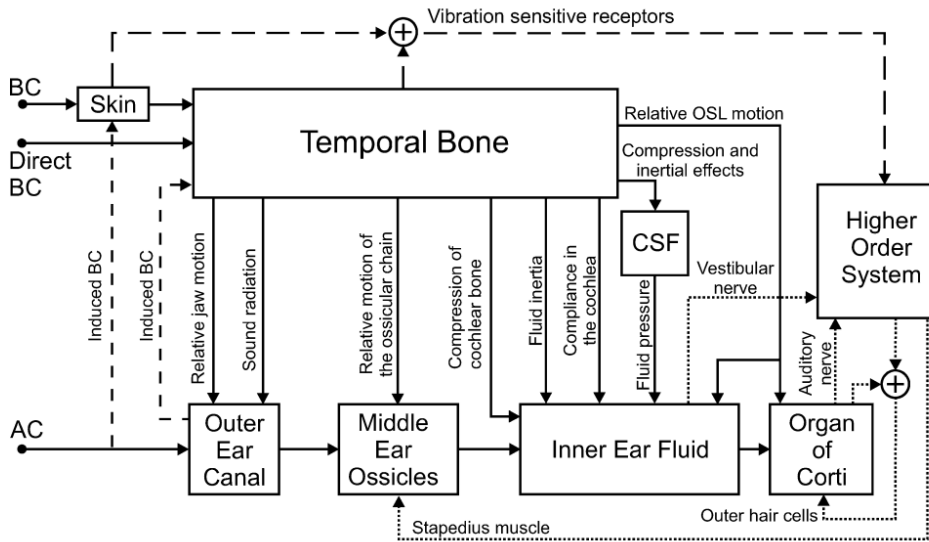


**Figure 3.1** The pathways contributing to BC hearing [70]

The relative weight of the given contributors to BC hearing is investigated in another study by Stenfelt [71]. Stenfelt argued that the inertia of cochlear fluids is the most important contributor to BC perception based on an inner ear model, especially at low frequencies below 1 kHz. It is estimated in the same study that the middle ear ossicles dominate BC hearing in frequencies from 1 kHz to 3 kHz. Eeg-Olofsson et al. [72] proposed that BC hearing perception is correlated to the velocity of the cochlear promontory at frequencies from 500 Hz to 5 kHz. Chang and Stenfelt [73] presented a finite element model of the human head study showing similarities between the frequency response pattern of the transmitted force on the skull and the vibrations of the cochlear promontory. It is deduced from [73] that the performance of a BC transducer can be quantified from the transmitted force to the skull. Hence, the mechanical point impedance of the stimulation location of BCHA is required to establish a transfer function between the driving voltage and the transmitted BC force on the skull.

There are also experimental studies investigating the dynamics of the human head under different BC stimulation conditions [74–78]. These studies focus on determining

point impedances and force transmissibility of BC stimulation location on the head. Point impedance measurements are also performed on dry skulls, cadavers, and live subjects. Cortes [75] investigated a group of healthy living subjects to determine the mean mechanical point impedance under on-skin stimulation. The measurement setup is illustrated in Figure 3.3. A dynamic force is applied to the living subjects with a mini-shaker coupled to an impedance head placed on the particular location of the head with a constant load (approx. 5.9 N). Living subjects are supported from their neck by employing a v-formed cushion. The mechanical impedance of the artificial mastoid B&K 4930 [79] is obtained experimentally for reference in [75]. Although the measured mechanical impedance of the artificial mastoid is lower than the average mechanical point impedance of all test subjects (Figure 3.2), the average stimulation force measured during live subject and artificial mastoid tests are close to each other, which can be considered as one of the most important outcomes of the Cortes study (Figure 3.4) [75].

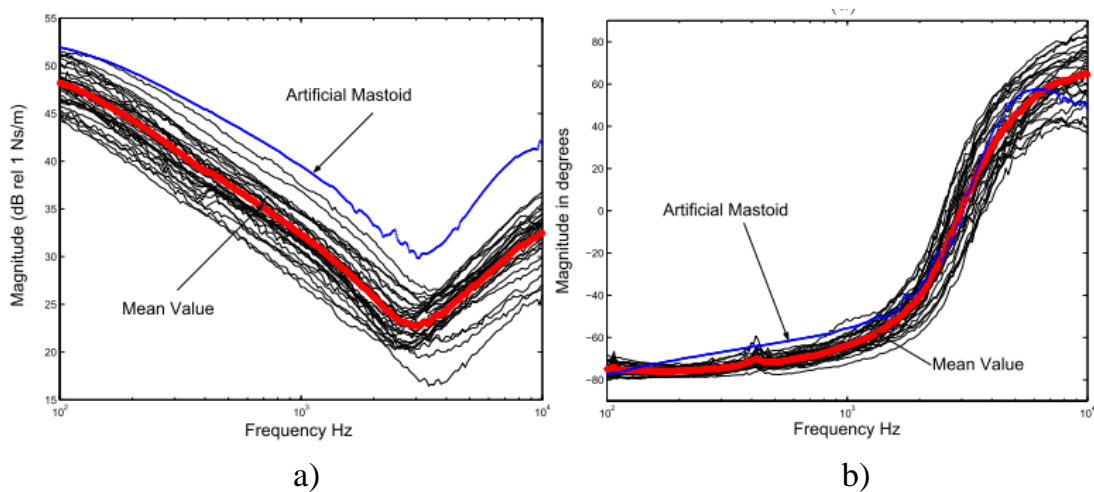
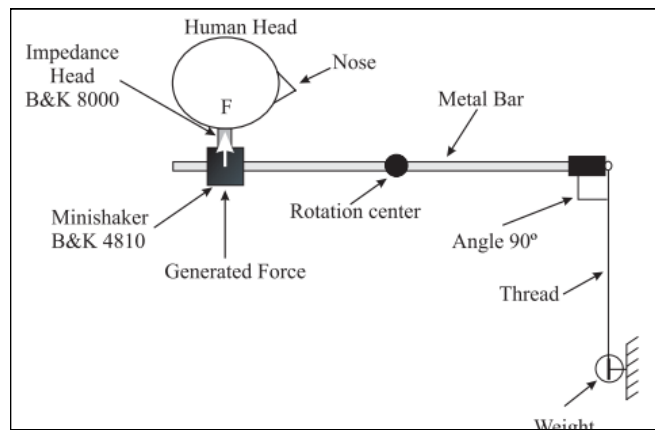
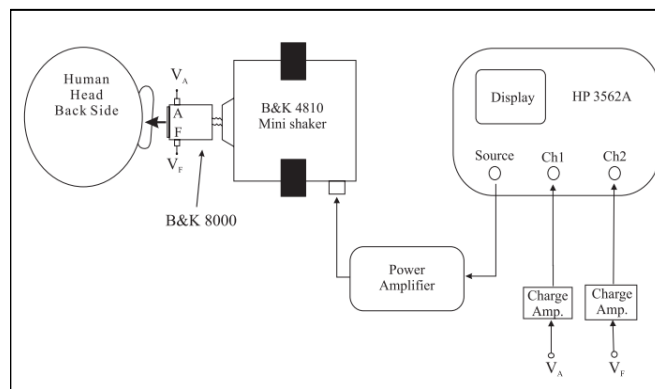


**Figure 3.2** The mechanical impedance (a) amplitude and (b) phase of live subjects, the mean values, and the artificial mastoid [75]



a)



b)

**Figure 3.3** Mechanical impedance measurement setup from Cortes's study [75]:

a) top view, b) back view

Relying on the results in Figure 3.4, the optimization procedure of the BC transducer aims to enhance the transmitted force-frequency response of the BC transducer through the Bruel & Kjaer type 4930 artificial mastoid [79] by adjusting the design parameters. The artificial mastoid is a test instrument that is used in the calibration of the BC hearing aids. The artificial mastoid consists of a mass and a rubber pad of viscous elastic material simulating the skull's total mass, skin, and underlying soft tissues. Figure 3.5 demonstrates the calibration setup of a BC transducer with the artificial mastoid. The artificial mastoid measures the transmitted force of the BC transducer to inertial mass underneath the rubber pad. The inertial mass of the artificial



mastoid is mounted on a base plate suspended on three compression springs. The BC transducer is placed on the rubber pad with an external static force that a preload mechanism could adjust. The mechanical impedance curves of the artificial mastoid (AM) given in Figure 3.6 are measured during the factory calibration under 5.4 N static force.

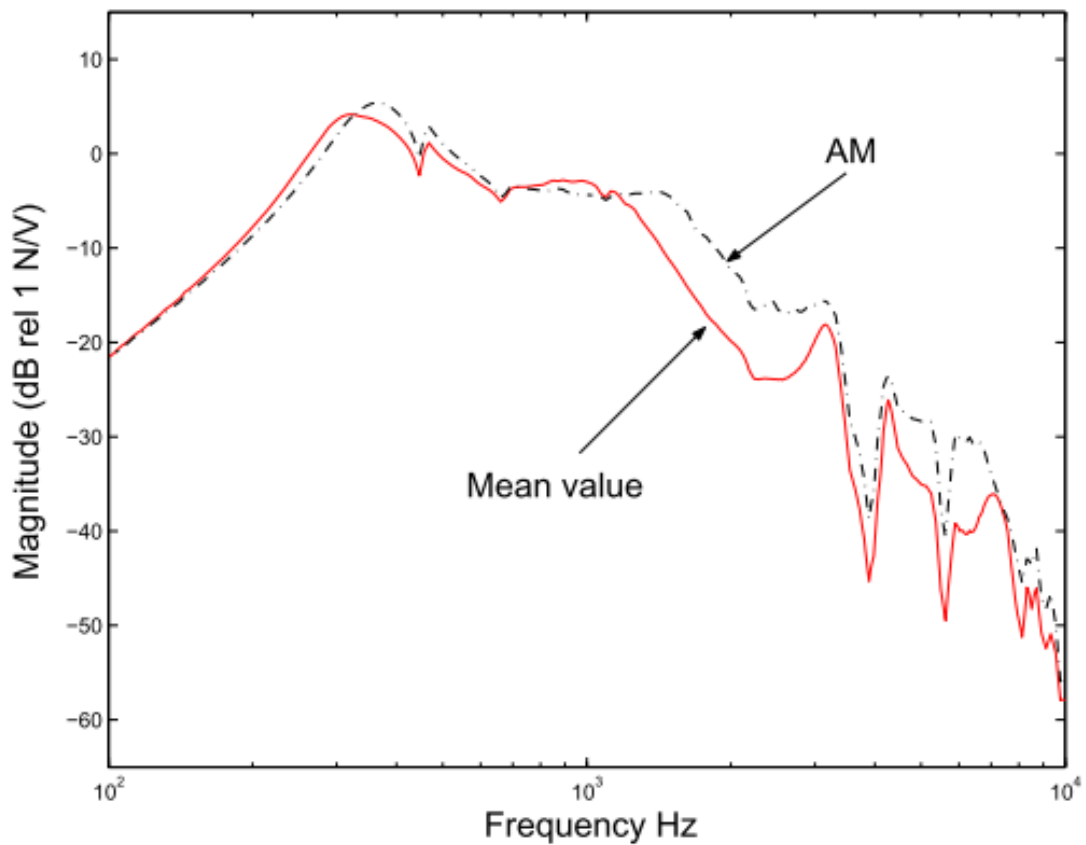


**Figure 3.4** Comparison of the measured stimulation force applied on the live subjects (mean values) and the artificial mastoid [75]

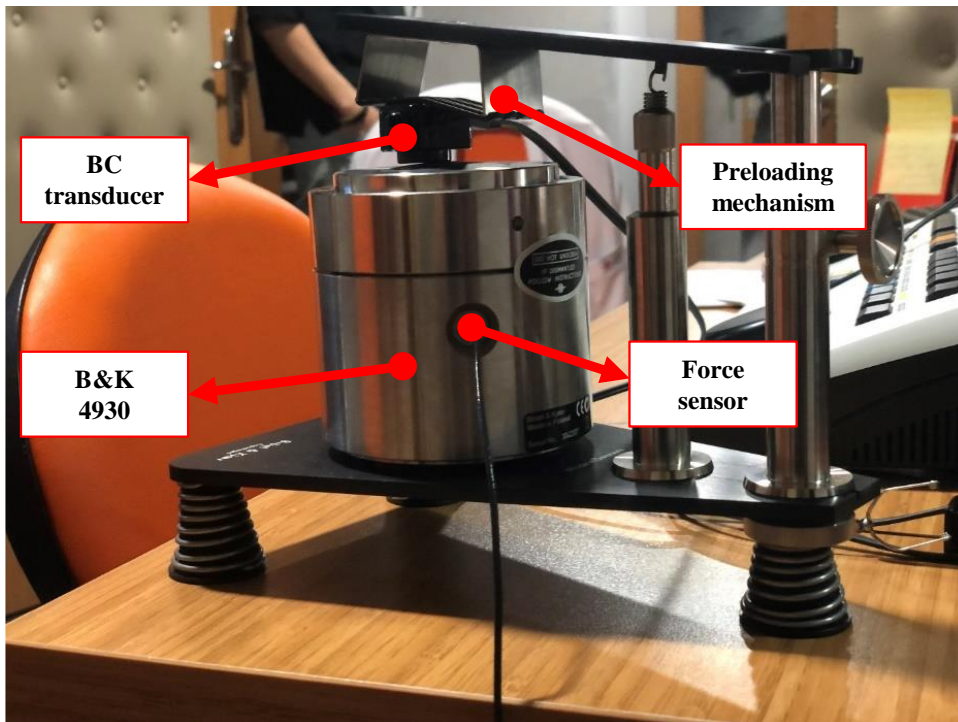


**Figure 3.5** The calibration arrangement of a BC transducer with the artificial mastoid

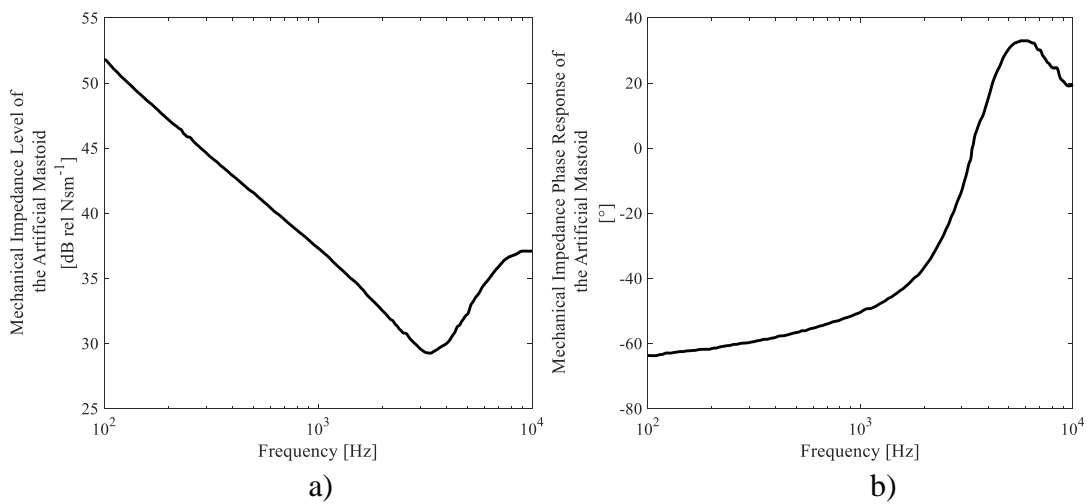


**Figure 3.6** Measured a) mechanical impedance and b) phase response of the artificial mastoid

The performance output of the B71 electrodynamic transducer is obtained experimentally by attaching it to the artificial mastoid shown in Figure 3.5. Additionally, the schematic view of the artificial mastoid test setup is shown in Figure 3.7. Data acquisition and closed-loop control operations are accomplished by the LMS SCADAS system and LMS Test Lab software [65]. During tests, B71 is driven with 1  $V_{rms}$  harmonic voltage input in the defined frequency range (100 Hz-8 kHz), where the transmitted force is measured via the force sensor placed in the artificial mastoid.

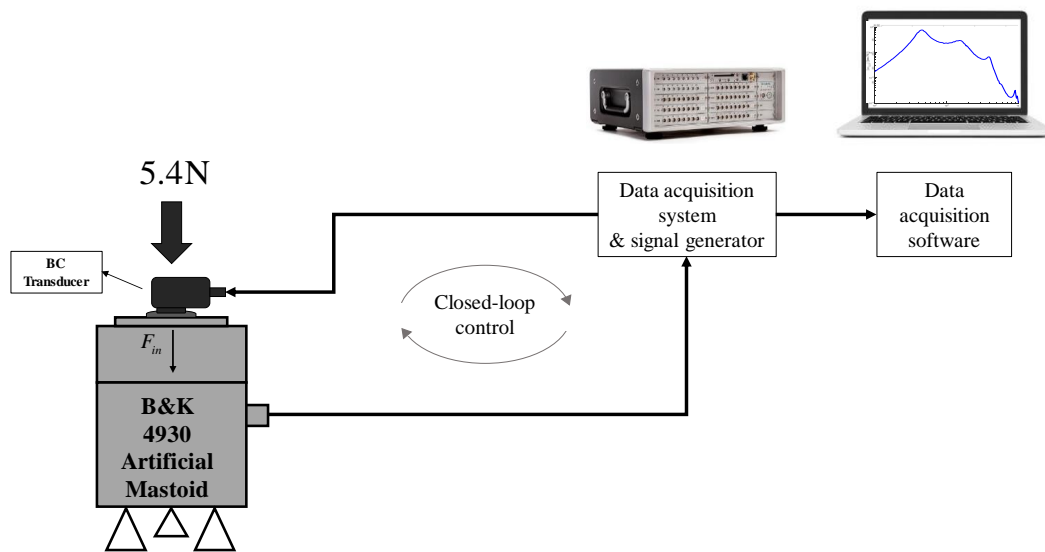


**Figure 3.7** The schematic view of the artificial mastoid test setup

In accordance with ISO 389-3 standard [80], the reference equivalent threshold force levels (RETFLs) are referred to as the dynamic force level transmitted by a BC transducer when it is excited at a harmonic voltage level corresponding to the threshold of hearing of young otologically healthy listeners (Figure 3.8). The hearing level in decibel (dB HL) is defined in Eq.(3.1) as the difference between the output force of a BC transducer,  $F_{in}$  and RETFL [31];

$$Hearing\ Level = F_{in}[dB] - RETFL[dB]. \quad (3.1)$$

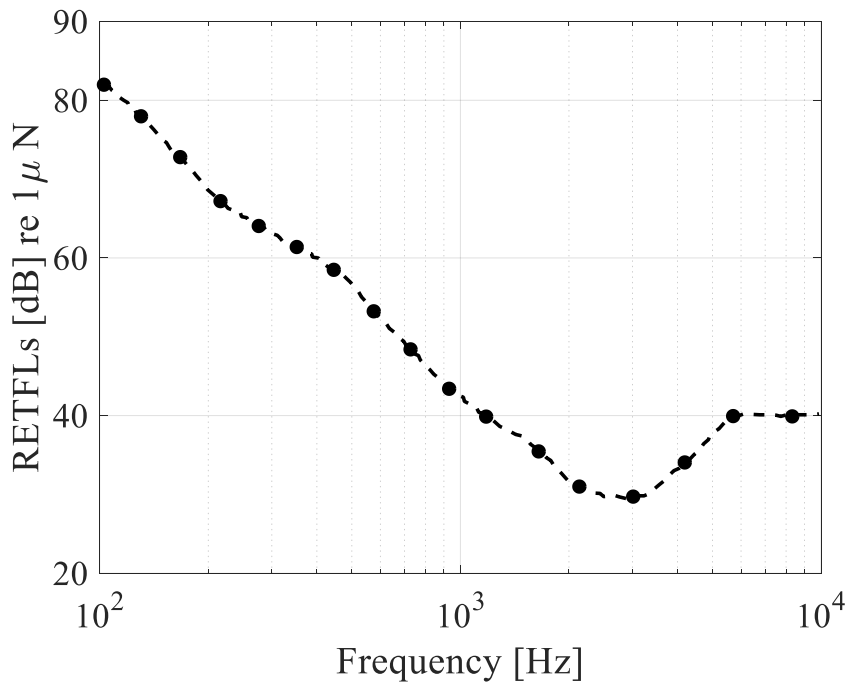


**Figure 3.8** The reference equivalent threshold force levels (RETFLs)[80]

A mathematical model of the BC transducer coupled with the artificial mastoid is required to define the optimization problem's objective function. The linear dynamic model of the APA has already been determined in Chapter 2 for different boundary conditions. The reduced dynamic model of the coupled system, shown in Figure 3.9, can be obtained by using the substructuring technique described in Chapter 2.

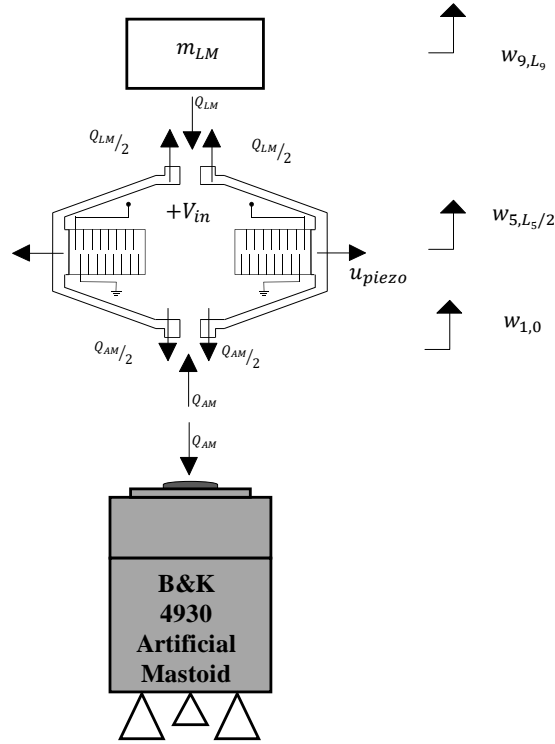


**Figure 3.9** The free-body diagram of the APA with a tip mass attached to the artificial mastoid

The dynamic stiffness matrix of the coupled structure is calculated based on the dynamic stiffness matrix of the APA, tip mass, and the artificial mastoid given in (3.2)

$$\begin{Bmatrix} W_{1,0}(\omega) \\ W_{9,L_9}(\omega) \\ U_{5,L_5/2}(\omega) \\ W_{5,L_5/2}(\omega) \\ \Psi_{5,L_5/2}(\omega) \end{Bmatrix} = \begin{bmatrix} Z_{APA}^{11} + \frac{1}{2}Z_{AM}^{11} & Z_{APA}^{12} & Z_{APA}^{13} & Z_{APA}^{14} & Z_{APA}^{15} \\ Z_{APA}^{21} & Z_{APA}^{22} - \frac{1}{2}\omega^2 m_{LM} & Z_{APA}^{23} & Z_{APA}^{24} & Z_{APA}^{25} \\ Z_{APA}^{31} & Z_{APA}^{32} & Z_{APA}^{33} & Z_{APA}^{34} & Z_{APA}^{35} \\ Z_{APA}^{41} & Z_{APA}^{42} & Z_{APA}^{43} & Z_{APA}^{44} & Z_{APA}^{45} \\ Z_{APA}^{51} & Z_{APA}^{52} & Z_{APA}^{53} & Z_{APA}^{54} & Z_{APA}^{55} \end{bmatrix}^{-1} \begin{Bmatrix} 0 \\ 0 \\ 0 \\ F_{act} \\ 0 \end{Bmatrix} \quad (3.2)$$

where  $W_{i,j}$  and  $U_{i,j}$  are the transverse and longitudinal displacements of the  $x_i = j$  coordinate of the  $i^{th}$  beam, respectively.  $\mathbf{Z}_{APA}$  and  $\mathbf{Z}_{AM}$  are the dynamic stiffness matrices of the APA and the artificial mastoid, respectively, and  $m_{LM}$  is the attached tip mass of the APA.  $F_{act}$  is the harmonic output force of the MSPA.

Before the design optimization stage, the performance of the APA35XS as a BC transducer is quantified by calculating the transmitted force through the artificial mastoid in the frequency domain of interest. The performance analysis is repeated for different tip masses from 0 to 15 grams, and the results are then compared with the measured performance output of the B71 electrodynamic transducer [81]. The transmitted force-frequency response curves of the B71 and APA35XS-based BC transducers are shown in Figure 3.10. It is observed from Figure 3.10 that APA35XS is not a suitable candidate as a BC transducer because of its poor performance at low frequencies.

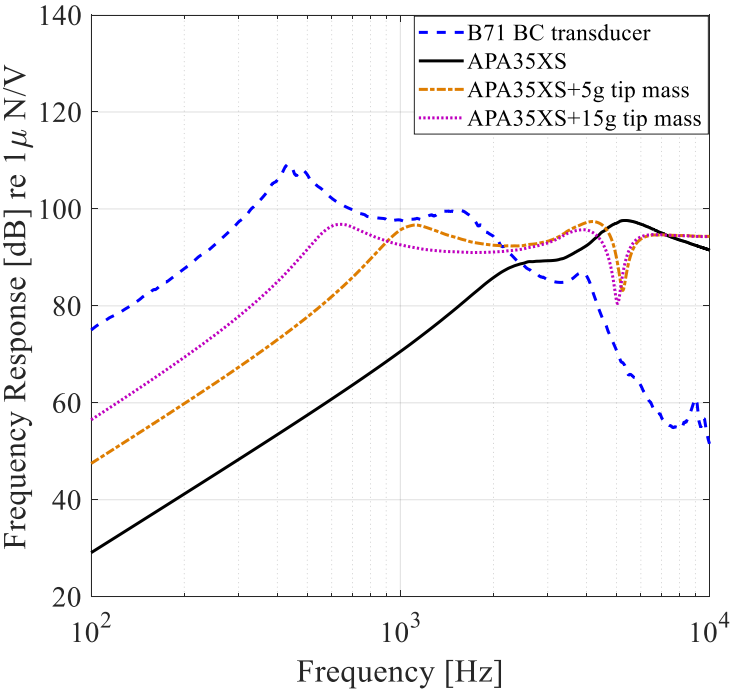


**Figure 3.10** The frequency response curves of B71(measured) and APA35XS (calculated) transducers with different tip masses

At this stage, the performance of the proposed bone conduction transducer is maximized by optimizing some of the design parameters (such as the thickness and the inclination angle of the RCM lever arms and the width of the RCM) in a predefined optimization domain via genetic algorithm. The material of the mechanical amplifier

is changed to Titanium Alloy Ti6Al4V due to medical and structural concerns, and the piezoelectric ceramic of the MSPA is changed from NEPEC N17 to NEPEC N10 to increase the APA's electromechanical efficiency. The maximum allowable tip deformation of the optimized APA is limited to a specific value of 0.15 mm to avoid stress concentrations at the root of the lever arms. The parameter optimization is performed by using MATLAB's optimization tool (*optimtool*), utilizing genetic algorithm as the optimization method. The objective function is defined as the mean squared error between the calculated transmitted force-frequency response and the aimed transmitted force level (120 dB rel. to 1  $\mu N/V$ ). The optimization tool returns a set of optimized design parameters in Table 3.1 at the end of the optimization operation. After the optimization process is completed, the performance outputs of the new APA design are calculated based on the parameters given in Table 3.1.

**Table 3.1** Optimized Parameters of the Amplified Piezoelectric Actuator

	<b>APA35XS</b>	<b>Optimized APA</b>
<b>Material of the RCM</b>	Stainless Steel	Titanium Alloy Ti6Al4V
<b>Material of the MSPA</b>	NEPEC N17	NEPEC N10
<b>Tip mass</b>	None	10 g
<b>The thickness of the lever arms</b>	0.3 mm	0.12 mm
<b>The inclination angle of the lever arms</b>	7°	4°
<b>The width of the RCM</b>	5 mm	9 mm

The calculated transmitted force-frequency response of the optimized APA is illustrated in Figure 3.11, including the ones presented in Figure 3.10. It can be deduced that the new APA becomes more flexible without compromising its strength, and the fundamental frequency of the resultant BC transducer becomes 413 Hz without adding an excessive tip mass. The output transmitted force levels of the BCHA outperform the B71 bone vibrator for frequencies above 3 kHz; however, there is a shift down up to 10 dB for frequencies below 3 kHz. The transmitted force of the

BCHA to the cochlea is higher for the direct bone conduction applications, considering the lack of skin attenuation by 10-20 dB [82]

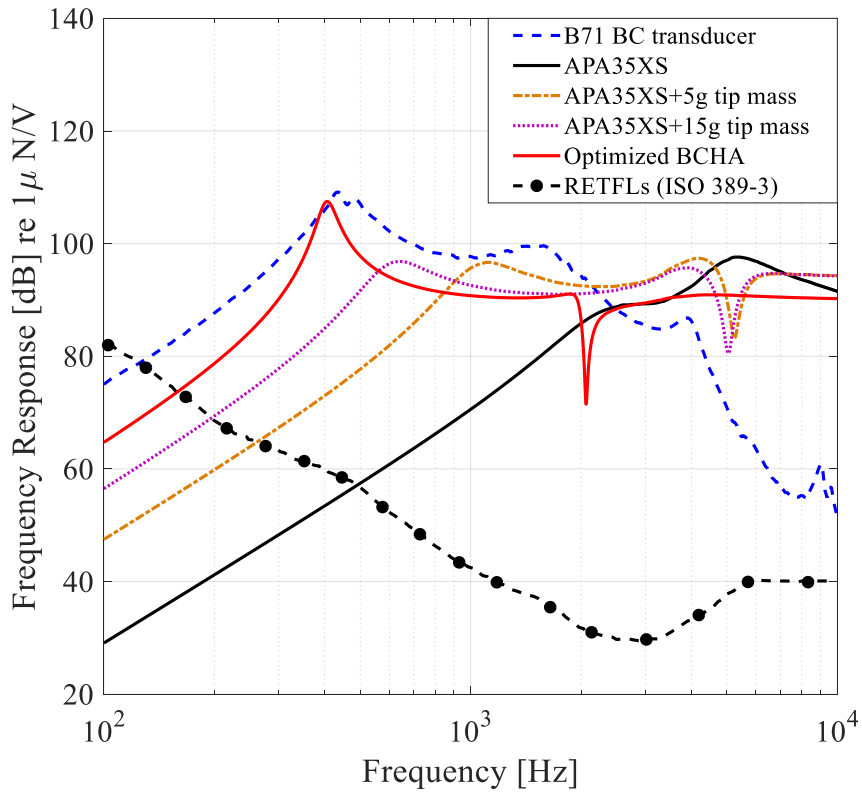


**Figure 3.11** Comparison of the frequency response curves of the B71(measured), APA35XS (calculated) with different tip masses, and the optimized BC transducer (calculated)

After completing the new BC transducer's design optimization steps, the new design was built in the CAD environment (Figure 3.12a) based on the parameters obtained from the optimization tool. Then the prototypes were manufactured by Cedrat Technologies (shown in Figure 3.12b). It is noted that the classical bone vibrators are designed for diagnostic hearing investigations of patients, and their size and weight are not the primary concern. However, an ideal BC implant should be light and small. The new BC transducer design is packed into a titanium casing (Figure 3.13a). The material of the tip mass is selected as platinum so that the total height of the BC implant



transducer will be as small as possible (Figure 3.13b). The outer dimensions of the new BC implant transducer, which are smaller than the outer dimension of the BC transducer of the active transcutaneous implantable BCHAs in the market, are shown in Figure 3.14a and Figure 3.14b.

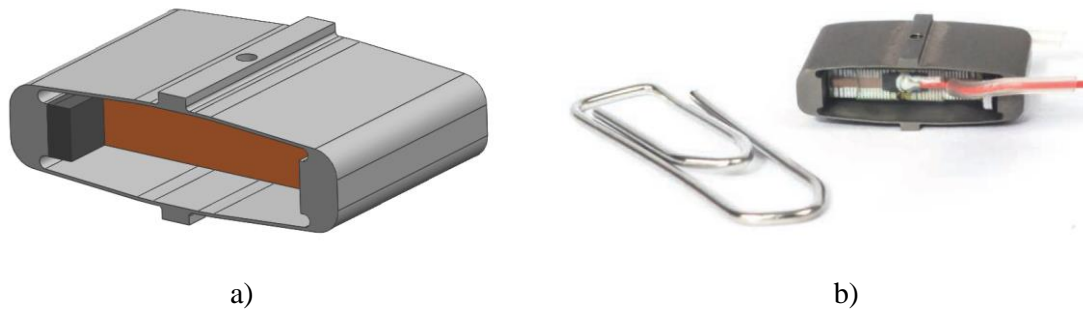


**Figure 3.12** a) The design of the optimized APA b) the prototype of the optimized APA

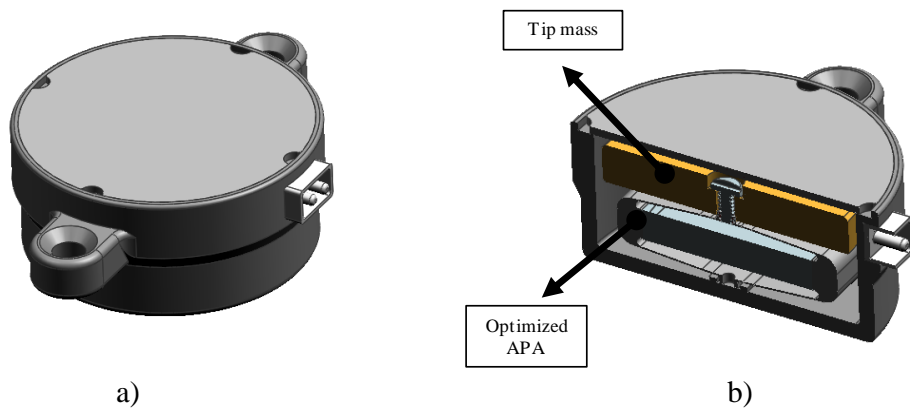


**Figure 3.13** a) The design of the new BC implant b) cross-sectional view of the new BC implant

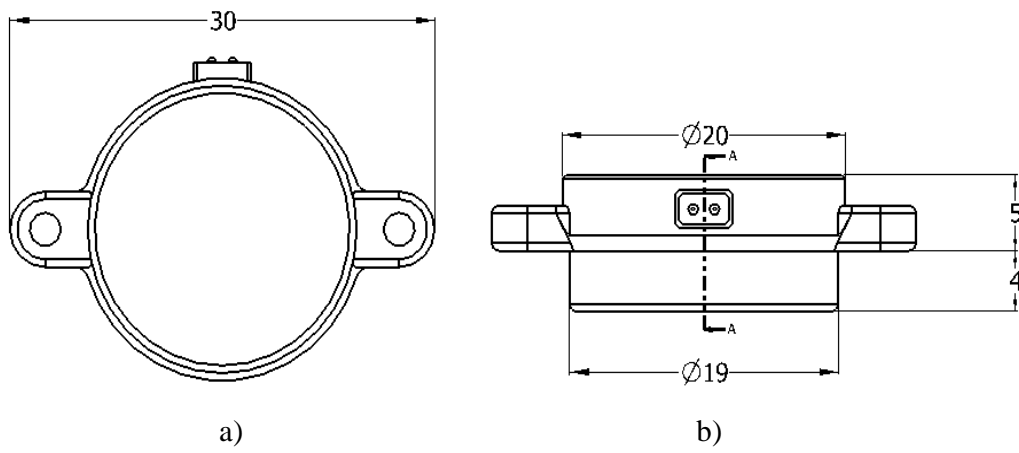


**Figure 3.14** Outer dimensions of the new BC implant design a) top view b) front view (*all the dimensions in mm*)

## CHAPTER 4

### **EXPERIMENTAL MODAL ANALYSIS OF NONLINEAR AMPLIFIED PIEZOELECTRIC ACTUATORS BY USING RESPONSE-CONTROLLED STEPPED-SINE TESTING**

Dynamic applications such as bone conduction sound transmission require predicting dynamic displacements of an APA under high frequency and resonant conditions [57]. In Chapter 2, miniature APAs have been considered low-power actuators and are expected to behave linearly under weak electric fields [83]. Accordingly, linear constitutive models have been utilized to estimate the dynamic behaviors of APAs. However, recent studies reveal that piezoelectric actuators exhibit nonlinear behavior even when subjected to weak electric fields [84–87]. A nonlinear model is required to describe the behavior of a piezoelectric actuator for dynamic applications.

There is an extensive body of literature for modeling and experimental identification of nonlinearities in patch-type piezoelectric actuators (see, e.g.,[88–94]). In the literature, the general approach is to presume a physical-driven (constitutive) nonlinear model for the piezoelectric material by observing measured constant-voltage frequency response data. The apriori model is then converted to a reduced-order modal model that can be used to carry out dynamic simulations. The identification is completed by tuning the parameters of the physical model in a manner to match the simulated frequency response (or backbone curve) data with the corresponding experimental data. A drawback of this approach is that it is quite possible to overlap the simulated and experimental data even with an incorrect model. For example, if the constitutive model assumes linear damping while the actual piezo-material exhibits nonlinear damping, the tuning process will compensate this modeling error by overshooting the actual parameters of the conservative part of the constitutive model. This issue may be handled possibly better by directly correlating the parameters of the

physical model with the measured nonlinear modal data instead of frequency response data. By virtue of the recent developments in the field of nonlinear structural dynamics, the accurate identification of nonlinear modal parameters, including the nonlinear modal damping ratio, is now within reach [95, 96].

Compared to patch-type piezo-actuators, the literature about the MSPAs is very limited [37, 52, 86, 87, 97–101]. Dynamic behaviors of both types of actuators considerably differ from each other. In the patch-type actuators, nonlinearity in the ‘31’-electromechanical coupling and its associated ‘1’-directional elasticity becomes important (Figure 4.1b). On the other hand, in the MSPAs, nonlinearity in the ‘33’-electromechanical coupling and ‘3’-directional elasticity has to be considered (Figure 4.1a).

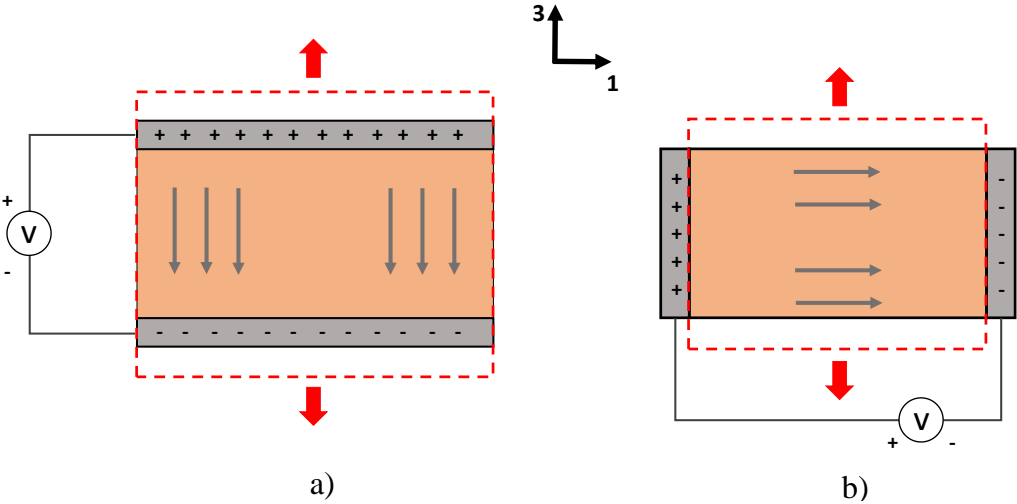


**Figure 4.1** Operation modes of piezoelectric actuators: a) the stacked type in d33 mode, b) the patch type in d31 mode

To the best of the authors' knowledge, the only comprehensive study that characterizes the nonlinearity of MSPAs has been recently published in [87]. In that work, Shivashankar et al. constructed a nonlinear constitutive model for longitudinal vibrations of MPSAs by following a procedure similar to the one previously mentioned for patch-type actuators. The experimentally extracted backbone curve plays the key

role in characterizing the nonlinearity, i.e., proposing a nonlinear constitutive model with unknown coefficients. These unknown coefficients are then identified by using constant-voltage frequency response data. Although constant-voltage (or force) testing may be suitable to extract the backbone curves in the case of relatively weak nonlinearities [87], it may result in considerable inaccuracy in the case of strong nonlinearities that exhibit the jump phenomenon due to unstable branches [102]. Fortunately, a prominent feature of the RCT method [95] is the accurate identification of turning points, unstable branches, and backbone curves of frequency response functions (FRFs), as shown later in this thesis. Furthermore, keeping the response amplitude constant during frequency sweep makes the RCT method very suitable for studying the frequency dependency of nonlinearity [103], which may also be a significant issue for the MPSAs, as discussed in [87, 104]. It is also possible to accurately identify the nonlinear modal damping by employing the RCT method using standard commercial modal test equipment, which is still challenging with other techniques. In the work of Shivashankar et al. [87], the damping is assumed to be linear, which is arguable, and may also affect the accuracy of the constitutive model. In literature, studies exist that investigate the nonlinear damping mechanism of patch-type piezo-actuators [91, 92]. However, no such study is available in the limited literature on stack-type piezo-actuators.

Similar to many nonlinear system identification techniques recently developed in the field of structural dynamics, the RCT method also relies only on the nonlinear normal mode (NNM) concept, which was first introduced by Rosenberg [105]. Analogous to linear normal modes, Rosenberg defined a nonlinear mode as a *vibration in unison* with a nonlinear system. Later, in 1979, Szemplinska-Stupnicka presented the modified “single nonlinear mode” method [106] to model near-resonant vibrations of nonlinear multi-degree of freedom (MDOF) systems by using the NNM concept. The proposed method shows that the near-resonant frequency responses of a nonlinear system can be expressed by using a single NNM and its corresponding natural frequency, presuming the modes are well separated and no internal resonances occur.

The single NNM and corresponding nonlinear modal parameters are functions of modal amplitude.

Until the 2010s, studies that used the NNM concept in nonlinear system identification were very few. Important early examples are [107, 108]. However, in the last decade, the number of nonlinear modal identification methods based on the NNM concept has increased significantly [109–112]. Although these state-of-the-art techniques successfully identify NNM backbone curves, the accurate identification of nonlinear modal damping is still a challenging issue. Furthermore, there exist few studies that identify a high degree of nonlinearities and that validate the identified nonlinear modal properties.

Recently, phase resonance testing with a phase-locked-loop (PLL) controller [112] successfully achieved the identification of nonlinear modal damping of a friction-damped joint resonator [96] by using the extended periodic motion concept [113]. This approach also proved its applicability for identifying much stronger nonlinearities, modal damping ratio of up to 15%, and a resonance frequency shift of 36% in the case of a cantilever beam with dry friction [114]. An important benefit of the phase resonance testing with the PLL controller is that only the points on the backbone curve need to be tested, which can reduce the test duration considerably. On the other side, a possible drawback is that it is currently not implemented in commercial modal test systems (e.g., LMS Test Lab) and, therefore, cannot easily be used by practicing engineers.

Another promising nonlinear modal identification method that can identify nonlinear modal damping ratio and that can accurately quantify a high degree of nonlinearities has been recently proposed by Karaağaçlı and Özgüven in [95] under the name of response-controlled stepped-sine testing (RCT). In this method, the displacement amplitude of the driving (excitation) point is kept constant in a closed-loop control during the stepped sine testing. Various applications ranging from simple benchmarks to real and complex engineering systems showed that this control strategy yields quasi-linear constant-response FRFs around resonance frequencies. The important merit of

the RCT method is that these quasi-linear FRFs can be easily measured using standard commercial modal test equipment. Then, they can be processed by standard linear analysis techniques to identify response level-dependent modal properties of nonlinear structures accurately. The RCT method has been successfully applied so far to a T-beam with local cubic stiffness [95], a missile structure with considerable damping nonlinearity mostly due to bolted joints [95], and a double-clamped beam with strong geometrical nonlinearity [115]. In [115], the RCT method accurately quantified about a 20% shift of the natural frequency and an order of magnitude change in modal damping ratio (from 0.5% to 4%).

It is worth mentioning that the idea of extracting response-level dependent modal parameters from constant-response testing essentially dates back more than a decade earlier than the RCT method [116, 117]. However, in [116], the theoretical base remains restricted to structures with local nonlinearities. On the other hand, in [117], although it is achieved to identify amplitude-dependent modal parameters of an engineering system with distributed nonlinearity by using constant-acceleration testing, the nonlinearity is weak; the method lacks theoretical justification and is based on intuition. Moreover, keeping acceleration amplitude constant is just an approximation to keeping displacement amplitude constant, and does not hold true when there is considerable resonance frequency shift, as in the case of geometric nonlinearities. The RCT method [95], on the other hand, provides a rigorous mathematical framework by combining the single nonlinear mode theory [106] with the Nonlinearity Matrix concept [118], and its applicability is experimentally demonstrated on various strongly nonlinear mechanical systems as mentioned above. It is also important to note that the contribution of the RCT is not limited to identifying response-dependent modal parameters. It uses these parameters to obtain constant force amplitude FRFs both in stable and unstable frequency regions. Furthermore, it provides the unstable branches of FRFs directly from measurements as well by using the harmonic force surface (HFS) concept [95, 102, 115].

The applicability of RCT to a miniature electromechanical system incorporating piezoelectric material could not be taken for granted for several reasons. Firstly, the frequency dependence of the nonlinearity in stack-type piezo-actuators could possibly be significant, as suspected by Shivashankar et al. [87], which could degrade the quasi-linearity of constant-response FRFs. Secondly, the miniature nature of the electromechanical device is required to conduct the test at very low response amplitudes (far below 10  $\mu\text{m}$ ) compared to previous RCT applications [95, 115]. Low response amplitude tests possibly lead to a considerably low S/N ratio which could distort the measurements and render response-control impossible. Thirdly, the small scale of the APA enforces considerable modifications in the usual implementation of the RCT method: a non-contact laser displacement sensor is chosen as the control sensor instead of an accelerometer, and the structure is excited with the embedded piezoelectric stack actuator instead of an electrodynamic shaker, and the excitation and response control points do not coincide. These modifications could cause unexpected complications that could obstruct the applicability and disrupt the accuracy of the RCT method.

In this chapter, the miniature amplified piezoelectric actuator APA35XS investigated in Chapter 2 is chosen as a test specimen for nonlinear modal analysis [97]. The displacement amplitude of the control point is kept constant, and the input voltage spectrum corresponding to each displacement amplitude level is measured during the stepped-sine tests. Eventually, frequency response functions (FRFs) come out quasi-linear. Modal parameters are experimentally identified from the quasi-linear FRFs through standard linear modal analysis tools. Nonlinear modal parameters of the miniature APA are then extracted as functions of response amplitude.

#### **4.1. Methodology of the Experimental Modal Analysis with RCT**

Nonlinear experimental modal analysis by using the RCT method has been recently proposed in [95], where its theoretical background and implementation are explained



in detail. For the sake of completeness, the fundamental steps and the key features of the method are explained below.

The experimental modal analysis with RCT consists of the following fundamental steps:

*Step 1:* Quasi-linear constant-response FRFs are measured at several different displacement amplitude levels by keeping the displacement amplitude of the control point constant throughout the stepped sine testing at each level.

*Step 2:* Modal parameters of each quasi-linear FRF are identified using standard linear modal analysis tools. A nonlinear modal model is then constructed by expressing the identified modal parameters as functions of the displacement (equivalently modal) amplitude.

*Step 3:* Required near-resonant constant-force (or voltage) frequency response curves are calculated employing the identified modal parameters in a Newton Raphson solution scheme with the arc-length continuation algorithm.

The quasi-linearity of constant-response FRFs mentioned above is theoretically based on the following receptance formula derived from the single nonlinear mode theory [106] and the Nonlinearity Matrix concept [118] as explained in [95]:

$$H_{jk}(\omega, q_r) = \frac{\bar{A}_{jkr}(q_r)}{\bar{\omega}_r^2(q_r) - \omega^2 + i\bar{\eta}_r(q_r)\bar{\omega}_r(q_r)} \quad (4.1)$$

where  $\bar{A}_{jkr}(q_r)$ ,  $\bar{\omega}_r(q_r)$ ,  $\bar{\eta}_r(q_r)$  and  $q_r$  are the complex modal constant, natural frequency, modal damping ratio, and the modal amplitude of the  $r^{\text{th}}$  nonlinear normal mode, respectively.  $j$  is the response coordinate,  $k$  is the excitation coordinate, and  $\omega$  represents the excitation frequency.

Obviously, all the modal parameters given in Eq.(4.1) are functions of a single parameter; the modal amplitude  $q_r$ . Accordingly, if the modal amplitude is kept

constant throughout the stepped-sine testing, the measured receptances come out in the quasi-linear form. In [95], it has been shown that the constant modal amplitude condition can be achieved by keeping the displacement amplitude of the control point constant. This also means that the modal amplitude can be mapped to the spatial displacement amplitude of the control point. Therefore, the receptance shown in Eq.(4.1) can be alternatively expressed as follows:

$$H_{jk}(\omega, |X_j|) = \frac{\bar{A}_{jkr}(|X_j|)}{\bar{\omega}_r^2(|X_j|) - \omega^2 + i\bar{\eta}_r(|X_j|)\bar{\omega}_r(|X_j|)} \quad (4.2)$$

where  $|X_j|$  is the displacement amplitude of the control point.

It is important to note that the single nonlinear mode theory does not provide a general mathematical proof that guarantees the validity of its fundamental hypothesis for any nonlinear structure, i.e., the dependence of nonlinear modal parameters on a single parameter; the modal (or displacement) amplitude. In order to turn this hypothesis into a well-established theory, it must be verified by experiments applied to different types of nonlinearities. The RCT has already been verified so far on joint nonlinearities [95] and continuously distributed (geometrical) nonlinearities [115], which are considered challenging problems for the current state-of-the-art. This study makes a third important contribution that further expands the application area of the single nonlinear mode theory and the RCT method to include miniature electromechanical devices that incorporate piezoelectric material.

Concluding this section, it is interesting to note that since the exciter, i.e., piezo-actuator, is an integral element of the test structure, it is not possible to quantify the excitation force in the units of Newton directly. However, this is not an important issue since the main objective of this study is to construct an accurate mathematical model that relates the input voltage to the displacement output. Accordingly, the receptance formula given in Eqs.(4.1) and (4.2) is also used somewhat differently than their classical definitions. The receptance represents the relation between the excitation

force and the output displacement in its classical definition. However, in this study, the receptance represents the transfer function between the input voltage and the output displacement.

## 4.2. Experimental Work

As reported in [87], most of the studies in the literature have focused on characterizing the nonlinear dynamic behavior of patch-type piezoelectric actuators. Since works about the elasticity of stack-type piezoelectric actuators are quite a few, their nonlinear dynamic behavior is not yet fully understood and is still an open research field. From this perspective, the significant merit of this experimental work of the thesis study is the identification of nonlinear modal parameters and the construction of an accurate nonlinear modal model of a commercial miniature APA, which may help to estimate the parameters of a physical-driven (constitutive) model and therefore to gain a better theoretical understanding about the nonlinear behavior of MSPAs and APAs.

### 4.2.1. Experimental Setup

The focus of this section was the fundamental transverse vibration mode of the APA in the actuation direction that exhibits possible nonlinearities. In order to study that mode, the APA was fixed to the ground from its base (Figure 4.2).

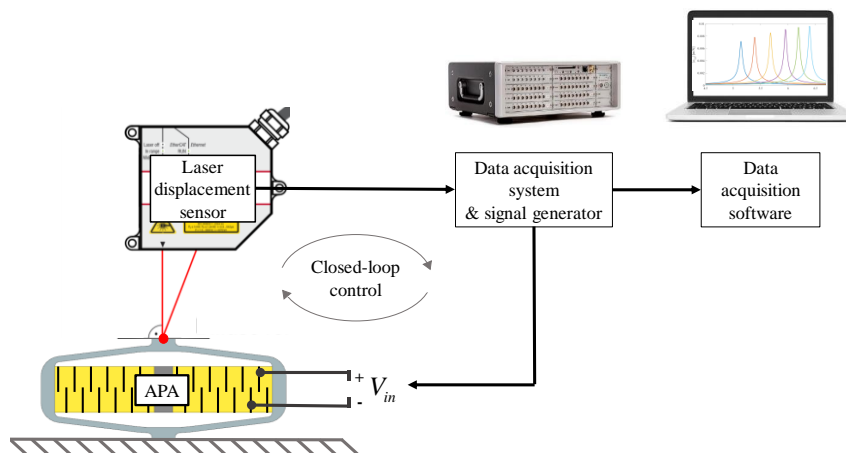


**Figure 4.2** Schematic view of the experimental setup

Since the APA is a self-exciting structure, it does not require an external excitation source. Therefore, the harmonic excitation force was generated by feeding the stack-type piezoelectric actuator embedded in the APA with harmonic voltage input. Since the excitation mechanism is part of the tested structure, the exciter-structure interaction is not very relevant to the application case studied herein. However, in the case of an external exciter such as an electrodynamic shaker, this interaction can be a significant issue [119, 120]. Suppose the basic assumptions of the single nonlinear mode theory [106], i.e., well-separated modes and negligible higher harmonics, hold true, and the shaker attachment does not significantly distort the modal deflection. In that case, the shaker-structure interaction is not pronounced [119], and the RCT method can be successfully applied by using standard modal test equipment. In practice, various damping mechanisms (e.g., friction at joints and/or material damping) naturally suppress the effects of higher harmonics [115, 119], and the single nonlinear mode theory remains valid for a wide range of applications as in the case of this thesis study and the previous applications of the RCT method [95, 102, 115]. However, at sufficiently high energy levels, strong higher harmonics may arise due to harmonically coupled modes (internal resonance) [121]. In such a case, the closed-loop response control has to be implemented with a noninvasive control scheme [122] so that the controlled structure behaves the same as the open-loop structure. Alternatively, internal resonance can be studied by phase resonance testing with a PLL controller, which is naturally noninvasive.

The vibration response of interest is the vertical tip displacement of the APA in the actuation direction (which is related to the transverse vibration mode). The tip displacement was measured by a non-contact laser displacement sensor (Micro-Epsilon OptoNCDT 2300) [64], which was installed on top of the actuator. During the experimental work, the LMS SCADAS system and LMS Test Lab software accomplished all the data acquisition and closed-loop control tasks. Both systems are also shown in Figure 4.2. The frequency range of interest encompassing the mode of interest was determined by preliminary fast sine sweep (periodic chirp) tests. During

all the constant-voltage and constant-response stepped sine tests, the frequency step was defined as 0.5 Hz.

#### 4.2.2. Results of Constant-Voltage Stepped Sine Tests

Before the application of the RCT method, a series of constant-voltage tests were conducted on the miniature APA similar to [87]. The amplitude of the input harmonic voltage is kept constant in closed-loop control, and the tip displacement of the APA is then measured as an output. FRFs measured at different constant voltage levels are shown in Figure 4.3. As the voltage level increases from 0.1 V to 3 V, an approximately 130 Hz drop of the resonance frequency is observed, indicating strong softening nonlinearity.

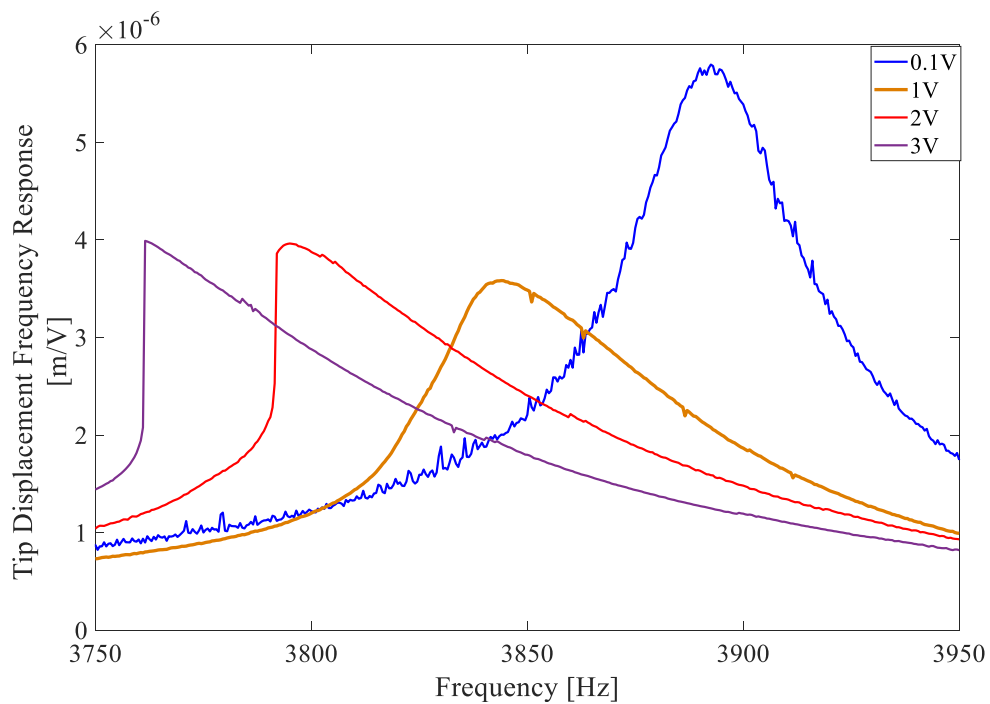


**Figure 4.3** FRFs measured by constant-voltage stepped-sine testing

Another important observation related to Figure 4.3 is the jump phenomenon observed at high voltage levels, indicating unstable regions. The observed jump phenomenon is one of the most striking differences between this study and the work of Shivashankar [87]. In the latter, the nonlinearity is relatively weak, and luckily no jump is encountered. During constant-voltage (or force) stepped-sine testing of structures in an unstable region, corrective voltage (or force) perturbation of the controller to capture the reference signal in the proximity of the FRF turning point may lead to a sudden jump before reaching the actual resonance peak [102]. In such a case, the accuracy of the measured backbone curve is always questionable.

It is also important to note that for most state-of-the-art techniques, including constant-voltage (or force) testing, identifying nonlinear modal damping is still a challenging issue. Regarding Figure 4.3, standard linear modal analysis techniques may only help to extract modal damping at the lowest voltage level, where the system's FRF looks linear. In [87], the damping of the stack-type piezoelectric actuator is assumed to be linear without solid proof.

#### **4.2.3. Identification of Nonlinear Modal Parameters by Using the RCT Method**

In the RCT method, first of all, a series of response-controlled stepped-sine tests were conducted at 11 different displacement amplitude levels of the tip point of the miniature APA ranging from 0.5  $\mu\text{m}$  to 10  $\mu\text{m}$ . During each test, the displacement amplitude of the tip point was kept constant throughout the frequency sweep in closed-loop control, and the corresponding harmonic input voltage spectrum was recorded. Then, dividing the constant harmonic displacement spectrum by the corresponding harmonic voltage spectrum, constant-response FRFs were obtained and shown in Figure 4.4.

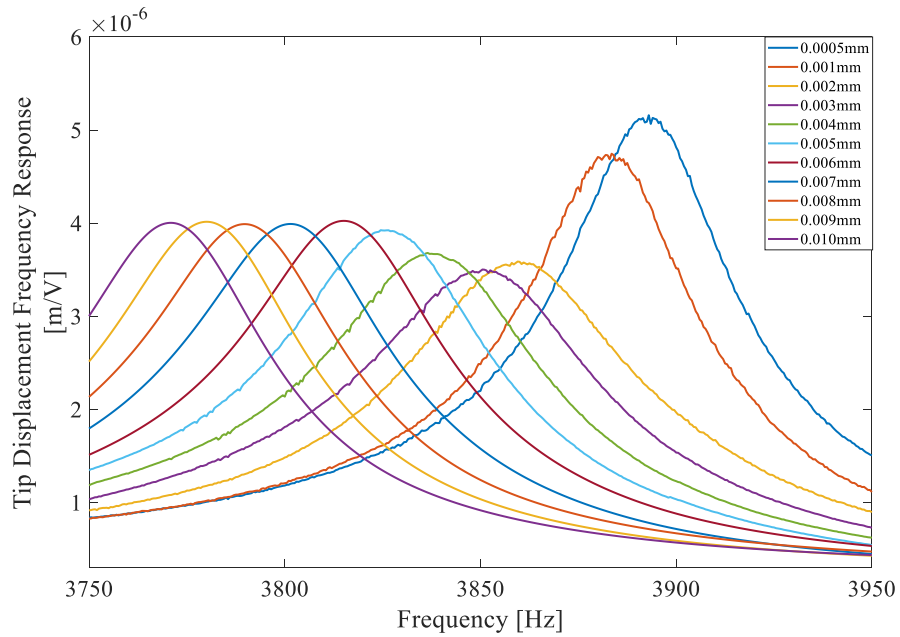


**Figure 4.4** Quasi-linear constant-response FRFs measured by RCT

The first important observation relevant to Figure 4.4 is that although the constant-response FRFs cover the voltage levels shown in Figure 4.3, they do not exhibit any jump phenomenon. This is due to the fact that the test structure settles in one stable orbit throughout the frequency sweep by virtue of the constant-response strategy of the RCT method. With this strategy, the competition of multiple stable orbits and, therefore, the jump phenomenon, typically encountered in constant-voltage (or force) testing, is avoided. The interested reader may refer to [115] for a detailed discussion of this issue.

The second important observation that can be made from Figure 4.4 is that the constant-response FRFs turn out to be quasi-linear. This means that the fundamental hypothesis of the single nonlinear mode theory [106], i.e., all the modal parameters being a function of a single parameter, the response (equivalently modal) amplitude, holds true for the miniature APA. It also means that the frequency dependence of the nonlinearity is negligible, at least in a narrow frequency band covering the resonance region of a specific mode. These results are consistent with the nonlinear constitutive model of MSPAs constructed in [87]. However, it is also important to note that in [87],

the coefficients of the constitutive model identified by using two different modes are considerably different from each other. Shivashankar et al. relate this issue to the frequency dependence of nonlinearity, which is still reasonable: Although the frequency dependence seems negligible in the neighborhood of specific modes, it may be pronounced over a wide frequency band covering multiple modes. The inconsistency of the coefficients of the constitutive model could also be related to the linear damping presumption of Shivashankar et al. [87].

Modal parameters of each quasi-linear FRF shown in Figure 4.4 can be extracted by using standard linear modal analysis methods. As an illustrative example, the quasi-linear FRF measured at 0.5 μm harmonic displacement amplitude is compared with the linear FRF synthesized from the identified modal parameters in Figure 4.5. The same procedure is repeated for the rest of the FRFs measured using the RCT method. After obtaining modal parameters for each quasi-linear FRF, curves are fitted onto the identified modal parameters by using the “fit” function of MATLAB with the piecewise cubic Hermite interpolation (*pchipinterp*) method, as shown in Figure 4.6 and Figure 4.7.

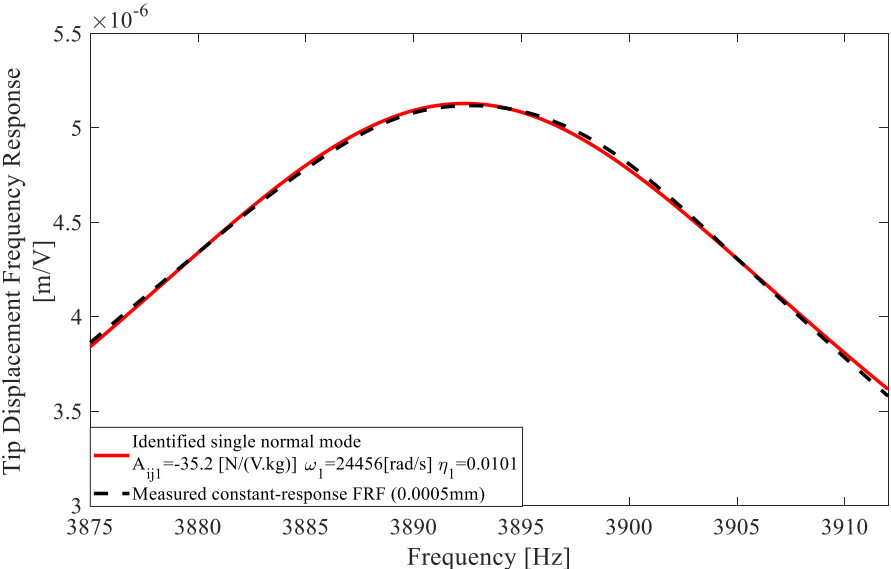


**Figure 4.5** Comparison of the constant-response FRF synthesized by using the identified modal parameters with the one measured by RCT



As indicated in Figure 4.6a, the resonance frequency decreases almost linearly with increasing response amplitude. As shown in the next stage, the backbone curve of the miniature APA is also an inclined straight line. This behavior is consistent with the nonlinear behavior of the MSPA studied in [87]. From Figure 4.6a, it is also observed that the drop of the resonance frequency is about 130 Hz, which indicates a strong softening nonlinearity. Figure 4.6b indicates that the modal damping ratio abruptly increases from 1.0% to 1.5% at relatively low response levels. However, it looks like to settle around a constant value at high response levels.

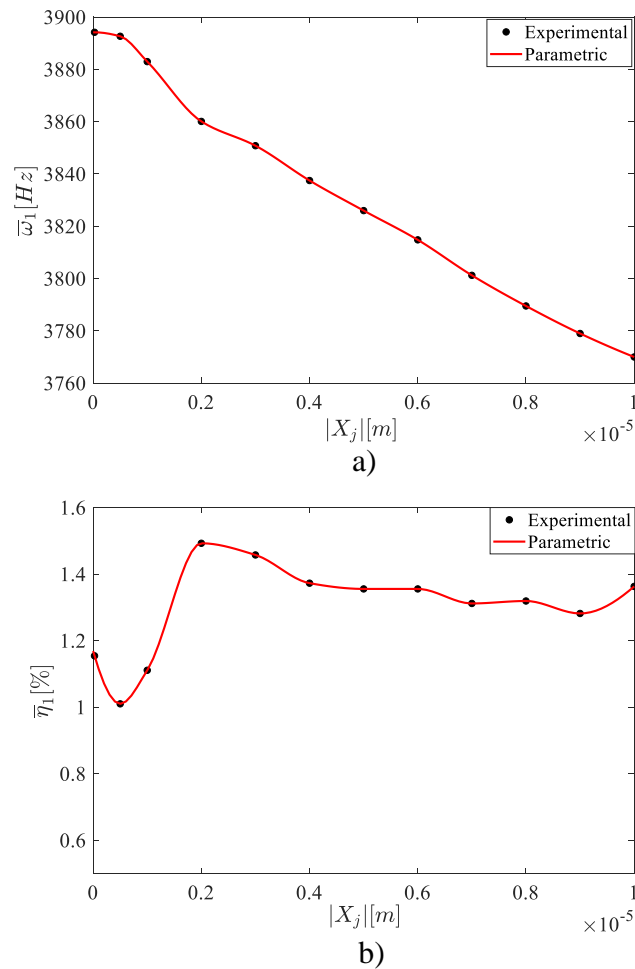


**Figure 4.6** Variation of the modal parameters corresponding to the nonlinear normal mode of the APA35XS with respect to the response level: a) Natural frequency, b) modal damping ratio

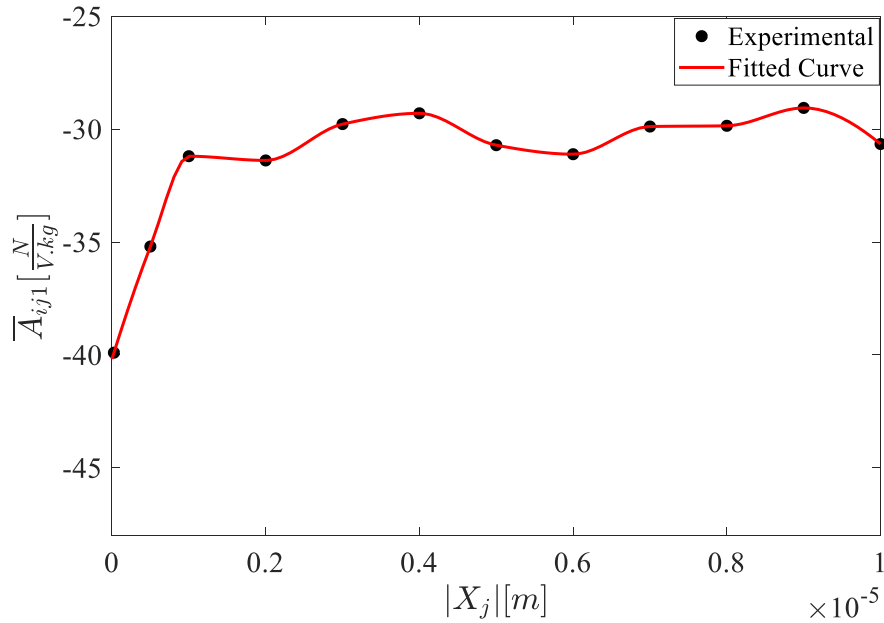


**Figure 4.7** Variation of the modal constant corresponding to the nonlinear normal mode of the APA35XS with respect to the response level

#### 4.2.4. Validation of the Nonlinear Modal Model

In order to validate the identified modal parameters, first of all, harmonic voltage spectra measured at constant-displacement amplitude levels are merged to construct the HFS by using linear interpolation, as shown in Figure 4.8. Slices of the HFS at constant voltage levels give constant-voltage frequency response curves, which are purely experimental data. The prominent feature of the HFS technique is the accurate extraction of the turning and unstable branches of these curves, which cannot be achieved by constant-voltage testing due to the jump phenomenon (Figure 4.3). A detailed discussion of the HFS approach can be found in [95, 102].

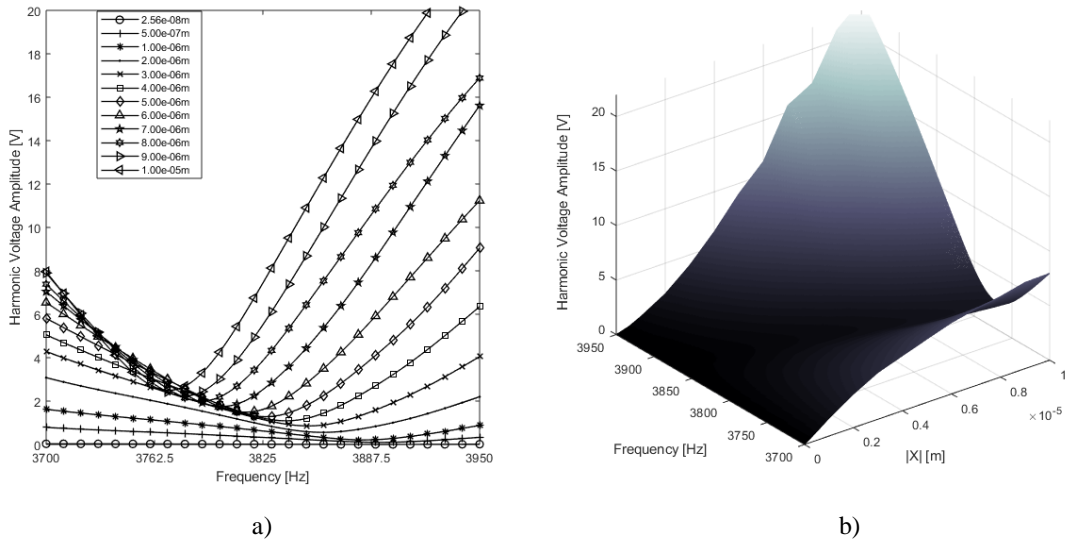


**Figure 4.8** a) Harmonic excitation voltage spectra of the APA measured during RCT, b) HFS of the free end constructed by combining harmonic excitation voltage spectra with linear interpolation

Identified nonlinear modal parameters are validated by comparing constant-voltage frequency response curves synthesized from these parameters by using the Newton-Raphson method and the arc-length continuation algorithm with the ones extracted from the HFS and are presented in Figure 4.9. It can be observed from this figure that the match between synthesized and extracted curves is almost perfect, which demonstrates the accuracy of the identified nonlinear modal parameters.

Finally, the NNM backbone curve, constructed using constant-voltage frequency response curves synthesized from the identified nonlinear modal parameters, is compared with the one directly extracted from the HFS, which is purely measured (nonparametric) data, as shown in Figure 4.10. The excellent match between both backbone curves once again validates the accuracy of the identified nonlinear modal model. It is also worth mentioning that the backbone curve is an inclined straight line consistent with the nonlinear behavior of the MSPA studied in [87], as discussed previously. It can be concluded that the nonlinearity of the miniature APA studied herein is most governed by the nonlinearity of the embedded piezo-actuator.

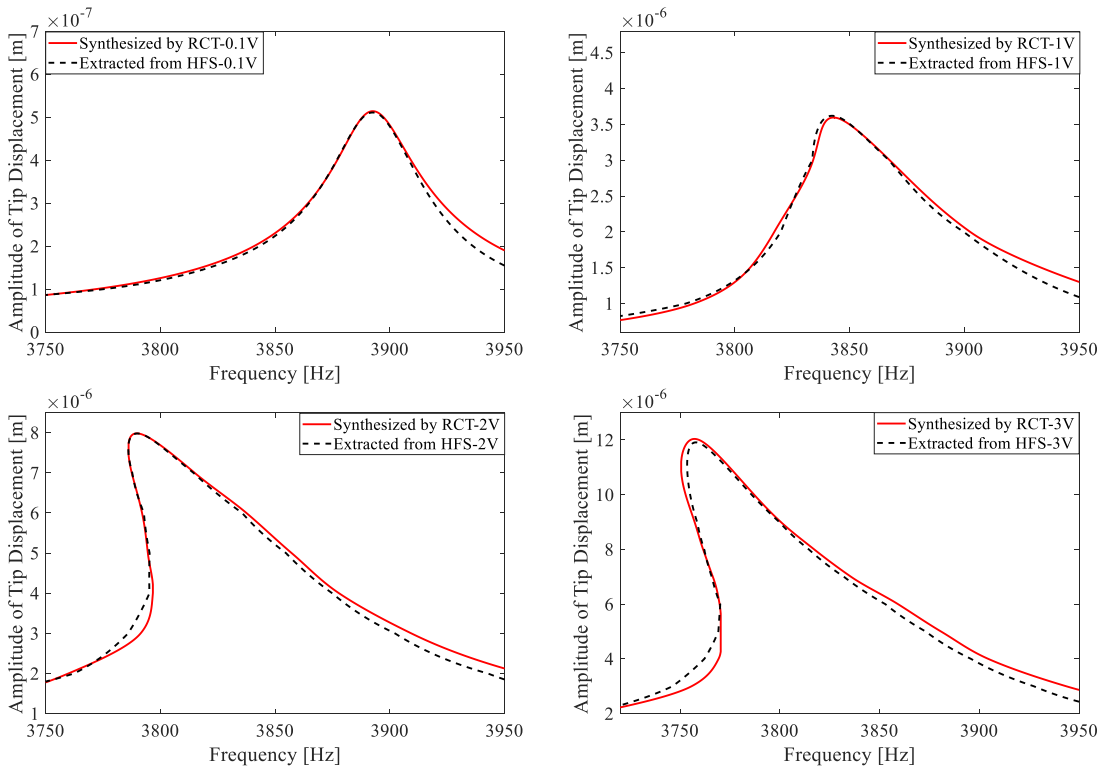


**Figure 4.9** Comparison of constant-voltage frequency response curves extracted from HFS with the ones synthesized by using nonlinear modal parameters

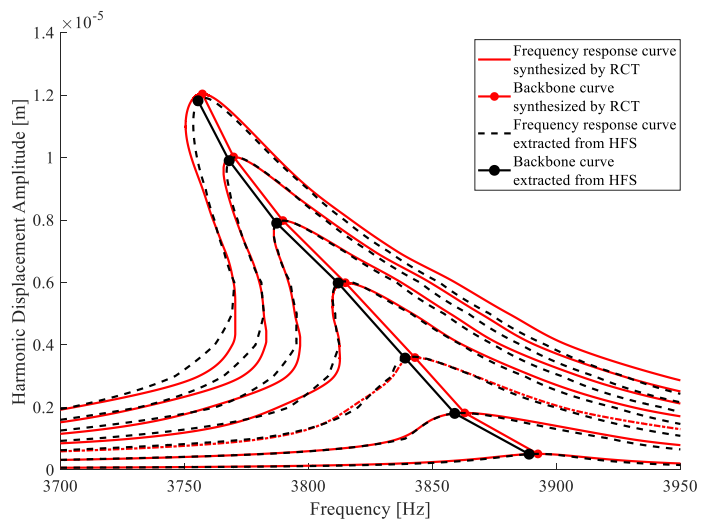


**Figure 4.10** Comparison of the backbone curve extracted from HFS with the one obtained by using nonlinear modal parameters

In the nonlinear mode of interest, the RCT quantifies about a 130 Hz change of natural frequency and a modal damping ratio ranging from 1% to 1.5% in the amplitude range of interest, which indicates considerably high stiffness and damping nonlinearities. Finally, in Figure 4.9, nonlinear modal parameters are validated by comparing the constant-force frequency response curves synthesized from these parameters with those extracted directly from the experiment using the harmonic force surface (HFS) approach proposed in [95].

The main purpose of this thesis study is to develop a piezoelectric-based BC transducer to efficiently transform the applied electrical energy into mechanical vibrations. However, the nonlinear nature of the APA deteriorates the output displacement of the BC transducer. The actual performance of the BC transducer needs to be known for design optimization and clinical studies. In this chapter, the RCT method is proposed to obtain a relation between the input voltage and output displacement of the APA in the frequency domain. This section is concluded by emphasizing another important contribution of this thesis study. The nonlinear modal model of the APA is obtained by utilizing the RCT method. As previously mentioned, the literature about the nonlinear dynamics of MSPAs and APAs is very limited, and the quantification and validation of the nonlinear modal damping of miniature MSPAs are achieved for the first time in this study.



## CHAPTER 5

### NONLINEAR IDENTIFICATION AND EXPERIMENTAL MODAL ANALYSIS OF THE BONE CONDUCTION ACTUATOR BY USING DESCRIBING SURFACE METHOD

In the early stages of this thesis study, a BCHA design consisting of an APA and a mass attached to its tip was proposed. In Chapter 2, a linear analytical model for an APA has been presented, and it has been shown that the outputs of the BCHA model are compatible with the measurements taken from APA35XS tested under low-level harmonic voltage excitations. Using the validated linear APA model, the design parameters of the APA and the amount of mass to be attached to the APA tip have been optimized to give the best performance in the BCHA application. The optimized APA prototypes are manufactured after the optimization scheme. In the previous chapter, a reliable nonlinear modal model of APA35XS is constructed by using the RCT method [95]. The nonlinear modal model of the optimized APA prototype can be obtained using the method described in Chapter 4. However, it is impossible to estimate the nonlinear dynamics of the optimized APA by using the nonlinear modal model of the APA tested under fixed-free boundary conditions when it is physically coupled to a dynamic structure. The state-of-art nonlinear substructuring and decoupling techniques acquire the knowledge of the interface DOFs [63, 123, 124]. This phenomenon requires a method that identifies the nonlinearity in the physical-driven model of the APA.

The nonlinearity matrix approach and describing function representation are the practical ways of defining an unknown nonlinearity in the physical-driven model in the frequency domain. Özer and Özgüven first used the nonlinear matrix approach to identify nonlinear systems [125, 126]. In [126], the proposed method can localize and identify a single localized nonlinearity between any two coordinates, provided that the

response of the coordinates under interest is known. Later, the method proposed in [126] was extended by Aykan and Özgüven [127] to eliminate the need for complete FRF data of the nonlinear system. The classical describing function methods (DFMs) assume that the behavior of the identified nonlinearity is a function of harmonic response amplitude. In contrast, Karaağaçlı and Özgüven proposed a nonparametric identification technique named as Describing Surface Method (DSM), which is applicable for nonlinear systems with a single localized ground nonlinearity which is a function of displacement and frequency [103]. DSM is introduced as a method having a particular requirement of coinciding excitation and response control points.

In this section, the describing function of the localized nonlinearity in the prototype of the optimized BCHA is extracted by using DFM and DSM based on the frequency response data measured with the RCT method. It is shown that DSM can be applied to systems where the excitation and response points are not coincident. The identified describing functions are validated by introducing the identified nonlinear element into the linear physical-driven model presented in Chapter 2 and obtaining tip mass FRFs for different harmonic input voltage amplitudes. The theoretical background of the DFM and DSM is revisited before introducing a new formulation for the describing function of the nonlinearity of the BCHA.

### 5.1. The Theory of the Describing Function and the Describing Surface Methods

The equations of motion for a nonlinear  $n$  degree of freedoms system can be written as

$$[M]\{\ddot{x}\} + [C]\{\dot{x}\} + [K]\{x\} + \{f_{NL}(x, \dot{x})\} = \{f\}, \quad (4.3)$$

where  $\{x\}$  and  $\{f\}$  displacement and external force vectors of the nonlinear system, respectively. Here,  $[M]$ ,  $[C]$ , and  $[K]$  are the linear mass, viscous damping, and stiffness matrices, respectively.  $\{f_{NL}\}$  represents the internal nonlinear restoring force vector.

The external harmonic forcing vector with excitation frequency  $\omega$  and amplitude  $\{F\}$



can be written in a complex form as;

$$\{f\} = \{F\} e^{i\omega t}. \quad (4.4)$$

The displacements and, of course, internal nonlinear restoring forces are assumed to be periodic under external harmonic forcing and can be expressed in the Fourier series. Assuming the structure oscillates in a single harmonic pattern, the internal nonlinear restoring force vector can be written as;

$$\{f_{NL}\} = \{N\} e^{i\omega t}, \quad (4.5)$$

where  $\{N\}$  is the amplitude of the internal nonlinear restoring force vector and can be expressed as;

$$\{N\} = [\Delta] \{X\}. \quad (4.6)$$

Here,  $[\Delta]$  is the response-dependent nonlinearity matrix. Elements of the nonlinearity matrix can be expressed by using describing function representation proposed by Tanrikulu et al. [118]

$$\Delta_{rr} = v_{rr} + \sum_{\substack{s=1 \\ s \neq r}}^n v_{rs} \quad (4.7)$$

$$\Delta_{rs} = -v_{rs} \quad (4.8)$$

The harmonic describing function  $v_{rs}$  can be obtained from Eq.(4.9)

$$v_{rs} = \frac{i}{\pi Y_{rs}} \int_0^{2\pi} N_{rs} e^{i\psi} d\psi, \quad \psi = \omega t, \quad (4.9)$$

where  $N_{rs}$  is the amplitude of the nonlinear internal force.  $Y_{rs}$  is the relative displacement between internal coordinates  $r$  and  $s$  for  $r \neq s$ , and the displacement of  $r^{th}$  coordinate for  $r = s$ .

Harmonic response amplitude can also be obtained from Eq.(4.3) by inserting the nonlinearity matrix and harmonic external force vector as follow;

$$\left( [H^L]^{-1} + [\Delta] \right) \{X\} = \{F\}. \quad (4.10)$$

Here,  $[H^L]$  is the receptance matrix of the underlying linear system. At this point, the nonlinear receptance matrix  $[H^{NL}]$ , which is dependent on the response level, is obtained from Eq.(8) as;

$$[H^{NL}]^{-1} = [H^L]^{-1} + [\Delta]. \quad (4.11)$$

Assuming that the nonlinearity in the APA can be modeled as an equivalent nonlinear element between ground and a single coordinate, the nonlinearity matrix can be simplified for a single grounded nonlinearity as

$$[\Delta] = \begin{pmatrix} 0 & \dots & 0 \\ \vdots & \Delta_{pp} & \vdots \\ 0 & \dots & 0 \end{pmatrix}. \quad (4.12)$$

In Eq.(4.12), the nonlinearity matrix  $[\Delta]$  has one non-zero element  $\Delta_{pp}$  which can be expressed as;

$$\Delta_{pp} = \nu_{pp} \quad (4.13)$$

Considering the nonlinear system is driven by an external harmonic force with an amplitude of  $F_j$  at an arbitrary coordinate  $j$ , the equation of motion of the nonlinear system becomes

$$\begin{Bmatrix} X_p \\ X_j \end{Bmatrix} = \begin{pmatrix} H_{pp}^L & H_{pj}^L \\ H_{jp}^L & H_{jj}^L \end{pmatrix} \begin{Bmatrix} -\nu_{pp} X_p \\ F_j \end{Bmatrix}, \quad (4.14)$$

where  $X_p$  and  $X_j$  are harmonic displacement amplitudes of the nonlinear coordinate and driven coordinate, respectively. The amplitude of the harmonic motion at the coordinate  $p$  can be derived from Eq.(4.14)

$$X_p = -H_{pp}^L \nu_{pp} X_p + H_{pj}^L F_j, \quad (4.15)$$

and Eq.(4.15) can be arranged as follows;

$$\frac{1}{H_{pj}^{NL}} - \frac{1}{H_{pj}^L} = \frac{H_{pp}^L}{H_{pj}^L} \nu_{pp} = \bar{\nu}_{pp}(|X_p|, \omega) \quad (4.16)$$

At this point, a new term  $\bar{\nu}_{pp}$ , which is called modified describing function of the localized nonlinearity at coordinate  $p$ , is defined to simplify subsequent expressions. The nonlinear receptance function  $H_{pj}^{NL}$  is to be measured under constant displacement amplitude level  $|X_p^k|$  using the RCT method. Eq.(4.17) can be written for each amplitude level.

$$\bar{\nu}_{pp}(|X_p^k|, \omega) = \frac{1}{H_{pj|X_p^k|}^{NL}} - \frac{1}{H_{pj}^L}. \quad (4.17)$$

Partial derivative of  $\bar{\nu}_{pp}(|X_p|, \omega)$  with respect to  $|X_p|$  can be obtained for each displacement amplitude level  $|X_p|$  by using finite difference approximation

$$\begin{aligned} \frac{\partial \bar{\nu}_{pp}}{\partial |X_p|} &= \frac{\bar{\nu}_{pp}(|X_p^{k+1}|, \omega) - \bar{\nu}_{pp}(|X_p^k|, \omega)}{|X_p^{k+1}| - |X_p^k|} \\ &= \left( \frac{1}{H_{pj|X_p^{k+1}|}^{NL}} - \frac{1}{H_{pj|X_p^k|}^{NL}} \right) / (|X_p^{k+1}| - |X_p^k|) \end{aligned} \quad (4.18)$$

Eq.(4.18) is solved numerically for each frequency point, and describing functions are determined for each displacement level. Describing surface is constructed by combining describing function curves. After obtaining describing functions, the receptance of the underlying linear system can be evaluated as follows;

$$H_{pj}^L = \left( \frac{1}{H_{pj|X_p^k|}^{NL}} - \bar{\nu}_{pp}(|X_p^k|, \omega) \right)^{-1}. \quad (4.19)$$

The relation between modified and unmodified describing functions is given as follows;

$$H_{pp}^L \nu_{pp}(|X_p^k|, \omega) = H_{pj}^L \bar{\nu}_{pp}(|X_p^k|, \omega). \quad (4.20)$$

Eventually, the response of the coordinate  $p$  under any external harmonic force can be determined by employing Newton's Method with the arc-length continuation algorithm to Eq.(4.21);

$$X_p = H_{pj}^L \left( F_j - \bar{v}_{pp} \left( |X_p|^k, \omega \right) X_p \right). \quad (4.21)$$

The expression given in Eq.(4.21) serves as a transfer function between the external harmonic force amplitude  $F_j$  and the amplitude of the tip displacement  $X_p$ , similar to the nonlinear model obtained by HFS in [95, 102]. However, the expression in Eq.(4.21) becomes invalid when the underlying linear system is modified. Eq.(4.22) gives the modified linear system equation of motion coupled with the describing function  $\Delta_{pp}$  of the identified nonlinearity;

$$\left( -\omega^2 [M + \Delta M] + i\omega [C + \Delta C] + [K + \Delta K] + \begin{pmatrix} 0 & \dots & 0 \\ \vdots & \Delta_{pp} & \vdots \\ 0 & \dots & 0 \end{pmatrix} \right) \mathbf{X} = \mathbf{F}, \quad (4.22)$$

where  $\Delta M$ ,  $\Delta C$ , and  $\Delta K$  are mass, damping, and stiffness modification matrices of the modified linear system, respectively. The identified describing function of the equivalent nonlinear element is expressed as follows;

$$\Delta_{pp} \left( |X_p|, \omega \right) = \bar{v}_{pp} \left( |X_p|, \omega \right) \frac{H_{pj}^L}{H_{pp}^L}. \quad (4.23)$$

## 5.2. Experimental Studies on the Proposed BCHA

The BCHA prototype introduced in Chapter 3 is tested for describing function identification. The test structure consists of a custom-designed APA and a tuning mass of 10 g (Figure 5.1a). The experimental study focuses on determining the transverse vibration modes of the tip displacement of the APA that exhibits strong softening nonlinearity. The APA was fixed to the ground from its base (Figure 5.1b) to study the mode of interest.

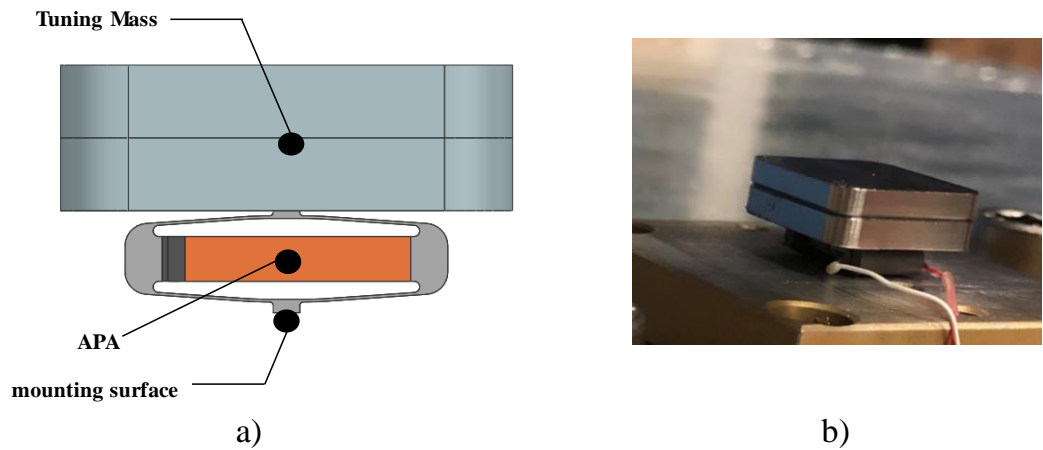


**Figure 5.1** a) Schematic view of the proposed BCHA design, b) photograph of the BCHA prototype under test

Similar to the study in Chapter 4, the harmonic excitation force was generated by driving the embedded MSPA in the APA with harmonic voltage input. The vertical displacement of the tip mass was measured from the top surface of the tip mass by a non-contact laser displacement sensor (Micro-Epsilon OptoNCDT 2300), which was installed on top of the actuator, as shown in Figure 5.2. The LMS SCADAS system and LMS Test Lab software, which are described in the previous chapter, fulfill the data acquisition and closed-loop control tasks. The schematic view of the experimental test setup is also illustrated in Figure 5.2.

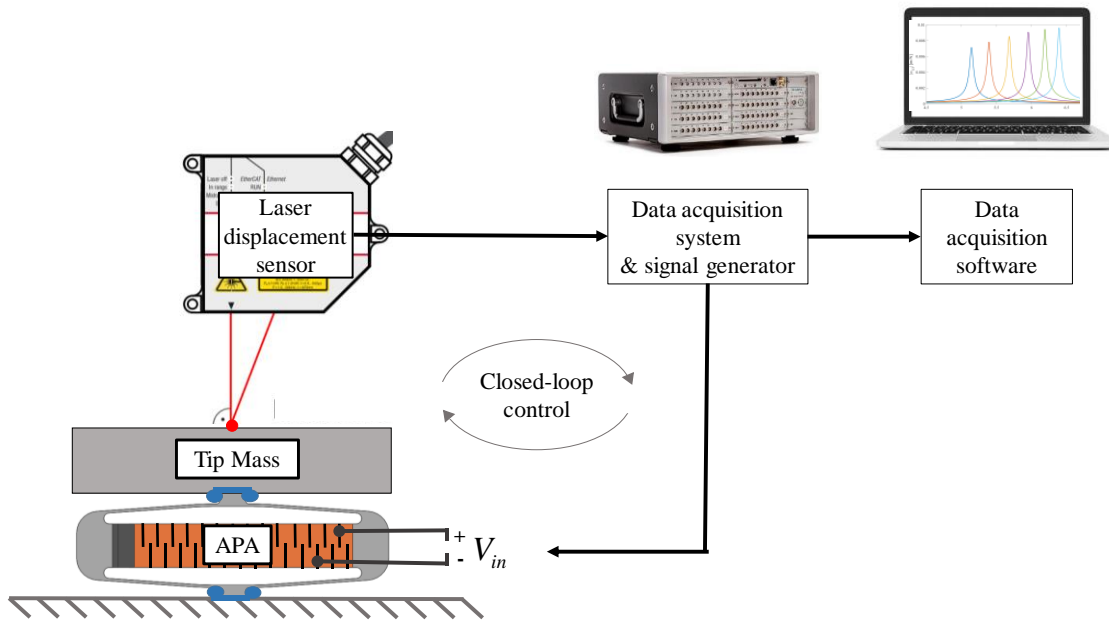


**Figure 5.2** Schematic view of the experimental test setup

The frequency step is set to 0.125 Hz for all the step-sine tests presented in this section. The frequency range of interest enclosing the fundamental mode of the BCHA is determined by preliminary linear analyses and periodic chirp tests shown in Figure 5.3. The fundamental resonance frequency of the proposed BCHA is determined as 430 Hz from the linear analytical model and the fast frequency sweep tests. Although the frequency response curves obtained from the analytical model and periodic-chirp tests match almost perfectly, there is a slight difference in the results around the fundamental resonance frequency. The difference is thought to be due to the damping coefficient identified previously by the stand-alone APA tests in the analytic model. Studies in the literature show that the a priori models of stand-alone linear substructures may lose their validity when interacting with any other structure, and the model of the linear substructure is to be modified by adding linear elements such as mass, spring, and damper [124, 128–130]. Hence, one can say that the lumped mass added to the APA changes the underlying linear properties of the substructure APA itself.

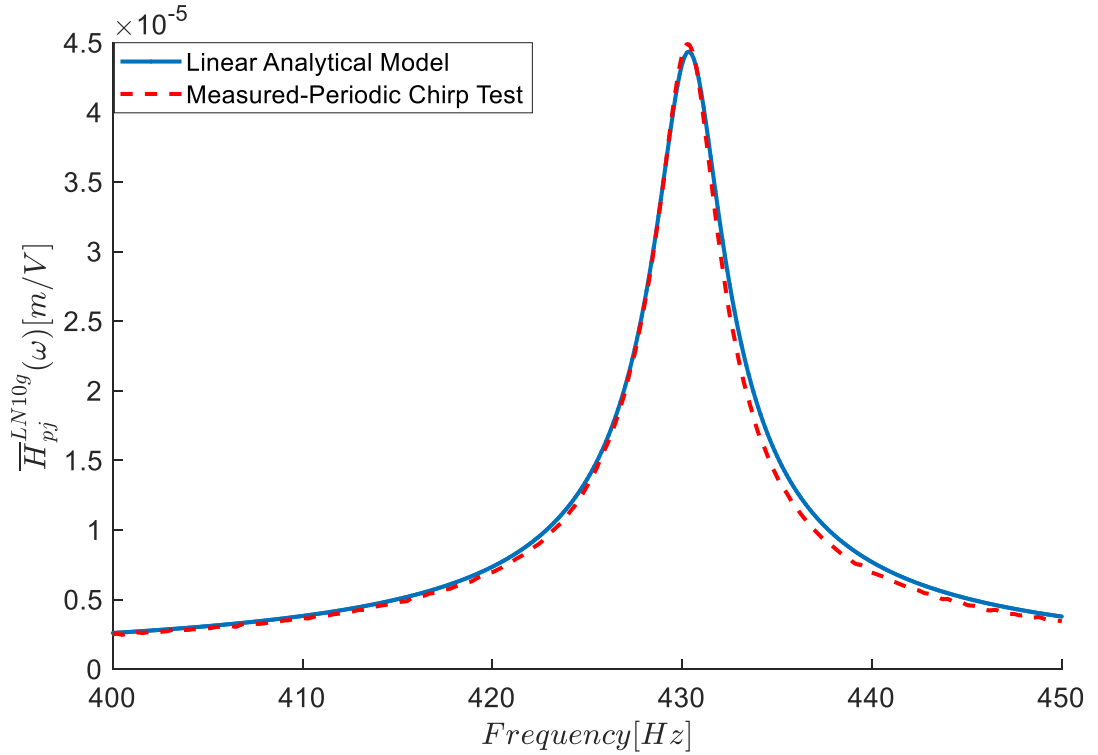


**Figure 5.3** The linear FRFs of the tip mass on the APA

### 5.2.1. Determination of Piezoelectric Actuation Force

Chapter 4 presents a nonlinear modal model that relates the output displacement and the input voltage. The constitutive relationship between the input voltage and the resultant piezoelectric actuation force needs to be obtained experimentally to acquire an accurate physical-driven BCHA model. Preliminary tests are performed on the stand-alone APA prototype by using the constant voltage stepped-sine test sequence explained in Chapter 3. Step-sine tests are repeated at different harmonic voltage levels from 0.1 V to 8 V in the frequency range from 550 Hz to 800 Hz. The harmonic voltage surface is constructed by combining constant-voltage frequency-response curves with linear interpolation, as shown in Figure 5.4. Under 8 V harmonic voltage amplitude, the displacement amplitude is not exceeding the 3  $\mu\text{m}$  level of vibrations at which nonlinear internal forces are considered negligible for the APA. The planar form of the harmonic voltage surface shows that the relation between the harmonic input voltage

and the resulting piezoelectric actuation force is linear up to 8 V. Since the BCHA is subjected to external voltage up to 5 V, the relation between the output piezoelectric actuation force and the input voltage turns out to be linear.

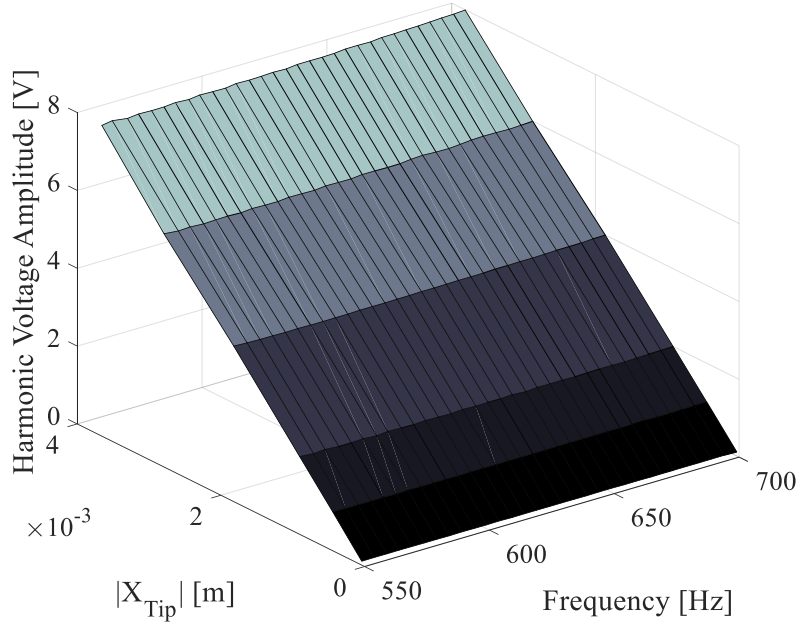


**Figure 5.4** HFS of the free end of the stand-alone APA is constructed by combining harmonic excitation voltage spectra with linear interpolation

In the first step, the point FRF of the APA at the point  $p$  is obtained by using the measured transfer FRFs of the APA and the BCHA. Under low voltage harmonic input, the equation of motion of the APA without tip mass can be formulated as;

$$\begin{Bmatrix} X_p \\ X_j \end{Bmatrix}_0 = \begin{pmatrix} H_{pp}^L & H_{pj}^L \\ H_{jp}^L & H_{jj}^L \end{pmatrix} \begin{Bmatrix} 0 \\ F_j(V_{in}) \end{Bmatrix}, \quad (4.24)$$

where  $X_{p,0}$  and  $X_{j,0}$  are the harmonic displacement amplitudes of the tip of the APA and tip of the MSPA, respectively.  $\mathbf{H}^L$  and  $F_j$  is the receptance matrix of the APA, and the piezoelectric actuation force, respectively.  $F_j$  is defined as a function of  $V_{in}$  which



is the harmonic voltage input. The response of the coordinate  $p$  can be determined from Eq.(4.24) as

$$X_{p,0} = H_{pj}^L F_j (V_{in}). \quad (4.25)$$

Eq.(4.24) can be re-written for the APA with attached tip mass  $M_{Tip}$  as follows

$$\begin{Bmatrix} X_p \\ X_j \end{Bmatrix}_{M_{Tip}} = \begin{pmatrix} H_{pp}^L & H_{pj}^L \\ H_{jp}^L & H_{jj}^L \end{pmatrix} \begin{Bmatrix} \omega^2 M_{Tip} X_p \\ F_j (V_{in}) \end{Bmatrix}, \quad (4.26)$$

where  $X_{p,M_{Tip}}$  and  $X_{j,M_{Tip}}$  are the harmonic displacement amplitudes of the tip of the APA with the attached tip mass, and the tip of the MSPA, respectively. The response of the coordinate  $p$  for the modified APA can be expressed as;

$$X_{p,M_{Tip}} = \omega^2 H_{pp}^L M_{Tip} X_{p,M_{Tip}} + H_{pj}^L F_j (V_{in}). \quad (4.27)$$

The point FRF of the coordinate  $p$  on the linear substructure of the APA can be expressed in terms of measured frequency responses of the coordinate  $p$

$$H_{pp}^L(\omega) = \frac{X_{p,M_{Tip}} / V_{in} - X_{p,0} / V_{in}}{\omega^2 M_{Tip} X_{p,M_{Tip}} / V_{in}} = \frac{\bar{H}_{pj,M_{Tip}}^L(\omega) - \bar{H}_{pj,0}^L(\omega)}{\omega^2 M_{Tip} \bar{H}_{pj,M_{Tip}}^L(\omega)}. \quad (4.28)$$

In Eq.(4.28),  $\bar{H}_{pj}$  is the displacement frequency responses of the coordinate  $p$  normalized with applied harmonic voltage input. In Figure 5.5, experimentally obtained FRFs are compared with the FRF curve determined from the analytical model. FRF curves prove that the analytical model agrees with the experimentally obtained point FRF of the APA's tip displacement under low harmonic voltage excitations.

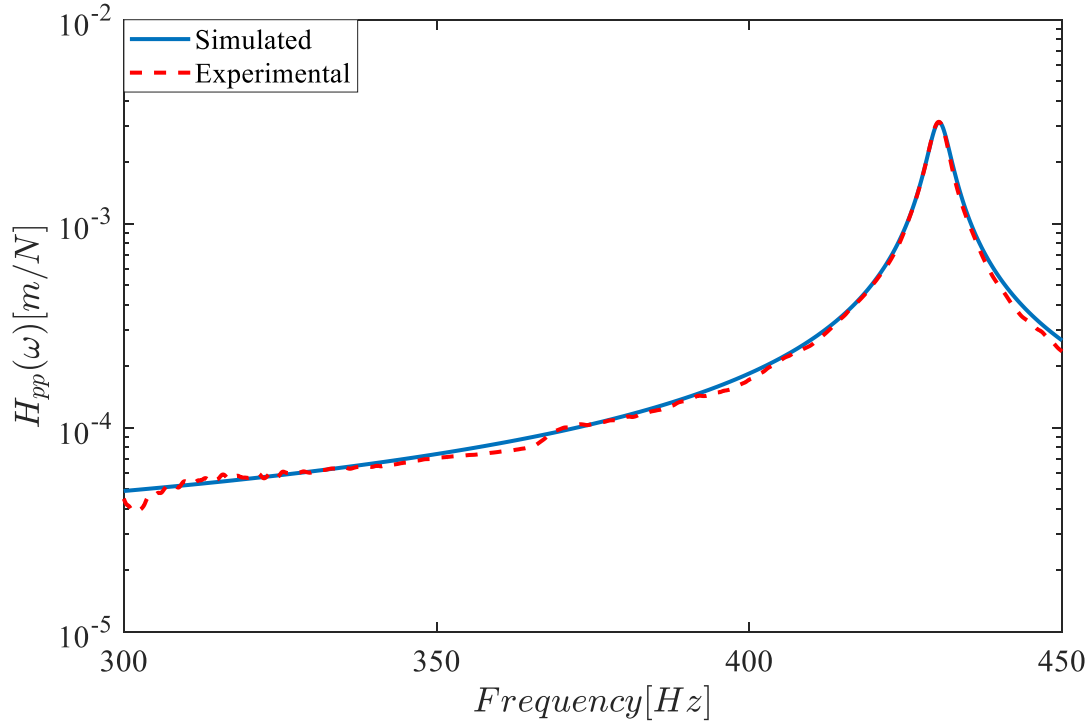


**Figure 5.5** The point FRFs of the coordinate  $p$  for the underlying linear APA without tip mass

The electromechanical relation between the applied voltage and the output piezoelectric force can be obtained by comparing the calculated and experimentally obtained voltage frequency responses under low levels of oscillations. The frequency response curves are obtained for the APA with and without tip mass in Figure 5.6a and Figure 5.6b, respectively. The mean value of the electromechanical coefficient of the MSPA,  $\bar{d}_0$  is calculated as 1.826 and 1.812 for stand-alone and tip mass attached cases, respectively.

$$\bar{d}_0 = \frac{F_j}{V_{in}} = \frac{\bar{H}_{pj}^L}{H_{pj}^L}, \quad (4.29)$$

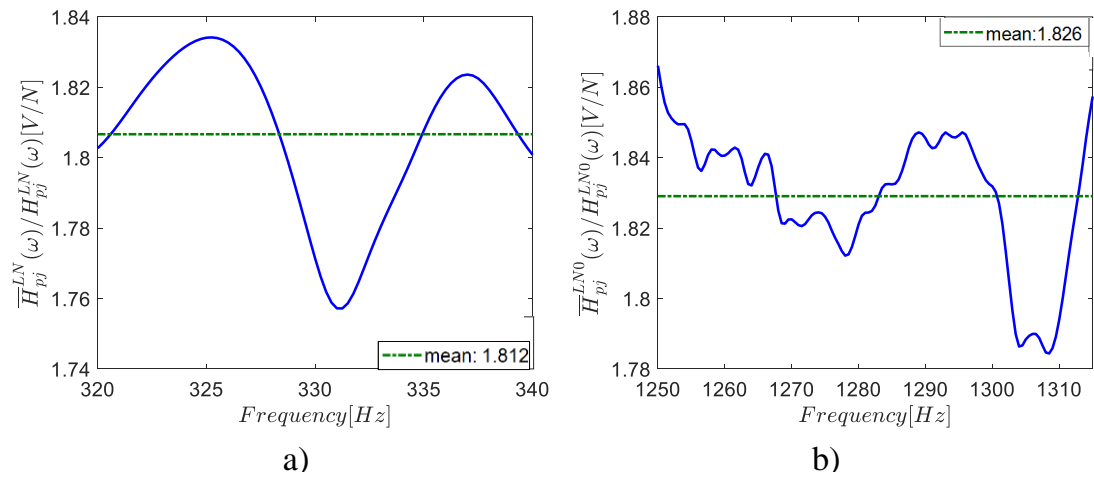


**Figure 5.6** Relation between analytical force-frequency response and experimentally obtained voltage frequency response under low level of oscillations a) with tip mass b) without tip mass

### 5.2.2. Preliminary Constant-Voltage Stepped Sine Tests

Constant-voltage tests were performed on the BCHA prototype prior to the RCT application to characterize the nonlinear behavior of the structure. The constant amplitude of the harmonic input voltage is supplied by the LMS SCADAS data acquisition system thanks to its closed-loop controller. The displacement frequency responses of the tip mass are measured during tests. FRFs measured at different constant voltage levels are shown in Figure 5.7. When the voltage level is increased from 1 V to 3 V, it has been observed that the resonance frequency has dropped by approximately 12 Hz, which indicates a nonlinear softening behavior.

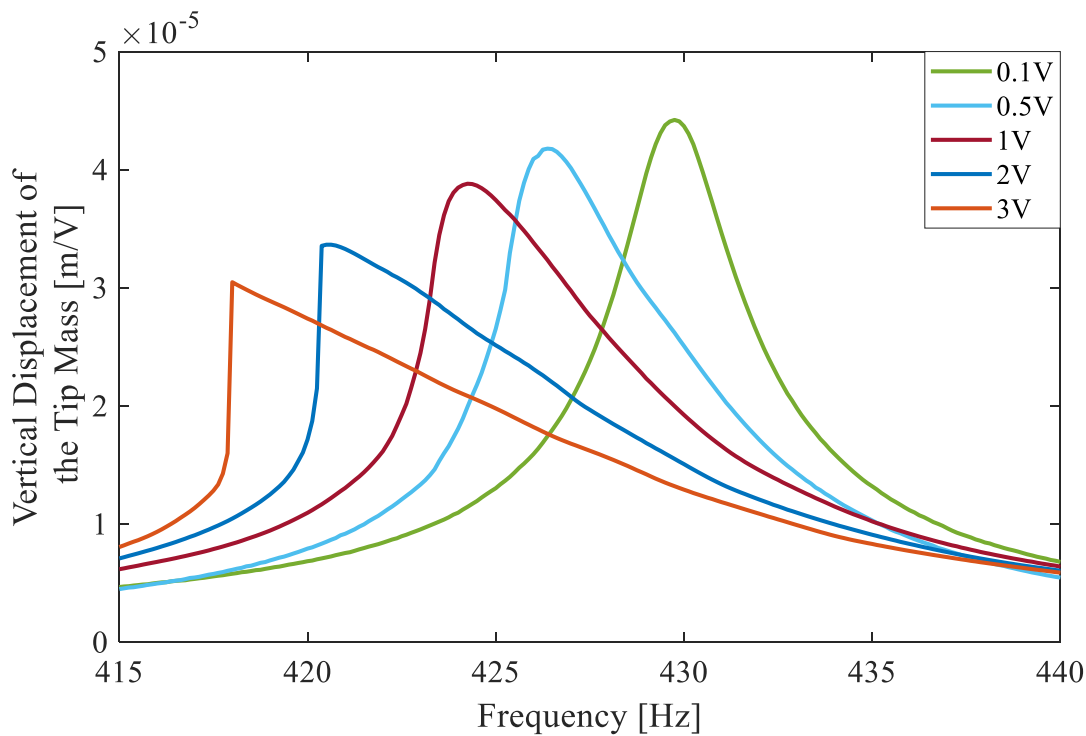


**Figure 5.7** FRFs measured by constant-voltage stepped-sine testing

### 5.2.3. Describing Surface Identification by using RCT Method

First, a series of response-controlled stepped-sine tests were conducted at five different displacement amplitude levels of the tip point of the miniature APA ranging from 0.5  $\mu\text{m}$  to 100  $\mu\text{m}$ . The displacement amplitude of the tip mass was kept constant throughout the stepped-sine test in closed-loop control, and the corresponding harmonic input voltage spectrum was recorded simultaneously. Eventually, the constant-response FRFs were obtained by dividing the constant harmonic displacements into the corresponding harmonic voltages in the frequency domain, as shown in Figure 5.8.

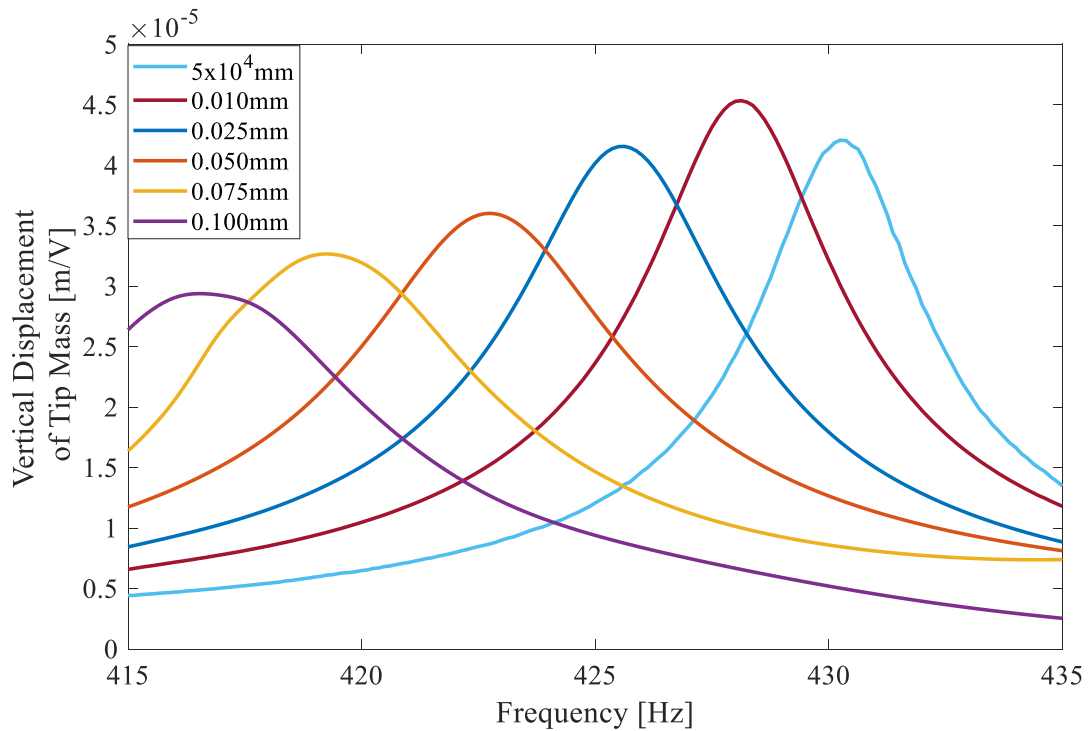


**Figure 5.8** Quasi-linear FRFs of the tip mass measured by RCT at various constant displacement amplitudes

The real and imaginary parts of the describing function's partial derivative, which are shown in Figure 5.9, are obtained as functions of tip displacement amplitude and the excitation frequency by inserting quasi-linear FRFs given in Figure 5.8 into Eq.(4.18). The partial derivative value between two consecutive displacement amplitude levels is taken to be constant. Then, Eq.(4.18) is solved numerically, which yields the describing surface of nonlinearity, as shown in Figure 5.10. The real and imaginary parts of the describing function values, shown in Figure 5.11, are calculated from describing the surface using the DFM.

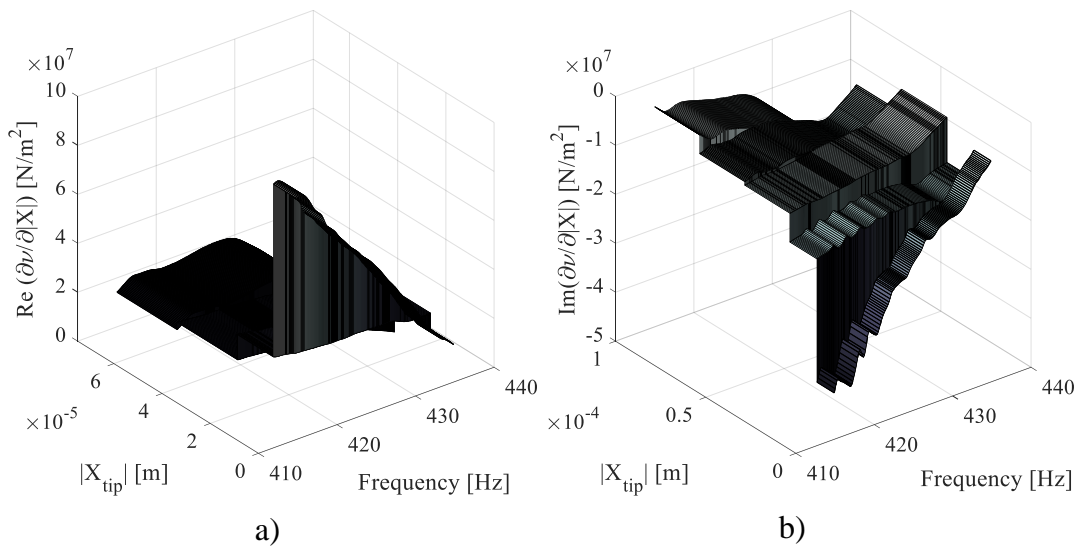


**Figure 5.9** Real (a) and imaginary (b) parts of the partial derivative of the describing surface of the nonlinearity

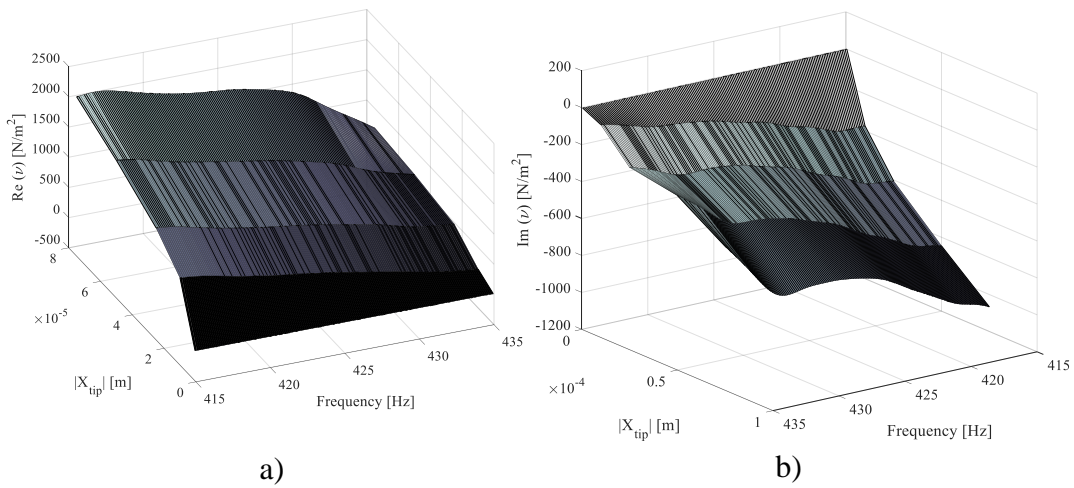


**Figure 5.10** Real (a) and imaginary (b) parts of the describing surface of nonlinearity

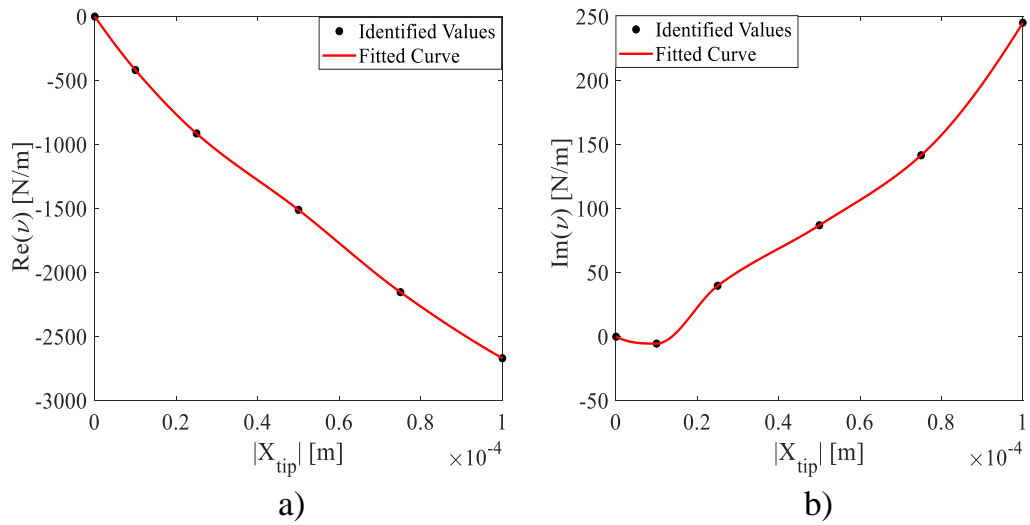
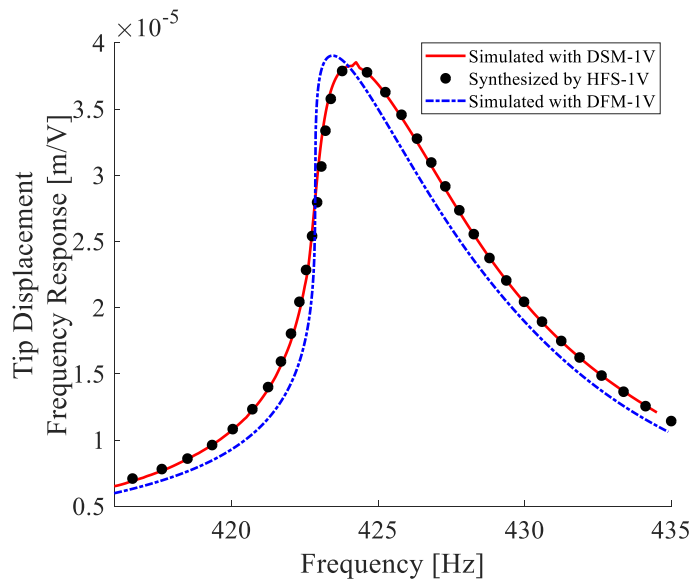


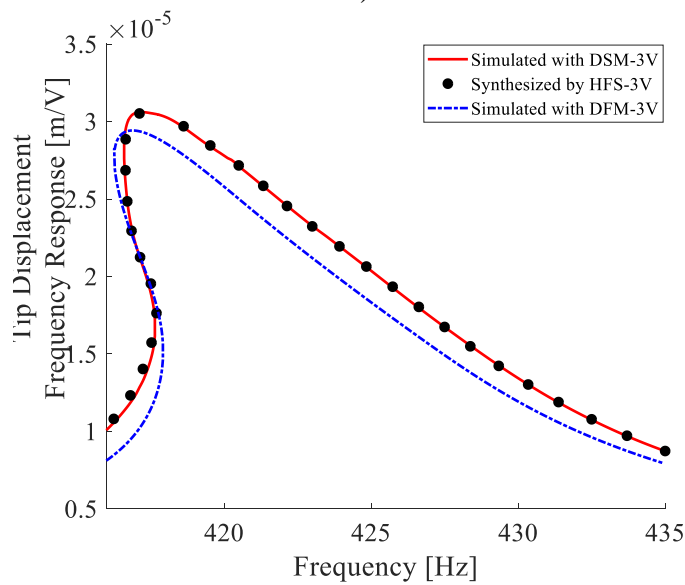
**Figure 5.11** Real (a) and imaginary (b) parts of the describing function of nonlinearity

#### 5.2.4. Validation of Identified Describing Function

The transfer FRFs of the APA with 10 g attached tip mass are calculated at the tip point by employing the DSM and the DFM for different voltage levels (1 V and 3 V), and the results are then compared with the experimentally measured ones. The results are shown in Figure 5.12, and it is observed that the simulation results of the DSM match perfectly with the experimental data. Although it seems that the results of DFM simulations are not as good as DSM, it should be noted that DFM simulations are based on the linear analytical model coupled with identified describing function, while the DSM simulations are obtained from the same experimental data used to compute the HFS. Finally, the tip point transfer FRFs of the APA with 16 g attached tip mass are simulated with the identified describing function for 1 V and 3 V harmonic voltage levels, and then the results are compared with the experimentally measured ones obtained from the voltage-controlled step sine tests (Figure 5.13). It is observed from Figure 5.13 that the results of the DFM simulations match satisfactorily with the experimental data. DSM simulation results are not shown in Figure 5.13 since DSM is not defined in the frequency range encompassing the fundamental resonance frequencies of the APA with 16 g attached tip mass.



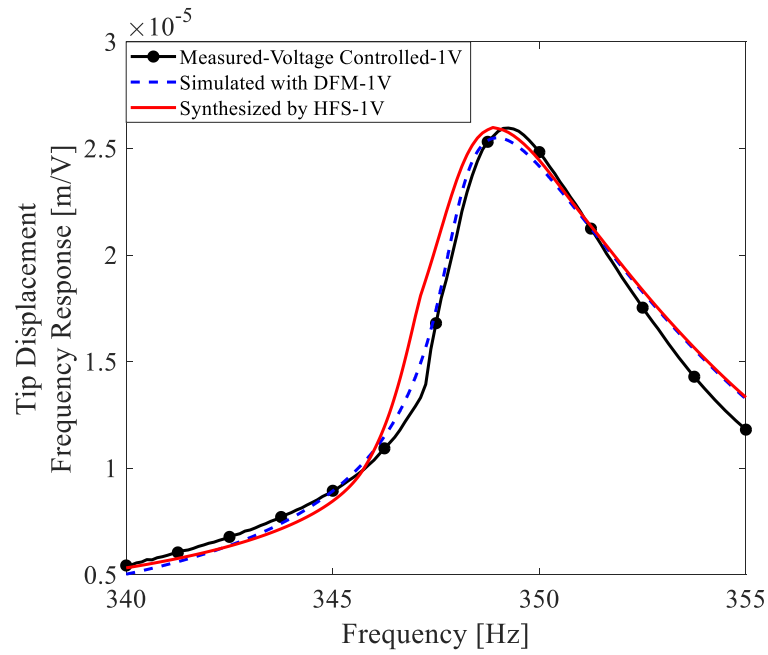
a)



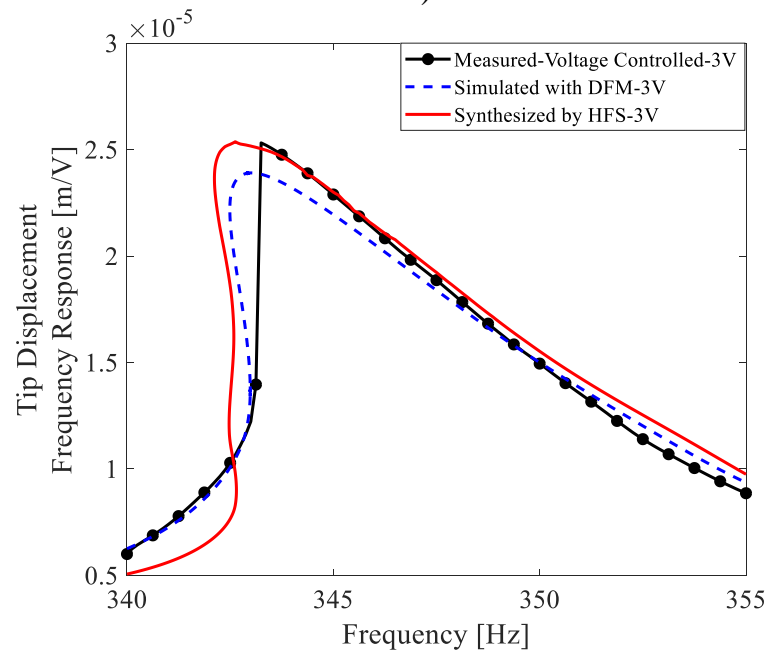
b)

**Figure 5.12** Comparison of tip point frequency responses of the APA with 10 g tip mass frequency responses obtained by the HFS, DSM, and DFM at 1 V (a) and 3 V (b) constant voltage levels





a)



b)

**Figure 5.13** Comparison of tip point frequency responses of the APA with 16 g tip mass frequency responses obtained by the HFS, DFM, and voltage-controlled stepped sine tests at 1 V (a) and 3 V (b) constant voltage levels

In this chapter, accurate identification of nonlinearity and the construction of a reliable physical-driven model of a BC transducer are achieved by using the parametric describing function method (DFM) [126] and recently developed nonparametric describing surface method (DSM) [103]. It can be deduced from Figure 5.11a that the real part of the describing function decreases with an increase in the displacement amplitude. On the other hand, the imaginary part of the describing function increases with an increase in the displacement amplitude (Figure 5.11b). One of the most conspicuous observations of this chapter is that the imaginary part of the describing surface changes slightly with frequency at higher displacement levels, as illustrated in Figure 5.10b. At the end of this chapter, a physical-driven nonlinear model for the BCHA is obtained for substructure coupling operations by considering that the accuracy of the identified describing functions is sufficient.

## CHAPTER 6

### ELECTRO-ACOUSTIC PERFORMANCE OF THE NOVEL BONE CONDUCTION HEARING AID

Percutaneous bone anchored hearing devices (BAHA) are one of the most popular treatment alternatives for patients suffering from conductive or mixed hearing loss. However, the reported limitation and drawbacks of the BAHA [131, 132] ushered in improvements in the active osseointegrated bone conduction implant technology [26, 133]. The need for skin-penetrating hearing implants has been eliminated with the emergence of new transcutaneous bone conduction implant solutions. Transcutaneous bone conduction implants also prevent the attenuations of the transmitted bone conduction force from the skin, hair, and other soft tissues and abutment-related soft tissue complications [73]. The transcutaneous implants are integrated into the skull bone through a titanium screw-in connection with a pre-drilled hole. The patient to be treated with the available transcutaneous implants must have sufficient skull bone thickness for the success of surgical practice [134, 135]. The eligibility criteria for skull bone thickness limit the applications of transcutaneous implants. Therefore, the overall depth of a transcutaneous bone conduction implant should be as small as possible while delivering satisfactory bone conduction stimulations to the mastoid. In this thesis study, a novel design offering a good compromise between the compactness and the performance of the BCHA is developed. The details of the BCHA design are already given in Chapters 2 and 3. In the present chapter, the pre-clinical electro-acoustic performance of the novel BCHA is evaluated by comparing it with conventional electromagnetic BC transducers.

After the nonlinear MDOF model of the BCHA is determined in Chapter 5, the tip mass of the BCHA is tuned to a new value to increase sound transmission efficiency.

The BCHA prototype is tested on the artificial mastoid, and the transmitted force spectra of the BCHA prototype are experimentally obtained by performing a series of constant voltage stepped-sine tests. Then, the harmonic voltage surface is generated by applying the previously introduced HFS method in a novel way [95, 102, 136]. The constant voltage FRFs estimated using HFS are then compared with the ones calculated by solving the corrected linear MDOF model of the complete test structure with a local nonlinear element identified in Chapter 5. In the next step, the bone conduction performance of the BCHA is determined by coupling the validated MDOF nonlinear model of the BCHA prototype with the experimentally obtained model of the skull simulator TU-1000 [137]. Finally, the transmitted BC forces and the corresponding hearing perception are compared through the audiometric measurements of BC hearing thresholds of live subjects.

### **6.1. Performance Evaluation Tests on the Artificial Mastoid Test Setup**

In the first stage, bone conduction tests of the BCHA prototype are performed by using the artificial mastoid test setup explained in Chapter 3 to quantitatively assess BCHA performance outputs. Frequency response and total harmonic distortion (THD), the ratio of the sum of powers of the distorted harmonics of a signal to the power of the fundamental harmonic [138], are measured from the BCHA prototype attached to the B&K type 4930 artificial mastoid using the experimental setup explained in Chapter 3. The BCHA prototype is tested under static preload of 5.4 N according to the acoustic equipment calibration standard ISO 389-3. The frequency response of the transmitted force to the artificial mastoid is measured by applying the harmonic input voltage at the 1 V<sub>rms</sub> level. The transmitted force-frequency response curves of the BCHA and B71 bone vibrator are compared in Figure 6.1. The fundamental resonance frequency of BCHA is below 400 Hz, indicating enhanced bone-conducted sound transfer at low frequencies. Unlike conventional electromagnetic BC transducers, the BCHA can generate bone conduction stimuli at frequencies above 4 kHz without a drop in the transmitted force. Although B71 performs relatively better than BCHA at frequencies between 400 Hz and 4000 Hz, given that the outer dimensions of the BCHA are almost

half of the B71 bone vibrator, the transmitted force spectra produced by BCHA can be considered highly promising. The THD spectra measured by LMS Test Lab software for B71 and the BCHA prototype during the artificial mastoid tests are presented in Figure 6.2. The low THD indicates that the hearing aid device produces more accurate sound waveforms. At frequencies of up to 2000 Hz, the THD values of BCHA are significantly lower than the B71 bone vibrator. The highest value in the THD spectrum of BCHA was measured at 3% at 177 Hz.

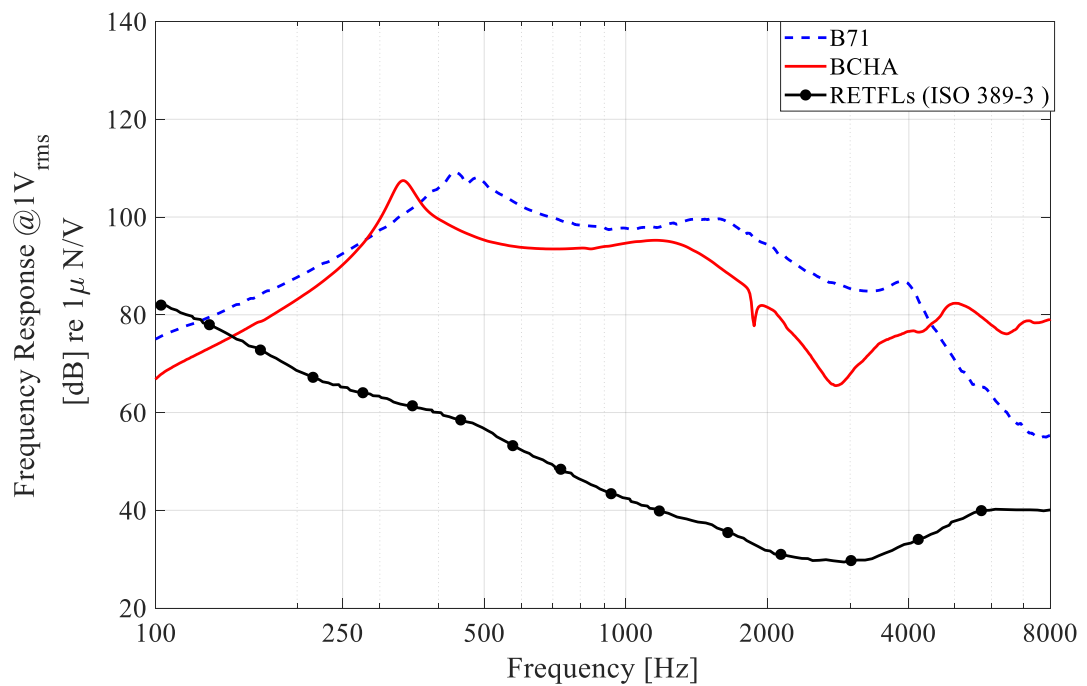


**Figure 6.1** The force transmitted from the B71 and the BCHA prototype to the artificial mastoid under 1 V<sub>rms</sub> input voltage level

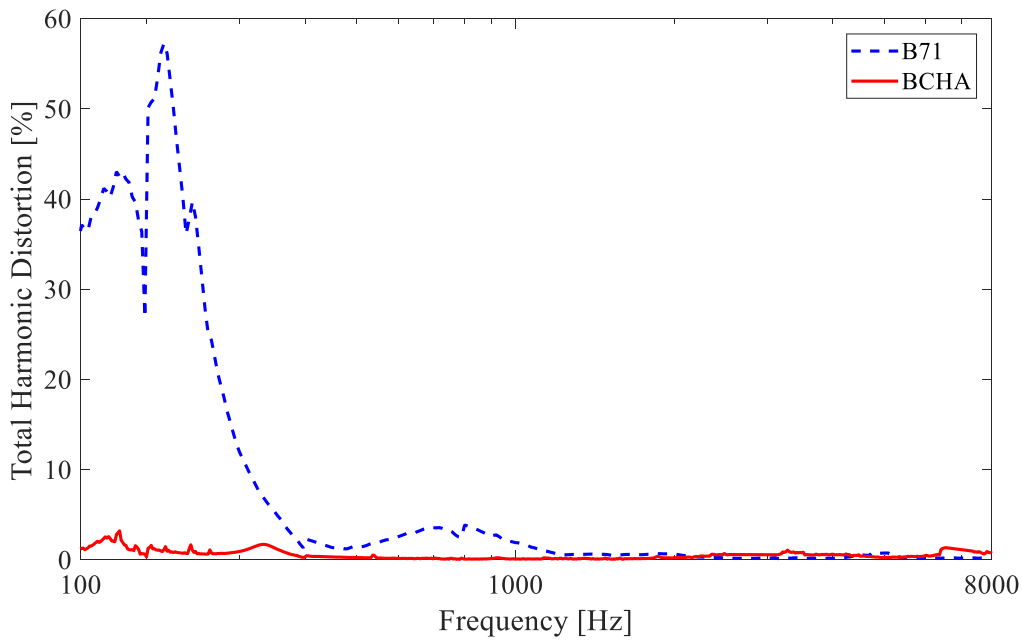


**Figure 6.2** A comparison of THDs of B71 and the BCHA prototype was driven at 1 V<sub>rms</sub> input voltage level

### 6.1.1. The Constant-Voltage Stepped Sine Tests

Preliminary constant-voltage tests are performed on the BCHA prototype attached to the artificial mastoid to gain knowledge about the nonlinear behavior of the BCHA prototype. The constant-voltage test sequence described in the previous chapters was applied precisely during the tests. The transmitted force to the artificial mastoid was measured during tests. The transmitted force frequency responses measured at each constant voltage level are presented in Figure 6.3. Previously identified softening nonlinear behavior is observed from the frequency response curves when the input harmonic voltage level is increased from 0.05 V to 4 V. It is observed that the nonlinear behavior of the BCHA attached to the artificial mastoid is not as strong as it is fixed from the base due to attenuation effect of the skin. However, the nonlinear behavior of the BCHA will be more significant if it is directly implanted in the skull bone.

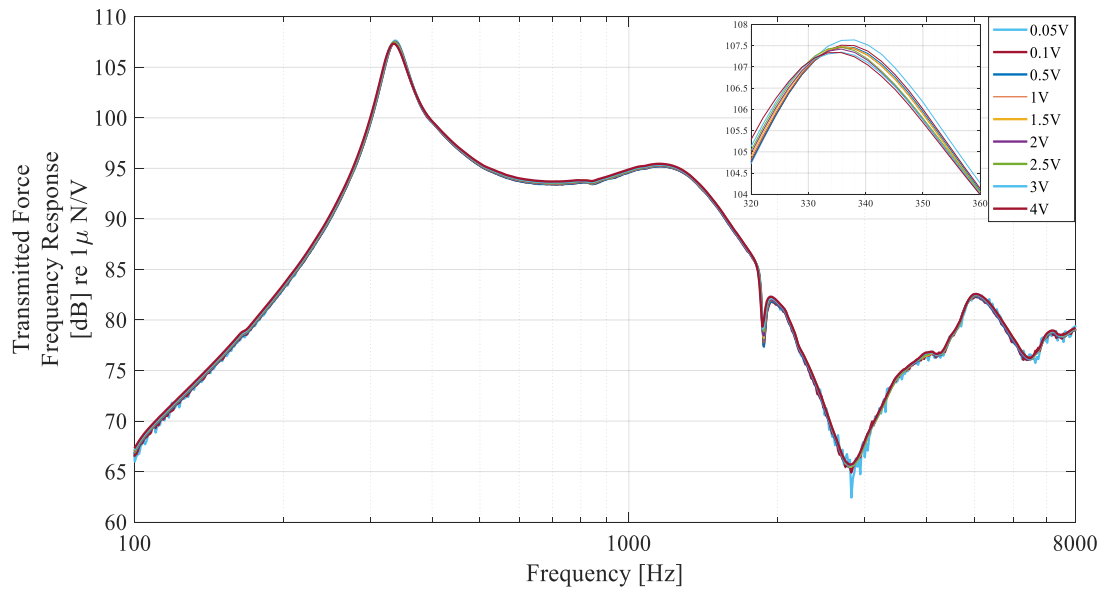


**Figure 6.3** Transmitted force-frequency response measured by constant-voltage stepped-sine testing

### 6.1.2. Identification of Nonlinear Modal Parameters by using the RCT Method

In all previous applications of the RCT method [95, 102, 115], the HFS has been constructed by merging harmonic force (or voltage) spectra measured at different constant-displacement amplitude levels, as illustrated in Chapter 4. However, this section aims to establish a relationship between the harmonic input voltage amplitudes and the corresponding transmitted force spectra, which is different from the method explained in Chapter 4. Luckily, the nonlinearity is not too strong, and the frequency response curves are smooth without any jump, as shown in Figure 6.4a. Therefore, this chapter demonstrates for the first time that if there is no jump, HFSs can also be constructed smoothly by combining constant-voltage (or force) frequency-response curves with linear interpolation, as shown in Figure 6.4b.

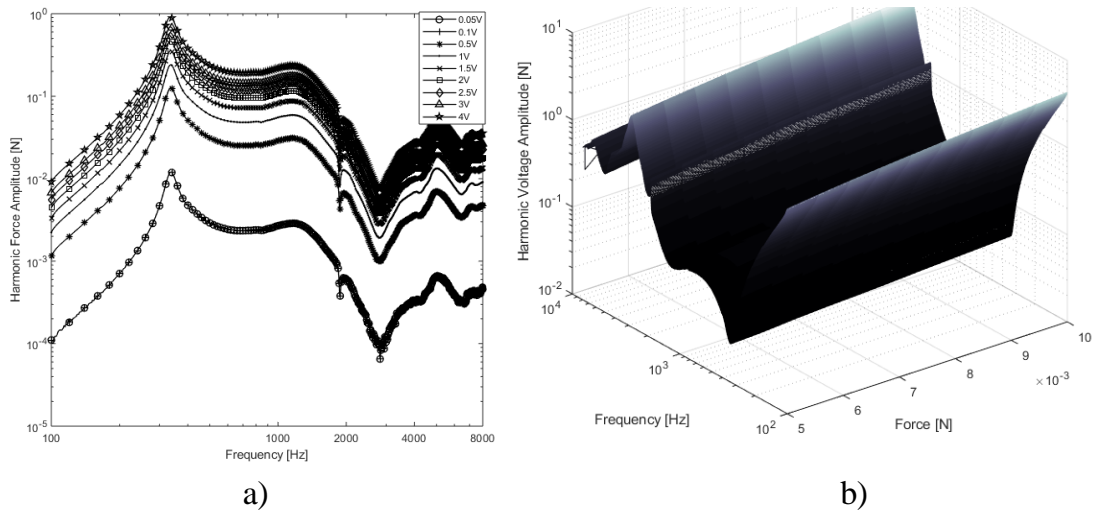


**Figure 6.4** Transmitted force-frequency response measured by constant-voltage stepped-sine testing

Once the HFS shown in Figure 6.4b is constructed from the constant-voltage FRFs given in Figure 6.4a, they are sliced by different force amplitude planes to obtain corresponding harmonic voltage spectra. By dividing each force amplitude value by the corresponding voltage spectrum, constant-force FRFs are obtained, as shown in Figure 6.5b. The nonlinear modal parameters corresponding to the fundamental nonlinear normal mode (Figure 6.5a) are identified by using the following accelerance formula,

$$\frac{F_{tr}}{V_{in}} = A_{jk}(\omega, |F_{tr}|) = \frac{-\omega^2 \bar{A}_{jkr}(|X_j|)}{\bar{\omega}_r^2(|F_{tr}|) - \omega^2 + i\eta_r(|F_{tr}|)\bar{\omega}_r(|F_{tr}|)}, \quad (5.1)$$

where  $F_{tr}$ , and  $V_{in}$  are the amplitude of the harmonic force transmitted to the artificial mastoid, and harmonic voltage amplitude, respectively.  $A_{jk}$  accelerance of the point  $j$  when excited from point  $k$



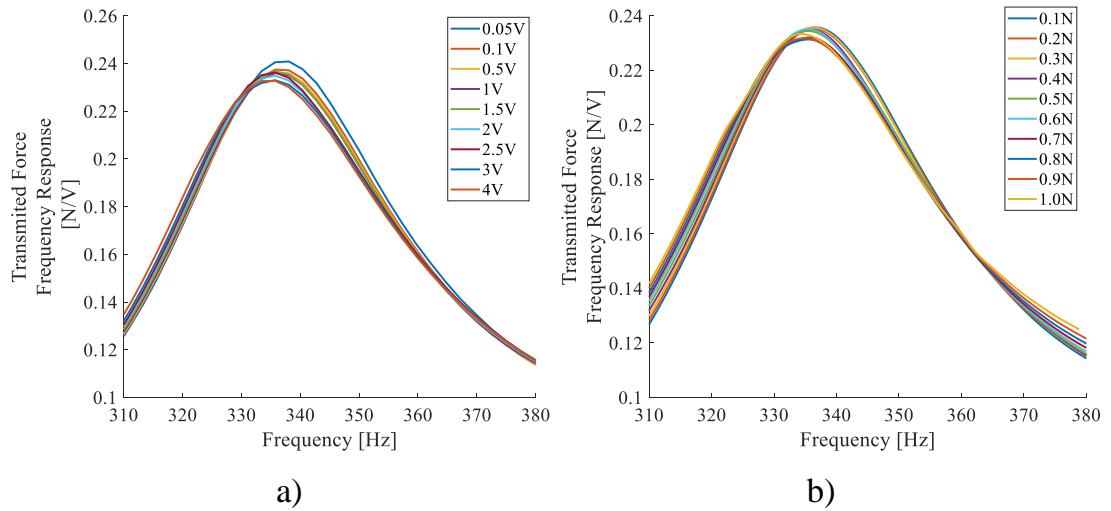


**Figure 6.5** Transmitted force frequency responses around fundamental resonance frequency: a) measured by constant-voltage stepped-sine testing, b) constant-response FRFs extracted from the HFS

The constant-force FRFs shown in Figure 6.5b turn out to be quasi-linear. Accordingly, modal parameters are extracted as functions of transmitted force amplitude, as shown in Figure 6.6 and Figure 6.7, by applying standard linear modal analysis techniques to the quasi-linear FRFs in Figure 6.5b. It is observed from Figure 6.6a that the resonance frequency decreases almost linearly with increasing transmitted force amplitude. On the other hand, modal damping ratio and modal constant values do not significantly change with the increase in the transmitted force level.

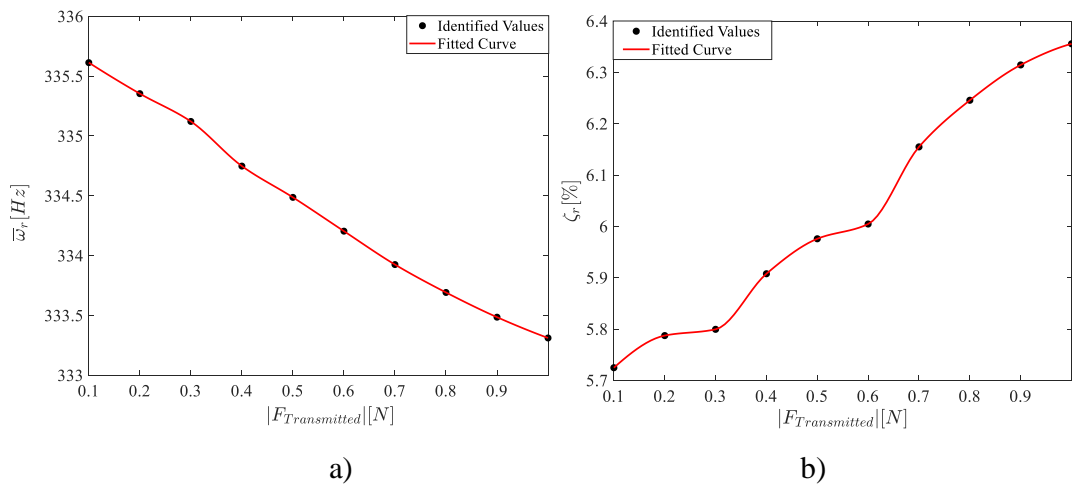


**Figure 6.6** Variation of the modal parameters of the quasi-linear FRFs with respect to the transmitted force level: a) natural frequency, b) modal damping ratio

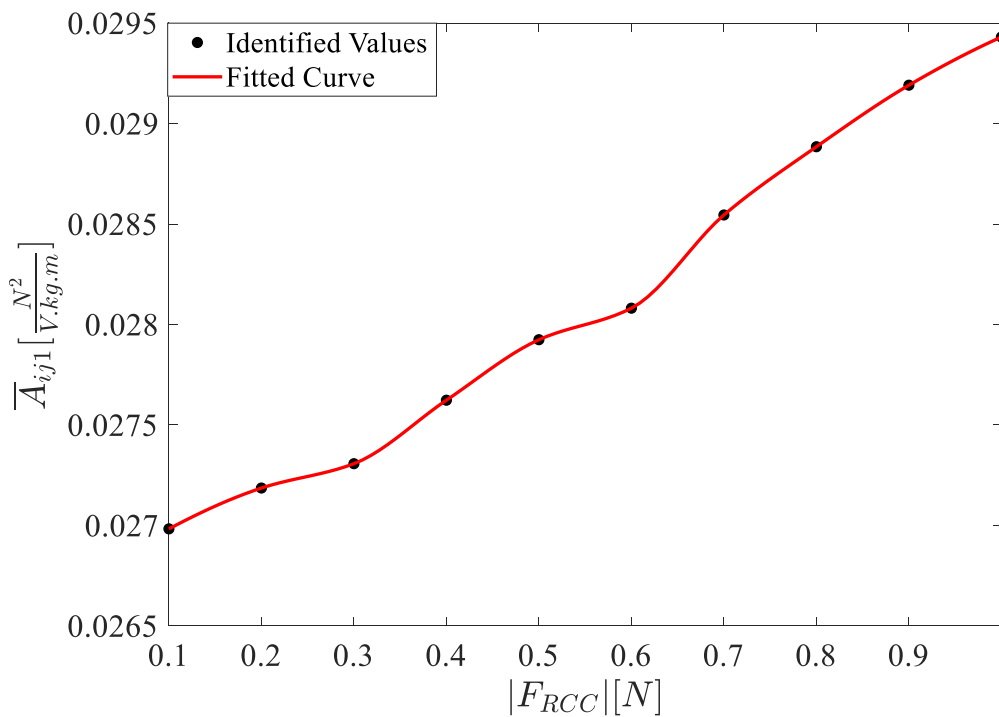


**Figure 6.7** Variation of the modal constants of the quasi-linear FRFs with respect to the transmitted force level

### 6.1.3. Validation of Nonlinear Modal Model and Describing Functions of the Identified Nonlinearity

Similar to the APA application in Chapter 4, the accuracy of the identified nonlinear modal parameters is demonstrated by comparing constant-voltage frequency response curves synthesized from these parameters with the measured data in Figure 6.8. The match between the measured and synthesized curves is almost perfect, and the percent relative error, which shows the accuracy of the identified modal parameters, is less than  $1 \times 10^{-4}$ . Figure 6.8 also presents the frequency response curves obtained from the nonlinear MDOF model. The MDOF nonlinear model is constructed by substructuring coupling the equivalent nonlinear subcomponent identified in Chapter 5 and the physically-driven linear mathematical model of the BCHA from Chapter 3. It can be observed from Figure 6.8a and Figure 6.8b that the match between measured and simulated FRF curves demonstrates the accuracy of the MDOF linear BCHA model and the identified describing function of the APA nonlinearity.

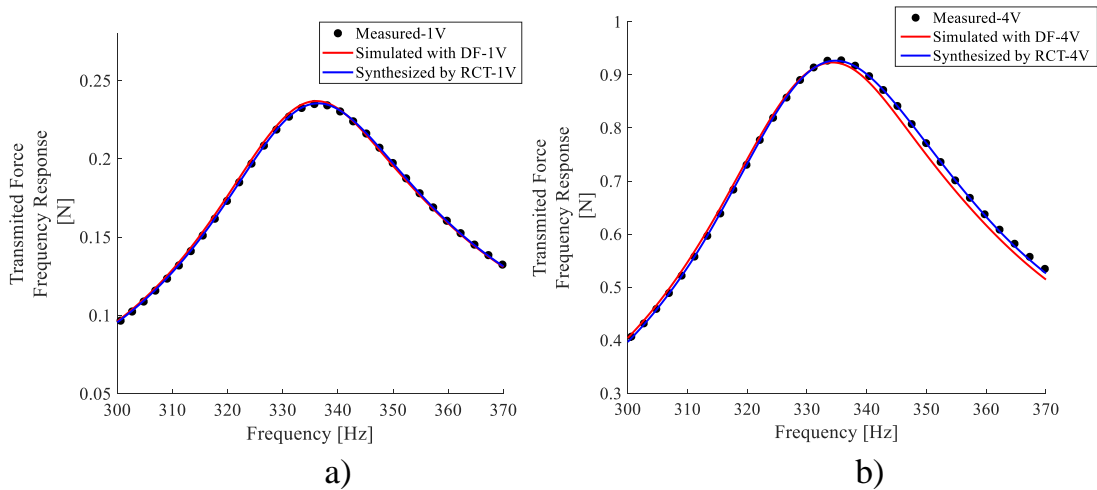


**Figure 6.8** Comparison of the measured transmitted force frequency responses with ones synthesized by using nonlinear modal parameters and simulated with the identified DF

## 6.2. Performance Simulation of the BCHA on the Skull Simulator

In the previous part of the present chapter, the accuracy of the nonlinear MDOF BCHA model is validated experimentally. Although the artificial mastoid simulations and the experiments provide a comparative assessment of the BC performance of the BCHA, it is also necessary to examine the actual performance of BCHA when it is integrated into the skull bone. In this stage, the application case in which the BCHA is connected to a miniaturized skull simulator TU-1000 (Figure 6.9a) will be carried out to compare BCHA with other transcutaneous BC implants. The mechanical impedance of the TU-1000 measured under IEC 373 test standards [139], taken from [137], is shown in Figure 6.9b.

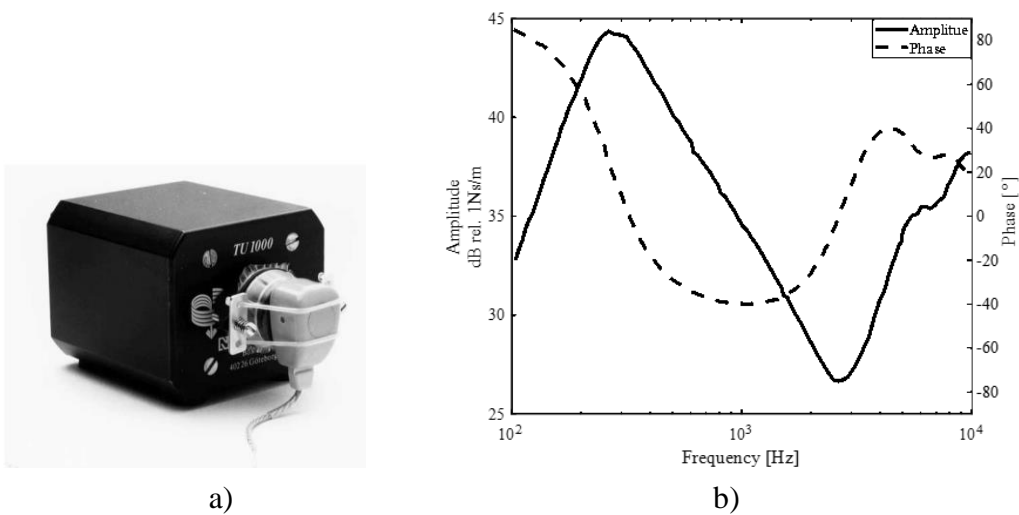


**Figure 6.9** a) The photograph and b) mechanical impedance of the miniaturized artificial mastoid TU-1000 [137]

The transmitted force of the BCHA to TU-1000 is simulated by using the coupled model of the nonlinear MDOF BCHA model and the experimentally obtained TU-1000 model. The system of equations that constitutes the coupled model is solved by the Newton-Raphson method and the arc-length continuation algorithm. The transmitted force-frequency response curve obtained by solving a nonlinear system of

equations is depicted in Figure 6.10. The measured frequency response of an electromagnetic bone conduction implant (BCI) given in the study of Jansson et al. [140] is also shown in Figure 6.10. In comparison with the frequency responses of the two devices, it is observed that the BCHA is more effective at lower frequencies below 400 Hz and operates at frequencies above 4 kHz without a drop in amplitude of the transmitted bone conduction oscillations.

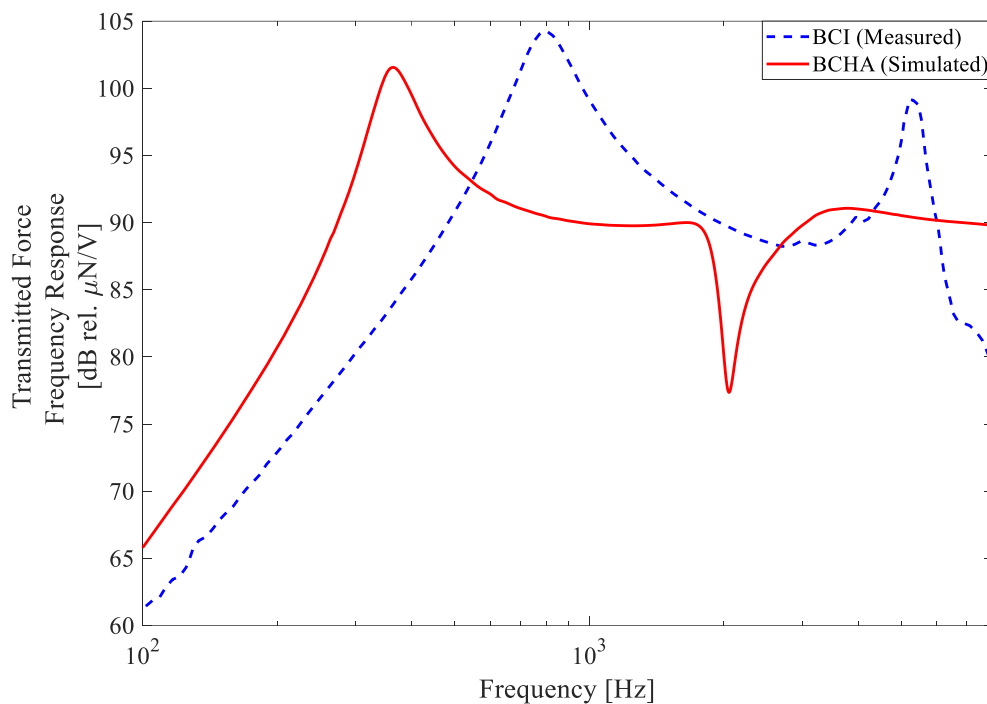


**Figure 6.10** The force transmitted from the BCHA and the BCI to the artificial mastoid under 1  $V_{\text{rms}}$  input voltage level

### 6.3. Evaluation of the Hearing Perception of the BCHA

The hearing threshold tests are a unique tool for detecting the type and severity of a patient's hearing loss (Figure 6.11a). The hearing thresholds are evaluated at discrete frequencies from 125 Hz to 8000 Hz and measured in dB HL (hearing loss) displayed on an audiogram (Figure 6.11b). The reference threshold value of the healthy ear is 0 dB HL. The banana-shaped gray-shaded region in the audiogram shows the zone of frequencies and sound levels used in speech.

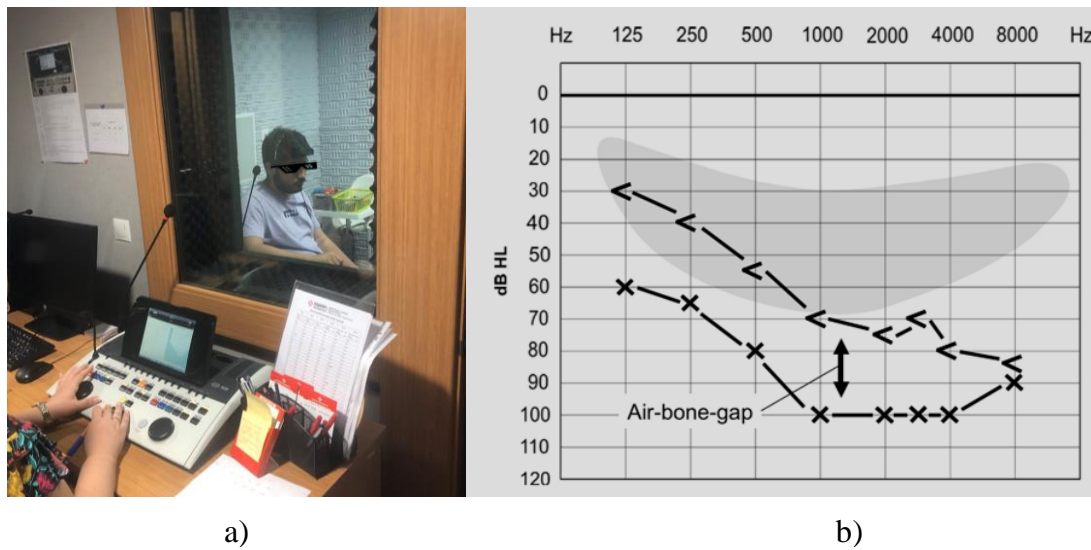


**Figure 6.11** a) A photograph from a hearing threshold test, b) an audiogram of left ear air and bone threshold values[141]

There are two types of hearing threshold tests, namely, air and bone conduction threshold tests. In air conduction threshold tests, pure tones are delivered to patients employing earphones. At each frequency, the pure tone level increases gradually until the patient perceives the sound, indicating the air conduction threshold value in dB HL. The air conduction thresholds are marked on the audiogram by " × " for the left ear. In bone conduction hearing threshold tests, on the other hand, the pure tones are provided through bone vibrators placed on a mastoid bone. The threshold values determined from the air conduction tests indicate the sum of conductive and sensorineural hearing loss. The bone conduction thresholds are marked on the audiogram by " < " for the left ear. The difference between the air and bone conduction threshold values is defined as an "air-bone gap," indicating conductive hearing loss (Figure 6.11b) [141]. A BCHA aims to improve the hearing thresholds in aided conditions, especially for main speech frequencies.

At the end of the thesis, as a particular case study, bone conduction threshold tests are performed on four healthy participants and three conductive hearing loss patients. The threshold tests are repeated with the B71 bone vibrator and the BCHA prototype for

both ears of each participant. Average hearing threshold differences between the B71 and the BCHA prototype are given in Table 6.1.

**Table 6.1** Bone conduction threshold difference between B71 and BCHA

Frequency [Hz]	BCHA-B71 (Normal Hearing ) [dB HL]	BCHA-B71 (Hearing Impaired) [dB HL]	BCHA-B71 (Artificial mastoid) [dB]
250	12	7	3
500	22	26	8
1000	17	13	4
2000	22	25	13
4000	15	12	10
8000	-10	-2	-25

The average threshold values in Table 6.1 indicate that the hearing perception of the BCHA prototype increases at frequencies below 500 Hz and above 4000 Hz. At mid frequencies, the bone conduction threshold increases for all patients aided with the BCHA prototype. One of the most critical findings from this particular case study is that the differences between the forces transmitted to the artificial mastoid from the B71 bone vibrator and the BCHA prototype are congruent with the differences in bone conduction threshold values measured in the hearing test. It is noted that the BCHA is designed as a BC implant which is supposed to be as small as possible, whereas the B71 bone vibrator is designed as a sizable audiometric instrument used to measure the hearing threshold levels. Although the level of force output is sacrificed at an acceptable level in exchange for getting a smaller implant, it is observed from Figure 6.1 that the levels of BCHA's transmitted force are significantly higher than RETFLs. The reduced BC transmission of the BCHA at the mid frequencies is expected to be tolerated by the human ear, sensitive to sounds in the range of 1 kHz to 4 kHz. Besides, the transmitted force of the BCHA to the cochlea is increased by 10-20 dB [82] if it is directly implanted in the skull bone with the casing proposed in Chapter 3. The results

in Figure 6.10 show that the BCHA can be a viable alternative to conventional transcutaneous BC implants. The BCHA transducer provides an effective solution for conductive hearing loss patients with proper surgical approaches as an active transcutaneous BC implant.



## CHAPTER 7

### SUMMARY AND CONCLUSIONS

#### 7.1. General Conclusions

It may not be possible to successfully treat patients with conductive and mixed hearing loss or unilateral deafness in the case of middle ear-induced functional disorders. Transmission of the sound signals via bone conduction (BC) pathways is an alternative treatment for patients suffering from conductive hearing loss. BC hearing is the phenomenon of the transmission of acoustic waves through the skull bones to stimulate the auditory nerves by using bone conduction hearing aids. Although there are different types of BC hearing aid (BCHA) treatments, most BCHAs in the market have electromagnetic BC transducers. While electromagnetic BC transducers are unique commercial products on the market, the limitations of current products led researchers to develop new BC transducer technologies.

The ultimate goal of this thesis study is to develop a novel design of implantable BC transducer that is:

- Lighter and smaller than conventional BC transducers,
- Operating efficiently in the frequency range from 100 Hz to 8000 Hz,
- Having low total harmonic distortion (THD) in the desired frequency range,
- Tuneable for different patient anatomy.

At the beginning of this study, the miniature actuator technologies in the literature were thoroughly examined, and the adaptability of piezoelectric actuators was assessed for BC applications. Among the piezoelectric actuator alternatives, a multilayer stack piezoelectric actuator (MSPA) with a rhombus-compliant mechanism (RCM) named

amplified piezoelectric actuator (APA) was chosen as the actuator of the BC transducer. In order to determine the dynamics of APAs at high frequencies, the hybrid structure of the APA must be modeled precisely. For this reason, the APA's detailed analytical dynamic model was developed in the first step. The analytical model of the APA was then validated by comparing the frequency responses obtained from the model with ones obtained from the finite element model (FEM) and stand-alone vibration tests under low voltage levels.

At the beginning of the design stage, the mechanical amplifier material and embedded MSPA were modified to improve the performance of the BC transducer. It was decided to attach a tip mass to the free end of the APA in order to enhance the force transmission at low frequencies. The basic dimensions of the mechanical amplifier and the weight of the attached tip mass were optimized using a genetic algorithm based on the verified model of the APA. The overall output force spectra of the proposed BC transducer transmitted to B&K type 4930 artificial mastoid were brought to the best possible level at the end of the optimization process. Cedrat Technologies manufactured the optimized APA design for this Ph.D. study.

The preliminary constant voltage level stepped-sine tests performed on the manufactured APA prototypes showed that the fundamental resonance frequency drops while the voltage level increases, indicating softening nonlinearity. The APA's nonlinear frequency response model was expressed using a single nonlinear normal mode (NNM), and the corresponding modal parameters were experimentally identified from the quasi-linear force frequency responses (FRFs) obtained from the response-controlled stepped-sine tests (RCT). The nonlinear modal model of the APA was constructed by synthesizing identified modal parameters, and a perfect match between the synthesized FRFs and the ones extracted experimentally showed the accuracy of the nonlinear modal model.

Although the NNM-based experimental modal modeling accurately estimated the nonlinear dynamics of the APA for the stand-alone test cases, a nonlinear multi-degree of freedom (MDOF) model would still be needed to predict the dynamics of BCHA

coupled to different structures. Modeling the nonlinearity of the APA with an equivalent nonlinear element at a single location, describing the surface of the nonlinearity was identified by using the constant displacement FRFs and linear model of the APA. The describing function was determined from the describing surface by curve fitting since the describing surface does not change significantly with the frequency. The displacement-controlled step sine tests were performed on the APA with different tip masses, and harmonic force surfaces (HFSs) were obtained from each test. The accuracy of the describing surface and describing function is validated experimentally by comparing the displacement frequency responses obtained from the nonlinear MDOF model with the ones extracted from HSFs.

After the design and modeling phases, the electro-acoustic performance of the piezoelectric BCHA prototype was evaluated by artificial mastoid tests. During the tests, the transmitted force frequency responses of the BCHA prototype were measured under constant voltage step sine tests. The electromagnetic BC transducer B71 was also tested on the same setup and the measured transmitted force frequency responses were compared with the frequency response of the BCHA prototype.

The relation between the amplitude of harmonic input voltage and the transmitted force spectra of the BCHA prototype attached to the artificial mastoid was obtained experimentally by applying HFS and RCT methods in a novel way. The measured constant voltage FRFs were then compared with those obtained from the RCT method and the outputs of the nonlinear MDOF model containing the previously identified nonlinearity. The results showed that the outputs of the experimentally obtained modal model of the BCHA and the nonlinear MDOF BCHA model perfectly match the measurements, having less than  $1 \times 10^{-4}$  percent relative error. In the next step, the bone conduction performance of the BCHA attached to the skull simulator TU-1000 was simulated by using the validated nonlinear MDOF model. The simulation results showed that the BCHA effectively transmits the bone conduction stimuli at lower frequencies below 400 Hz and operates at high frequencies above 4 kHz without a drop, while it produces acceptable stimulation forces for mid frequencies according to

the reference equivalent threshold force levels (RETFLs) corresponding to threshold values of normal hearing.

At the final stage of this thesis study, bone conduction threshold tests were performed on healthy and hearing impaired participants by employing the BCHA prototype and the B71 bone vibrator separately. The difference between the transmitted BC force level of the BCHA prototype and the B71 bone vibrator was compared with the threshold values of the participants tested with both devices. Differences between the force levels transmitted to the artificial mastoid from the B71 bone vibrator and the BCHA prototype were found to be consistent with the differences in bone conduction threshold values measured in the hearing test. The reduced bone conduction transmission of the BCHA at the mid frequencies is expected to be tolerated by the human ear, sensitive to sounds in the range of 1 kHz to 4 kHz.

## **7.2. Novel Contributions**

The main original contributions of this thesis study are listed below:

- A novel BCHA transducer based on a miniature piezoelectric actuator is developed (designed, manufactured, and tested).
- It is the first time a stacked piezoelectric actuator has been used as a BC transducer.
- The nonlinear modal parameters and the construction of a reliable modal model of a miniature APA have been identified accurately by using a recently developed nonlinear modal identification framework, RCT.
- It is the first time that HFS is constructed smoothly by combining constant-voltage (or force) frequency-response curves with linear interpolation if there is no jump.

### **7.3. Recommendation for Future Work**

The first future direction would be performing live subject hearing threshold tests with a broader group of participants to minimize the statistical errors.

This study can be expanded to investigate the performance of the proposed BCHA on fresh cadaver heads. In the scope of cadaver head experiments, the relation between the promontory motions, which are accepted as an estimator of hearing perception, and the transmitted BCHA stimulations can be determined by using the methods employed in this thesis study. Another future recommendation would be designing a complementary electronic unit to multiply the voltage input of the BCHA without exceeding the total power capacity of a standard audio processor unit.



## REFERENCES

- [1] Biographixmedia, “ear anatomy drawing sketch image illustration,” 2015. [Online]. Available: <https://www.biographixmedia.com/human/ear-anatomy.html>. [Accessed: 21-Jul-2022].
- [2] P. W. Alberti, “The Anatomy and Physiology of the Ear and Hearing,” *Occupational exposure to noise: evaluation, prevention and control*, pp. 53–62, 2001.
- [3] H. Møller and C. S. Pedersen, “Hearing at Low and Infrasonic Frequencies,” *Noise and Health*, vol. 6, no. 23, pp. 37–57, 2004.
- [4] WHO, “Addressing The Rising Prevalence of Hearing Loss,” 2018.
- [5] WHO, “WHO Global Estimates on Prevalence of Hearing Loss,” 2012.
- [6] H. Lundgren, “Bone Conduction Transducers and Output Variability,” Chalmers University of Technology, 2010.
- [7] British Society of Audiology, “Recommended Procedure. Bone-Conduction Threshold Audiometry with and without Masking,” 2012.
- [8] “how-hearing-aid-work.” [Online]. Available: <https://drrajivdesaimd.com/wp-content/uploads/2016/08/how-hearing-aid-work.jpg>. [Accessed: 21-Jul-2022].
- [9] “HowWeHear\_withBaha\_soundwaves.” [Online]. Available: [https://alynsimardaudio.com/wp-content/uploads/2014/02/HowWeHear\\_withBaha\\_soundwaves.jpg](https://alynsimardaudio.com/wp-content/uploads/2014/02/HowWeHear_withBaha_soundwaves.jpg). [Accessed: 21-Jul-2022].
- [10] “Vibrant Soundbridge Middle Ear Implant.” [Online]. Available: <https://www.medel.com/hearing-solutions/vibrant-soundbridge>. [Accessed: 21-Jul-2022].
- [11] G. Rauterkus, A. K. Maxwell, J. B. Kahane, and J. J. Lentz, “Conversations in Cochlear Implantation : The Inner Ear Therapy of Today,” *Biomolecules*, vol.

- 12, no. 649, pp. 1–18, 2022.
- [12] “Cochlear implant.” [Online]. Available: [https://adamantiumjoy.files.wordpress.com/2017/07/cochlearimpant\\_420x315\\_rd1\\_enil.jpg](https://adamantiumjoy.files.wordpress.com/2017/07/cochlearimpant_420x315_rd1_enil.jpg). [Accessed: 21-Jul-2022].
- [13] S. Reinfeldt, B. Håkansson, and H. Taghavi, “New developments in bone-conduction hearing implants: a review,” *Medical Devices: Evidence and Research*, vol. 2015, no. 8, pp. 79–93, 2015.
- [14] “Bone-anchored-hearing-device.” [Online]. Available: <https://successforkidswithhearingloss.com/wp-content/uploads/2017/06/bone-anchored-hearing-device.jpg>. [Accessed: 21-Jul-2022].
- [15] “Bone-conduction glasses.” [Online]. Available: <https://www.cochlea.org/en/treatments/hearing-aids>. [Accessed: 22-Jul-2022].
- [16] B. Hakansson, A. Tjellström, U. Rosenhall, and P. Carlsson, “The Bone-Anchored Hearing Aid: Principal Design and a Psychoacoustical Evaluation,” *Acta Oto-Laryngologica*, vol. 100, no. 3–4, pp. 229–239, 1985.
- [17] G. Liden *et al.*, “Ten Years of Experience with the Swedish Bone-Anchored Hearing System,” *Annals of Otolaryngology, Rhinology & Laryngology*, vol. 99, no. 10 II SUPPL. 151, pp. 1–16, 1990.
- [18] T. Davis, K. A. Gordon, D. Clutton, and B. C. Papsin, “Bone-Anchored Hearing Aids in Infants and Children Younger Than 5 Years,” *Arch Otolaryngol Head Neck Surg*, vol. 133, pp. 51–55, 2007.
- [19] A. Hagr, “BAHA: Bone-Anchored Hearing Aid,” *International Journal of Health Sciences*, vol. 1, no. 2, pp. 265–276, 2007.
- [20] J. J. Wazen, B. Wycherly, and J. Daugherty, “Complications of bone-anchored hearing devices,” *Advances in oto-rhino-laryngology*, vol. 71, pp. 63–72, Mar. 2011.



- [21] H. Taghavi, “A Novel Bone Conduction Implant System,” Chalmers University of Technology, 2012.
- [22] R. Siegert and J. Kanderske, “Semi-implantable transcutaneous bone conduction hearing devices,” *HNO*, vol. 62, no. 7, pp. 502–508, 2014.
- [23] D. Bernardeschi *et al.*, “Audiological Results and Quality of Life of Sophono Alpha 2 Transcutaneous Bone-Anchored Implant Users in Single-Sided Deafness,” *Audiology and Neurotology*, vol. 21, no. 3, pp. 158–164, Jul. 2016.
- [24] R. Siegert, “Partially implantable bone conduction hearing aids without a percutaneous abutment (otomag): Technique and preliminary clinical results,” *Advances in Oto-Rhino- Laryngology*, vol. 71, pp. 41–46, 2011.
- [25] J. W. Shin *et al.*, “Surgical and audiologic comparison between sophono and bone-anchored hearing aids implantation,” *Clinical and Experimental Otorhinolaryngology*, vol. 9, no. 1, pp. 21–26, 2016.
- [26] B. Håkansson *et al.*, “A novel bone conduction implant (BCI): Engineering aspects and pre-clinical studies,” *International Journal of Audiology*, vol. 49, no. 3, pp. 203–215, 2010.
- [27] M. E. Zernotti and A. B. Sarasty, “Active Bone Conduction Prosthesis: Bonebridge™,” *International Archives of Otorhinolaryngology*, vol. 19, pp. 343–348, 2015.
- [28] J. Adler and J. Gabrielsson, “Evaluation of Transcutaneous Bone Conduction Implant with a Capsuled Transducer,” Chalmers University of Technology, 2009.
- [29] R. F. Bento, P. T. Lopes, and F. Da Chagas Cabral, “Bonebridge bone conduction implant,” *International Archives of Otorhinolaryngology*, vol. 19, no. 4, p. 277, 2015.
- [30] B. E. V Håkansson, “The Balanced Electromagnetic Separation Transducer a New Bone Conduction Transducer.,” *The Journal of the Acoustical Society of*

- America*, vol. 113, no. 2, pp. 818–825, 2003.
- [31] K. F. Jansson, B. Håkansson, L. Johannsen, and T. Tengstrand, “Electroacoustic performance of the new bone vibrator Radioear B81 : A comparison with the conventional Radioear B71,” *International Journal of Audiology*, vol. 54, no. 5, pp. 334–340, 2014.
- [32] L. Pickelmann, “Piezo Vibrations and Piezo Shakers.” pp. 1–8, 2006.
- [33] J. Sun, B. Wu, G. Cheng, J. Wen, and P. Zeng, “Research on Circular Bimorph Piezoelectric Bone- conduction Hearing Device,” in *International Conference on Mechatronics and Automation*, 2009, pp. 3359–3363.
- [34] R. B. A. Adamson, M. Bance, and J. A. Brown, “A Piezoelectric Bone-Conduction Bending Hearing Actuator,” *The Journal of the Acoustical Society of America*, vol. 128, no. July, pp. 2003–2008, 2010.
- [35] Q. M. Wang, Q. Zhang, B. Xu, R. Liu, and L. E. Cross, “Nonlinear piezoelectric behavior of ceramic bending mode actuators under strong electric fields,” *Journal of Applied Physics*, vol. 86, no. 6, pp. 3352–3360, 1999.
- [36] M. Märten and H. Waller, “Piezoelectric Actuators - A Comparison Of Bimorph And Stack Actuators,” in *Proceedings of the 6" International Conference on New Actuator*, 1998, pp. 269–27.
- [37] T. Yeom, T. W. Simon, M. Zhang, M. T. North, and T. Cui, “High frequency , large displacement , and Low Power Consumption Piezoelectric Translational Actuator Based on an Oval Loop Shell,” *Sensors and Actuators A: Physical*, vol. 176, pp. 99–109, Apr. 2012.
- [38] A. V. Carazo and A. Malla, “Bone-Conduction Hearing-Aid Transducer Having Improved Frequency Response,” 2007.
- [39] J. Parker, H. Jaeger, and C. M., “A Piezoelectric Bone Conduction Device Having Enhanced Transducer Stroke,” 2009.

- [40] I. Dobrev *et al.*, “Performance evaluation of a novel piezoelectric subcutaneous bone conduction device,” *Hearing Research*, vol. 370, pp. 94–104, 2018.
- [41] T. Mcpherson and J. Ueda, “Piezoelectric self-sensing technique for tweezer style end-effector,” *IEEE International Conference on Intelligent Robots and Systems*, pp. 1940–1945, 2011.
- [42] A. Safari and E. K. Akdoğan, *Piezoelectric and acoustic materials for transducer applications*. 2008.
- [43] C. K. Lee, S. H. Chang, and P. Z. Chang, “Miniature piezoelectric actuators: Design concept, fabrication and performance evaluation,” *Smart Materials and Structures*, vol. 7, no. 3, pp. 312–326, 1998.
- [44] J. Minase, T. F. Lu, B. Cazzolato, and S. Grainger, “A review, supported by experimental results, of voltage, charge and capacitor insertion method for driving piezoelectric actuators,” *Precision Engineering*, vol. 34, no. 4, pp. 692–700, 2010.
- [45] P. Ge and M. Jouaneh, “Modeling hysteresis in piezoceramic actuators,” *Precision Engineering*, vol. 17, no. 3, pp. 211–221, 1995.
- [46] G. Zhang, C. Zhang, and J. Gu, “A memory-based hysteresis model in piezoelectric actuators,” *Journal of Control Science and Engineering*, vol. 2012, pp. 1–7, 2012.
- [47] C. Niezrecki, D. Brei, S. Balakrishnan, and a. Moskalik, “Piezoelectric Actuation: State of the Art,” *The Shock and Vibration Digest*, vol. 33, no. 4, pp. 269–280, 2001.
- [48] J. P. Wulfsberg *et al.*, “A novel methodology for the development of compliant mechanisms with application to feed units,” *Production Engineering Research and Development*, vol. 7, no. 5, pp. 503–510, 2013.
- [49] F. Dirksen and R. Lammering, “On mechanical properties of planar flexure hinges of compliant mechanisms,” *Mechanical Sciences*, vol. 2, pp. 109–117,

2011.

- [50] J. Cao, M. Ling, D. J. Inman, and J. Lin, “Generalized constitutive equations for piezo- actuated compliant mechanism,” *Smart Materials and Structures*, vol. 25, no. 9, pp. 1–10, 2016.
- [51] H. W. Ma, S. M. Yao, L. Q. Wang, and Z. Zhong, “Analysis of the displacement amplification ratio of bridge-type flexure hinge,” *Sensors and Actuators, A: Physical*, vol. 132, no. 2, pp. 730–736, 2006.
- [52] M. Ling, L. Yuan, Z. Luo, T. Huang, and X. Zhang, “Enhancing Dynamic Bandwidth of Amplified Piezoelectric Actuators by a Hybrid Lever and Bridge-Type Compliant Mechanism,” *Actuators*, vol. 11, no. 134, pp. 1–18, 2022.
- [53] M. Ling, J. Cao, M. Zeng, J. Lin, and D. J. Inman, “Enhanced Mathematical Modeling of the displacement Amplification Ratio for Piezoelectric Compliant Mechanisms,” *Smart Materials and Structures*, vol. 25, no. 7, pp. 1–11, 2016.
- [54] F. Claeysen, R. Le Letty, F. Barillot, and O. Sosnicki, “Amplified Piezoelectric Actuators: Static & Dynamic Applications,” in *Ferroelectrics*, 2007, vol. 351, no. 1, pp. 3–14.
- [55] J. Ueda, T. W. Secord, and H. H. Asada, “Large Effective-Strain Piezoelectric Actuators Using Nested Cellular Architecture With Exponential Strain Amplification Mechanisms,” *IEEE/ASME Transactions on Mechatronics*, vol. 15, no. 5, pp. 770–782, 2010.
- [56] L. Tolliver, T. Xu, and X. Jiang, “Finite element analysis of the piezoelectric stacked-HYBATS transducer,” *Smart Materials and Structures*, vol. 22, no. 3, pp. 1–11, 2013.
- [57] A. Kumar and A. DasGupta, “Dynamics of a shell-type amplified piezoelectric actuator,” *Journal of Vibration and Acoustics*, vol. 140, no. 4, pp. 1–9, Aug. 2018.
- [58] “APA35XS,” *CEDRAT TECHNOLOGIES*, 2014. [Online]. Available:

<https://www.cedrat-technologies.com/fileadmin/datasheets/APA35XS.pdf>.

[Accessed: 09-Oct-2021].

- [59] F. Qian, T. B. Xu, and L. zuo, “A distributed parameter model for the piezoelectric stack harvester subjected to general periodic and random excitations,” *Engineering Structures*, vol. 173, no. July, pp. 191–202, 2018.
- [60] W. Zhu, F. Yang, and X. Rui, “A fully dynamic model of a multi-layer piezoelectric actuator incorporating the power amplifier,” *Smart Materials and Structures*, vol. 26, pp. 1–10, 2017.
- [61] W. Zhu, G. Chen, L. Bian, and X. Rui, “Transfer matrix method for multibody systems for piezoelectric stack actuators,” *Smart Materials and Structures*, vol. 23, no. 9, 2014.
- [62] N. Jalili, *Piezoelectric-Based Vibration Control*. 2010.
- [63] D. De Klerk, D. J. Rixen, and S. N. Voormeeren, “General Framework for Dynamic Substructuring : History , Review , and Classification of Techniques,” *AIAA Journal*, vol. 46, no. 5, pp. 1169–1181, 2008.
- [64] “Instruction Manual optoNCDT 2300,” *MICRO-EPSILON MESSTECHNIK GbmH & Co. KG*, 2021. [Online]. Available: <http://www.micro-epsilon.de/download/manuals/man--optoNCDT-2300--en.pdf>. [Accessed: 09-Oct-2021].
- [65] “LMS SCADAS,” *Siemens PLM Software*, 2017. [Online]. Available: [https://www.plm.automation.siemens.com/fr\\_fr/Images/Siemens-PLM-LMS-SCADAS-br\\_tcm68-221355.pdf](https://www.plm.automation.siemens.com/fr_fr/Images/Siemens-PLM-LMS-SCADAS-br_tcm68-221355.pdf). [Accessed: 09-Oct-2021].
- [66] E. Barány, *A Contribution to the physiology of bone conduction*. Appelberg, 1938.
- [67] G. von Békésy, *Experiments in hearing*. New York: McGraw - Hill, 1960.
- [68] J. Tonndorf, *Bone conduction. Studies in experimental animals*, vol. 213. 1966.

- [69] S. Stenfelt, “Acoustic and physiologic aspects of bone conduction hearing,” *Advances in Otorhinolaryngology*, vol. 71, pp. 10–21, Mar. 2011.
- [70] S. Stenfelt and R. L. Goode, “Bone-conducted sound: Physiological and clinical aspects,” *Otology and Neurotology*, vol. 26, no. 6, pp. 1245–1261, 2005.
- [71] S. Stenfelt, “Model predictions for bone conduction perception in the human,” *Hearing Research*, vol. 340, pp. 135–143, 2016.
- [72] M. Eeg-olofsson *et al.*, “Transmission of bone conducted sound - Correlation between hearing perception and cochlear vibration,” *Hearing Research*, vol. 306, no. September 2013, pp. 11–20, 2013.
- [73] Y. Chang and S. Stenfelt, “Characteristics of Bone-Conduction Devices Simulated in a Finite-Element Model of a Whole Human Head,” *Trends in Hearing*, vol. 23, pp. 1–20, 2019.
- [74] B. Håkansson, P. Carlssonanders, and A. Tjellstrom, “The mechanical point impedance of the human head , with and without skin penetration,” *Journal of Acoustical Society of America*, vol. 80, no. 4, pp. 1065–1075, 1986.
- [75] D. Cortes, “Bone Conduction Transducers : output force dependency on load condition,” Chalmers University of Technology, 2002.
- [76] F. Woelflin, “The mechanical point impedance of the skin-penetrated human skull in vivo,” Chalmers University of Technology, 2011.
- [77] M. Eeg-Olofsson, “Transmission of bone-conducted sound in the human skull based on vibration and perceptual measures,” The University of Gothenburg, 2012.
- [78] S. Stenfelt, B. Håkansson, and A. Tjellström, “Vibration characteristics of bone conducted sound in vitro,” *The Journal of the Acoustical Society of America*, vol. 107, no. 1, p. 422, 2000.
- [79] Brüel & Kjær, “Artificial Mastoid-Type 4930,” 2017. [Online]. Available:

<http://www.bk.dk>.

- [80] ISO 389-3, “Acoustics-Reference Zero for the Calibration of Audiometric Equipment-Part 3:Reference Equivalent Threshold Force Levels for Pure Tones and Bone Vibrators (International Organization for Standardization, Geneva),” 1994.
- [81] RadioEar, “Bone Transducers-B71,” 2021. [Online]. Available: [https://wdh02.azureedge.net/-/media/radio-ear/main/datasheets/datasheet\\_b71\\_03\\_21.pdf](https://wdh02.azureedge.net/-/media/radio-ear/main/datasheets/datasheet_b71_03_21.pdf). [Accessed: 09-Sep-2021].
- [82] I. Gründer, R. O. Seidl, A. Ernst, and I. Todt, “Relative value of BAHA testing for the postoperative audiological outcome,” *HNO*, vol. 56, no. 10, pp. 1020–1024, Oct. 2008.
- [83] H. F. Tiersten, *Linear Piezoelectric Plate Vibrations- Elements of the Linear Theory of Piezoelectricity and the Vibrations of Piezoelectric Plates*. Springer, 2013.
- [84] S. K. Parashar and U. Von Wagner, “Nonlinear longitudinal vibrations of transversally polarized piezoceramics: Experiments and modeling,” *Nonlinear Dynamics*, vol. 37, no. 1, pp. 51–73, 2004.
- [85] P. Shivashankar and S. B. Kandagal, “Characterization of elastic and electromechanical nonlinearities in piezoceramic plate actuators from vibrations of a piezoelectric-beam,” *Mechanical Systems and Signal Processing*, vol. 116, pp. 624–640, 2019.
- [86] P. Shivashankar, S. Gopalakrishnan, and S. . B. Kandagal, “Nonlinear characterization of piezoelectric patches and piezoelectric stacks from vibrations of piezo-actuated structures,” in *SPIE*, 2019, pp. 1–17.
- [87] P. Shivashankar, S. Gopalakrishnan, and S. B. Kandagal, “Nonlinear modeling of d33-mode piezoelectric actuators using experimental vibration analysis,” *Journal of Sound and Vibration*, vol. 505, 2021.

- [88] U. Von Wagner and P. Hagedorn, “Piezo-beam systems subjected to weak electric field: Experiments and modelling of non-linearities,” *Journal of Sound and Vibration*, vol. 256, no. 5, pp. 861–872, 2002.
- [89] S. N. Mahmoodi and N. Jalili, “Piezoelectrically actuated microcantilevers: An experimental nonlinear vibration analysis,” *Sensors and Actuators A: Physical*, vol. 150, no. 1, pp. 131–136, Mar. 2009.
- [90] F. Goldschmidtboeing, M. Wischke, C. Eichhorn, and P. Woias, “Nonlinear Effects in Piezoelectric Vibration Harvesters,” in *PowerMEMS 2009*, 2009, vol. 1, no. 4, pp. 364–367.
- [91] S. C. Stanton, A. Erturk, B. P. Mann, and D. J. Inman, “Nonlinear piezoelectricity in electroelastic energy harvesters: Modeling and experimental identification,” *Journal of Applied Physics*, vol. 108, no. 7, pp. 1–9, 2010.
- [92] S. C. Stanton, A. Erturk, B. P. Mann, E. H. Dowell, and D. J. Inman, “Nonlinear nonconservative behavior and modeling of piezoelectric energy harvesters including proof mass effects,” *Journal of Intelligent Material Systems and Structures*, vol. 23, no. 2, pp. 183–199, 2012.
- [93] S. Leadenham and A. Erturk, “Unified nonlinear electroelastic dynamics of a bimorph piezoelectric cantilever for energy harvesting, sensing, and actuation,” *Nonlinear Dynamics*, vol. 79, no. 3, pp. 1727–1743, 2014.
- [94] P. Shahabi, H. Ghafarirad, and A. Taghvaeipour, “Nonlinear vibration analysis of piezoelectric bending actuators: Theoretical and experimental studies,” *Comptes Rendus Mécanique*, vol. 347, no. 12, pp. 953–966, Dec. 2019.
- [95] T. Karaağaçlı and H. N. Özgüven, “Experimental modal analysis of nonlinear systems by using response-controlled stepped-sine testing,” *Mechanical Systems and Signal Processing*, vol. 146, Jan. 2021.
- [96] M. Scheel, S. Peter, R. I. Leine, and M. Krack, “A phase resonance approach for modal testing of structures with nonlinear dissipation,” *Journal of Sound*



*and Vibration*, vol. 435, pp. 56–73, Nov. 2018.

- [97] F. Claeysen, R. Le Letty, F. Barillot, and O. Sosnicki, “Amplified Piezoelectric Actuators: Static & Dynamic Applications,” *Ferroelectrics*, vol. 351, no. 1, pp. 3–14, 2007.
- [98] S. Sherrit, A. Trebi-ollennu, R. Bonitz, Y. Bar-cohen, and J. T. Yen, “Compact sensitive piezoelectric mass balance for measurement of unconsolidated materials in space,” in *Sensors and Smart Structures Technologies for Civil, Mechanical, and Aerospace System*, 2010.
- [99] M. A. Cabrera, B. Caicedo, and L. Thorel, “Dynamic actuator for centrifuge modeling of soil-structure interaction,” *Geotechnical Testing Journal*, vol. 35, no. 4, 2012.
- [100] A. Pagès, S. Rowe, S. Duc, O. Sosnicki, G. Jaussaud, and F. Claeysen, “Amplified Piezo Actuators (APA®) Enhancement for Active Vibration Control (AVC),” in *16th International Conference on New Actuators*, 2018, pp. 528–531.
- [101] M. Ling and X. Zhang, “Coupled dynamic modeling of piezo-actuated compliant mechanisms subjected to external loads,” *Mechanism and Machine Theory*, vol. 160, pp. 1–16, 2021.
- [102] T. Karaağaçlı and H. N. Özgüven, “Experimental Identification of Backbone Curves of Strongly Nonlinear Systems by Using Response-Controlled Stepped-Sine Testing (RCT),” *Vibration*, vol. 3, no. 3, pp. 266–280, Sep. 2020.
- [103] T. Karaağaçlı and H. N. Özgüven, “A frequency domain nonparametric identification method for nonlinear structures: Describing surface method,” *Mechanical Systems and Signal Processing*, vol. 144, Oct. 2020.
- [104] D. Damjanovic, “Logarithmic frequency dependence of the piezoelectric effect due to pinning of ferroelectric-ferroelastic domain walls,” *Physical Review B*, vol. 55, no. 2, p. R649, Jan. 1997.

- [105] R. M. Rosenberg, “On Nonlinear Vibrations of Systems with Many Degrees of Freedom,” *Advances in Applied Mechanics*, vol. 9, no. C, pp. 155–242, 1966.
- [106] W. Szemplińska-Stupnicka, “The modified single mode method in the investigations of the resonant vibrations of non-linear systems,” *Journal of Sound and Vibration*, vol. 63, no. 4, pp. 475–489, 1979.
- [107] S. Setio, H. D. Setio, and L. Jezequel, “A method of non-linear modal identification from frequency response tests,” *Journal of Sound and Vibration*, vol. 158, no. 3, pp. 497–515, Nov. 1992.
- [108] C. Gibert, “Fitting measured frequency response using non-linear modes,” *Mechanical Systems and Signal Processing*, vol. 17, no. 1, pp. 211–218, 2003.
- [109] M. Peeters, G. Kerschen, and J. C. Golinval, “Dynamic testing of nonlinear vibrating structures using nonlinear normal modes,” *Journal of Sound and Vibration*, vol. 330, no. 3, pp. 486–509, Jan. 2011.
- [110] J. M. Londoño, S. A. Neild, and J. E. Cooper, “Identification of backbone curves of nonlinear systems from resonance decay responses,” *Journal of Sound and Vibration*, vol. 348, pp. 224–238, Jul. 2015.
- [111] L. Renson, A. Gonzalez-Buelga, D. A. W. Barton, and S. A. Neild, “Robust identification of backbone curves using control-based continuation,” *Journal of Sound and Vibration*, vol. 367, pp. 145–158, Apr. 2016.
- [112] S. Peter and R. I. Leine, “Excitation power quantities in phase resonance testing of nonlinear systems with phase-locked-loop excitation,” *Mechanical Systems and Signal Processing*, vol. 96, pp. 139–158, Nov. 2017.
- [113] M. Krack, “Nonlinear modal analysis of nonconservative systems: Extension of the periodic motion concept,” *Computers & Structures*, vol. 154, pp. 59–71, Jul. 2015.
- [114] M. Scheel, T. Weigle, and M. Krack, “Challenging an experimental nonlinear modal analysis method with a new strongly friction-damped structure,” *Journal*

*of Sound and Vibration*, vol. 485, p. 115580, Oct. 2020.

- [115] T. Karaağaçlı and H. N. Özgüven, “Experimental Quantification and Validation of Modal Properties of Geometrically Nonlinear Structures by Using Response-Controlled Stepped-Sine Testing,” *Experimental Mechanics*, vol. 62, no. 2, pp. 199–211, 2022.
- [116] Ö. Arslan and H. N. Özgüven, “Modal Identification of Non-Linear Structures and the Use of Modal Model in Structural Dynamic Analysis,” in *Proceedings of the 26th International Modal Analysis Conference (IMAC)*, 2008.
- [117] M. Link, M. Boeswald, S. Laborde, M. Weiland, and A. Calvi, “An approach to non-linear experimental modal analysis,” in *Proceedings of the 28th International Modal Analysis Conference (IMAC)*, 2010, pp. 119–128.
- [118] Ö. Tanrikulu, B. Kuran, H. N. Özgüven, and M. İmregün, “Forced Harmonic Response Analysis of Nonlinear Structures,” *AIAA JOURNAL*, vol. 31, no. 7, pp. 1313–1320, 1993.
- [119] M. Krack, “Extension of the single-nonlinear-mode theory by linear attachments and application to exciter-structure interaction,” *Journal of Sound and Vibration*, vol. 505, p. 116120, Aug. 2021.
- [120] B. R. Pacini, R. J. Kuether, and D. R. Roettgen, “Shaker-structure interaction modeling and analysis for nonlinear force appropriation testing,” *Mechanical Systems and Signal Processing*, vol. 162, p. 108000, Jan. 2022.
- [121] L. Renson, A. D. Shaw, D. A. W. Barton, and S. A. Neild, “Application of control-based continuation to a nonlinear structure with harmonically coupled modes,” *Mechanical Systems and Signal Processing*, vol. 120, pp. 449–464, Apr. 2019.
- [122] G. Abeloos, L. Renson, C. Collette, and G. Kerschen, “Stepped and swept control-based continuation using adaptive filtering,” *Nonlinear Dynamics*, vol. 104, no. 4, pp. 3793–3808, Jun. 2021.

- [123] W. D'Ambrogio and A. Fregolent, "The role of interface DoFs in decoupling of substructures based on the dual domain decomposition," *Mechanical Systems and Signal Processing*, vol. 24, no. 7, pp. 2035–2048, 2010.
- [124] T. Kalaycıoğlu and H. N. Özgüven, "FRF decoupling of nonlinear systems," *Mechanical Systems and Signal Processing*, vol. 102, pp. 230–244, Mar. 2018.
- [125] M. B. Özer and H. N. Özgüven, "A New Method For Localization And Identification Of Non-Linearities In Structures," in *6th Biennial Conference on Engineering Systems Design and Analysis*, 2002.
- [126] M. B. Özer, H. N. Özgüven, and T. J. Royston, "Identification of structural nonlinearities using describing functions and the Sherman–Morrison method," *Mechanical Systems and Signal Processing*, vol. 23, no. 1, pp. 30–44, Jan. 2009.
- [127] M. Aykan, D. Systems, T. Division, H. N. Özgüven, D. Systems, and T. Division, "Parametric Identification of Nonlinearity from Incomplete FRF Data Using Describing Function Inversion," in *Proceedings of SEM IMAC XXX Conference*, 2012, pp. 323–334.
- [128] A. Koyuncu, E. Cigeroglu, and H. N. Özgüven, "Localization and identification of structural nonlinearities using cascaded optimization and neural networks," *Mechanical Systems and Signal Processing*, vol. 95, pp. 219–238, 2017.
- [129] J. V Ferreira, "Dynamic Response Analysis of Structures with Nonlinear Components," Ph.D. thesis, Imperial College of Science, Technology and Medicine, 1998.
- [130] H. R. E. Siller, H. Ramon, E. Siller, and H. R. E. Siller, "Non-Linear Modal Analysis Methods For Engineering," Ph.D. thesis, Imperial College London / University of London, 2004.
- [131] A. Tjellström and B. Håkansson, "The bone-anchored hearing aid. Design principles, indications, and long-term clinical results.," *Otolaryngologic clinics of North America*, vol. 28 1, pp. 53–72, 1995.

- [132] A. Tjellström, B. O. Håkansson, and G. Granström, “Bone-anchored hearing aids: Current status in adults and children,” *Otolaryngologic Clinics of North America*, vol. 34, no. 2, pp. 337–364, Apr. 2001.
- [133] M. R. Goldstein, S. Bourn, and A. Jacob, “Early Osia® 2 bone conduction hearing implant experience: Nationwide controlled-market release data and single-center outcomes,” *American Journal of Otolaryngology - Head and Neck Medicine and Surgery*, vol. 42, no. 1, 2021.
- [134] S. K. Plontke, G. Götze, C. Wenzel, T. Rahne, and R. Mlynski, “Implantation of a new active bone conduction hearing device with optimized geometry,” *HNO*, vol. 68, no. July, pp. 106–115, Aug. 2020.
- [135] S. Arndt, A. K. Rauch, and I. Speck, “Active transcutaneous bone-anchored hearing implant: how I do it,” *European Archives of Oto-Rhino-Laryngology*, vol. 278, no. 10, pp. 4119–4122, 2021.
- [136] A. Koyuncu, T. Karaağaçlı, M. Şahin, and H. N. Özgüven, “Experimental Modal Analysis of Nonlinear Amplified Piezoelectric Actuators by Using Response Controlled Stepped-Sine Testing,” *Experimental Mechanics*, pp. 1–16, 2022.
- [137] S. P. Stenfelt and B. E. Håkansson, “A miniaturized artificial mastoid using a skull simulator.,” *Scandinavian audiology*, vol. 27, no. 2, pp. 67–76, 1998.
- [138] “Total harmonic distortion - Wikipedia.” [Online]. Available: [https://en.wikipedia.org/wiki/Total\\_harmonic\\_distortion](https://en.wikipedia.org/wiki/Total_harmonic_distortion). [Accessed: 10-Aug-2022].
- [139] “IEC 60373:1990 Mechanical Coupler For Measurements of Bone Vibrator.” [Online]. Available: [https://infostore.saiglobal.com/en-us/standards/iec-60373-1990-563148\\_saig\\_iec\\_iec\\_1284445/](https://infostore.saiglobal.com/en-us/standards/iec-60373-1990-563148_saig_iec_iec_1284445/). [Accessed: 10-Aug-2022].
- [140] K. J. F. Jansson, B. Håkansson, C. Rigato, M. Eeg-Olofsson, and S. Reinfeldt, “Robustness and lifetime of the bone conduction implant – a pilot study,”

*Medical Devices: Evidence and Research*, vol. 12, pp. 89–100, 2019.

- [141] H. Bernhard, “Design Methodology and Innovative Device Concept for Acoustic Hearing Implants,” EPFL, 2011.

## APPENDICES

### A. Boundary Conditions of the RCM

Displacement boundary conditions of the first and the last beam is given in Eqs.(A.1) and (A.2).

$$u_1(0,t) = 0, \quad (\text{A.1})$$

$$u_9(L_9,t) = 0. \quad (\text{A.2})$$

For the fixed-free boundary conditions of the RCM, an additional boundary condition equation is introduced as follows

$$w_1(0,t) = 0. \quad (\text{A.3})$$

The continuity of displacements at intermediate beam connections are given in Eqs.(A.4) and (A.5).

$$u_i(L_i,t) = \cos(\theta_{i+1}) \left( u_{i+1}(0,t) - e_{i+1} \frac{\partial w_{i+1}(x_{i+1},t)}{\partial x_{i+1}} \Big|_{x_{i+1}=0} \right) + \sin(\theta_{i+1}) w_{i+1}(0,t) \quad i = 1, 2, \dots, 8 \quad (\text{A.4})$$

$$w_i(L_i, t) = \cos(\theta_{i+1})w_{i+1}(0, t) - \sin(\theta_{i+1}) \left( u_{i+1}(0, t) - e_{i+1} \frac{\partial w_{i+1}(x_{i+1}, t)}{\partial x_{i+1}} \Big|_{x_{i+1}=0} \right) \quad i = 1, 2, \dots, 8 \quad (\text{A.5})$$

Axial force, shear force, and bending moment compatibility conditions at the joint connections are given in the following equations, respectively.

$$EA_i \frac{\partial u_i(x_i, t)}{\partial x_i} \Big|_{x_i=L_i} = \cos(\theta_{i+1})EA_{i+1} \frac{\partial u_{i+1}(x_{i+1}, t)}{\partial x_{i+1}} \Big|_{x_{i+1}=0} - \sin(\theta_{i+1})EI_{i+1} \frac{\partial^3 w_{i+1}(x_{i+1}, t)}{\partial x_{i+1}^3} \Big|_{x_{i+1}=0} \quad i = 1, 2, \dots, 8 \quad (\text{A.6})$$

$$EI_i \frac{\partial^3 w_i(x_i, t)}{\partial x_i^3} \Big|_{x_i=L_i} = \cos(\theta_{i+1})EI_{i+1} \frac{\partial^3 w_{i+1}(x_{i+1}, t)}{\partial x_{i+1}^3} \Big|_{x_{i+1}=0} + \sin(\theta_{i+1})EA_{i+1} \frac{\partial u_{i+1}(x_{i+1}, t)}{\partial x_{i+1}} \Big|_{x_{i+1}=0} \quad i = 1, 2, \dots, 8 \quad (\text{A.7})$$

$$EI_i \frac{\partial^2 w_i(x_i, t)}{\partial x_i^2} \Big|_{x_i=L_i} = EI_{i+1} \frac{\partial^2 w_{i+1}(x_{i+1}, t)}{\partial x_{i+1}^2} \Big|_{x_{i+1}=0} + e_{i+1}EA_{i+1} \frac{\partial u_{i+1}(x_{i+1}, t)}{\partial x_{i+1}} \Big|_{x_{i+1}=0} \quad i = 1, 2, \dots, 8 \quad (\text{A.8})$$

The shear force boundary condition of the last beam is given in Eq.(A.9).

$$EI_9 \frac{\partial^3 w_9(x_9, t)}{\partial x_9^3} \Big|_{x_9=L_9} = 0 \quad (\text{A.9})$$

For the fixed-free boundary conditions of the RCM, an additional shear force boundary



condition is defined instead of the boundary condition equation in Eq.(A.3).

$$EI_1 \frac{\partial^3 w_1(x_1, t)}{\partial x_1^3} \Big|_{x_1=0} = 0 \quad (\text{A.10})$$

Slope boundary conditions of the first and the last beam are given in Eqs.(A.11) and (A.12).

$$\frac{\partial w_1(x_1, t)}{\partial x_1} \Big|_{x_1=0} = 0, \quad (\text{A.11})$$

$$\frac{\partial w_9(x_9, t)}{\partial x_9} \Big|_{x_9=L_9} = 0. \quad (\text{A.12})$$

Continuity of angular deformations at the beam ends is given in Eq.(A.13).

$$\frac{\partial w_{i+1}(x_{i+1}, t)}{\partial x_{i+1}} \Big|_{x_{i+1}=0} - \frac{\partial w_i(x_i, t)}{\partial x_i} \Big|_{x_i=L_i} = 0 \quad i = 1, 2, \dots, 8. \quad (\text{A.13})$$



## B. Derivation of the Transfer Matrices of the RCM

Derivatives of eigenfunctions is given in Eqs.(B.1)-(B.4) as follows

$$\frac{dU_i(x_i)}{dx_i} = -\lambda^2 c_1^i \sin(\lambda^2 x_i) + \lambda^2 c_2^i \cos(\lambda^2 x_i), \quad (\text{B.1})$$

$$\begin{aligned} \frac{dW_i(x_i)}{dx_i} = & C_i \lambda d_1^i \sinh(C_i \lambda x_i) + C_i \lambda d_2^i \cosh(C_i \lambda x_i), \\ & - C_i \lambda d_3^i \sin(C_i \lambda x_i) + C_i \lambda d_4^i \cos(C_i \lambda x_i), \end{aligned} \quad (\text{B.2})$$

$$\begin{aligned} \frac{d^2 W_i(x_i)}{dx_i^2} = & (C_i \lambda)^2 d_1^i \cosh(C_i \lambda x_i) + (C_i \lambda)^2 d_2^i \sinh(C_i \lambda x_i), \\ & - (C_i \lambda)^2 d_3^i \cos(C_i \lambda x_i) - (C_i \lambda)^2 d_4^i \sin(C_i \lambda x_i), \end{aligned} \quad (\text{B.3})$$

$$\begin{aligned} \frac{d^3 W_i(x_i)}{dx_i^3} = & (C_i \lambda)^3 d_1^i \sinh(C_i \lambda x_i) + (C_i \lambda)^3 d_2^i \cosh(C_i \lambda x_i), \\ & (C_i \lambda)^3 d_3^i \sin(C_i \lambda x_i) - (C_i \lambda)^3 d_4^i \cos(C_i \lambda x_i). \end{aligned} \quad (\text{B.4})$$

Boundary condition equations at the intermediate beam connections are given in Eqs.(B.5)-(B.8).

$$U_i(L_i) = \cos(\theta_{i+1}) \left( U_{i+1}(0) - e_{i+1} \frac{dW_{i+1}(x)}{dx} \Big|_{x=0} \right) + \sin(\theta_{i+1}) W_{i+1}(0) \quad i = 1, \dots, 8, \quad (\text{B.5})$$

$$W_i(L_i) = \cos(\theta_{i+1}) W_{i+1}(0) - \sin(\theta_{i+1}) \left( U_{i+1}(0) - e_{i+1} \frac{dW_{i+1}(x)}{dx} \Big|_{x=0} \right) \quad i = 1, \dots, 8. \quad (\text{B.6})$$

$$\begin{aligned} \left. \frac{dU_i(x)}{dx} \right|_{x=L_i} &= \cos(\theta_{i+1}) \frac{A_{i+1}}{A_i} \left. \frac{dU_{i+1}(x)}{dx} \right|_{x=0} \\ &\quad - \sin(\theta_{i+1}) \frac{I_{i+1}}{A_i} \left. \frac{d^3W_{i+1}(x)}{dx^3} \right|_{x=0} \end{aligned} \quad , \quad i = 1 \dots, 8 \quad (\text{B.7})$$

$$\left. \frac{dW_i(x)}{dx} \right|_{x=L_i} = \left. \frac{dW_{i+1}(x)}{dx} \right|_{x=0} \quad i = 1 \dots, 8, \quad (\text{B.8})$$

$$\begin{aligned} \left. \frac{d^3W_i(x)}{dx^3} \right|_{x=L_i} &= \cos(\theta_{i+1}) \frac{I_{i+1}}{I_i} \left. \frac{d^3W_{i+1}(x,t)}{dx^3} \right|_{x=0} \\ &\quad + \sin(\theta_{i+1}) \frac{A_{i+1}}{I_i} \left. \frac{dU_{i+1}(x)}{dx} \right|_{x=0} \end{aligned} \quad , \quad i = 1 \dots, 8 \quad (\text{B.9})$$

$$\left. \frac{d^2W_i(x)}{dx^2} \right|_{x=L_i} = \frac{I_{i+1}}{I_i} \left. \frac{d^2W_{i+1}(x)}{dx^2} \right|_{x=0} + e_{i+1} \frac{A_{i+1}}{I_i} \left. \frac{dU_{i+1}(x)}{dx} \right|_{x=0} \quad i = 1 \dots, 8. \quad (\text{B.10})$$

Boundary condition equations of the first beam segment for fixed-free and free-free cases are given in Eqs.(B.11)-(B.13).

$$\text{Fixed-free: } U_1(0) = 0$$

$$\text{Free-free: } \left. \frac{d^3W_1(x_1)}{dx_1^3} \right|_{x_1=0} = 0, \quad (\text{B.11})$$

$$W_1(0) = 0, \quad (\text{B.12})$$

$$\left. \frac{dW_1(x_1)}{dt} \right|_{x_1=0} = 0. \quad (\text{B.13})$$

The constants of the first beam segment (Table B.1) are determined for fixed-free and free-free cases by inserting Eqs.(2.9) and (2.10) into boundary condition equations which are Eqs.(B.11)-(B.13) given above.

**Table B.1** The constants of the first beam segment for the fixed-free and free-free conditions

Fixed-free case	Free-free case
$c_1^1 = 0$	$c_1^1 = 0$
$d_1^1 + d_3^1 = 0$	$d_2^1 = 0$
$d_2^1 + d_4^1 = 0$	$d_4^1 = 0$

The vector of the first beam constants can be expressed as follows for fixed-free and free-free cases in Eq.(B.14) and Eq.(B.15), respectively.

$$\begin{Bmatrix} 0 \\ c_2 \\ d_1 \\ d_2 \\ -d_1 \\ -d_2 \end{Bmatrix}^1 = \begin{bmatrix} 0 & 0 & 0 \\ 1 & 0 & 0 \\ 0 & 1 & 0 \\ 0 & 0 & 1 \\ 0 & -1 & 0 \\ 0 & 0 & -1 \end{bmatrix} \begin{Bmatrix} c_2 \\ d_1 \\ d_2 \end{Bmatrix}^1 = \bar{\Lambda}_1(\lambda) \begin{Bmatrix} c_2 \\ d_1 \\ d_2 \end{Bmatrix}^1, \quad (\text{B.14})$$

$$\begin{Bmatrix} 0 \\ c_2 \\ d_1 \\ 0 \\ d_3 \\ 0 \end{Bmatrix}^1 = \begin{bmatrix} 0 & 0 & 0 \\ 1 & 0 & 0 \\ 0 & 1 & 0 \\ 0 & 0 & 0 \\ 0 & 0 & 1 \\ 0 & 0 & 0 \end{bmatrix} \begin{Bmatrix} c_2 \\ d_1 \\ d_3 \end{Bmatrix}^1 = \bar{\Lambda}_1(\lambda) \begin{Bmatrix} c_2 \\ d_1 \\ d_3 \end{Bmatrix}^1. \quad (\text{B.15})$$

where  $\bar{\Lambda}_1(\lambda)$  is the transfer matrix between the full constant vector and the non-trivial constant vector of the first beam segment. Boundary condition equations of the last beam segment are given in Eqs.(B.16)-(B.18).

$$U_9(L_9) = 0, \tag{B.16}$$

$$\left. \frac{dW_9(x)}{dt} \right|_{x=L_9} = 0, \tag{B.17}$$

$$\left. \frac{d^3W_9(x)}{dx^3} \right|_{x=L_9} = 0. \tag{B.18}$$

Eqs.(B.16), (B.17), and (B.18) are written in matrix form as follows

$$\bar{\Lambda}_9(\lambda) \begin{Bmatrix} c_1 \\ c_2 \\ d_1 \\ d_2 \\ d_3 \\ d_4 \end{Bmatrix}^9 = \begin{Bmatrix} 0 \\ 0 \\ 0 \end{Bmatrix}, \quad (\text{B.19})$$

where  $\bar{\Lambda}_9(\lambda)$  is the transfer matrix between the full constant vector and the non-trivial constant vector of the last beam segment given in

$$\bar{\Lambda}_9(\lambda) = \begin{bmatrix} \cos(\lambda^2 L_9) & \sin(\lambda^2 L_9) & 0 & 0 & 0 & 0 \\ 0 & 0 & C_9 \lambda \sinh(C_9 \lambda L_9) & C_9 \lambda \cosh(C_9 \lambda L_9) & -C_9 \lambda \sin(C_9 \lambda L_9) & C_9 \lambda \cos(C_9 \lambda L_9) \\ 0 & 0 & (C_9 \lambda)^3 \sinh(C_9 \lambda L_9) & (C_9 \lambda)^3 \cosh(C_9 \lambda L_9) & (C_9 \lambda)^3 \sin(C_9 \lambda L_9) & -(C_9 \lambda)^3 \cos(C_9 \lambda L_9) \end{bmatrix}. \quad (\text{B.20})$$

Eqs.(B.1)-(B.4) are written in matrix form in Eq.(B.21).

$$\left\{ \begin{array}{l} U_i(L_i) \\ W_i(L_i) \\ U_i'(L_i) \\ W_i'(L_i) \\ W_i''(L_i) \\ W_i'''(L_i) \end{array} \right\} = \mathbf{B}_i(\lambda) \left\{ \begin{array}{l} c_1 \\ c_2 \\ d_1 \\ d_2 \\ d_3 \\ d_4 \end{array} \right\}, \quad (\text{B.21})$$

where  $\mathbf{B}_i(\lambda)$  is the transfer matrix between the constant vector and eigenfunction state vector for  $i^{\text{th}}$  beam segment



$$\mathbf{B}_i(\lambda) = \begin{bmatrix} \cos(\lambda^2 L_i) & \sin(\lambda^2 L_i) & 0 & 0 & 0 & 0 \\ 0 & 0 & \cosh(C_i \lambda L_i) & \sinh(C_i \lambda L_i) & \cos(C_i \lambda L_i) & \sin(C_i \lambda L_i) \\ -\lambda^2 \sin(\lambda^2 L_i) & \lambda^2 \cos(\lambda^2 L_i) & 0 & 0 & 0 & 0 \\ 0 & 0 & C_i \lambda \sinh(C_i \lambda L_i) & C_i \lambda \cosh(C_i \lambda L_i) & -C_i \lambda \sin(C_i \lambda L_i) & C_i \lambda \cos(C_i \lambda L_i) \\ 0 & 0 & (C_i \lambda)^2 \cosh(C_i \lambda L_i) & (C_i \lambda)^2 \sinh(C_i \lambda L_i) & -(C_i \lambda)^2 \cos(C_i \lambda L_i) & -(C_i \lambda)^2 \sin(C_i \lambda L_i) \\ 0 & 0 & (C_i \lambda)^3 \sinh(C_i \lambda L_i) & (C_i \lambda)^3 \cosh(C_i \lambda L_i) & (C_i \lambda)^3 \sin(C_i \lambda L_i) & -(C_i \lambda)^3 \cos(C_i \lambda L_i) \end{bmatrix}. \quad (\text{B.22})$$

After making necessary substitutions, Eqs.(B.5)-(B.10) can be written in matrix form

$$\left\{ \begin{array}{l} U_i(L_i) \\ W_i(L_i) \\ U'_i(L_i) \\ W'_i(L_i) \\ W''_i(L_i) \\ W'''_i(L_i) \end{array} \right\} = \mathbf{T}_{i+1}(\lambda) \left\{ \begin{array}{l} c_1 \\ c_2 \\ d_1 \\ d_2 \\ d_3 \\ d_4 \end{array} \right\}^{i+1}, \quad (\text{B.23})$$

where  $\mathbf{T}_{i+1}(\lambda)$  is the transfer matrix between the constant vector of  $(i+1)^{th}$  beam segment and eigenfunction state vector of the  $i^{th}$  beam segment

$$\mathbf{T}_{i+1}(\lambda) = \begin{bmatrix} \cos(\alpha_{i+1}) & 0 & \sin(\alpha_{i+1}) & -\cos(\alpha_{i+1})e_{i+1}C_{i+1}\lambda & \sin(\alpha_{i+1}) & -\cos(\alpha_{i+1})e_{i+1}C_{i+1}\lambda \\ -\sin(\alpha_{i+1}) & 0 & \cos(\alpha_{i+1}) & \sin(\alpha_{i+1})e_{i+1}C_{i+1}\lambda & \cos(\alpha_{i+1}) & \sin(\alpha_{i+1})e_{i+1}C_{i+1}\lambda \\ 0 & \cos(\alpha_{i+1})\frac{A_{i+1}}{A_i}\lambda^2 & 0 & -\sin(\alpha_{i+1})\frac{I_{i+1}}{A_i}(C_{i+1}\lambda)^3 & 0 & \sin(\alpha_{i+1})\frac{I_{i+1}}{A_i}(C_{i+1}\lambda)^3 \\ 0 & 0 & 0 & C_{i+1}\lambda & 0 & C_{i+1}\lambda \\ 0 & e_{i+1}\frac{A_{i+1}}{I_i}\lambda^2 & \frac{I_{i+1}}{I_i}(C_{i+1}\lambda)^2 & 0 & -\frac{I_{i+1}}{I_i}(C_{i+1}\lambda)^2 & 0 \\ 0 & \sin(\alpha_{i+1})\frac{A_{i+1}}{I_i}\lambda^2 & 0 & \cos(\alpha_{i+1})\frac{I_{i+1}}{I_i}(C_{i+1}\lambda)^3 & 0 & -\cos(\alpha_{i+1})\frac{I_{i+1}}{I_i}(C_{i+1}\lambda)^3 \end{bmatrix}. \quad (\text{B.24})$$

Receptance matrix of the RCM approximated by 4-DOF

$$\mathbf{H}_{RCM}(\omega) = \sum_{r=1}^K \frac{1}{k_r - \omega^2 m_r + i\omega c_r} \times \begin{bmatrix} W_{9r}(L_9)^2 & W_{9r}(L_9)U_{5r}\left(\frac{L_5}{2}\right) & W_{9r}(L_9)W_{5r}\left(\frac{L_5}{2}\right) & W_{9r}(L_9)W'_{5r}\left(\frac{L_5}{2}\right) \\ U_{5r}\left(\frac{L_5}{2}\right)W_{9r}(L_9) & U_{5r}\left(\frac{L_5}{2}\right)^2 & U_{5r}\left(\frac{L_5}{2}\right)W_{5r}\left(\frac{L_5}{2}\right) & U_{5r}\left(\frac{L_5}{2}\right)W'_{5r}\left(\frac{L_5}{2}\right) \\ W_{5r}\left(\frac{L_5}{2}\right)W_{9r}(L_9) & W_{5r}\left(\frac{L_5}{2}\right)U_{5r}\left(\frac{L_5}{2}\right) & W_{5r}\left(\frac{L_5}{2}\right)^2 & W_{5r}\left(\frac{L_5}{2}\right)W'_{5r}\left(\frac{L_5}{2}\right) \\ W'_{5r}\left(\frac{L_5}{2}\right)W_{9r}(L_9) & W'_{5r}\left(\frac{L_5}{2}\right)U_{5r}\left(\frac{L_5}{2}\right) & W'_{5r}\left(\frac{L_5}{2}\right)W_{5r}\left(\frac{L_5}{2}\right) & W'_{5r}\left(\frac{L_5}{2}\right)^2 \end{bmatrix} \cdot \quad (\text{B.25})$$



### C. Proof of the Normal Mode Orthogonality for the RCM

$U_{ir}$  and  $U_{is}$  are the  $r^{th}$  and  $s^{th}$  eigenfunctions of Eq.(2.4) , which satisfy Eq.(C.1) and Eq.(C.2), respectively.

$$U_{ir}(x_i)'' + \lambda_r^4 U_{ir}(x_i) = 0, \quad (C.1)$$

$$U_{is}(x_i)'' + \lambda_s^4 U_{is}(x_i) = 0. \quad (C.2)$$

Eq (C.3) is obtained by multiplying Eq.(C.1) with  $U_{is}$  and integrating from 0 to  $L_i$  as follows

$$U_{ir}(x_i)' U_{is}(x_i) \Big|_0^{L_i} - \int_0^{L_i} U_{ir}(x_i)' U_{is}(x_i)' dx + \lambda_r^4 \int_0^{L_i} U_{ir}(x_i) U_{is}(x_i) dx = 0. \quad (C.3)$$

A similar procedure is applied to Eq.(C.2).

$$U_{is}(x_i)' U_{ir}(x_i) \Big|_0^{L_i} - \int_0^{L_i} U_{ir}(x_i)' U_{is}(x_i)' dx + \lambda_s^4 \int_0^{L_i} U_{ir}(x_i) U_{is}(x_i) dx = 0. \quad (C.4)$$

$W_{ir}$  and  $W_{is}$  are the  $r^{th}$  and  $s^{th}$  eigenfunctions of Eq.(2.5) which satisfy Eq.(C.5) and Eq.(C.6).

$$W_{ir}(x_i)'''' - C_i^4 \lambda_r^4 W_{ir}(x_i) = 0, \quad (C.5)$$

$$W_{is}(x_i)'''' - C_i^4 \lambda_s^4 W_{is}(x_i) = 0. \quad (C.6)$$

Eq (C.7) is obtained by multiplying Eq.(C.5) with  $W_{is}$  and integrating from 0 to  $L_i$ .

$$\begin{aligned}
& W_{ir}(x_i)''' W_{is}(x_i) \Big|_0^{L_i} - W_{ir}(x_i)'' W_{is}'(x_i) \Big|_0^{L_i} \\
& + \int_0^{L_i} W_{ir}(x_i)'' W_{is}''(x_i) dx_i - C_i^4 \lambda_r^4 \int_0^{L_i} W_{ir}(x_i) W_{is}(x_i) dx_i = 0
\end{aligned} \tag{C.7}$$

A similar procedure is applied to Eq.(C.8) as follows

$$\begin{aligned}
& W_{is}(x_i)''' W_{ir}(x_i) \Big|_0^{L_i} - W_{is}(x_i)'' W_{ir}'(x_i) \Big|_0^{L_i} \\
& + \int_0^{L_i} W_{ir}(x_i)'' W_{is}''(x_i) dx_i - C_i^4 \lambda_s^4 \int_0^{L_i} W_{ir}(x_i) W_{is}(x_i) dx_i = 0
\end{aligned} \tag{C.8}$$

Eq.(C.3) is multiplied with  $C_i^4$  and substituted from Eq.(C.7).

$$\begin{aligned}
& W_{ir}(x_i)''' W_{is}(x_i) \Big|_0^{L_i} - W_{ir}(x_i)'' W_{is}'(x_i) \Big|_0^{L_i} - C_i^4 U_{ir}(x_i)' U_{is}(x_i) \Big|_0^{L_i} \\
& \int_0^{L_i} \left( W_{ir}(x_i)'' W_{is}''(x_i) + C_i^4 U_{ir}(x_i)' U_{is}(x_i)' \right) dx_i \\
& - C_i^4 \lambda_r^4 \int_0^{L_i} \left( W_{ir}(x_i) W_{is}(x_i) + U_{ir}(x_i) U_{is}(x_i) \right) dx_i = 0
\end{aligned} \tag{C.9}$$

The first three terms of Eq.(C.9) are rewritten in Eq.(C.10).

$$\begin{aligned}
& W_{ir}(x_i)''' W_{is}(x_i) \Big|_0^{L_i} - W_{ir}(x_i)'' W_{is}'(x_i) \Big|_0^{L_i} - C_i^4 U_{ir}(x_i)' U_{is}(x_i) \Big|_0^{L_i} \\
& = -\frac{A_i}{I_i} U_{ir}(L_i)' U_{is}(L_i) + \frac{A_i}{I_i} U_{ir}(0)' U_{is}(0) + W_{ir}(L_i)''' W_{is}(L_i) \\
& - W_{ir}(0)''' W_{is}(0) - W_{ir}(L_i)'' W_{is}'(L_i) + W_{ir}(0)'' W_{is}'(0)
\end{aligned} \tag{C.10}$$

The terms of Eq.(C.9) are expanded by making necessary substitutions Eqs (C.11)-(C.13).

$$U_{ir}'U_{is}^{(x_i=L_i)} = \left( \cos(\theta_{i+1}) \frac{A_{i+1}}{A_i} \frac{dU_{i+1,r}(x_{i+1})}{dx} \Big|_{x_{i+1}=0} - \sin(\theta_{i+1}) \frac{I_{i+1}}{A_i} \frac{d^3W_{i+1,r}(v)}{dx_{i+1}^3} \Big|_{x_{i+1}=0} \right) \times \left( \cos(\theta_{i+1}) \left( U_{i+1}(0) - e_{i+1} \frac{dW_{i+1,s}(x_{i+1})}{dx_{i+1}} \Big|_{x_{i+1}=0} \right) + \sin(\theta_{i+1}) W_{i+1,s}(0) \right), \quad (C.11)$$

$$W_{ir}'''W_{is}^{(x_i=L_i)} = \left( \cos(\theta_{i+1}) \frac{I_{i+1}}{I_i} \frac{d^3W_{i+1,r}(x_{i+1},t)}{dx_{i+1}^3} \Big|_{x=0} + \sin(\theta_{i+1}) \frac{A_{i+1}}{I_i} \frac{dU_{i+1,r}(x_{i+1})}{dx_{i+1}} \Big|_{x_{i+1}=0} \right) \times \left( \cos(\theta_{i+1}) W_{i+1,s}(0) - \sin(\theta_{i+1}) \left( U_{i+1,s}(0) - e_{i+1} \frac{dW_{i+1,s}(x_{i+1})}{dx_{i+1}} \Big|_{x_{i+1}=0} \right) \right), \quad (C.12)$$

$$W_{ir}''W_{is}'^{(x_i=L_i)} = \left( \frac{I_{i+1}}{I_i} \frac{d^2W_{i+1,r}(x_{i+1})}{dx_{i+1}^2} \Big|_{x_{i+1}=0} + e_{i+1} \frac{A_{i+1}}{I_i} \frac{dU_{i+1,r}(x_{i+1})}{dx_{i+1}} \Big|_{x_{i+1}=0} \right) \frac{dW_{i+1,s}(x_{i+1})}{dx_{i+1}} \Big|_{x_{i+1}=0}. \quad (C.13)$$

The terms of Eq.(C.10) which are the integral evaluations at  $L_i$  are collected on the left side of Eq.(C.14). Eqs.(C.11)-(C.13) are substituted with these terms on the right side of Eq.(C.14).

$$\begin{aligned}
& W_{ir}(L_i)''' W_{is}(L_i) - W_{ir}(L_i)'' W_{is}'(L_i) - \frac{A_i}{I_i} U_{ir}(L_i)' U_{is}(L_i) \\
&= \cos(\alpha_{i+1})^2 \frac{I_{i+1}}{I_i} \frac{d^3 W_{i+1,r}(x_{i+1}, t)}{dx_{i+1}^3} \Big|_{x_{i+1}=0} W_{i+1,s}(0) \\
&\quad - \sin(\alpha_{i+1})^2 \frac{A_{i+1}}{I_i} \frac{dU_{i+1,r}(x_{i+1})}{dx_{i+1}} \Big|_{x_{i+1}=0} \left( U_{i+1,s}(0) - e_{i+1} \frac{dW_{i+1,s}(x_{i+1})}{dx_{i+1}} \Big|_{x_{i+1}=0} \right) \\
&\quad + \sin(\alpha_{i+1}) \cos(\alpha_{i+1}) \frac{A_{i+1}}{I_i} \frac{dU_{i+1,r}(x_{i+1})}{dx_{i+1}} \Big|_{x_{i+1}=0} W_{i+1,s}(0) \\
&\quad - \sin(\alpha_{i+1}) \cos(\alpha_{i+1}) \frac{I_{i+1}}{I_i} \frac{d^3 W_{i+1,r}(x_{i+1}, t)}{dx_{i+1}^3} \Big|_{x=0} \left( U_{i+1,s}(0) - e_{i+1} \frac{dW_{i+1,s}(x_{i+1})}{dx_{i+1}} \Big|_{x_{i+1}=0} \right) \\
&\quad - \frac{I_{i+1}}{I_i} \frac{d^2 W_{i+1,r}(x_{i+1})}{dx_{i+1}^2} \Big|_{x_{i+1}=0} \frac{dW_{i+1,s}(x_{i+1})}{dx_{i+1}} \Big|_{x_{i+1}=0} \\
&\quad - e_{i+1} \frac{A_{i+1}}{I_i} \frac{dU_{i+1,r}(x_{i+1})}{dx_{i+1}} \Big|_{x_{i+1}=0} \frac{dW_{i+1,s}(x_{i+1})}{dx_{i+1}} \Big|_{x_{i+1}=0} \\
&\quad - \sin(\alpha_{i+1}) \cos(\alpha_{i+1}) \frac{A_{i+1}}{I_i} \frac{dU_{i+1,r}(x_{i+1})}{dx_{i+1}} \Big|_{x_{i+1}=0} W_{i+1,s}(0) \\
&\quad + \sin(\alpha_{i+1})^2 \frac{I_{i+1}}{I_i} \frac{d^3 W_{i+1,r}(x_{i+1})}{dx_{i+1}^3} \Big|_{x_{i+1}=0} W_{i+1,s}(0) \\
&\quad - \cos(\alpha_{i+1})^2 \frac{A_{i+1}}{I_i} \frac{dU_{i+1,r}(x_{i+1})}{dx_{i+1}} \Big|_{x_{i+1}=0} \left( U_{i+1}(0) - e_{i+1} \frac{dW_{i+1,s}(x_{i+1})}{dx_{i+1}} \Big|_{x_{i+1}=0} \right) \\
&\quad + \sin(\alpha_{i+1}) \cos(\alpha_{i+1}) \frac{I_{i+1}}{I_i} \frac{d^3 W_{i+1,r}(x_{i+1})}{dx_{i+1}^3} \Big|_{x=0} \left( U_{i+1}(0) - e_{i+1} \frac{dW_{i+1,s}(x_{i+1})}{dx_{i+1}} \Big|_{x_{i+1}=0} \right) \\
&= \frac{I_{i+1}}{I_i} \frac{d^3 W_{i+1,r}(x_{i+1}, t)}{dx_{i+1}^3} \Big|_{x_{i+1}=0} W_{i+1,s}(0) - \frac{A_{i+1}}{I_i} \frac{dU_{i+1,r}(x_{i+1})}{dx_{i+1}} \Big|_{x_{i+1}=0} U_{i+1,s}(0) \\
&\quad - \frac{I_{i+1}}{I_i} \frac{d^2 W_{i+1,r}(x_{i+1})}{dx_{i+1}^2} \Big|_{x_{i+1}=0} \frac{dW_{i+1,s}(x_{i+1})}{dx_{i+1}} \Big|_{x_{i+1}=0} . \tag{C.14}
\end{aligned}$$



Eq.(C.10) is rewritten for the  $(i + 1)^{th}$  beam.

$$\begin{aligned}
& W_{i+1,r}(x_{i+1})''' W_{i+1,s}(x_{i+1}) \Big|_0^{L_{i+1}} - W_{i+1,r}(x_{i+1})'' W_{i+1,s}'(x_{i+1}) \Big|_0^{L_{i+1}} \\
& - C_{i+1}^4 U_{i+1,r}(x_{i+1})' U_{i+1,s}(x_{i+1}) \Big|_0^{L_{i+1}} \\
& = \frac{A_{i+1}}{I_{i+1}} U_{i+1,r}(L_{i+1})' U_{i+1,s}(L_{i+1}) - \frac{A_{i+1}}{I_{i+1}} U_{i+1,r}(0)' U_{i+1,s}(0) . \\
& + W_{i+1,r}(L_{i+1})''' W_{i+1,s}(L_{i+1}) - W_{i+1,r}(0)''' W_{i+1,s}(0) \\
& - W_{i+1,r}(L_{i+1})'' W_{i+1,s}'(L_{i+1}) + W_{i+1,r}(0)'' W_{i+1,s}'(0)
\end{aligned} \tag{C.15}$$

It can be easily seen that if Eq.(C.14) and Eq.(C.15) are multiplied with  $I_i$  and  $I_{i+1}$  respectively and added, some of the terms will cancel each other. If Eq.(C.9) for each beam is added up, all the terms coming from intermediate boundary conditions will vanish. Hence, orthogonality of the eigenfunctions can be check using Eq.(C.16) and Eq.(C.17).

$$\begin{aligned}
& \sum_{i=1}^9 \int_0^{L_i} \left( I_i W_{ir}(x_i)'' W_{is}''(x_i) + A_i U_{ir}(x_i)' U_{is}(x_i)' \right) dx \\
& - \lambda_r^4 \sum_{i=1}^9 \int_0^{L_i} \left( A_i W_{ir}(x_i) W_{is}(x_i) + A_i U_{ir}(x_i) U_{is}(x_i) \right) dx = 0
\end{aligned} \tag{C.16}$$

$$\begin{aligned}
& \sum_{i=1}^9 \int_0^{L_i} \left( I_i W_{is}(x_i)'' W_{ir}''(x_i) + A_i U_{is}(x_i)' U_{ir}(x_i)' \right) dx_i \\
& - \lambda_s^4 \sum_{i=1}^9 \int_0^{L_i} \left( A_i W_{is}(x_i) W_{ir}(x_i) + A_i U_{is}(x_i) U_{ir}(x_i) \right) dx_i = 0
\end{aligned} \tag{C.17}$$

Finally, it is shown that the conditions given in Eq.(C.18) (C.19) are satisfied by using the property of normal mode orthogonality for the RCM.

$$\sum_{i=1}^9 \int_0^{L_i} \left( I_i W_{ir}''(x_i) W_{is}''(x_i) + A_i U_{ir}'(x_i) U_{is}'(x_i) \right) dx_i = 0 \text{ for } r \neq s, \quad (\text{C.18})$$

$$\sum_{i=1}^9 \left( \int_0^{L_i} A_i (W_{ir}(x_i) W_{is}(x_i) + U_{ir}(x_i) U_{is}(x_i)) dx_i \right) = 0 \text{ for } r \neq s. \quad (\text{C.19})$$

## D. Derivation Of The Transfer Matrices of the MSPA

The eigenvalue problem of the MSPA in the longitudinal and the transverse directions are given in Eqs.(D.1) and (D.2), respectively.

$$\rho_p A_p \frac{\partial^2 u_p(x_p, t)}{\partial t^2} = E_p A_p \frac{\partial^2 u_p(x_p, t)}{\partial x_p^2} \quad , \quad (D.1)$$

$$E_p I_p \frac{\partial^4 w_p(x_p, t)}{\partial x_p^4} + \rho_p A_p \frac{\partial^2 w_p(x_p, t)}{\partial t^2} = 0 \quad . \quad (D.2)$$

The longitudinal and transverse displacements of the MSPA are assumed to be in separable form given in Eqs.(D.3) and (D.4).

$$U_p(x_p) = c_1^p \cos(\lambda_p^2 x_p) + c_2^p \sin(\lambda_p^2 x_p), \quad (D.3)$$

$$W_p(x_p) = d_1^p \cosh(C_p \lambda_p x_p) + d_2^p \sinh(C_p \lambda_p x_p) + d_3^p \cos(C_p \lambda_p x_p) + d_4^p \sin(C_p \lambda_p x_p), \quad (D.4)$$

where  $\lambda_p$  and  $C_p$  terms are introduced in Eqs.(D.5)

$$\lambda_p^2 = \sqrt{\frac{\rho_p}{E_p}} \omega, \quad C_p = \sqrt[4]{\frac{A_p}{I_p}} \quad (D.5)$$

Derivatives of eigenfunctions are given in Eqs.(D.6)-(D.9)

$$\frac{dU_p(x_p)}{dx_p} = -\lambda_p^2 c_1^p \sin(\lambda_p^2 x_p) + \lambda_p^2 c_2^p \cos(\lambda_p^2 x_p), \quad (\text{D.6})$$

$$\begin{aligned} \frac{dW_p(x_p)}{dx_p} &= C_p \lambda d_1^p \sinh(C_p \lambda_p x_p) + C_p \lambda_p d_2^p \cosh(C_p \lambda_p x_p), \\ &\quad - C_p \lambda d_3^p \sin(C_p \lambda_p x_p) + C_p \lambda_p d_4^p \cos(C_p \lambda_p x_p), \end{aligned} \quad (\text{D.7})$$

$$\begin{aligned} \frac{d^2 W_p(x_p)}{dx_p^2} &= (C_p \lambda)^2 d_1^p \cosh(C_p \lambda_p x_p) + (C_p \lambda_p)^2 d_2^p \sinh(C_p \lambda_p x_p), \\ &\quad - (C_p \lambda)^2 d_3^p \cos(C_p \lambda_p x_p) - (C_p \lambda_p)^2 d_4^p \sin(C_p \lambda_p x_p), \end{aligned} \quad (\text{D.8})$$

$$\begin{aligned} \frac{d^3 W_p(x_p)}{dx_p^3} &= (C_p \lambda_p)^3 d_1^p \sinh(C_p \lambda_p x_p) + (C_p \lambda_p)^3 d_2^p \cosh(C_p \lambda_p x_p) \\ &\quad + (C_p \lambda_p)^3 d_3^p \sin(C_p \lambda_p x_p) - (C_p \lambda_p)^3 d_4^p \cos(C_p \lambda_p x_p). \end{aligned} \quad (\text{D.9})$$

The boundary conditions of the MPSA lead to the following compatibility equations at  $x_p = 0$

$$U_p(0) = 0, \quad (\text{D.10})$$

$$\left. \frac{dW_p(x_p)}{dt} \right|_{x_p=0} = 0, \quad (\text{D.11})$$

$$\left. \frac{d^3 W_p(x_p)}{dt^3} \right|_{x_p=0} = 0, \quad (\text{D.12})$$

Three of the eigenfunction coefficients can be evaluated from the boundary conditions equation at  $x_p = 0$  as follows

$$c_1^p = 0, d_2^p = 0, d_4^p = 0. \quad (\text{D.13})$$

The boundary condition equations at  $x_p = L_p$  are given by

$$\left. \frac{dU_p(x_p)}{dt} \right|_{x_p=L_p} = 0, \quad (\text{D.14})$$

$$\left. \frac{d^2W_p(x_p)}{dt^2} \right|_{x_p=L_p} = 0, \quad (\text{D.15})$$

$$\left. \frac{d^3W_p(x_p)}{dt^3} \right|_{x_p=L_p} = 0. \quad (\text{D.16})$$

The boundary condition equations can be written in a matrix form

$$\mathbf{R}_p(\lambda_p) = \begin{bmatrix} \lambda_p^2 \cos(\lambda_p^2 L_p) & 0 & 0 \\ 0 & (C_p \lambda_p)^2 \cosh(C_p \lambda_p L_p) & -(C_p \lambda_p)^2 \cos(C_p \lambda_p L_p) \\ 0 & (C_p \lambda_p)^3 \sinh(C_p \lambda_p L_p) & (C_p \lambda_p)^3 \sin(C_p \lambda_p L_p) \end{bmatrix} \begin{Bmatrix} c_2 \\ d_1 \\ d_3 \end{Bmatrix}^p, \quad (\text{D.17})$$

where the determinant of  $\mathbf{R}_p(\lambda_p)$  provides the characteristic equation for the solution of the eigenvalues  $\lambda_p$ . The receptance matrix of the RCM is approximated by 3-DOF, which is  $U_p(K)$ ,  $W_p$  and  $W_p''$ .

$$\mathbf{H}_{MSPA}(\omega) = \sum_{r=1}^K \left( \begin{array}{c} \frac{1}{k_{pr} - \omega^2 m_{pr} + i\omega c_{pr}} \\ \times \begin{bmatrix} W_{pr}(L_p)^2 & W_{pr}(L_p)U_{pr}(L_p) & W_{pr}(L_p)\Psi_{pr}(L_p) \\ U_{pr}(L_p)W_{pr}(L_p) & U_{pr}(L_p)^2 & U_{pr}(L_p)\Psi_{pr}(L_p) \\ \Psi_{pr}(L_p)W_{pr}(L_p) & \Psi_{pr}(L_p)U_{pr}(L_p) & \Psi_{pr}(L_p)^2 \end{bmatrix} \end{array} \right). \quad (\text{D.18})$$

## E. Published Papers During Phd

Experimental Mechanics  
https://doi.org/10.1007/s11340-022-00878-y



RESEARCH PAPER



### Experimental Modal Analysis of Nonlinear Amplified Piezoelectric Actuators by Using Response-Controlled Stepped-Sine Testing

A. Koyuncu<sup>1,2</sup> · T. Karaağaçlı<sup>3</sup> · M. Şahin<sup>1</sup> · H. N. Özgüven<sup>1</sup>

Received: 17 February 2022 / Accepted: 27 June 2022  
© Society for Experimental Mechanics 2022

#### Abstract

**Background** The nonlinear dynamic behavior of miniature stack-type piezoelectric actuators is not yet fully investigated and is still an open research field.

**Objective** The objective of this paper is to determine an accurate dynamical model of an amplified stack-type piezoelectric actuator by using a recently developed nonlinear system identification method, namely Response-Controlled stepped-sine Testing (RCT).

**Method** The nonlinear modal identification of a miniature stack-type piezoelectric actuator combined with a rhombus-type compliant mechanism is accomplished by using the RCT method. Several important modifications in the implementation of the RCT method imposed by the miniature nature of the piezo-actuator are successfully achieved for the first time in this study.

**Results** Preliminary constant-voltage tests indicate strong softening nonlinearity with jump phenomenon at high voltage levels. In the nonlinear mode of interest, the RCT method quantifies about a 130 Hz change of natural frequency which corresponds to a 3% frequency shift, and a nonlinear modal damping ratio ranging from 1% to 1.5%, corresponding to a 50% change in the amplitude range of interest.

**Conclusion** The validity of the single nonlinear mode theory on stack-type piezo-actuators and the quantification of the nonlinear modal damping of this type of actuators are achieved for the first time in this study to the best of the authors' knowledge. Consequently, an accurate nonlinear modal model is constructed which may help to estimate the parameters of a physical-driven (constitutive) model and therefore gain a better theoretical understanding of the nonlinear behavior of stack-type piezo-actuators. Furthermore, it is shown that the RCT method can be successfully applied for the modal identification of nonlinear miniature electro-mechanical systems.

**Keywords** Nonlinear identification of piezoelectric actuators · Nonlinear modeling of piezoelectric actuators · Nonlinear experimental modal analysis · Amplified piezoelectric actuator · Response-controlled stepped-sine test

#### Introduction

Piezoelectric actuators are widely used in small-scale applications [1]. Multi-layer piezoelectric stack actuators (MPSAs) are superior to other types of piezoelectric actuators in terms of precision, resolution, stiffness, output force,

and compactness. Despite the promising features, MPSAs suffer from low displacement as an output. The output displacement of the MPSAs is enhanced by employing compliant mechanisms while reducing the output force [2, 3]. MPSAs with rhombus-type flexensional compliant mechanisms are utilized in various engineering fields under the name of amplified piezoelectric actuators (APAs). APAs are available in the market as a family of products (Fig. 1). Miniature APAs are used as positioners, motors, and vibration dampers in various micro-systems such as precise positioning mechanisms in optical devices, small-scale ultrasonic motors, and active vibration controllers in space structures [4].

Dynamic applications require predicting dynamic displacements of an APA under high frequency and resonant conditions [6]. In early studies, miniature APAs have been

✉ A. Koyuncu  
ankoyuncu@hotmail.com

<sup>1</sup> Middle East Technical University, 06800 Ankara, Turkey

<sup>2</sup> Defense Systems Technologies Business Sector, ASELSAN A.Ş., Ankara 06172, Turkey

<sup>3</sup> Defense Industries Research and Development Institute, The Scientific and Technological Research Council of Turkey, TÜBİTAK-SAGE, P.K. 16, 06261 Mamak, Ankara, Turkey

Published online: 05 August 2022

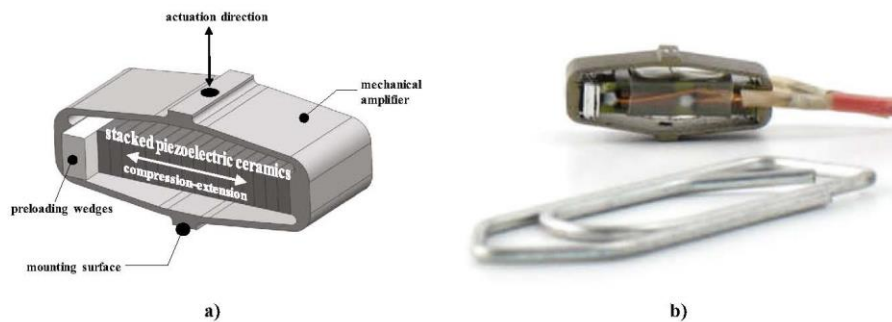


**Fig. 1** (a) Working principle of an amplified piezo-actuator (APA), (b) photograph of the amplified piezo-actuator-APA35XS by Cedrat Technologies [5]

considered low-power actuators and expected to behave linearly under weak electric fields [7]. Accordingly, linear constitutive models have been utilized to estimate the dynamic behaviors of APAs. However, recent studies reveal that piezoelectric actuators exhibit nonlinear behavior even when subjected to weak electric fields [8–11]. A nonlinear model is required to describe the behavior of a piezoelectric actuator for dynamic applications.

There is an extensive body of literature for modeling and experimental identification of nonlinearities in patch-type piezoelectric actuators (see, e.g., [12–18]). In the literature, the general approach is to presume a physical-driven (constitutive) nonlinear model for the piezoelectric material by observing measured constant-voltage frequency response data. The a priori model is then converted to a reduced-order modal model that can be used to carry out dynamic simulations. The identification is completed by tuning the parameters of the physical model in a manner to match the simulated frequency response (or backbone curve) data with the corresponding experimental data. A drawback of this approach is that it is quite possible to overlap the simulated and experimental data even with an incorrect model. For example, if the constitutive model assumes linear damping while the actual piezo-material exhibits nonlinear damping, the tuning process will compensate this modeling error by overshooting the actual parameters of the conservative part of the constitutive model. This issue may be handled possibly better by directly correlating parameters of the physical model with the measured nonlinear modal data instead of frequency response data. By virtue of the recent developments in the field of nonlinear structural dynamics, the accurate identification of nonlinear modal parameters including the nonlinear modal damping ratio is now within reach [19, 20].

Compared to patch-type piezo-actuators, the literature about the stack-type piezo-actuators is very limited [4, 10,

11, 21–26]. Dynamic behaviors of both types of actuators considerably differ from each other. In the patch-type actuators, nonlinearity in the '31'-electromechanical coupling and its associated '1'-directional elasticity becomes important. On the other hand, in the stack-type actuators nonlinearity in the '33'-electromechanical coupling and '3'-directional elasticity has to be taken into account. To the best of the authors' knowledge, the only comprehensive study that characterizes the nonlinearity of stack-type actuators has been recently published in [11]. In that work, Shivashankar et al. constructed a nonlinear constitutive model for longitudinal vibrations of MPSAs by following a procedure similar to the one previously mentioned for patch-type actuators. The experimentally extracted backbone curve plays the key role to characterize the nonlinearity, i.e., in proposing a nonlinear constitutive model with unknown coefficients. These unknown coefficients are then identified by using constant-voltage frequency response data. Although constant-voltage (or force) testing may be suitable to extract the backbone curves in the case of relatively weak nonlinearities [11], it may result in considerable inaccuracy in the case of strong nonlinearities that exhibit the jump phenomenon due to unstable branches [27]. Fortunately, a prominent feature of the RCT method [19] is the accurate identification of turning points, unstable branches, and backbone curves of frequency response functions (FRFs), as shown later in this paper. Furthermore, keeping the response amplitude constant during frequency sweep makes the RCT method very suitable to study the frequency dependency of nonlinearity [28], which may also be a considerable issue for the MPSAs as discussed in [11, 29]. It is also possible to identify the nonlinear modal damping accurately by employing the RCT method using standard commercial modal test equipment, which is still a difficult task with other techniques. In the work of Shivashankar et al. [11], the damping is assumed



to be linear which is arguable, and which may also affect the accuracy of the constitutive model. In literature, there exist studies that investigate the nonlinear damping mechanism of patch-type piezo-actuators [15, 16]. However, no such study is available in the limited literature on stack-type piezo-actuators.

Similar to many nonlinear system identification techniques recently developed in the field of structural dynamics, the RCT method also relies only on the nonlinear normal mode (NNM) concept which was first introduced by Rosenberg [30]. Analogous to linear normal modes, Rosenberg defined a nonlinear mode as a *vibration in unison* of a nonlinear system. Later, in 1979, Szemplinska-Stupnicka presented the modified “single nonlinear mode” method [31] to model near-resonant vibrations of nonlinear multi-degree of freedom (MDOF) systems by using the NNM concept. The proposed method shows that the near-resonant frequency responses of a nonlinear system can be expressed by using a single NNM and its corresponding natural frequency, presuming the modes are well separated and no internal resonances occur. The single NNM and corresponding nonlinear modal parameters are functions of modal amplitude.

Until the 2010s, studies that used the NNM concept in nonlinear system identification were very few in number. Important early examples are [32, 33]. However, in the last decade, the number of nonlinear modal identification methods based on the NNM concept has increased significantly [34–37]. Although these state-of-the-art techniques successfully identify NNM backbone curves, the accurate identification of nonlinear modal damping is still a challenging issue. Furthermore, there exist few studies that identify a high degree of nonlinearities and that validate the identified nonlinear modal properties.

Recently, phase resonance testing with a phase-locked-loop (PLL) controller [37] successfully achieved the identification of nonlinear modal damping of a friction-damped joint resonator [20] by using the extended periodic motion concept [38]. This approach proved also its applicability for the identification of much stronger nonlinearities; modal damping ratio of up to 15% and a resonance frequency shift by 36% in the case of a cantilever beam with dry-friction [39]. An important benefit of the phase resonance testing with the PLL controller is that only the points on the backbone curve need to be tested, which can reduce the test duration considerably. On the other side, a possible drawback is that it is currently not implemented in commercial modal test systems (e.g., LMS Test Lab), and therefore cannot easily be used by practicing engineers.

Another promising nonlinear modal identification method that can identify nonlinear modal damping ratio and that can accurately quantify a high degree of nonlinearities has been recently proposed by Karaağaçlı and Özgüven in [19] under the name of response-controlled stepped-sine testing (RCT).

In this method, the displacement amplitude of the driving (excitation) point is kept constant in a closed-loop control during the stepped sine testing. Various applications ranging from simple benchmarks to real and complex engineering systems showed that this control strategy yields quasi-linear constant-response FRFs around resonance frequencies. The important merit of the RCT method is that these quasi-linear FRFs can be easily measured using standard commercial modal test equipment. Then, they can be processed by standard linear analysis techniques to accurately identify response level-dependent modal properties of nonlinear structures. The RCT method has been successfully applied so far to a T-beam with local cubic stiffness [19], a missile structure with considerable damping nonlinearity mostly due to bolted joints [19], and a double clamped beam with strong geometrical nonlinearity [40]. In [40], the RCT method accurately quantified about a 20% shift of the natural frequency and an order of magnitude change in modal damping ratio (from 0.5% to 4%).

It is worth mentioning that the idea of extracting response-level dependent modal parameters from constant-response testing essentially dates back more than a decade earlier than the RCT method [41, 42]. However, in [41], the theoretical base remains restricted to structures with local nonlinearities. On the other hand, in [42], although it is achieved to identify amplitude-dependent modal parameters of an engineering system with distributed nonlinearity by using constant-acceleration testing, the nonlinearity is weak; the method lacks theoretical justification and is based on intuition. Moreover, keeping acceleration amplitude constant is just an approximation to keeping displacement amplitude constant, and does not hold true when there is considerable resonance frequency shift as in the case of geometric nonlinearities. The RCT method [19], on the other hand, provides a rigorous mathematical framework by combining the single nonlinear mode theory [31] with the Nonlinearity Matrix concept [43], and its applicability is experimentally demonstrated on various strongly nonlinear mechanical systems as mentioned above. It is also important to note that the contribution of the RCT is not limited to the identification of response-dependent modal parameters. It uses these parameters to obtain constant force amplitude FRFs both in stable and unstable frequency regions. Furthermore, it provides the unstable branches of FRFs directly from measurements as well by using the harmonic force surface (HFS) concept [19, 27, 40].

The applicability of RCT on a miniature electro-mechanical system that incorporates piezoelectric material could not be taken for granted for several reasons. Firstly, the frequency dependence of the nonlinearity in stack-type piezo-actuators could possibly be significant as suspected by Shivashankar et al. [11], which could degrade the quasi-linearity of constant-response FRFs. Secondly, the miniature nature of the

electro-mechanical device required to conduct the test at very low response amplitudes (far below 10 μm) compared to previous RCT applications [19, 40]. This could possibly lead to a considerably low S/N ratio which could distort the measurements and render response-control impossible. Thirdly, the small scale of the APA enforces considerable modifications in the usual implementation of the RCT method: a non-contact laser displacement sensor is chosen as the control sensor instead of an accelerometer, the structure is excited with the embedded piezoelectric stack actuator instead of an electrodynamic shaker, and the excitation and response control points do not coincide. These modifications could possibly cause unexpected complications that could obstruct the applicability and disrupt the accuracy of the RCT method. Therefore, one of the important contributions of this paper is to clarify all these issues and to demonstrate the applicability of the RCT method to miniature electromechanical devices.

In this work, the miniature amplified piezoelectric actuator APA35XS shown in Fig. 1(b) from Cedrat Technologies is selected as a test specimen [5]. The displacement amplitude of the control point is kept constant, and the input voltage spectrum corresponding to each displacement amplitude level is measured during the stepped-sine tests. Eventually, frequency response functions (FRFs) come out in the quasi-linear form. Modal parameters are experimentally identified from the quasi-linear FRFs through standard linear modal analysis tools. Nonlinear modal parameters of the miniature APA are then extracted as functions of response amplitude. In the mode of interest, the RCT quantifies about a 130 Hz change of natural frequency and a modal damping ratio ranging from 1% to 1.5% in the amplitude range of interest, which indicates considerably high stiffness and damping nonlinearities. Finally, nonlinear modal parameters are validated by comparing the constant-force frequency response curves synthesized from these parameters with those extracted directly from the experiment using the harmonic force surface (HFS) approach proposed in [19].

This section is concluded by emphasizing another important contribution of this paper. As previously mentioned, the literature about the nonlinear dynamics of stack-type piezo-actuators is very limited, and this is the first work that investigates the nonlinear damping of this type of actuator. In the Experimental Work section, it is shown that, similar to APA35XS, the stack-type actuator studied in [11] also exhibits considerable damping nonlinearity contrary to the linear damping assumption of Shivashankar et al. More importantly, this is achieved in a novel way by constructing the HFS for the first time from the constant-voltage frequency response curves (instead of constant-response harmonic voltage (or force) spectra), which is the only available experimental data in [11]. The HFS is then sliced by constant displacement amplitude planes that give quasi-linear constant-response FRFs. These FRFs are processed

with standard linear modal analysis techniques to extract nonlinear modal parameters, including modal damping ratio. Finally, it is shown that the constant-voltage FRFs synthesized by using the identified nonlinear modal damping ratio match with the real experimental data significantly better than the ones synthesized by using the linear damping model of Shivashankar et al. [11].

### Methodology

Nonlinear experimental modal analysis by using the RCT method has been recently proposed in [19] where its theoretical background and implementation are explained in detail. For the sake of completeness, the fundamental steps and the key features of the method are explained below.

The experimental modal analysis with RCT consists of the following fundamental steps:

- Step 1:* Quasi-linear constant-response FRFs are measured at several different displacement amplitude levels by keeping the displacement amplitude of the control point constant throughout the stepped sine testing at each level.
- Step 2:* Modal parameters of each quasi-linear FRF are identified using standard linear modal analysis tools. A nonlinear modal model is then constructed by expressing the identified modal parameters as functions of the displacement (equivalently modal) amplitude.
- Step 3:* Required near-resonant constant-force (or voltage) frequency response curves are calculated employing the identified modal parameters in a Newton Raphson solution scheme with the arc-length continuation algorithm.

The quasi-linearity of constant-response FRFs mentioned above is theoretically based on the following receptance formula derived from the single nonlinear mode theory [31] and the Nonlinearity Matrix concept [43] as explained in [19]:

$$\alpha_{jk}(\omega, q_r) = \frac{\bar{A}_{jkr}(q_r)}{\bar{\omega}_r^2(q_r) - \omega^2 + i\bar{\eta}_r(q_r)\bar{\omega}_r^2(q_r)} \quad (1)$$

where  $\bar{A}_{jkr}(q_r)$ ,  $\bar{\omega}_r(q_r)$ ,  $\bar{\eta}_r(q_r)$  and  $q_r$  are the complex modal constant, natural frequency, modal damping ratio, and the modal amplitude of the  $r^{\text{th}}$  nonlinear normal mode, respectively.  $j$  is the response coordinate,  $k$  is the excitation coordinate, and  $\omega$  represents the excitation frequency.

Obviously, all the modal parameters given in equation (1) are functions of a single parameter; the modal amplitude  $q_r$ . Accordingly, if the modal amplitude is kept constant throughout the stepped-sine testing, the measured receptances come out in the quasi-linear form. In [19], it has been shown that the constant modal amplitude condition can be achieved by keeping the displacement amplitude of

the control point constant. This also means that the modal amplitude can be mapped to the spatial displacement amplitude of the control point. Therefore, the receptance shown in equation (1) can be alternatively expressed as follows:

$$\alpha_{jk}(\omega, |X_j|) = \frac{\bar{A}_{jkr}(|X_j|)}{\bar{\omega}_r^2(|X_j|) - \omega^2 + i\eta_r(|X_j|)\bar{\omega}_r^2(|X_j|)} \quad (2)$$

where  $|X_j|$  is the displacement amplitude of the control point.

It is important to note that the single nonlinear mode theory does not provide a general mathematical proof that guarantees the validity of its fundamental hypothesis for any nonlinear structure, i.e., the dependence of nonlinear modal parameters on a single parameter; the modal (or displacement) amplitude. In order to turn this hypothesis into a well-established theory, it must be verified by experiments applied to different types of nonlinearities. The RCT has already been verified so far on joint nonlinearities [19] and continuously distributed (geometrical) nonlinearities [40], which are considered challenging problems for the current state-of-the-art. This particular research paper makes a third important contribution that further expands the application area of the single nonlinear mode theory and the RCT method to include miniature electro-mechanical devices that incorporate piezoelectric material.

Concluding this section, it is interesting to note that since the exciter, i.e., piezo-actuator, is an integral element of the test structure, it is not possible to quantify the excitation force in the units of Newton directly. However, this is not an important issue since the main objective of this study is to construct an accurate mathematical model that relates the input voltage to the displacement output. Accordingly, the receptance formula given in equations (1) and (2) are also used somewhat differently than their classical definitions. The receptance represents the relation between the excitation force and the output displacement in its classical definition. However, in this study, it represents the transfer function between the input voltage and the output displacement.

### Experimental Work

As reported in [11], most of the studies in the literature have focused on characterizing the nonlinear dynamic behavior of patch-type piezoelectric actuators. Since works about the elasticity of stack-type piezoelectric actuators are quite a few, their nonlinear dynamic behavior is not yet fully understood and is still an open research field. From this perspective, an important merit of this experimental work is the identification of nonlinear modal parameters and the construction of an accurate nonlinear modal model of a commercial miniature APA, which may help to estimate the

parameters of a physical-driven (constitutive) model and therefore to gain a better theoretical understanding about the nonlinear behavior of stack-type piezoelectric actuators.

### Experimental Setup

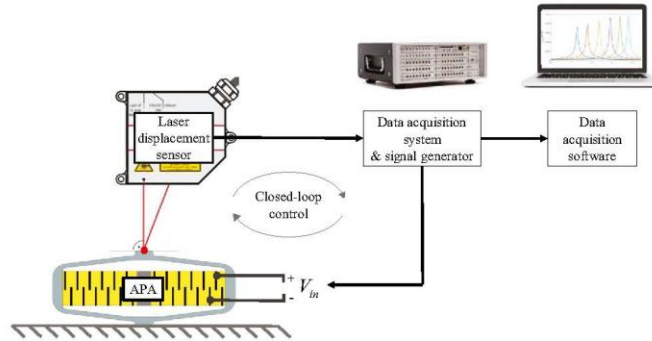
The test structure is the APA35XS model miniature actuator manufactured by Cedrat Technologies [5] (Fig. 1(b)). It consists of two components: A multi-layer stack type piezoelectric actuator and a rhombus type compliant mechanism that converts the lateral (horizontal) motion of the piezoelectric actuator into transverse (vertical) motion. The focus of this study was the fundamental transverse vibration mode of the APA in the actuation direction that exhibits strong softening nonlinearity. In order to study that mode, the APA was fixed to the ground from its base (Fig. 2).

Since the APA is a self-exciting structure, it does not require an external excitation source. Therefore, the harmonic excitation force was generated by feeding the stack-type piezoelectric actuator embedded in the APA with harmonic voltage input. Since the excitation mechanism is part of the tested structure, the exciter-structure interaction is not very relevant to the application case studied herein. However, in the case of an external exciter such as an electrodynamic shaker, this interaction can be a considerable issue [44, 45]. If the basic assumptions of the single nonlinear mode theory [31], i.e. well-separated modes and negligible higher harmonics, hold true, and the shaker attachment does not significantly distort the modal deflection, then the shaker-structure interaction is not pronounced [44] and the RCT method can be successfully applied by using standard modal test equipment. In practice, various damping mechanisms (e.g., friction at joints and/or material damping) naturally suppress the effects of higher harmonics [40, 44] and the single nonlinear mode theory remains valid for a wide range of applications as in the case of this paper and the previous applications of the RCT method [19, 27, 40]. However, at sufficiently high energy levels, strong higher harmonics may arise due to harmonically coupled modes (internal resonance) [46]. In such a case, the closed-loop response-control has to be implemented with a noninvasive control scheme [47] so that the controlled structure behaves the same as the open-loop structure. Alternatively, internal resonance can be studied by phase resonance testing with a PLL controller, which is naturally noninvasive.

The vibration response of interest is the vertical tip displacement of the APA in the actuation direction (which is related to the transverse vibration mode). The tip displacement was measured by a non-contact laser displacement sensor (Micro-Epsilon OptoNCDT 2300) [48], which was installed on top of the actuator, as shown in Fig. 2.

During the experimental work, all the data acquisition and closed-loop control tasks were accomplished by the

**Fig. 2** Schematic view of the experimental setup



LMS SCADAS system and LMS Test Lab software. The schematic view of the experimental test setup is shown in Fig. 2. The frequency range of interest encompassing the mode of interest was determined by preliminary fast sine sweep (periodic chirp) tests. During all the constant-voltage and constant-response stepped sine tests, the frequency step was taken to be 0.5 Hz.

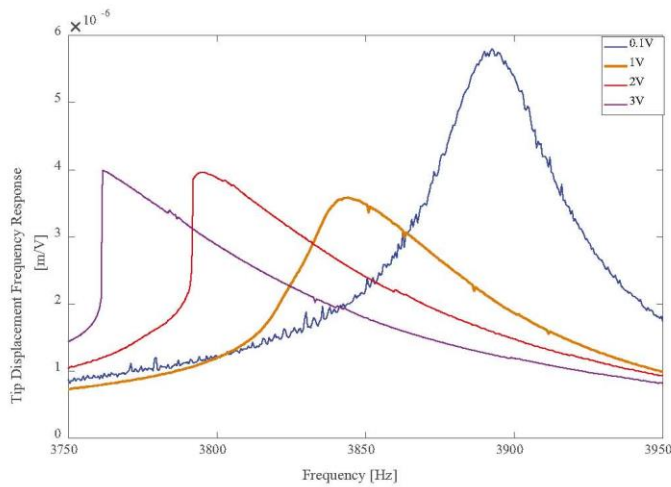
**Results of Constant-Voltage Stepped Sine Tests**

Before the application of the RCT method, a series of constant-voltage tests were conducted on the miniature APA similar to [11]. The amplitude of the input harmonic voltage

is kept constant in closed-loop control. The measured output is the tip displacement of the APA. FRFs measured at different constant voltage levels are shown in Fig. 3. As the voltage level is increased from 0.1 V to 3 V, an approximately 130 Hz drop of the resonance frequency is observed, which indicates strong softening nonlinearity.

Another important observation related to Fig. 3 is the jump phenomenon observed at high voltage levels, which is an indication of unstable regions. This is an interesting difference between this study and the work of Shivashankar [11]. In the latter, the nonlinearity is relatively weak, and luckily no jump is encountered. During constant-voltage (or force) stepped-sine testing of structures in an unstable

**Fig. 3** FRFs measured by constant-voltage stepped-sine testing



region, corrective voltage (or force) perturbation of the controller to capture the reference signal in the proximity of the FRF turning point may lead to a premature jump before reaching the actual resonance peak [27]. In such a case, the accuracy of the measured backbone curve is always questionable.

It is also important to note that for most state-of-the-art techniques including constant-voltage (or force) testing, identifying nonlinear modal damping is still a challenging issue. Regarding Fig. 3, standard linear modal analysis techniques may only help to extract modal damping at the lowest voltage level, where the system's FRF looks linear. In [11], the damping of the stack-type piezoelectric actuator is assumed to be linear without solid proof.

**Identification of Nonlinear Modal Parameters by Using the RCT Method**

In the RCT method, first of all, a series of response-controlled stepped-sine tests were conducted at 11 different displacement amplitude levels of the tip point of the miniature APA ranging from 0.5 μm to 10 μm. During each test, the displacement amplitude of the tip point was kept constant throughout the frequency sweep in closed-loop control, and the corresponding harmonic input voltage spectrum was recorded. Then, dividing the constant harmonic displacement spectrum by the corresponding harmonic voltage spectrum, constant-response FRFs were obtained, as shown in Fig. 4.

The first important observation relevant to Fig. 4 is that although the constant-response FRFs cover the voltage

levels shown in Fig. 3, they do not exhibit any jump phenomenon. This is due to the fact that the test structure settles in one stable orbit throughout the frequency sweep by virtue of the constant-response strategy of the RCT method. With this strategy, the competition of multiple stable orbits and, therefore the jump phenomenon, which is typically encountered in constant-voltage (or force) testing, is avoided. The interested reader may refer to [40] for a detailed discussion of this issue.

The second important observation that can be made from Fig. 4 is that the constant-response FRFs turn out to be quasi-linear. This means that the fundamental hypothesis of the single nonlinear mode theory [31], i.e., all the modal parameters being a function of a single parameter, the response (equivalently modal) amplitude, holds true for the miniature APA. It also means that the frequency dependence of the nonlinearity is negligible at least in a narrow frequency band covering the resonance region of a specific mode. These results are consistent with the nonlinear constitutive model of stack-type piezo-electric actuators constructed in [11]. However, it is also important to note that in [11], the coefficients of the constitutive model identified by using two different modes are considerably different from each other. Shivashankar et al. relate this issue to the frequency dependence of nonlinearity, which is still reasonable: Although the frequency dependence looks to be negligible in the neighborhood of specific modes, it may be pronounced over a wide frequency band covering multiple modes. The inconsistency of the coefficients of the constitutive model could also be related

**Fig. 4** Quasi-linear constant-response FRFs measured by RCT

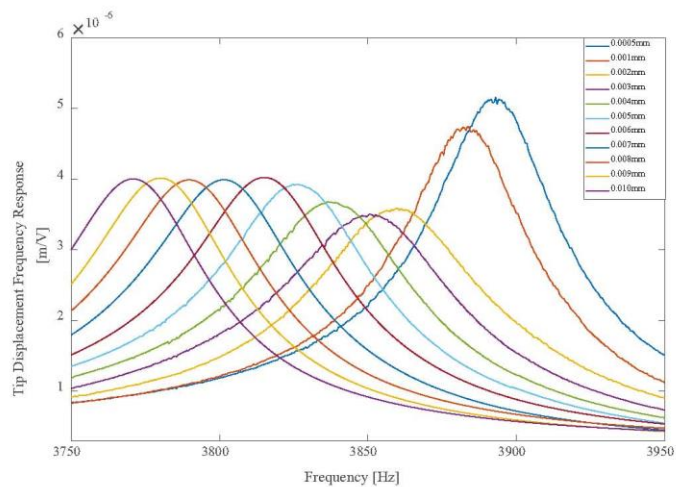
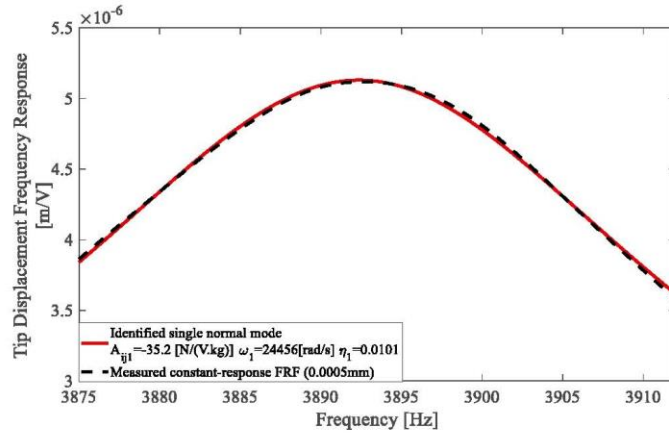


**Fig. 5** Comparison of the constant-response FRF synthesized by using the identified modal parameters with the one measured by RCT



to the linear damping presumption of Shivashankar et al. [11]. Later in this section, the nonlinear modal damping ratio is identified as a function of displacement amplitude by processing the constant-voltage frequency response curves measured in [11] and using the HFS concept. It is demonstrated that constant-voltage FRFs synthesized by using the nonlinear modal damping ratio match with the experimental data significantly better compared to the case where linear damping assumption is used.

Modal parameters of each quasi-linear FRF shown in Fig. 4 can be extracted by using standard linear modal analysis methods. As an illustrative example, the quasi-linear FRF measured at 0.5  $\mu\text{m}$  harmonic displacement amplitude

is compared with the linear FRF synthesized from the identified modal parameters in Fig. 5. The same procedure is repeated for the rest of the FRFs measured using the RCT method. After obtaining modal parameters for each quasi-linear FRF, curves are fitted onto the identified modal parameters by using the *fit* function of MATLAB with the piecewise cubic Hermite interpolation (*pchipinterp*) method, as shown in Figs. 6 and 7.

As indicated in Fig. 6(a), the resonance frequency decreases almost linearly with increasing response amplitude. As shown in the next section, the backbone curve of the miniature APA is also an inclined straight line. This behavior is consistent with the nonlinear behavior of the stack-type

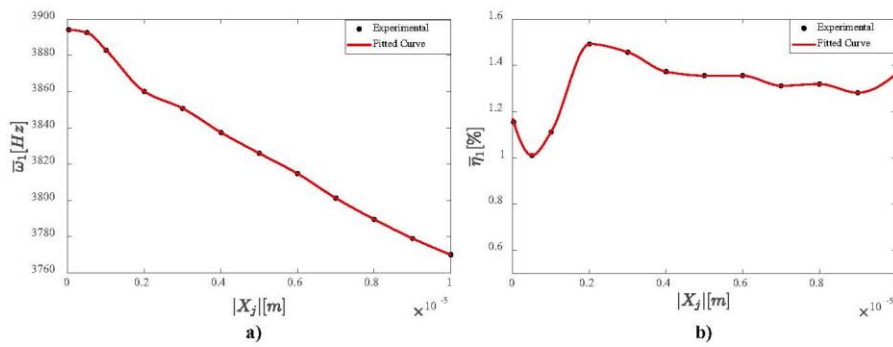
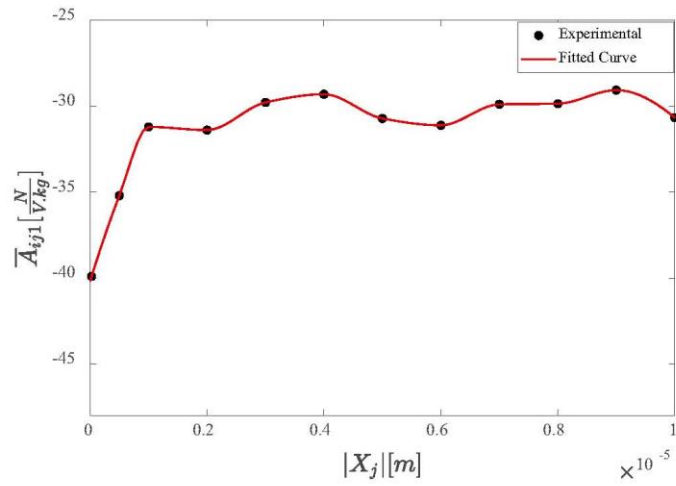


**Fig. 6** Variation of the modal parameters corresponding to the nonlinear normal mode of the APA35XS with respect to the response level: (a) natural frequency, (b) modal damping ratio

**Fig. 7** Variation of the modal constant corresponding to the nonlinear normal mode of the APA35XS with respect to the response level



piezo-actuator studied in [11]. From Fig. 6(a), it is also observed that the drop of the resonance frequency is about 130 Hz, which indicates a strong softening nonlinearity.

Figure 6(b) indicates that the modal damping ratio exhibits an abrupt increase from 1.0% to 1.5% at relatively low response levels. However, it looks like to settle around a constant value at high response levels.

**Validation of the Nonlinear Modal Model**

In order to validate the identified modal parameters, first of all, harmonic voltage spectra measured at constant-displacement amplitude levels are merged to construct the HFS by using linear interpolation, as shown in Fig. 8. Slices of the HFS at constant voltage levels

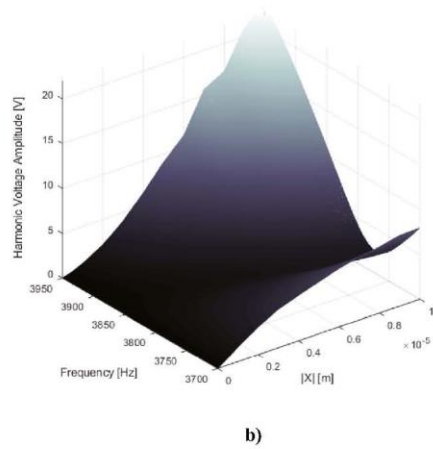
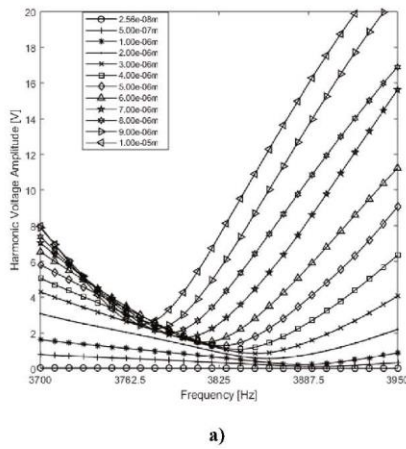


**Fig. 8** (a) Harmonic excitation voltage spectra of the APA measured during RCT (b) HFS of the free end constructed by combining harmonic excitation voltage spectra with linear interpolation

give constant-voltage frequency response curves, which are purely experimental data. The prominent feature of the HFS technique is the accurate extraction of the turning and unstable branches of these curves, which cannot be achieved by constant-voltage testing due to the jump phenomenon (Fig. 3). A detailed discussion of the HFS approach is given in [19, 27].

Identified nonlinear modal parameters are validated by comparing constant-voltage frequency response curves synthesized from these parameters, by using the Newton–Raphson method and the arc-length continuation algorithm, with the ones extracted from the HFS. The comparison is shown in Fig. 9. It can be observed from the figure that the match between synthesized and extracted curves is almost perfect, which demonstrates the accuracy of the identified nonlinear modal parameters.

Finally, the NNM backbone curve constructed by using constant-voltage frequency response curves synthesized from the identified nonlinear modal parameters is compared with the one directly extracted from the HFS, which is purely measured (nonparametric) data, as shown in Fig. 10. The good match between both backbone curves once again validates the accuracy of the identified nonlinear modal model. It is also worth mentioning that the backbone curve is an inclined straight line which is consistent with the

nonlinear behavior of the stack type piezo-actuator studied in [11] as discussed in the previous section. It can be concluded that the nonlinearity of the miniature APA studied herein is most governed by the nonlinearity of the embedded piezo-actuator.

### Identification of Nonlinear Modal Damping Ratio of Stack Piezoelectric Actuators by Using the Harmonic Force Surface Concept

In previous sections, it has been discussed that the linear damping assumption of the Shivashankar et al. [11] for stack-type actuators does not rely on solid proof. This section demonstrates that they could actually extract the nonlinear modal damping ratio accurately by just constructing the Harmonic Force Surface (HFS) from already available measurements without any extra experimental effort.

In all the previous applications of the RCT method [19, 27, 40], the HFS has been constructed by merging harmonic force (or voltage) spectra measured at different constant-displacement amplitude levels as illustrated in the previous section. However, in the work of Shivashankar et al. [11], the experimental data consists of the frequency response curves

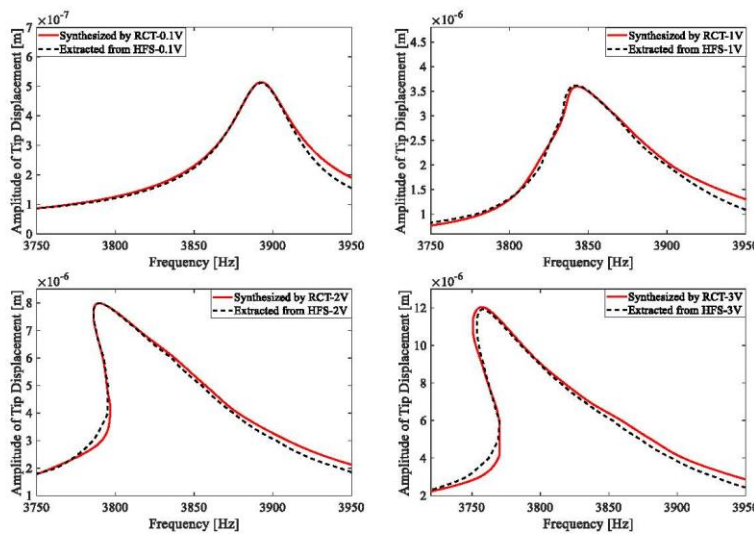
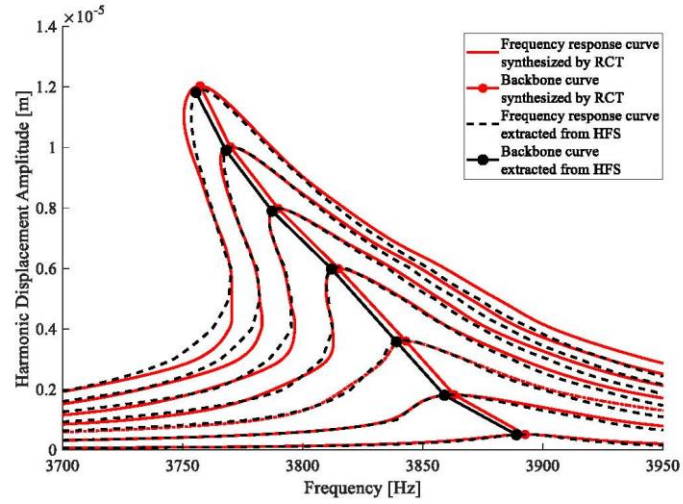


Fig. 9 Comparison of constant-voltage frequency response curves extracted from HFS with the ones synthesized by using nonlinear modal parameters

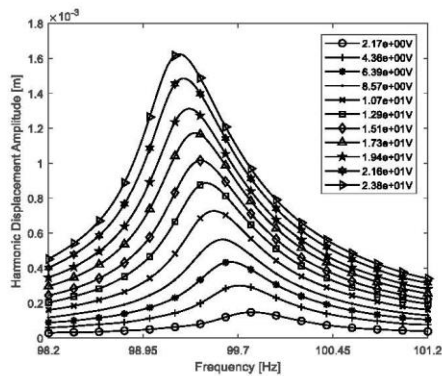


**Fig. 10** Comparison of the backbone curve extracted from HFS with the one obtained by using nonlinear modal parameters

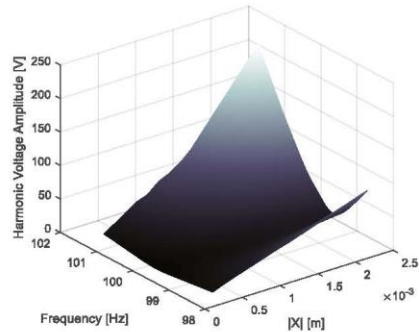


measured by constant-voltage testing, as shown in Figs. 11(a) and 12(a). Luckily, the nonlinearity is not too strong and these curves are very smooth without any jump. Therefore, in this paper, it is demonstrated for the first time that if there is no jump, HFSs can also be constructed smoothly by combining constant-voltage (or force) frequency–response curves with linear interpolation, as shown in Figs. 11(b) and 12(b).

Once the HFSs are constructed, they are sliced by different constant-displacement amplitude planes to obtain corresponding V-shaped harmonic voltage spectra. By dividing each constant-displacement amplitude value by the corresponding voltage spectrum, constant-response FRFs are obtained, as shown in Fig. 13. Similar to the APA studied in the previous section, constant-response FRFs



**a)**



**b)**

**Fig. 11** (a) Harmonic displacement spectra measured by constant-voltage testing in the first mode [11] (b) HFS constructed by combining harmonic displacement spectra with linear interpolation for the first mode

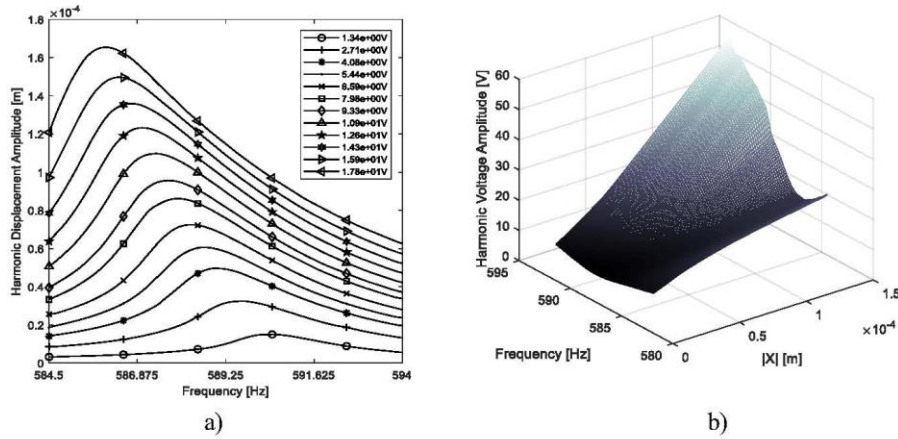


Fig. 12 (a) Harmonic displacement spectra measured by constant-voltage testing in the second mode [11] (b) HFS constructed by combining harmonic displacement spectra with linear interpolation for the second mode

turn out to be quasi-linear. Accordingly, modal parameters corresponding to the two modes of the stack-type actuator are extracted as functions of displacement amplitude, as shown in Figs. 14 and 15, by applying standard linear modal analysis techniques. Figures 14(b) and 15(b) show that the modal damping ratios exhibit considerably nonlinear behavior, which contradicts the linear damping assumption of the Shivashankar et al. [11]. In both modes, the modal damping ratio increases with increasing response amplitude. It should be noted that in this application a

nonlinear viscous damping model is assumed instead of structural damping, just to be able to directly compare it with the linear viscous damping model of [11]. Therefore, the nonlinear modal parameters are identified by using the following receptance formula:

$$\alpha_{jk}(\omega, |X_j|) = \frac{\bar{A}_{jkr}(|X_j|)}{\omega_r^2(|X_j|) - \omega^2 + i2\omega\zeta_r(|X_j|)\omega_r(|X_j|)} \quad (3)$$

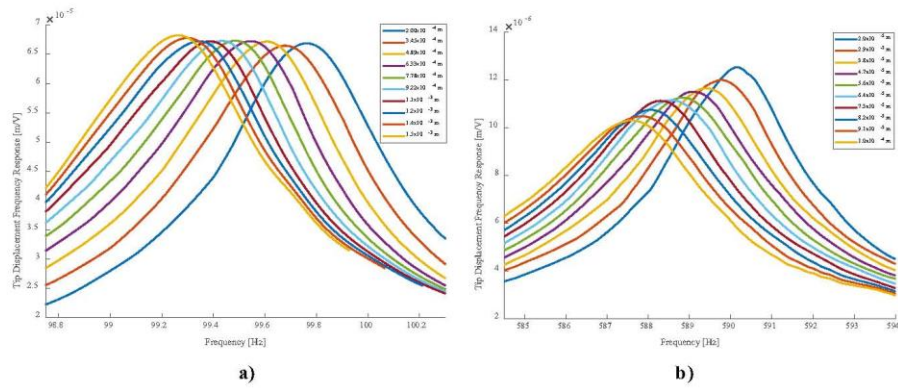


Fig. 13 Quasi-linear constant-response FRFs extracted from HFSs for (a) the first mode and (b) the second mode

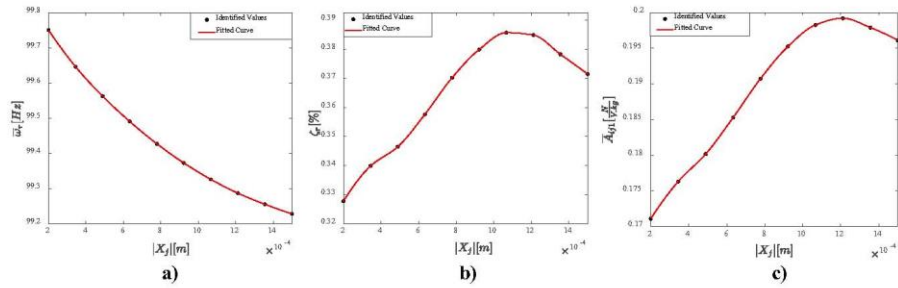


Fig. 14 Nonlinear modal parameters of the stack type-actuator of Shivashankar et al. [11] identified by the HFS for the first mode: (a) natural frequency (b) modal damping ratio and (c) modal constant

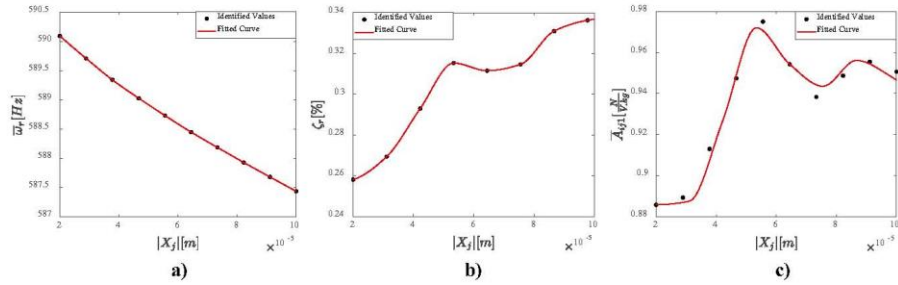


Fig. 15 Nonlinear modal parameters of the stack type-actuator of Shivashankar et al. [11] identified by the HFS for the second mode: (a) natural frequency (b) modal damping ratio and (c) modal constant

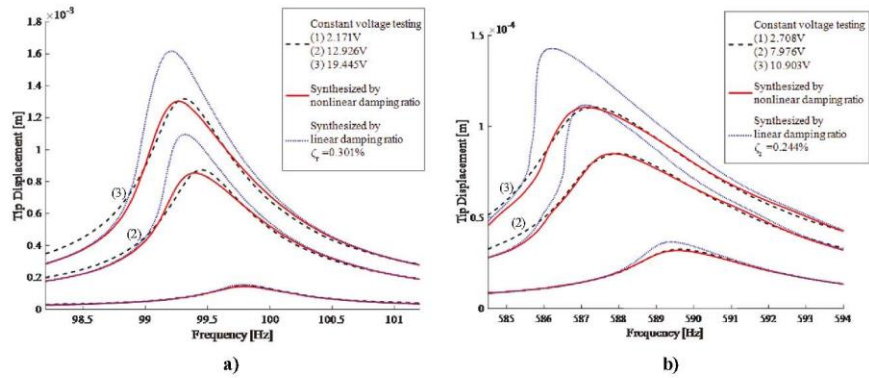


Fig. 16 Comparison of the measured constant-voltage frequency response curves [11] with the ones synthesized by using nonlinear and linear modal damping ratios (a) first mode (b) second mode

Similar to the APA application in the previous section, the accuracy of the identified nonlinear modal parameters is demonstrated by comparing constant-voltage frequency response curves synthesized from these parameters with the measured data in Fig. 16. The match between the measured and synthesized curves is quite good, which shows the accuracy of the identified modal parameters. In the same figure, frequency response curves are also synthesized by using linear modal damping values of Shivashankar et al. [11]; 0.301% and 0.244% for the first and second modes, respectively. Obviously, the nonlinear damping model predicts frequency response curves considerably better than the linear modal damping assumption, especially at moderate and high voltage levels. It can be concluded that if Shivashankar et al. could use the nonlinear modal damping model in their derivations, they would probably extract the parameters of their physical model more accurately.

## Conclusions

A great majority of work in the literature has focused on characterizing the nonlinear dynamic behavior of patch-type piezoelectric actuators. However, studies about the elasticity of stack-type piezoelectric actuators are quite a few in number. Therefore, their nonlinear dynamic behavior is not yet fully investigated and is still an open research field. An important contribution of this paper is the accurate identification of nonlinear modal parameters and the construction of a reliable modal model of a miniature Amplified Piezoelectric Actuator (APA) by using a recently developed nonlinear modal identification framework, namely the Response Controlled stepped-sine Testing (RCT) method. In the nonlinear mode of interest, the RCT method quantifies about a 130 Hz drop of natural frequency, which corresponds to a 3% frequency shift, and an increase of modal damping ratio from 1.0% to 1.5%, corresponding to a 50% change in the amplitude range of interest. This indicates considerably high stiffness and damping nonlinearities. It is important to note that the accurate identification of nonlinear modal damping is still a challenging issue. The quantification and validation of the nonlinear modal damping of miniature stack-type piezo-actuators are achieved for the first time in this study.

The RCT method has been successfully applied so far on various structures ranging from simple benchmarks to complex engineering systems. However, the applicability of RCT on a miniature electro-mechanical system that incorporates piezoelectric material could not be taken for granted for several reasons: a possible frequency dependence of nonlinearity could degrade the quasi-linearity of constant-response FRFs, a possible low S/N due to considerably low amplitude oscillators could degrade the accuracy of the RCT method and modifications in the implementation of the RCT

method by the miniature nature of APA could possibly cause unexpected complications. In this paper, all these issues are clarified, and the applicability of the RCT method on miniature electromechanical devices is successfully demonstrated.

Finally, it is demonstrated in this paper for the first time that if there is no jump (weak nonlinearity), HFS can also be constructed smoothly by combining constant-voltage (or force) frequency–response curves with linear interpolation, and then the HFS can be sliced by constant-displacement planes to obtain quasi-linear constant-response FRFs from which the nonlinear modal parameters including nonlinear modal damping ratio can be identified by applying standard linear modal analysis techniques. This approach is applied to the experimental results of recent work [11], and it is shown that the stack-type actuator studied in that study exhibits considerable damping nonlinearity contrary to the linear damping assumption. It is also demonstrated that the constant-voltage FRFs synthesized by using the identified nonlinear modal damping ratio match with the real experimental data significantly better than the ones synthesized by using the linear damping model of [11], revealing that including the nonlinearity of the damping in stack-type actuators will improve the accuracy of the dynamic model considerably.

**Acknowledgements** This research was funded by ASELSAN Inc. The financial support is gratefully acknowledged.

## Declarations

**Conflict of Interest** The authors declare that they have no conflict of interest.

## References

- Ouyang PR, Tjiptoprodo RC, Zhang WJ, Yang GS (2008) Micro-motion devices technology: The state of arts review. *Int J Adv Manuf Technol* 38(5–6):463–478
- Claeysen F, Ducamp A, Barillot F et al (2008) Stepping piezoelectric actuators based on APAs. *Proc Actuator* 2008:623–626
- Jing Z, Xu M, Wu T, Tian Z (2016) Development of a tilt-positioning mechanism driven by flextensional piezoelectric actuators. *Rev Sci Instrum* 87:8
- Claeysen F, Letty RL, Barillot F, Sosnicki O (2007) Amplified piezoelectric actuators: Static dynamic applications. *Ferroelectrics* 351(1):3–14
- APA35XS (2014) Cedrat Technologies, [Online]. Available: <https://www.cedrat-technologies.com/fileadmin/datasheets/APA35XS.pdf>. [Accessed: 09 Oct 2021]
- Kumar A, DasGupta A (2018) Dynamics of a shell-type amplified piezoelectric actuator. *J Vib Acoust* 140(4):1–9
- Tiersten HF (2013) Linear piezoelectric plate vibrations- elements of the linear theory of piezoelectricity and the vibrations of piezoelectric plates. Springer
- Parashar SK, Von Wagner U (2004) Nonlinear longitudinal vibrations of transversally polarized piezoceramics: Experiments and modeling. *Nonlinear Dyn* 37:51–73

9. Shivashankar P, Kandagal SB (2019) Characterization of elastic and electromechanical nonlinearities in piezoceramic plate actuators from vibrations of a piezoelectric-beam. *Mech Syst Signal Process* 116:624–640
10. Shivashankar P, Gopalakrishnan S, Kandagal SB (2019) Non-linear characterization of piezoelectric patches and piezoelectric stacks from vibrations of piezo-actuated structures. *Proc SPIE* 10967:1–17
11. Shivashankar P, Gopalakrishnan S, Kandagal SB (2021) Nonlinear modeling of d33-mode piezoelectric actuators using experimental vibration analysis. *J Sound Vib* 505
12. Von Wagner U, Hagedorn P (2002) Piezo-beam systems subjected to weak electric field: experiments and modelling of nonlinearities. *J Sound Vib* 256(5):861–872
13. Mahmoodi SN, Jalili N (2009) Piezoelectrically actuated micro-cantilevers: An experimental nonlinear vibration analysis. *Sens Actuators A Phys* 150(1):131–136
14. Goldschmidtboeing F, Wischke M, Eichhorn C, Woias P (2009) Nonlinear effects in piezoelectric vibration harvesters with high coupling factors. *Proc PowerMEMS* 364–367
15. Stanton SC, Erturk A, Mann BP, Inman DJ (2010) Nonlinear piezoelectricity in electrostatic energy harvesters: modeling and experimental identification. *J Appl Phys* 108(7)
16. Stanton SC, Erturk A, Mann BP, Inman DJ (2012) Nonlinear nonconservative behavior and modeling of piezoelectric energy harvesters including proof mass effects. *J Intell Mater Syst Struct* 23(2):183–199
17. Leadenham S, Erturk A (2015) Unified nonlinear electroelastic dynamics of a bimorph piezoelectric cantilever for energy harvesting, sensing and actuation. *Nonlinear Dyn* 79(3):1727–1743
18. Shahabi P, Ghafarirad H, Tagvaeipour A (2019) Nonlinear vibration analysis of piezoelectric bending actuators: theoretical and experimental studies. *Comptes Rendus Mec* 347(12):953–966
19. Karaağaçlı T, Özgüven HN (2021) Experimental modal analysis of nonlinear systems by using response-controlled stepped-sine testing. *Mech Syst Signal Process* 146
20. Scheel M, Peter S, Leine RI, Krack M (2018) A phase resonance approach for modal testing of structures with nonlinear dissipation. *J Sound Vib* 435:56–73
21. Sherrit S, Trebi-Ollennu A, Bonitz R, Bar-Cohen Y, Yen JT (2010) Compact sensitive piezoelectric mass balance for measurement of unconsolidated materials in space. *Sens Smart Struct Technol Civil Mech Aerosp Syst* 7647. SPIE
22. Cabrera MA, Caicedo B, Thorel L (2012) Dynamic actuator for centrifugal modeling of soil-structure interaction. *Geotech Test J* 35(4)
23. Yeom T, Simon TW, Zhang M, North MT, Cui T (2012) High frequency, large displacement, and low power consumption piezoelectric translational actuator based on an oval loop sheel. *Sens Actuators A Phys* 176:99–109
24. Pages A, Rowe S, Duc S, Sonsnicki O, Jaussaud G, Claeysen F (2018) Amplified piezo-actuators (APA) enhancement for active vibration control (AVC). *ACTUATOR 2018; 16th International Conference on New Actuators*, pp. 1–4
25. Ling M, Zhang X (2021) Coupled dynamic modeling of piezo-actuated compliant mechanisms subjected to external load. *Mech Mach Theory* 160
26. Ling M, Yuan L, Luo Z, Huang T, Zhang X (2022) Enhancing dynamic bandwidth of amplified piezoelectric actuators by a hybrid lever and bridge-type compliant mechanism. *Actuators* 11(5):134
27. Karaağaçlı T, Özgüven HN (2020) Experimental identification of backbone curves of strongly nonlinear systems by using response-controlled stepped-sine testing (RCT). *Vibration* 3(3):266–280
28. Karaağaçlı T, Özgüven HN (2020) A frequency domain nonparametric identification method for nonlinear structures: Describing surface method. *Mech Syst Signal Process* 144
29. Damjanovic D (1997) Logarithmic frequency dependence of the piezoelectric effect due to pinning of ferroelectric-ferroelastic domain walls. *Phys Rev B* 55(2)
30. Rosenberg RM (1966) On nonlinear vibrations of systems with many degrees of freedom. *Adv Appl Mech* 9:155–242
31. Szeplifiska-Stupnicka W (1979) The modified single mode method in the investigations of the resonant vibrations of nonlinear systems. *J Sound Vib* 63(4):475–489
32. Setio S, Setio HD, Jezequel L (1992) A method of non-linear modal identification from frequency response tests. *J Sound Vib* 158(3):497–515
33. Gibert C (2003) Fitting measured frequency response using nonlinear modes. *Mech Syst Signal Process* 17(1):211–218
34. Peeters M, Kerschen G, Golival JC (2011) Dynamic testing of nonlinear vibrating structures using nonlinear normal modes. *J Sound Vib* 330(3):486–509
35. Londoño JM, Neild SA, Cooper JE (2015) Identification of backbone curves of nonlinear systems from resonance decay responses. *J Sound Vib* 348:224–238
36. Renson L, Gonzalez-Buelga A, Barton DAW, Neild SA (2016) Robust identification of backbone curves using control-based continuation. *J Sound Vib* 367:145–158
37. Peter S, Leine RI (2017) Excitation power quantities in phase resonance testing of nonlinear systems with phase-locked-loop excitation. *Mech Syst Signal Process* 96:139–158
38. Krack M (2015) Nonlinear modal analysis of nonconservative systems: extension of the periodic motion concept. *Comput Struct* 154:59–71
39. Scheel M, Weigle T, Krack M (2020) Challenging an experimental nonlinear modal analysis method with a new strongly friction-damped structure. *J Sound Vib* 485
40. Karaağaçlı T, Özgüven HN (2022) Experimental quantification and validation of modal properties of geometrically nonlinear structures by using response-controlled stepped-sine testing. *Exp Mech* 62:199–211
41. Arslan Ö, Özgüven HN (2008) Modal identification of nonlinear structures and the use of modal model in structural dynamic analysis. In *Proceedings of the 26th International Modal Analysis Conference (IMAC)*, Orlando, FL, USA
42. Link M, Boeswald M, Laborde S, Weiland M, Calvi A (2010) An approach to nonlinear experimental modal analysis. In *Proceedings of the 28th International Modal Analysis Conference (IMAC)*, Jacksonville, FL, USA
43. Tannkulu Ö, Kuran B, Özgüven HN, İmregün M (1993) Forced harmonic response analysis of nonlinear structures. *AIAA J* 31(7):1313–1320
44. Krack M (2021) Extension of the single nonlinear mode theory by linear attachments and application to exciter-structure interaction. *J Sound Vib* 505
45. Pacini BR, Kuether RJ, Roettgen DR (2022) Shaker-structure modeling and analysis for nonlinear force appropriation testing. *Mech Syst Signal Process* 162
46. Renson L, Shaw AD, Barton DAW, Neild SA (2019) Application of control-based continuation to a nonlinear structure with harmonically coupled modes. *Mech Syst Signal Process* 120:449–464
47. Abelos G, Renson L, Collette C, Kerschen G (2021) Stepped and swept control-based continuation using adaptive filtering. *Nonlinear Dyn* 104:3793–3808
48. *Instruction Manual optoNCDT 2300* (2021) Micro-epsilon messtechnik GbmH & Co. KG [Online]. Available: <http://www.micro-epsilon.de/download/manuals/man--optoNCDT-2300--en.pdf>. [Accessed: 09 Oct 2021]

**Publisher's Note** Springer Nature remains neutral with regard to jurisdictional claims in published maps and institutional affiliations.

---

Springer Nature or its licensor holds exclusive rights to this article under a publishing agreement with the author(s) or other rightsholder(s); author self-archiving of the accepted manuscript version of this article

is solely governed by the terms of such publishing agreement and applicable law.

## Chapter 11

# Extended Abstract: Dynamic Behavior of a Compliant Mechanism Driven by Stacked Piezoelectric Actuators



A. Koyuncu, M. Şahin, and H. N. Özgüven

**Abstract** Mechanical amplifiers are employed to enhance output displacement of piezoelectric actuators. Dynamic behavior of such an amplified piezoelectric actuator needs to be known accurately in order to verify its suitability for the driven system. The objective of this study is to present a theoretical approach to determine a mathematical model for an amplified piezoelectric actuator (APA) which consists of a stacked piezoelectric actuator (SPA) with rhombus type mechanical amplifier (RPA). Dynamics of the mechanical amplifier is formulated based on distributed-parameter system approach, and Hamilton's principle is used to obtain a reduced order model. The SPA is then dynamically coupled with the reduced order model of a flexural amplifier by employing the constitutive relations between two substructures. The responses of the coupled system are calculated using linear vibration analysis under harmonic voltage input. Finally, the validity of the developed mathematical model is verified by comparing the calculated velocities with that of finite element solutions and experimental measurements in the frequency domain. The finite element (FE) solution is obtained using ANSYS software. Output velocity of the sample RPA is measured with the aid of a laser vibrometer. It is observed that the results obtained from the mathematical model show a very good agreement with those of the finite element analysis and test measurements.

**Keywords** Amplified piezoelectric actuators · Rhombus type · Strain amplification · Compliant mechanism

### 11.1 Introduction

Piezoelectric actuators have become widespread in robotics and mechatronics. These actuators are used as positioners, motors and vibration dampers in various applications such as precise positioners in optical devices, small scale ultrasonic motors, and active vibration controllers in space structures. High resolution, large output force, compact size, wide frequency bandwidth and solid-state design are the unique features of the piezoelectric actuators. The major limitation of the piezoelectric actuators, on the other hand, is their small output displacement range. Compliant mechanisms are integrated with multi-layered stacked piezoelectric actuators (SPA) to enhance these output displacements. There are different types of compliant mechanisms in the literature [1]. Amplified piezoelectric actuators (APAs) with flexensional compliant mechanisms are widely used in various engineering fields. Kinematic and dynamic modelling of piezoelectric actuators with compliant mechanisms are required in design and optimization stages of the actuators. Most of the studies in the literature are based on kinematic analysis of the actuators under static loading conditions [1–3]. Statically determined constitutive relations of an actuator may not be valid under dynamic actuation cases [4]. Some of the studies perform dynamic analysis considering only inertial properties of the lumped elements such as the SPA. The inertial effects of the compliant mechanism become important while the piezoelectric actuator is driven by high frequency input voltage. In this study, generalized constitutive equations of an APA with a compliant mechanism are determined based on structural dynamic analysis. A Rhombus type flexensional compliant mechanism (RCM) is formulated in the current study since rhombus type amplified piezoelectric actuators (RPAs) are the most popular and available amplified piezoelectric actuators in the market (Fig. 11.1a).

---

A. Koyuncu (✉)  
Middle East Technical University, Ankara, Turkey  
Defense Systems Technologies Business Sector, ASELSAN A.Ş., Ankara, Turkey

M. Şahin · H. N. Özgüven  
Middle East Technical University, Ankara, Turkey

© The Society for Experimental Mechanics, Inc. 2019  
C. Niezrecki, J. Baqersad (eds.), *Structural Health Monitoring, Photogrammetry & DIC, Volume 6*,  
Conference Proceedings of the Society for Experimental Mechanics Series, [https://doi.org/10.1007/978-3-319-74476-6\\_11](https://doi.org/10.1007/978-3-319-74476-6_11)

77

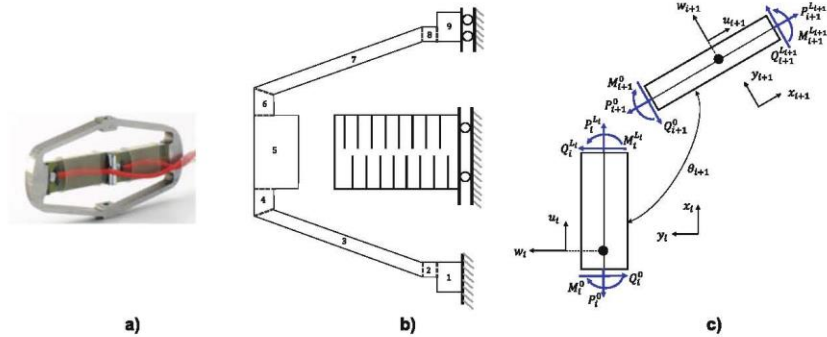


Fig. 11.1 (a) Sample RPA (b) Half RPA model (c) Planar beams connected in series

## 11.2 Methodology

According to proposed method, the RCM and the SPA are to be analyzed separately. The RPA model can be reduced to a half model by defining appropriate symmetry boundary conditions (Fig. 11.1b). A standard RCM can be decomposed into planar beams connected in series with different angles (Fig. 11.1c). Equations of motions for each beam can be written considering longitudinal and transverse deflections in the beam coordinate systems as shown in Fig. 11.1c. The generalized boundary condition equations are written for intermediate beam connections points. A closed form solution is then obtained in matrix form using eigenfunctions and boundary condition equations. Numerical methods are utilized to determine the eigenvalues and the coefficients of eigenfunctions for each beam. Then, the solution for the dynamic model of the entire RCM is obtained by means of modal superposition. The analytical solution of the half SPA is determined by using a similar approach. Tip displacement of the RCM and coupled degree of freedoms (DOFs) between the RCM and SPA are selected as master DOFs. The half RCM and the half SPA models are reduced to four and three DOF systems respectively based on master coordinates. Then, dynamic coupling methods are utilized to couple the half RCM and the half SPA in modal domain.

## 11.3 Verification of the Mathematical Model

Mathematical model of the RPA is verified by means of experimental studies and FE analysis. A miniature piezoelectric actuator CEDRAT APA35xs is selected for this purpose. Tip velocity of the actuator is measured by means of laser vibrometer while the actuator is driven by sinusoidal input voltage. Tests are performed by fixing the actuator at the bottom (Fig. 11.2a). The experimental case study is simulated on ANSYS as well. Velocity frequency responses under harmonic voltage inputs are calculated by using ANSYS Multiphysics solver with piezoelectric extension (Fig. 11.2b). Comparison of the calculated velocity response with the experimental one is illustrated in Fig. 11.3.

## 11.4 Conclusion

In this paper, a new method is proposed to obtain dynamic response of APAs with compliant mechanisms. In order to verify the analytical model, frequency responses calculated by using the mathematical model developed are compared with those obtained with FE analysis, as well as with experimentally measured ones for a sample piezoelectric actuator. It is observed from the comparison of the analytical solutions with the finite element and experimental measurement results that the mathematical model gives promising results, although the analytical response predictions are not as good as those obtained with finite element analysis.



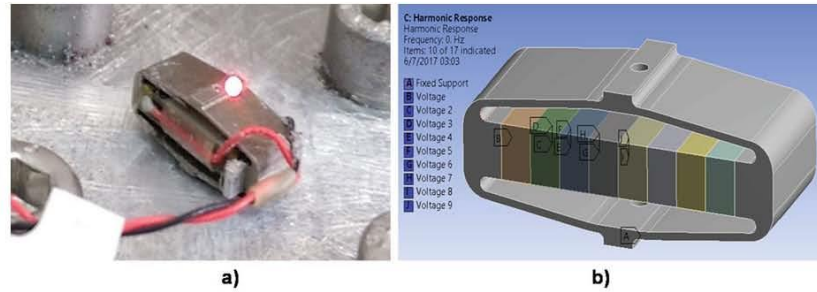


Fig. 11.2 (a) Vibration tests measurements with laser vibrometer (APA35xs), (b) FE model of APA35xs

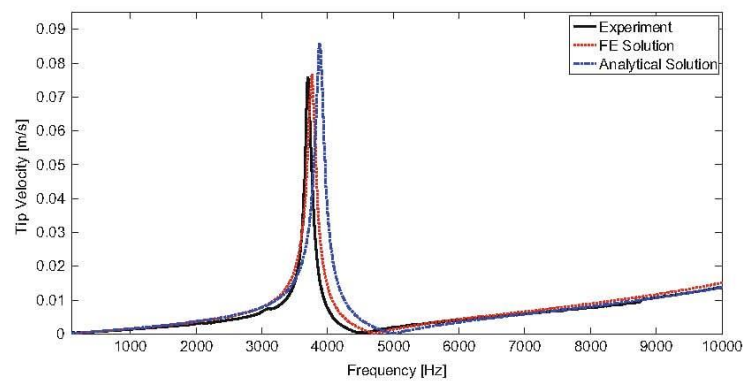


Fig. 11.3 Calculated and measured tip velocity frequency responses

## References

1. Ling, M., Cao, J., Zeng, M., Lin, J., Inman, D.J.: Enhanced mathematical modeling of the displacement amplification ratio for piezoelectric compliant mechanisms. *Smart Mater. Struct.* **25**(7), 1–11 (2016)
2. Ueda, J., Secord, T.W., Asada, H.H.: Large effective-strain piezoelectric actuators using nested cellular architecture with exponential strain amplification mechanisms. *IEEE/ASME Trans. Mechatron.* **15**(5), 770–782 (2010)
3. Cao, J., Ling, M., Inman, D.J., Lin, J.: Generalized constitutive equations for piezo-actuated compliant mechanism. *Smart Mater. Struct.* **25**(9), 1–10 (2016)
4. Yeom, T., Simon, T.W., Zhang, M., North, M.T., Cui, T.: Physical high frequency, large displacement, and low power consumption piezoelectric translational actuator based on an oval loop shell. *Sensors and Actuators, A: Physical* **176**, 99–109 (2012)



## CURRICULUM VITAE

### PERSONAL INFORMATION

Surname, Name: Koyuncu, Anıl

Nationality: Turkish (T.C.)

Date and Place of Birth: 10 March 1988, Akçakale

Marital Status: Married

Phone: +90 543 343 17 75

Email: [anlkoyuncu@hotmail.com](mailto:anlkoyuncu@hotmail.com)

### EDUCATION

<u>Degree</u>	<u>Institution</u>	<u>Year of Graduation</u>
MS	METU Mechanical Engineering	2013
BS	METU Mechanical Engineering	2010
High School	Ankara Atatürk Anadolu Lisesi	2006

### WORK EXPERIENCE

<u>Year</u>	<u>Place</u>	<u>Enrollment</u>
2017-Present	ASELSAN Inc.	System Architect
2010-2017	ASELSAN Inc.	Mechanical Design Engineer
2009 July	BİAS Mühendislik	Intern Engineering Student
2008 August	TAI	Intern Engineering Student

## **FOREIGN LANGUAGES**

Advanced English

## **PUBLICATIONS**

1. A. Koyuncu, M. Şahin, and H. N. Özgüven. "Dynamic behavior of a compliant mechanism driven by stacked piezoelectric actuators." *Structural Health Monitoring, Photogrammetry & DIC, Volume 6*. Springer, Cham, 2019. 77-79.
2. A. Koyuncu, T. Karaağaçlı, M. Şahin, and H. N. Özgüven, "Experimental Modal Analysis of Nonlinear Amplified Piezoelectric Actuators by Using Response Controlled Stepped-Sine Testing," *Exp Mech* (2022).